Terahertz Hollow Core Antiresonant Fibre

by

Jakeya Sultana

Master of Science in Electrical & Electronic Engineering
Islamic University of Technology, 2018

Bachelor of Science in Electronics & Telecommunication Engineering
Rajshahi University of Engineering & Technology, 2014

Thesis submitted for the degree of

Doctor of Philosophy

in

Electrical and Electronic Engineering,
Faculty of Engineering,
Computer and Mathematical Sciences
The University of Adelaide, Australia

September, 2022

Supervisors:
Prof. Derek Abbott, School of Electrical & Electronic Engineering
A/Prof. Brian W.-H. Ng, School of Electrical & Electronic Engineering
Dr Mayank Kaushik, School of Electrical & Electronic Engineering

Candidate:
Jakeya Sultana
Researcher Profile
Google Scholar
Researchgate
Publons
ORCiD
Linkedin

THE UNIVERSITY OF ADELAIDE
AUSTRALIA

Dedication: This work is dedicated to my parents (**Md. Saidur Rahman & Mst. Monsura Begum**) and my husband (**Dr Md. Saiful Islam**) for their constant support and patience throughout my academic life. The work is also dedicated to my principal supervisor **Prof. Derek Abbott** for his constant support, and guidance throughout the PhD journey.

Abstract

Research on fibres operating in the terahertz frequency range is rapidly growing with numerous potential applications such as in spectroscopy, imaging, security, and transmission. However, designing a terahertz fibre with controllable and desirable transmission characteristics is challenging due to the complex cladding structure. In this thesis, we study hollow core antiresonant photonic crystal fibre (HC-ARPCF) for electromagnetic transmission and refractometric sensing in the terahertz regime. The HC-ARPCF consists of an air-core surrounded by a structured polymer cladding, which confines most of the power within the air-core region. The idea behind hollow-core antiresonant fibres is that light is guided in the hollow air core, thus drastically reducing the transmission loss. Guidance of light is achieved via reflection provided by thin membranes of the antiresonant tubes that surround the core, behaving effectively as a Fabry-Pérot cavity. At antiresonant frequencies, the thin membranes reflect the light towards the core because of the higher refractive index of the membranes. The guidance mechanism of the HC-ARPCF can also be explained due to the inhibited coupling mechanism (coupling between core and cladding mode is forbidden in guidance), where the cladding mode maintains a lower density of states (η_{eff}) than the fundamental core mode. Inhibited coupling guidance in HC-ARPCF offers broad bandwidth. At resonance frequencies, the light couples to the thin membranes and the core mode becomes more lossy, which can assist in gas sensing.

The idea for the terahertz HC-ARPCF is inspired by those in the well-developed infrared and mid-infrared range. The effect of cladding pattern, cladding material, and cladding sector angle are analysed to investigate and tune the transmission loss, bending loss, and modal properties. The detailed simulations of several designs give a new understanding of the effect of the cladding elements on the leakage loss. The HC-ARPCFs are considered as a suitable candidate for low loss and broadband terahertz transmission.

In addition, we model and simulate a simple hollow-core antiresonant terahertz waveguide, show the linear properties and explore the mechanism of achieving nonlinearity. First, the linear properties of HC-ARPCF are discussed, and then the nonlinear properties of the same structure are demonstrated, considering a gas-filled core in the terahertz regime.

Furthermore, this thesis describes two different fabrication techniques for terahertz HC-ARPCF, using Zeonex and UV-resin as the bulk materials via a 3D printing process. The Zeonex filaments are made by using a *Filabot EX2 Filament Extruder* designed for filament production. To measure the effective material loss of the Zeonex, a circular disc with an uneven thickness of 0.65 ± 0.05 mm and a diameter of 24 mm is printed. We demonstrate the first successful fabrication of Zeonex and UV resin fibre using Fused Decomposition modelling (FDM) and Steriolithography Apparatus (SLA) methods, respectively, to investigate the surface quality and thickness variations of the printed structure. These printing approaches have potential to replace conventional costly terahertz fibre drawing process. The fabricated fibres are then experimentally investigated for terahertz transmission. Fibres fabricated using the FDM and SLA methods are also investigated numerically and the results are compared against the experimental results. The detailed simulations suggest their attenuation can be improved by orders of magnitude with improvements in the quality of the fabrication process. We also discuss the possible post-processing techniques that can be useful for improving fibre quality and consistency in future work.

Statement of Originality

I certify that this work contains no material which has been accepted for the award of any other degree or diploma in my name, in any university or other tertiary institution and, to the best of my knowledge and belief, contains no material previously published or written by another person, except where due reference has been made in the text.

In addition, I certify that no part of this work will, in the future, be used in a submission in my name, for any other degree or diploma in any university or other tertiary institution without the prior approval of the University of Adelaide and where applicable, any partner institution responsible for the joint-award of this degree.

I give permission for the digital version of my thesis to be made available on the web, via the University's digital research repository, the Library Search and also through web search engines, unless permission has been granted by the University to restrict access for a period of time.

I acknowledge the support I have received for my research through the provision of Adelaide Scholarship International (ASI) and full fee Scholarship.

Signature

21/09/2022

Date

Acknowledgments

I would like to take the opportunity to express my gratitude to all those people whose support, skills, friendship and encouragement have helped me to complete this thesis successfully. First of all, I would like to convey special thanks to my supervisors, Prof. Derek Abbott, A/Prof. Brian Wai-Him Ng, and Dr Mayank Kaushik. Their encouraging attitude has been valuable throughout my candidature, and helped me to grow as an engineer and research scientist. I have learned many positive and life time skills from them, which cannot be summarized in a few lines. However, I would like to highlight the ones that have inspired me the most. There is nothing defined as impossible in Derek's world. Any result of my work is treated as a major discovery by his enthusiasm and readiness for discussion. Derek's passion about research has driven me towards my limits and consequently better outcomes. Derek, Brian and Mayank's feedback on my research caused me to look at problems differently.

My thesis has been an exceptionally rewarding and memorable journey. During this journey I have worked with many engineers, scientists, and technicians, who have broadened my view and approach to tackle problems. Special thanks to Prof. Cristiano Monteiro de Barros Cordeiro, University of Campinas, Brazil, for his continuous feedback regarding the first steps in fibre printing and assistance in so many ways. I would like to thank Prof. Heike Ebendorff-Heidepriem, deputy director of Institute for Photonics and Advanced Sensing (IPAS) from School of Chemistry and Physics at University of Adelaide, for her assistance and fruitful discussion regarding various experiments.

This thesis would not have been possible without the collaboration and directions from Dr Md. Selim Habib, Department of Electrical and Computer Engineering, Florida Polytechnic University, USA, specially for guiding my first steps in fibre simulation.

I acknowledge the guidance and support from Dr Alex Dinovitser who helped me carry out the experiments correctly. He spent a lot of time with me in the lab carrying out the experimental analysis together. Based on my requirements he made a number

of devices to support my experiments. Besides, he is the person with whom I discussed every issue throughout the journey. Alex also supported me in checking and commenting on my research papers.

I would like to thank Gildo Rodrigues from UNICAMP for 3D printing (SLA samples) and Alson K. L. Ng of IPAS from University of Adelaide for technical help during the fibre measurements. Thanks goes to my external collaborator, Istihad Mahmud Ankan from Rajshahi University of Engineering & Technology, Bangladesh.

Much vital support was provided by the administrative staff of the School of Electrical and Electronic Engineering. Thanks are due to staff who keep the machine of the department running, including: Sharyn Liersch, Jodie Schluter, Sanaz Orandi, Franca Guest, and Laura McNamara.

Thanks go to my friends and colleagues from the University of Adelaide who always encouraged me for a bright future. Thanks to Mr Wing Hang (Henry) Ho for T-ray laboratory hardware and experimental assistance, Hayden Westell for conducting 3D printing in our 3D Printing Lab.

I greatly acknowledge the support from the Australian Research Council (ARC) LIEF Project (grant no. LE90100124), Sao Paulo Research Foundation (FAPESP) under grant 2018/10409, the ARC Centre of Excellence for Nanoscale BioPhotonics (CE14010003), in part, at the Optofab node of the Australian National Fabrication Facility (ANFF) supported by the Commonwealth and South Australian State Government.

I am grateful to the Australian Government, the University of Adelaide, and Faculty of Engineering, Computer & Mathematical Sciences (ECMS) for the Adelaide Scholarship International (ASI) award in 2018, as well as to the School of Electrical and Electronic Engineering of University of Adelaide for providing travel funding. I would like to thank the committee members who awarded me the Frank Perry Traveling Award to attend the 44th IRMMW-THz conference, 2019, in Paris, France.

Last but not the least, I would like to sincerely thank my husband, Dr Md. Saiful Islam for encouraging me throughout the whole journey, and my parents, Md. Saidur Rahman and Mst. Monsura Begum, for their endless and tremendous support, encouragement, and generous patience.

Jakeya Sultana

Thesis Conventions

The following conventions have been adopted in this Thesis:

Typesetting

This thesis is typeset using the LaTeX2e software. TEXnic Center is used as an effective interface to LaTeX.

Referencing

Harvard style is used for referencing and citation in this thesis.

Spelling

Australian English spelling is adopted, as defined by the Macquarie English Dictionary Dictionary, Macquarie Library, Sydney, 1982.

System of units

The units comply with the international system of units recommended in an Australian Standard: As ISO 1000–1998 (Standards Australia Committee ME/71, Quantities, Units and Conversions 1998).

Physical constants

The physical constants comply with a recommendation by the Committee on Data for Science and Technology: CODATA Mohr *et al.* (2008).

Frequency band definition

We will consider T-rays as lying in the 0.1–10 THz band as argued by Abbott and Zhang (2007). T-rays have frequencies that correspond to the so-called terahertz-gap. Thus in the field, when we refer to terahertz radiation this is an alternative term for T-rays. In this context, the term terahertz radiation is understood as meaning radiation in the terahertz-gap or T-rays and the word terahertz is not to be confused with the units of terahertz that spans three decades from 10^{12} Hz.

Publications

Journal Articles

- **J. Sultana**, M. S. Islam, C. M. B. Cordeiro, M. S. Habib, A. Dinovitser, M. Kaushik, B. W.-H. Ng, H. E. Heidepriem, and D. Abbott, "Terahertz properties of 3D printed tubular-lattice antiresonant hollow-core optical fibres," *Journal of Lightwave Technology*, (Under review), 2022.

- **J. Sultana**, M. S. Islam, C. M. B. Cordeiro, M. S. Habib, M. Kaushik, A. Dinovitser, B. W.-H. Ng, H. E. Heidepriem, and D. Abbott, "Hollow core inhibited coupled antiresonant terahertz fiber: A numerical and experimental study," *IEEE Transaction on Terahertz Science & Technology*, vol. 11, no. 3, pp. 245–260, 2021.

- **J. Sultana**, M. S. Islam, M. S. Habib, A. Dinovitser, M. Kaushik, B. W.-H. Ng, and D. Abbott, "Linearity and nonlinearity in hollow-core antiresonant fiber sensors in the terahertz regime," *IEEE Instrumentation and Measurement Magazine*, vol. 24, no. 5, pp. 5–11, 2021.

- **J. Sultana**, M. S. Islam, C. M. B. Cordeiro, A. Dinovitser, M. Kaushik, B. W.-H. Ng, and D. Abbott, "Exploring low loss and single-mode in antiresonant tube lattice terahertz fibers," *IEEE Access*, vol. 8, pp. 113309–113317, 2020.

- **J. Sultana**, M. S. Islam, C. M. B. Cordeiro, A. Dinovitser, M. Kaushik, B. W.-H. Ng, and D. Abbott, "Terahertz hollow core antiresonant fiber with metamaterial cladding," *Fibers*, vol. 8, no. 2, Art. No. 14, 2020.

- *__J. Sultana__, M. R. Islam, M. Faisal, K. Md. Abu Talha, and M. S. Islam, "Design and analysis of a Zeonex based diamond-shaped core kagome lattice photonic crystal fiber for T-ray wave transmission," *Opt. Fiber Technol.*, vol. 47, pp. 55–60, 2019.

- *__J. Sultana__, M. S. Islam, M. R. Islam, and D. Abbott, "High numerical aperture, highly birefringent novel photonic crystal fibre for medical imaging applications," *Electronics Letters*, vol. 54, no. 2, pp. 61–62, 2018.

- *__J. Sultana__, M. S. Islam, K. Ahmed, A. Dinovitser, B. W.-H. Ng, and D. Abbott, "Terahertz detection of alcohol using a photonic crystal fiber sensor," *Applied optics*, vol. 57, no. 10, pp. 2426–2433, 2018.

- *__J. Sultana__, M. S. Islam, M. R. Islam, and D. Abbott, "Highly birefringent elliptical core photonic crystal fiber for terahertz application," *Optics Communications*, vol. 407, no. 15, pp. 92–96, 2018.

- M. S. Islam, __J. Sultana__, J. Osório, B. W.-H. Ng, A. Dinovitser, F. Benabid, H. E. Heidepriem, D. Abbott, and C. M. B. Cordeiro, "Single-step tabletop fabrication for low-attenuation terahertz special optical fibers," *Advanced Photonics Research*, vol. 2, no. 12, Art. No. 2100165, 2021.

- I. M. Ankan, M. A. Mollah, __J. Sultana__, and, M. S. Islam, "Negative curvature hollow-core anti-resonant fiber for terahertz sensing," *Appl. Opt.*, vol. 59, no. 28, pp. 8519–8525, 2020.

- *M. S. Islam, __J. Sultana__, C. M. B. Cordeiro, M. J. Nine, A. L. S. Cruz, A. Dinovitser, B. W.-H. Ng, H. E. Heidepriem, D. Losic, and D. Abbott, "Experimental study on glass and polymers: Determining the optimal material for potential use in terahertz technology," *IEEE Access*, vol. 8, pp. 97204–97214, 2020.

- M. S. Islam, C. M. B. Cordeiro, M. Franco, __J. Sultana__, A. L. S. Cruz, and D. Abbott, "Terahertz optical fibers **[Invited]**," *Optics Express*, vol. 28, no. 1, pp. 16089–16117, 2020.

- *M. S. Islam, __J. Sultana__, M. Biabanifard, M. J. Nine, Z. Vafapour, C. M. B. Cordeiro, A. Dinovitser, B. W.-H. Ng, and D. Abbott, "Tunable localized surface plasmon graphene metasurface for multiband superabsorption and terahertz sensing," *Carbon*, vol. 158, pp. 559–567, 2020.

- *M. S. Islam, Cristiano. M. B. Cordeiro, __J. Sultana__, A. A. Rifat, R. Ahmed, S. Feng, A. Dinovitser, B. W.-H. Ng, and D. Abbott, "A hi-bi ultra-sensitive surface plasmon resonance fiber sensor," *IEEE Access*, vol. 7, no. 21, pp. 7908–79094, 2019.

- *M. S. Islam, __J. Sultana__, A. A. Rifat, M. S. Habib, A. Dinovitser, B. W.-H. Ng, and D. Abbott, "Localized surface plasmon resonance biosensor: an improved technique for SERS response intensification," *Opt. Lett.*, vol. 44, no. 5, pp. 1134–1137, 2019.

- M. S. Islam, **J. Sultana**, A. Dinovitser, M. Faisal, M. R. Islam, B. W.-H. Ng, and D. Abbott, "Zeonex based asymmetrical terahertz photonic crystal fiber for multi-channel communication and polarization maintaining applications," *Applied Optics,* vol. 57, no. 4, pp. 666–672, 2018.
- *M. S. Islam, **J. Sultana**, A. A. Rifat, A. Dinovitser, B. W.-H. Ng, and D. Abbott, "Dual-polarized highly sensitive plasmonic sensor in the visible to near-IR spectrum," *Optics Express*, vol. 26, no. 21, pp. 30347–30361, 2018.
- *M. S. Islam, **J. Sultana**, K. Ahmed, A. Dinovitser, M. R. Islam, B. W.-H. Ng, and D. Abbott, "Sensing of toxic chemicals using polarized photonic crystal fiber in the terahertz region," *Optics Communications,* vol. 426, pp. 341–347, 2018.
- M. S. Islam, **J. Sultana**, K. Ahmed, A. Dinovitser, B. W.-H. Ng, and D. Abbott "A novel Zeonex based oligoporous-core photonic crystal fiber for polarization preserving terahertz applications," *Optics Communications,* vol. 413, no. 15, pp. 242–248, 2018.
- M. S. Islam, **J. Sultana**, K. Ahmed, A. Dinovitser, B. W.-H. Ng, and D. Abbott, "Design and characterization of a low-loss, dispersion-flattened photonic crystal fiber for T-ray wave propagation," *Optik - International Journal for Light and Electron Optics,* vol. 145, pp. 398–406, 2018.
- M. S. Islam, **J. Sultana**, M. Faisal, M. R. Islam, A. Dinovitser, B. W.-H. Ng, and D. Abbott, "A modified hexagonal photonic crystal fiber for terahertz applications," *Optical Materials,* vol. 79, pp. 336–339, 2018.
- M. S. Islam, **J. Sultana**, A. A. Roni, A. Dinovitser, B. W.-H. Ng, and D. Abbott, "Terahertz sensing in a hollow core photonic crystal fiber," *IEEE Sensors Journal,* vol. 18, no. 10, pp. 4073–4080, 2018.
- M. S. Islam, **J. Sultana**, K. Ahmed, A. Dinovitser, B. W.-H. Ng, and D. Abbott, "A novel approach for spectroscopic chemical identification using photonic crystal fiber in the terahertz regime," *IEEE Sensors Journal,* vol. 18, no. 2, pp. 575–582, 2018.
- M. S. Islam, **J. Sultana**, M. Dorraki, J. Atai, M. R. Islam, A. Dinovitser, B. W.-H. Ng, and D. Abbott, "Low loss and low dispersion hybrid core photonic cystal fiber for terahertz propagation," *Phot. Net. Comm.,* vol. 35, no. 3, pp. 364–373, 2018.

Conference Papers

- **J. Sultana**, M. S. Islam, C. M. B. Cordeiro, M. S. Habib, A. Dinovitser, M. Kaushik, B. W.-H. Ng, and D. Abbott, "3D printed terahertz antiresonant fibers for controllable guiding properties," *47th Int. Conf. on Infra. Milli. & Terahertz Waves, 2022.* (Accepted, June 2022).

- **J. Sultana**, M. S. Islam, C. M. B. Cordeiro, A. Dinovitser, B. W.-H. Ng, and D. Abbott, "Novel hollow core antiresonant terahertz fiber with metamaterial cladding," *44th Int. Conf. on Infra. Milli. & Terahertz Waves, 2019.* DOI: 10.1109/IRMMW-THz.2019.8873836.

- **J. Sultana**, M. S. Islam, C. M. B. Cordeiro, A. Dinovitser, B. W.-H. Ng, and D. Abbott, "Five-capillary cladded terahertz fiber with low loss and single mode," *44th Int. Conf. on Infra. Milli. & Terahertz Waves, 2019.* DOI: 10.1109/IRMMW-THz.2019.8874476.

- *M. S. Islam, A. Upadhyay, R. T. Ako, **J. Sultana**, B. W.-H Ng, M. Bhaskaran, S. Sriram, and D. Abbott, "Terahertz ultrahigh-Q metasurface enabled by out-of-plane asymmetry," *45th Int. Conf. on Infra. Milli. & Terahertz Waves, 2020.* DOI: 10.1109/IRMMW-THz46771.2020.9370414.

- M. S. Islam, **J. Sultana**, A. Dinovitser, K. Ahmed, M. R. Islam, M. Faisal, B. W.-H. Ng, and D. Abbott, "A novel Zeonex based photonic sensor for alcohol detection in beverages," *IEEE International Conference on Telecommunication and Photonics (ICTP), 2018.* DOI: 10.1109/ICTP.2017.8285905.

***All publications indicated with an asterisk resulted from side projects not directly related to this thesis.**

Contents

List of Figures

List of Tables

Introduction

THIS introductory chapter offers a brief introduction to terahertz radiation, and explains unique properties, associated challenges, waveguides and prospective applications of terahertz. This chapter also includes the motivations for pursuing the research, and outlines the structure of the thesis, contents in each chapter, and the original contributions.

1.1 Terahertz radiation or T-rays

Terahertz or T-ray radiation lies between well explored microwave and infrared frequencies and bridges the gap between electronics and optics, respectively. Microwaves mark the upper frequency limit of electronics, and infrared marks the lower frequency limit of optics. This thesis will specify the unit for terahertz spectrum as THz (10^{12} Hz), although the different forms of unit are also used. The units that are directly relevant are as follows:

- Frequency: $f = 0.1$–10 THz
- Time: $t = 1/f = 0.1$–10 ps
- Wavelength: $\lambda = c/f = 30$ μm–3 mm
- Wavenumber: $\bar{k} = 1/\lambda = 3.3$–$333$ cm^{-1}
- Photon energy: $hf = \hbar\omega$ = 410 μeV–41 meV

where, c and $h = 2\pi\hbar$ indicate the speed of light in free space and Planck's constant respectively.

Figure 1.1(a) depicts a broad view of the electromagnetic spectrum in terms of frequency together with the application areas. The electromagnetic spectrum contains the familiar electromagnetic waves including visible light, x-rays and radio waves. Any variations in spectra are fundamentally defined by how radiation interacts with matter. For example, the terahertz spectrum interacts strongly with systems that have characteristic lifetimes in the picosecond range and/or energies in the meV range. Such systems include bound electrical charges (Cole *et al.* 2001), free charge plasmas (Huber *et al.* 2001), strongly confined charge plasmas (Cooke *et al.* 2006), transient molecular dipoles (Beard *et al.* 2002), phonons in crystalline solids (Schall *et al.* 2001), hydrogen bonds in chemicals (Walther *et al.* 2003), intermolecular forces in liquids (Ronne *et al.* 1997), and biological matter (Whitmire *et al.* 2003).

Figure 1.1(b) depicts an enlarged terahertz spectrum. In general, terahertz electromagnetic radiation lies between microwave EHF (extremely high-frequency waves) and far infrared frequencies and overlaps somewhere between them. This type of overlap is

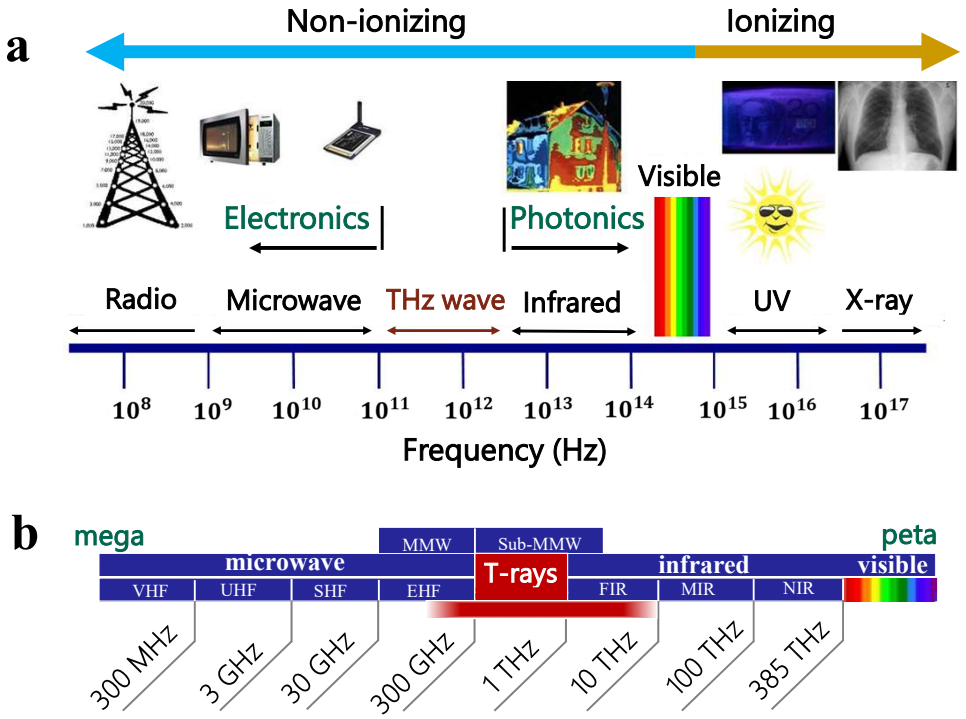

Figure 1.1. Electromagnetic spectrum. (a) Broad-view of electromagnetic spectrum showing the T-ray band and its neighboring electronics and photonics band. (b) Expanded view of the neighborhood of the T-ray band, indicating the lower and upper ends of the T-ray band overlaps the EHF and FIR bands, respectively. After Woolard *et al.* (2005), Withayachumnankul (20o9).

not unusual in other parts of the electromagnetic spectrum (Abbott and Zhang 2007). The microwave EHF (millimeter), sub-millimeter (extremely far-infrared) (Wiltse 1984) and far infrared band span between 0.03–0.3 THz, 0.3–3 THz and 3–30 THz, respectively. Therefore, there is no exact quantified limit in the literature for the terahertz frequency regime. Terahertz radiation is usually defined within the frequency range of 0.1–10 THz (Abbott and Zhang 2007, Mittleman 2013a, Mittleman 2013b, Nielsen 2011, Barh *et al.* 2015, Van Putten 2019, Chen *et al.* 2006), while some researchers extend it up to 0.1–30 THz (Tonouchi 2007) or narrow it down to 0.3–3 THz (Siegel 2010).

1.2 Terahertz gap

The *terahertz gap* defines the relatively unused frequency band between "electronic" and "photonic" approaches. Although semiconductor devices are the enabling components for all of the technologies where the signals are carried by radiation at 100 kHz

(radio wave), 3 GHz (microwave) or 300 THz (near infrared light), conventional solid-state optical and electronic technologies simply cannot attain useful output power at frequencies across the gap. Therefore, before 1986, artificial generation and detection of terahertz radiation was extremely difficult, while holding enormous promise. The explanations for the *terahertz gap* refer to the challenges in terahertz generation and detection.

There are essentially two ways of generating coherent radiation from solid-state devices. The former one is classical electronic oscillators, in which charge is made to oscillate back and forth within a device. The frequency of radiation corresponds to the frequency of charge oscillation. Classical oscillators based on high-speed transistors efficiently produce radiation in the low-frequency region (Huang *et al.* 1997, Eisele and Haddad 1998), which stop working at high frequencies (limited to about 0.3 THz), because the speed of oscillation is limited by capacitive effects and the transit time for electrons to move around the device. The parasitic capacitances work as low-pass filters that block the terahertz spectrum (Sedra *et al.* 2020) and typical semiconductor response times are not well-suited for operation in the terahertz range. Therefore, electronics-oriented devices cause unwanted resistances and capacitances that reduce the output power with respect to increase in frequency and they are typically unusable at moderate terahertz frequencies.

Higher frequency sources commonly exploit solid-state lasers, in which charge-carriers undergo a transition typically between two energy levels. At high frequencies, semiconductor lasers generate coherent light for telecommunication links based on optical fibres that can extend down to 10 THz (Sirtori 2002). Here, the frequency corresponds to the energy separation between the states (band gap). Conventional semiconductor lasers stop working at high frequencies because the band gap of materials is too large (1 THz = 4 meV). That means terahertz generation is limited by lack of suitable narrow band-gap semiconductors (Siegel 2002, Mullins 2002). The band-gaps corresponding to lower terahertz frequencies ($<$ 10 THz) become comparable to the lattice vibration energy, and hence they are associated with large thermal noise (Siegel 2002). Therefore, 0.1 to 10 THz range was previously referred to as the terahertz gap with prior established technologies because semiconductor technology was not invented to efficiently convert electrical power into terahertz electromagnetic radiation (Nichols and

Tear 1925). Achieving intense, broadband, and coherent spectroscopic measurement in the terahertz regime has remained a technical challenge.

Another limiting factor in semiconductors comes from reststrahlen absorption in which photons are absorbed by mechanical vibrations (phonons) in the crystal lattice. Reststrahlen absorption depends on the material, for example, in GaAs (Gallium arsenide, the most common THz quantum cascade lasers (QCL) material), the reststrahlen absorption occurs around 36 meV (or $\sim$ 9 THz). In that cases, the reststrahlen absorption effectively makes terahertz radiation impossible to generate anywhere near that frequency. Apart from this source limitation, terahertz propagation at ambient temperature suffers from high atmospheric absorption.

Together, the problem with a low power terahertz source (due to low generation efficiencies), the long signal acquisition times (due to long detector integration times and slow delay line speeds), the relatively expensive femtosecond pump lasers and high atmospheric absorption, weak interaction signatures, and standing wave interference have inhibited the development of practical technologies that exploit terahertz.

1.3 Application of T-rays

Terahertz technological advances have experienced an exponential growth (Lewis 2014) in three principle application areas: sensing, imaging and communications.

Terahertz systems provide the sensing capabilities for many research fields including security screening/package inspection (Luukanen *et al.* 2012, Karpowicz *et al.* 2005, Kawase *et al.* 2003), biological spectroscopy (Nagel *et al.* 2002), industrial process control, safe medical imaging (Reid *et al.* 2010, Yu *et al.* 2012, Woodward *et al.* 2002), nondestructive evaluation of priceless artefacts and art (Walker *et al.* 2013, Krumbholz *et al.* 2009), environment monitoring, explosive detection (Yamamoto *et al.* 2004), drug identification and pharmaceutical quality control (Taday *et al.* 2003, Zeitler *et al.* 2007, Shen 2011), food quality inspection, electronics fault monitoring (Kiwa *et al.* 2003), astro-observation, and in material science (Hu and Nuss 1995, Mittleman *et al.* 1996, Woodward *et al.* 2002, Kemp *et al.* 2003, Tribe *et al.* 2004, Woolard *et al.* 2005, Shen *et al.* 2005, Leahy-Hoppa *et al.* 2007, Song and Nagatsuma 2011, Kleine-Ostmann

and Nagatsuma 2011, Kemp 2011, Kulesa 2011, Kawano 2013, O'Hara *et al.* 2019, Jackson *et al.* 2011, Dexheimer 2017, Mittleman 2013a).

Initially, the invention of terahertz radiation involves passive applications, where the terahertz signal is detected for molecular spectral analysis, and astronomical and atmospheric remote sensing (Siegel 2010, Kulesa 2011, Beckman and Harries 1975, Siegel 2003, Siegel 2002). Terahertz frequencies show the signature variations (unique molecular resonance) for three different states characterisations: crystalline vibrations in solids, intermolecular interactions in liquids, and rotational transitions in gases. The absorption bands serve as their chemical fingerprints (McClatchey 1972, Van Exter *et al.* 1989, Ho *et al.* 2008, Walther *et al.* 2002, Mantsch and Naumann 2010, Fukunaga *et al.* 2007). These vibrational or rotational transitions of a wide range of molecular clusters, and electronic transitions of many nanocomposites (chemical and biological substances) are the key factors that have fueled a long term focus on laboratory-based molecular spectral analysis (medicines, cancer tissue, DNA, proteins and bacteria) (Löffler *et al.* 2001, Taday *et al.* 2003, Fischer *et al.* 2005, Walther *et al.* 2003, Whitmire *et al.* 2003, Chen *et al.* 2005, Nagel *et al.* 2002, Ogawa *et al.* 2008) and in astronomical and atmospheric remote sensing.

Terahertz waves can deeply penetrate through non-polar, dry, and non-metallic materials, for example, cloth, ceramics, brick, wood, paper, dry air, polymers etc., but they are absorbed by water vapour, dust, clouds, and sufficiently dense objects or are generally reflected by metals (Yang *et al.* 2012). All these excellent qualities of terahertz radiation make it suitable for imaging of hidden objects, such as explosives, metallic weapons etc. (Davies *et al.* 2008, Puc *et al.* 2015, Federici *et al.* 2005, Tonouchi 2007, Woolard *et al.* 2005). It is also useful for monitoring buried defects in IC packages, layers of paint, tiles, spacecraft components etc. (Oyama *et al.* 2009, Groves *et al.* 2009, Abraham *et al.* 2010). The possibility of material characterisation, classification or recognition by means of terahertz spectroscopy has also been investigated (Sakai 2005, Naftaly and Miles 2007, Fischer *et al.* 2007, Islam *et al.* 2019, Islam *et al.* 2020, Ferguson and Zhang 2002, Beard *et al.* 2001, Grischkowsky *et al.* 1990, Shi *et al.* 2019, Anthony *et al.* 2011a, Bolivar *et al.* 2003, Cunningham *et al.* 2011, Chang *et al.* 2017). Most importantly, the strong absorption of T-rays by water molecules makes it suitable for sensing the hydration level in biological tissue, primarily focused on skin conditions.

This technology has already begun to make deep inroads in non-invasive medical diagnostics, such as detection of skin cancer (Löffler *et al.* 2001, Chiu *et al.* 2009), tooth decay, and identification of human thin tissues based on the unusual reflections from affected tissues, and different refractive indices and linear absorption coefficients at terahertz frequencies (Zhang 2002, Löffler *et al.* 2001, Woodward *et al.* 2001, Pickwell and Wallace 2006, Humphreys *et al.* 2004, Woodward *et al.* 2002, Wallace *et al.* 2004, Siegel 2004, Yu *et al.* 2012). Also, terahertz radiation is less susceptible to scattering than optical waves due to its longer wavelength, has low photon energy (for example, 4 meV at 1 THz) making it non-ionizing, and can yield high resolution images (Zhang 2002, Siebert *et al.* 2002, Fitzgerald *et al.* 2002, Chen *et al.* 2003, Reid *et al.* 2010). Moreover, terahertz is not harmful to human health when applied at low power levels (Kowalski *et al.* 2015, Löffler *et al.* 2001, Han *et al.* 2000, Mittleman *et al.* 1997, Smye *et al.* 2001, Berry *et al.* 2003, Clothier and Bourne 2003, Yu *et al.* 2012, Woodward *et al.* 2002).

Communications technology also benefits from terahertz technology where it is used for a wide range of applications, such as wireless communication, high-speed data processing and satellite communication. Terahertz can wirelessly transfer bulk data files (Kleine-Ostmann and Nagatsuma 2011, Koenig *et al.* 2013, O'Hara *et al.* 2019) in a short-range communication systems (Hirata *et al.* 2006, Hirata *et al.* 2009), and can significantly increase the data rate over existing microwave technology (Kleine-Ostmann and Nagatsuma 2011, Koenig *et al.* 2013, Piesiewicz *et al.* 2007, Song and Nagatsuma 2011). To-date, most noteworthy demonstrations of terahertz communication have been limited to carrier frequencies at or below 0.4 THz, achieving reliable transmission with data rates of several tens of Gbps (Nagatsuma *et al.* 2009, Song *et al.* 2012, Koenig *et al.* 2013, Song *et al.* 2014, Nagatsuma *et al.* 2016). Additionally, higher carrier frequencies have been demonstrated (Ishigaki *et al.* 2012, Kitagawa *et al.* 2016), and with advances in source technology, as well as multi-level modulation schemes, it is anticipated that carrier frequencies up to and beyond 1 THz will become viable for high-volume communication links.

1.4 Thesis outline

As outlined in Figure 1.2, the thesis encompasses six chapters. The original contributions of this thesis are provided in Chapters 3 to 5. The fundamentals necessary for

understanding the main idea of each chapter are provided in the respective chapters. An additional review chapter revolving around terahertz hollow fibres with key optical properties such as loss, guiding mechanism, geometrical structures, fabrication and characterization mechanisms is discussed in Chapter 2. In Chapter 6 the summary of the thesis, the aim of each chapter, the methodology, the results, and the future directions are discussed. The detailed description for each chapter of the thesis is as follows:

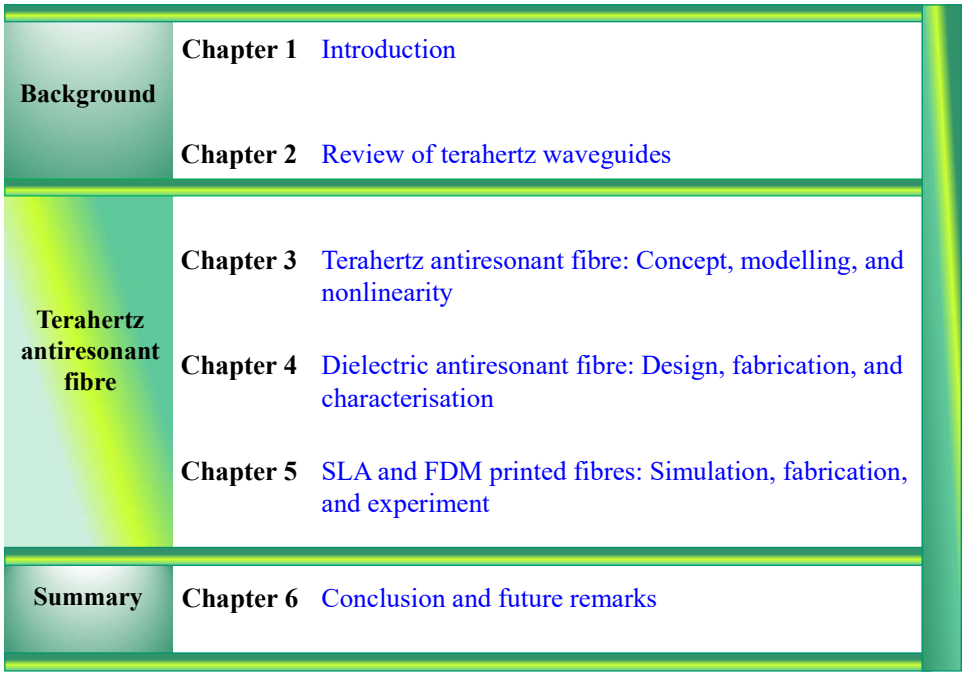

Figure 1.2. Thesis outline. The thesis is composed of six chapters where the original contributions are from Chapter 3 to Chapter 5. Chapter 6 provides an overall summary and future direction of the thesis.

Chapter 1: Introduction provides a detail overview of terahertz and its applications, the structure of the thesis, motivation of the work, and a detailed discussion of the original contribution.

Chapter 2: Review of terahertz waveguides include a literature review of terahertz optical fibres (mostly aimed at dielectric hollow waveguides) in terms of loss, dispersion, the background material, guiding mechanisms, waveguide structure, the fabrication methodologies, the experimental procedures, and key terahertz applications. This chapter provides a guideline to identify the research gap for further development of

terahertz technologies.

Chapter 3: Terahertz antiresonant fibre: Concept, modelling, and nonlinearity. In this chapter, typical, nested and adjacent nested designs of terahertz dielectric antiresonant fibres is presented to determine an optimal fibre for terahertz applications. In addition, an ideal approach for improving the confinement and stripping of undesired higher order modes is demonstrated. The effect of cladding air-tubes on the guiding properties of antiresonant fibres especially transmission loss, bending loss, and modal properties are investigated. Transmission properties such as effective material loss, core power fraction, confinement loss, core mode, cladding mode, core higher-order modes (HOMs), and the angle dependence of adjacent tubes are analyzed to choose optimal fibres for transmission applications. Analysis of the fibre designs shows that the nested tube-based antiresonant fibre exhibits lower transmission loss and superior HOM suppression, exceeding 140. To our knowledge, this is the largest higher-order mode extinction ratio (HOMER) value for any kind of terahertz fibre

Chapter 3 also describes a novel class of terahertz antiresonant fibres with metamaterial cladding. The metamaterial cladding is created by adding sub-wavelength metal wires (aluminium) into the dielectric Zeonex cladding. The guiding properties such as effective material loss, core power fraction, confinement loss, modal properties and signal degradation (loss) of these antiresonant fibres are evaluated and quantitatively compared to that of an antiresonant fibres with dielectric cladding. Simulation results show that broadband terahertz radiation can be guided with six times lower loss in such hollow core fibres with metallic inclusions, compared to tube lattice fibre, covering a single mode bandwidth (BW) of 700 GHz.

A possible mechanism to obtain nonlinearity from a linear terahertz hollow core antiresonant fibre is also discussed in **Chapter** 3. The fibre designs and simulations are carried out using COMSOL multiphysics software.

Chapter 4: Dielectric antiresonant fibre: Design, fabrication, and characterisation involves fabrication of terahertz hollow core antiresonant fibre exploiting the 3D printing technique. Zeonex filaments are made in-house with a *Filabot EX2 Filament Extruder* and the filament is compatible with the Fused Decomposition Method (FDM) for 3D fibre printing. For the first time we study printing parameters for Zeonex, including nozzle temperature, and extrusion velocity and investigate their impact on optical performance in the terahertz regime. The experimental analysis of the Zeonex based fibre is also carried out using Menlo terahertz system. A promising result is found for short distance low loss data transmission.

Chapter 5: SLA and FDM printed fibres: Simulation, fabrication, and experiment includes investigation of loss of fabricated polymer hollow core antiresonant fibres using two differnt printing methods. The structures are first simulated and afterwards analyzed by a standard THz-TDS system. The optimized fibre is fabricated with the FDM and SLA techniques. No previous studies have compared these techniques and the corresponding impact on terahertz performance. For the first time we consider the thickness variation, roughness and transparency of the printed object, quantify the thickness variation as a function of antiresonant tube number for a constant adjacent gap, and measure the performance based on the printing method, thickness variation and antiresonant tube number. In order to investigate the variation of designed and fabricated fibre cross-sections, the effective loss for both techniques are numerically modelled and compared. Imperfections caused by the limitations of the printer available are studied in more detail in the post-fabrication analysis, showing possible improvements in the waveguide's performance when the print quality can be improved.

Chapter 6: Conclusion and future remarks summarize the major outcomes, the methodologies, author's contribution, and conclusions of this work. It also provides future research perspectives for this field.

Several appendices at the end provide supporting information and technical details. Appendix A provides the step-by-step simulation procedure using COMSOL multi-physics simulation software. Appendix B describes the equipment used to characterise the terahertz hollow core antiresonant fibres.

1.5 Summary of original contribution

This thesis makes a number of original contributions in the field of hollow core antiresonant fibre-based terahertz transmission, as declared in this section.

Terahertz hollow core aniresonant fibre can be an ideal candidate for spectroscopic analysis, short-range terahertz transmission, and gas-based nonlinear applications. The typical, nested and adjacent nested antiresonant hollow core tube lattice fibres are proposed to determine the optimal waveguide structure for low loss and broad bandwidth terahertz transmission (Sultana *et al.* 2019c, Sultana *et al.* 2020b). These waveguides consist of node-free negative curvature cladding pattern transverse cross-section, that leads to the enhancement and confinement of the mode field within the hollow core. The non-touching core boundary assists in the reduction of the loss caused by the Fano-resonance. The HC-ARPCF is a relatively simple design for fabrication with excellent mode qualities and controllable bandwidth. For the first time, we have analyzed five-tube HC-ARPCF in-depth and compared the performance when the tube number is more than five and the adjacent antiresonant tube gap is constant. We have established that a five-tube fibre is advantageous both in lower transmission loss and higher-order mode suppression. Additionally, the adjacent nested HC-ARPCF is very new in terahertz and we have demonstrated that adjacent nested HC-ARPCF shows very similar loss characteristics to nested HC-ARPCF with proper optimization. With optimized fibre dimensions, the fundamental core mode, cladding mode, core higher-order modes (HOMs), bending loss, and the angle dependence of adjacent tubes are analyzed to obtain the optimal design for low loss terahertz transmission. Analysis of the fibre designs shows that the nested tube-based antiresonant fibre exhibits lower transmission loss and superior HOM suppression, exceeding 140. To our knowledge, this is the highest HOMER value for any kind of terahertz fibre. The nested HC-ARPCF is feasible for fabrication using existing fabrication technologies and opening up the possibility of efficient transmission of terahertz waves.

The thesis investigates a novel class of HC-ARPCF with metal inclusions and compares the result with typical dielectric HC-ARPCF (Sultana *et al.* 2019a, Sultana *et al.* 2020a). The proposed structure consists of seven non-touching, circular-dielectric antiresonant tubes, where the cladding dielectric layer contains metal wires, employing Zeonex dielectric and aluminum metal. Numerical study of fundamental and HOMs of the proposed fibre shows wide-range single mode guidance (covering a single mode bandwidth of 700 GHz), strong light confinement and six times lower loss than the tube lattice fibre. We also address the impact of effective refractive index (η_{eff}) and waveguide modes on transmission characteristics for HC-ARPCF with and without metal wires. The results show that the LP_{11} is influenced mostly by changes to the cladding pattern. The proposed structure with a hollow core is a potential candidate for a low loss terahertz waveguide.

This thesis further demonstrates a novel approach for preparing ultrashort pulses from a gas-filled antiresonant fibre that has been presented to achieve efficient broadband terahertz generation and detection (Sultana *et al.* 2021, Sultana *et al.* 2020c). We model and simulate a simple dielectric HC-ARPCF, showing the linear properties to explore the mechanism of achieving nonlinearity with the established technology, considering a gas-filled HC-ARPCF in the terahertz regime. An open research problem is the lack of high power terahertz laser sources that can create linear and nonlinear pulses simultaneously for nonlinear applications such as terahertz supercontinuum generation, terahertz high harmonic generation. The linear properties of an evacuated waveguide become nonlinear by tuning the gas pressure, creating a broadband terahertz spectrum due to Self-phase modulation (SPM). The approach is interesting due to the low cost of the technology and the simplicity of the waveguide architecture.

This thesis also demonstrates a seven non-touching, circular-dielectric antiresonant tubes fabrication, and experiments of terahertz HC-ARPCF (Sultana *et al.* 2020c). The inhibited coupled HC-ARPCF is fabricated by fused deposition modeling (FDM) of 3D printing technology. For the first time, the methodology of Zeonex filament fabrication, Zeonex 3D fibre printing, and terahertz material loss of printed Zeonex are discussed in detail. The polymer pellets are obtained from the Zeon corporation, Japan, for forming filaments of Zeonex with a *Filabot EX2 Filament Extruder*. Guidance through air-core is examined for transmission and for charactering the coupling loss using five different

fibre lengths. The experimental analysis is carried out using terahertz time domain spectroscopy (THz-TDS) for low loss transmission of terahertz waves.

Finally, experimental results to characterize a controllable cladding field that controls the low and high loss spectra, corresponding bandwidths, and mode interference in the HC-ARPCF by variation of cladding tube number and strut thickness with fixed adjacent tube gap is reported in detail. We analyze the transmission properties as a function of cladding sector angle, cladding-strut thickness, and cladding tube number, where the adjacent cladding gap is constant. Using inexpensive FDM with Zeonex polymer and SLA with UV-resin, we subsequently analyse the print quality and thickness variation of HC-ARPCFs. The UV-resin fibres are obtained from the University of Campinas, Brazil. No previous studies have compared these two printing approaches for the same fibre geometry and the corresponding impact on terahertz performance. This thesis reveals the cause of surface roughness and the affect on performance of surface roughness, thickness variation, non transparent structure of the two different printing approaches and provides systematic studies of post-fabrication quality improvements through chemical treatment, CO_2, laser treatment, annealing process (FDM technique) or laser power intensity and spot diameter, scan speed, curing or the exposure time, layer thickness, and lift speed of the build plate (SLA technique), respectively. Terahertz time-domain spectroscopy (THz-TDS) is used to characterize the HC-ARPCFs manufactured by FDM and SLA, using the TERA K15 system from Menlo Systems GmbH.

These original contributions in this Thesis serve to advance terahertz transmission through printed HC-ARPCF. The broad impact may be envisaged in the applications to terahertz sensing, transmission and non-linear applications, where a strong interaction of terahertz radiation and sample under investigation can be achieved utilising a HC-ARPCF.

Review of terahertz waveguides

IN this chapter we review the mathematical model, background history, guiding mechanisms, characterisation methods, recent advances, mode profile, fabrication methodologies and applications of terahertz antiresonant fibre. We first review non-planar terahertz hollow fibres to illustrate the inhibited coupling guiding mechanism. We also examine the difference between the inhibited coupling guiding mechanism and the photonic band-gap mechanism in hollow core fibre. We also summarize various types of dielectric and metal based terahertz optical fibre including hollow core, solid core, porous-core fibres, and their key optical properties.

2.1 Introduction

Dry air is considered to be the best terahertz transmission media in terms of both low-loss and low-dispersion. However, free space terahertz transmission experiences many undesirable losses due to the presence of water vapour, dust, and cloud that significantly reduce transmission efficiency and may vary with weather, climate change, geographical location, altitude etc. Therefore, the terahertz applications in practice are only limited to laboratory based experimental research as most of the terahertz devices depend on free space transmission and manipulation. The bulk optics used for manipulating the terahertz radiation in free space terahertz time-domain spectroscopy systems (TDS) require expert alignment and servicing, making the systems vulnerable to environmental disturbance. One part of the solution is to replace the free-space optical components with low-loss waveguides due to the need for a compact, reliable, and flexible terahertz system for a wide range of applications (Mittleman *et al.* 1996, Mittleman *et al.* 1998). Therefore, in order to upgrade terahertz systems it is necessary to build up low loss, low-dispersion, broadband waveguides for a number of applications, such as remote sensing, long range communication, collimated and diffraction limited beam guiding, and medical imaging. In free space-based terahertz systems, terahertz waves are generated very close to the target, which is directly illuminated for reflection or transmission spectroscopic analysis. A low-loss waveguide, on the other hand, can deliver the terahertz waves around bends and corners to the desired target, and permit mechanical or medical diagnostics by enabling flexible endoscopes and fibrescopes. Low-dispersion is also needed, especially in spectroscopic applications, to avoid the broadening of the pulses.

One of the largest remaining hurdles is terahertz waveguiding. There has been a great challenge to achieve low loss and low dispersion waveguides for undistorted propagation of terahertz pulses. The primary barrier comes from the limited number of suitable materials, complex waveguide structure, and difficulties in fabrication procedure. As lowest is vacuum absorption loss for terahertz waves occurs in dry air, the transmission losses of the terahertz fibres can be reduced significantly by maximizing the fraction of the terahertz power guided in low-loss air. Based on this strategy, various terahertz waveguides and fibres have been proposed. There are many demonstrations of terahertz waveguides based on the material: dielectric waveguide, metallic waveguide, and in some cases metal-dielectric hybrid waveguide. Metals that are suitable

for microwave frequencies have high Ohmic losses, while polymers and glasses that work properly for infrared (IR) and optical frequencies have unacceptable frequency dependent absorption losses. Metal waveguides experience strong dispersion near the cut-off frequency of the guiding mode unless they support a transverse electric and magnetic (TEM) mode that has no cutoff frequency. Whereas, dielectric waveguides suffer mainly from waveguide dispersion. Although the dispersion can be tailored around a frequency, it is challenging to find a dielectric waveguide that offers almost zero dispersion for the entire broad spectrum of terahertz.

The idea of terahertz waveguides (Hasnain *et al.* 1986, Frankel *et al.* 1991) has come from well developed parts of the frequency spectrum microwaves, composed of coplanar transmission lines. They suffer from a high attenuation coeffecient (20 cm^{-1}) due to the combined effects of Ohmic loss, absorption loss inside a dielectric substrate, and radiation loss. Therefore, non-planar terahertz waveguide structures have beome an attractive option for terahertz pulse propagation, and the concepts come from well developed parts of the frequency spectrum, either microwaves or optics. Metal-based waveguides include metal wire and have reported attenuation coeffecient of order 0.01 to 1 cm^{-1}. Hollow metallic circular waveguides (McGowan *et al.* 1999, Gallot *et al.* 2000), hollow metallic rectangular waveguides (Gallot *et al.* 2000), sapphire fibre (Jamison *et al.* 2000), plastic ribbon waveguides (Mendis and Grischkowsky 2000, Yeh *et al.* 2005), air-filled parallel-plate waveguides (Mendis and Grischkowsky 2001a, Mendis and Grischkowsky 2001b), plastic photonic crystal fibres (Han *et al.* 2002), metal wire waveguides (Wang and Mittleman 2004, Jeon *et al.* 2005, Wåchter *et al.* 2005), coaxial waveguides (Jeon and Grischkowsky 2004), metal-coated dielectric tubes (Ito *et al.* 2007), parallel-plate photonic waveguides (Bingham and Grischkowsky 2008), metal sheet waveguides (Jeon and Grischkowsky 2006), the dielectric-filled parallel-plate waveguides (Mendis 2006), low-index discontinuity terahertz waveguides (split rectangular and tube waveguides) (Nagel *et al.* 2006b), and metallic slit waveguides (Wächter *et al.* 2007), sub-wavelength fibres (Chen *et al.* 2006), porous fibres (Hassani *et al.* 2008a, Islam *et al.* 2016, Islam *et al.* 2017c), and photonic band-gap (Nielsen *et al.* 2011, Bao *et al.* 2012), kagome hollow fibres (Anthony *et al.* 2011b), and antiresonant fibre (Wu *et al.* 2011b).

As a classical optical fibre, electromagnetic waves can be confined to dielectric waveguides via the total internal reflection effect/index guiding (IG) (Agrawal 2012), the modified total internal reflection (mTIR) (Poli *et al.* 2007) in microstructured fibres (or Photonic Crystal fibre-PCF), the photonic band-gap effect (PBG) (Knight *et al.* 1998), the anti-resonant effect with inhibited coupling of core and cladding modes (Vincetti and Setti 2010) and the topological channel effect in helically twisted structures (Beravat *et al.* 2016). All of them have already been explored for making fibre structures for terahertz transmission.

2.1.1 Objective and framework

We first review the one-dimensional dielectric ribbon waveguides, two-dimensional solid and porous core fibre to illustrate the total internal reflection and in some cases, photonic band gap guidance in Section 2.3 and 2.4. Pipe waveguide, kagome lattice fibres, and more specifically antiresonant tube lattice fibres are illustrative of inhibited guiding and antiresonant guiding mechanisms in Section 2.5. The previous advancements in geometry, applications and fabrication of hollow fibres are discussed also. We also review photonic band-gap structures in Section 2.6. The objective of Section 2.6 is to understand more about the antiresonant tube lattice fibres. We place our hollow core antiresonant fibre discussions into two categories: dielectric and metamaterial in 2.7. We outline the most recent technological advancements in the design, fabrication and characterization of negative curvature tube lattice fibres for applications in the terahertz waveband in 2.8.

2.2 Dielectric waveguide

Research on terahertz dielectric waveguides begins with identifying which polymers will remain flexible at relatively large diameters (on the mm scale), have low absorption, and suitable refractive index. This has led to investigations into solid-core, porous-core, and hollow-core terahertz waveguides based on microstructured polymer fibres.

2.3 Solid core fibres/Index guiding-fibres

The core of a solid (index guiding) fibre has higher refractive index than the surrounding cladding region, and light is guided in the core via total internal reflection at the

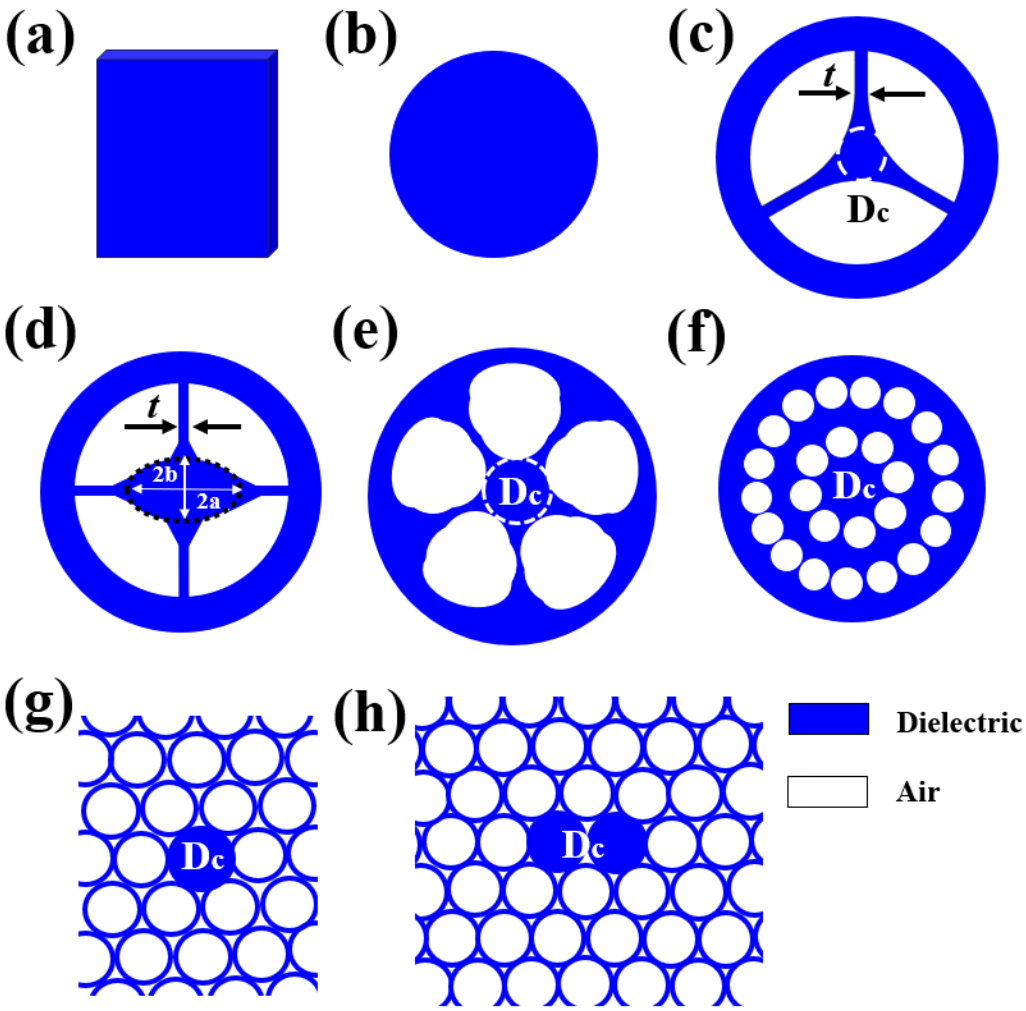

Figure 2.1. Total internal reflection at the solid core in terahertz. (a) Ribbon waveguide (Mendis and Grischkowsky 2000) (b) Wired fibre (Jamison *et al.* 2000, Chen *et al.* 2006, Roze *et al.* 2011, Chiu *et al.* 2009, Chen *et al.* 2009, Chen *et al.* 2011, Lu *et al.* 2008a, You *et al.* 2009, You *et al.* 2010) (c) Suspended solid core fibre (Roze *et al.* 2011, Talataisong *et al.* 2020, Xiao and Lu 2017) (d) Suspended elliptical core fibre (e) Suspended core microstructured fibre (Anthony *et al.* 2011a) (f) Solid-core microstructured fibre (Goto *et al.* 2004, Nielsen *et al.* 2009) (g) Solid-core microstructured fibre (Han *et al.* 2002) (h) Asymmetric solid core microstructured fibre (Cho *et al.* 2008).

Solid core fibre	Material	Core size	Loss	Dispersion	Guiding mechanism
Ribbon waveguide (Mendis and Grischkowsky 2000)	HDPE	150 and 120 μm	< 1 cm^{-1} at 0.1–3.5 THz	1 ps pulse broadens to 20–40 ps	Dominanted single TM_0 mode
Sapphire fibres (Jamison *et al.* 2000)	High-resistivity silicon	D_c = 150, 250, 350 μm, L = 8 mm	6 cm^{-1} at 0.5–2.5 THz	–	Dominanted single HE_{11} mode
Wired fibre (Chen *et al.* 2006)	PE	D_c = 200 μm	$< 10^{-2}$ cm^{-1} at 310–360 GHz	–	–
Non porous rod (Dupuis *et al.* 2010)	PE	D_c = 445 μm	0.024 ± 0.004 cm^{-1} at 0.19 THz	–	Single mode
Non porous rod (Dupuis *et al.* 2010)	PE	D_c = 695 μm	0.040 ± 0.008 cm^{-1} at 0.117 THz	–	Single mode

Table 2.1. Air-clad dielectric waveguides with sub-wavelength core in terahertz. Summarizes the materials used in those air clad fibres, the core dimension, the associated guiding mechanism and other optical properties.

core-cladding interface. The solid-core waveguides suffer from material absorption since most of the mode is guided within a dielectric medium and there is no known low loss dielectric material in terahertz. Therefore, the material choice and waveguide structure have a great impact on the fibre performance, not only on transmission loss but also on dispersion. Two kinds of cross-sectional geometries have been proposed for index guiding-fibres in this Section. One is a conventional step-index fibre, shown in Figure 2.1(a–b), where the core is composed of uniform dielectric material and the cladding region is of air only (Mendis and Grischkowsky 2000, Jamison *et al.* 2000, Chen *et al.* 2006). The guidance mechanism relays on total internal

reflection and therefore supports a true guided mode. The second type is a solid core microstructured fibre, where a uniform solid core is surrounded by a cladding, consisting of micron scale (order of operating wavelength) periodic or non-periodic refractive index features that run along the fibre length (Roze *et al.* 2011, Talataisong *et al.* 2020, Han *et al.* 2002, Goto *et al.* 2004, Nielsen *et al.* 2009, Anthony *et al.* 2011a, Cho *et al.* 2008), sketched in Figure 2.1(c–h). In order to obtain low-loss in dielectric waveguides it is therefore necessary to use structures where only a low fraction of power is confined in the lossy material, while a large fraction is guided in the air.

2.3.1 Air-clad dielectric waveguides with sub-wavelength solid core

The first index-guiding terahertz polymer waveguides were reported using polymer ribbon structures (Mendis and Grischkowsky 2000) in Figure 2.1(a). High-density polyethylene (HDPE) was used for the first low-loss polymer ribbon waveguide. The plastic (HDPE) ribbon of rectangular cross-section was used as the core and the surrounding air acted as the cladding. Though the achieved attenuation coefficient was low ($<$1 cm^{-1} over 0.1–3.5 THz) for 10 mm length of ribbon, dispersion was too high (1 ps pulse broadens to 20–40 ps, depending on the number of cycles of oscillation).

Solid core fibres, however, do not appear very useful, due to the high intrinsic material losses. In 2000, the single-mode propagation of sub-ps terahertz pulses in unclad single-crystal sapphire fibres was considered in Figure 2.1(b). High-resistivity silicon based fibres were made of sapphire core with diameters of 150, 250, and 350 μm, and the surrounding air acted as the cladding (Jamison *et al.* 2000). The length of all the sapphire fibres were cut to 8 mm approximately. The structure offers lower attenuation coefficient than the bulk material loss, less than 1 to 6 cm^{-1} for the frequencies between 0.5–2.5 THz. The dominance of the single HE_{11} mode is attributed to free-space to waveguide coupling, despite the fibre dimensions allowing for multimode propagation. The terahertz temporal pulse is negatively and positively chirped after propagating through sapphire and plastic ribbon waveguides, respectively. The absorption losses of these waveguides are much lower than terahertz coplanar waveguides

2.3.1 Air-clad dielectric waveguides with sub-wavelength solid core

In the optical domain, reducing the fibre core size to the subwavelength scale has proven to be an efficient method for low-loss guidance as the diffraction limited spot-size can be reduced further and tight mode confinement can be achieved (Tong *et al.* 2003). The first simpliest plastic subwavelength fibre in the terahertz regime was demonstrated with a polyethylene (PE) wire of a circular diameter of 200 μm (Chen *et al.* 2006). Compared to sapphire waveguide (Jamison *et al.* 2000), this waveguide only has different host material and is analysed at low frequencies where the waveguide dimension is smaller than the operating wavelengths (830–970 μm). This step-index plastic fibre ensures single-mode HE_{11} operation via the total internal reflection guiding mechanism. Due to the subwavelength diameter of the solid core, the fundamental guided mode has a strong presence in the low-loss air cladding. The attenuation coefficient of this fibre can be reduced to 0.01 cm^{-1} as the guided mode field in sub-wavelength fibres extends far into the surrounding air to minimize the overlap of the propagation mode and the lossy fibre material, and has a high power fraction (90%) outside the core. This value of the propagation loss is at a level that can be considered effective for practical application in sensing or spectroscopic systems. The sub-wavelength air-clad waveguides are flexible due to their sub-wavelength dimension (a few hundred microns).

These types of sub-wavelength diameter terahertz fibres and couplers have enabled the developments of some terahertz systems such as a terahertz fibre-scanning near-field microscope (Chiu *et al.* 2009, Chen *et al.* 2009, Chen *et al.* 2011) and a terahertz fibre endoscope (Lu *et al.* 2008a). The evanescent wave sensing based on subwavelength terahertz plastic wire provides demonstration for liquid detection and powder sensing at the outside plastic wire (You *et al.* 2009, You *et al.* 2010).

In summary, sub-wavelength air-clad waveguides are very sensitive to external perturbations. Because of the strong presence of fundamental guided mode outside the core, the mode confinement is poor, which limits its propagation length and this weak guiding regime does not allow fibre bends since the HE_{11} mode would not be guided along a fibre bend. The high bending loss (Chen *et al.* 2009) is very challenging in many applications. In such step index structures, the dispersion management is difficult as it depends primarily on material dispersion. The narrowness of the transmission window associated with a large group velocity dispersion (GVD $\sim$ 34 ps/(THz·m) at 0.33 THz) that does not enable the propagation of broadband terahertz pulses. The

Suspended solid core microstructured fibre	Material	Core size	Loss	Dispersion	Guiding mechanism
Suspended solid-core fibre (Roze *et al.* 2011)	LDPE	D_c = 150 μm; OD = 5.1 mm	< 0.02 cm^{-1} at 0.28–0.48 THz	–	HE_{11}, TIR at the subwavelength-core and and antiresonant guiding by the tube of finite thickness.
Suspended core microstructured fibre (Anthony *et al.* 2011a)	Zeonex	D_c = 400 μm, OD = 3 mm, L = 30–70 mm (in steps of 10 mm); D_c = 600 μm, OD = 4 mm, L = 20, 40, 50 mm	$< 10^{-2}$ cm^{-1} at 310–360 GHz	–	–
Suspended solid-core fibre (Talataisong *et al.* 2020)	TOPAS	D_c = 300 μm; OD = 1.6 mm	< 0.11 dB/mm at 0.4–0.1.1 THz	zero	Single mode guidance, TIR at the subwavelength-core.

Table 2.2. Solid-core microstructured waveguides in terahertz. It also summarizes the materials used in those solid core fibres, the core dimension, the associated guiding mechanism and other optical properties.

reduction of the effective index of the HE_{11} mode induced by a bend would match the effective index values of radiative modes. Severe cross-talk may be encountered if two such waveguides are placed close together (Chen *et al.* 2009).

2.3.2 Suspended dielectric clad fibres with sub-wavelength solid-core

In order to solve the sensitive external perturbations of sub-wavelength air-clad waveguides, Roze *et al.* (2011) experimentally demonstrated a suspension outside of the sub-wavelength core (OD = 5.1 mm; D_{core} = 150 μm) in Figure 2.1(c). The suspended core fibres are fabricated using low density polyethylene (PE) and demonstrated attenuation coeffecient as low as 0.02 cm^{-1}. A combination of drilling and stacking techniques

are used to fabricate a solid suspended core fibre. The presence of the outer cladding provides good protection for the guided mode, thus reducing sensitivity to environmental changes, such as dusts, core surface contamination, coupling to adjacent fibres, or fibre holders. Furthermore, it enables direct fibre manipulations and dry air encapsulation into the fibre for eliminating losses from water present in ambient air. In the regime of very weak guidance when the propagation is limited by radiation losses, the outer cladding acts as a tube and improve the guiding properties by antiresonant reflecting mechanism as in hollow-core terahertz pipe. Radiation losses induced by fibre irregularities impose therefore a limitation on the smallest fibre diameter. Roze *et al.* (2011) have demonstrated that this additional guiding mechanism results in the formation of a narrow transmission window in the low frequency side. The first guidance regime occurs due to antiresonant reflecting optical waveguide ("ARROW") guidance by the encapsulating tube and second propagation regime is guided by the TIR in the suspended-in-air high-refractive-index core. The propagation in this case is effectively-single-mode (HE_{11}).

In order to achieve a direct drawing of microstructured polymer optical fibres using a low-cost desktop 3D printer, a TOPAS based suspended core microstructured fibre with a core of D_c = 300 μm, t = 500 μm and a OD = 4 mm was experimentally demonstrated (Talataisong *et al.* 2020). The core is optically isolated from the outer polymer region by three fine supporting struts. A large ratio of strut length to core diameter in the fibre is needed to prevent leakage of the guided mode into the cladding. The length of the fibre is gradually shortened from 73 to 31 mm to measure the average propagation loss. The average propagation loss was 0.11 dB/mm across the frequency range 0.4–1.1 THz. Cladding modes were removed by coating the fibre outer surface with graphite paste. Before removing the cladding modes, there is evidence of dispersion at 0.4–1.2 THz. This dispersion is associated to the modal dispersion of multimode guiding. After cladding modes were stripped, the zero-dispersion frequency range is estimated to be at 0.5–1.0 THz.

Xiao *et al.* proposed a novel terahertz circular polarizer based on the suspended solid-core subwavelength fibre (Xiao and Lu 2017). The fibre structural parameters are supposed to be D_c = 120 μm, t = 30 μm. The fibre polarizer is possible to fabricate by spinning the fibre preform while drawing. The terahertz mode is guided within the

subwavelength-scale core, which is suspended in a polymer tube. The dry air surrounded by the tube not only suppresses the absorption loss of the core mode but also supports the leaky cladding modes, which couple the circularly polarized core mode with the same handedness of the grating and radiate its power out. The refractive index of the outer cladding is higher than that of the inner cladding (air), there are no discrete guiding modes in the cladding but only continuous radiation modes.

The Zeonex waveguide uses a suspended core (D_c = 400 μm, OD = 3 mm, D_c = 600 μm, OD = 4 mm) design with five holes surrounding the core as shown in Figure 2.1(e) (Anthony *et al.* 2011a). The fibres investigated were cut from a single cane to several different lengths: 20 mm, 40 mm, and 50 mm for the 4 mm outer diameter fibre and 30 mm to 70 mm in steps of 10 mm for the 3 mm outer diameter fibre. The Zeonex waveguide loss spectrum shows attenuation coefficient of order 0.1 cm^{-1} over the 0.2–1.2 THz range for the 3 mm outer diameter fibre, essentially matching the material loss.

Suspended solid-core subwavelength fibres are promising because they can effectively isolate the core-guided mode from interacting with the surrounding space. This type of subwavelength fibre has great potential for bio-sensing applications (Mazhorova *et al.* 2012a), sketched in Figure 2.1(c). This is beneficial for terahertz sensing applications specifically for the noninvasive and label-free molecular detection, and gas and liquid spectroscopy. A minute sample can be placed in or at the vicinity of the waveguide where strong interaction with a terahertz pulse is achieved due to the large power fraction of the guided mode. As for the optical fibre taper with sub-wavelength scale, the very large fraction of evanescent power can potentially be exploited for sensing the surrounding environment. The delivery of the terahertz beam to enclosed locations such as chemical reactors are difficult in free space, so the ability to confine the beam to a bendable fibre is extremely beneficial even if at the expense of relatively large losses.

Nevertheless, the application of subwavelength fibres in terahertz communications is still limited by significant group velocity dispersion (GVD) as these fibres typically operate in a frequency range where the guided mode confinement changes dramatically from weak confinement (high presence in the gaseous cladding) at low frequencies, to strong confinement (high presence in the solid core) at high frequencies.

Solid core microstructured fibre	Material	Core size	Loss	Dispersion	Guiding mechanism
Hexagonal hole-array microstructured fibre (Han *et al.* 2002)	HDPE	L = 2 cm	0.5 cm^{-1} at 0.1–3 THz	-0.3 ps/(THz·cm) above 0.6 THz	single mode propagation
Solid core microstructured fibre (Goto *et al.* 2004)	PTFE	D_c = 1 mm, L = 10 cm	< 0.12 cm^{-1} for the 0.1–1.3 THz	–	TIR
Asymmetric solid core microstructured fibre (Cho *et al.* 2008)	HDPE	–	$\sim$ 0.5 and 4 dB/cm at 0.3 and 1 THz; Birefringence = 0.021 at 0.3 THz	–	TIR

Table 2.3. Solid-core microstructured waveguides in terahertz. The used material, core dimension, the associated guiding mechanism and other optical properties are also addressed.

2.3.3 Microstructured-clad dielectric waveguides with solid-core

A further variation is to take a solid core fibre and surround it by a porous, low-index cladding threaded with sub-wavelength diameter air holes. Microstructured fibres in Figure 2.1(f–h) are quite promising, since light guidance is not only controlled by index change but can be easily manipulated through multi-parameters of the wave guiding geometry, and the total dispersion becomes a strong function of waveguide dispersion (Eggleton *et al.* 2001, Russell 2003, Poli *et al.* 2004). The guiding mechanism of a solid-core microstructured waveguide, also known as a solid core photonic crystal fibre (PCF), is achieved by total internal reflection. The porous cladding guide is similar to a conventional step index fibre but with a much larger difference in effective refractive index between core and cladding and has been intensively studied in near infrared Microstructured fibres (Birks *et al.* 1997).

In 2002, solid-core microstructured waveguides based on the common hexagonal hole array, depicted in Figure 2.1(g) exhibited losses of the order of 0.5 cm^{-1} using HDPE when propagating over 2 cm (Han *et al.* 2002). By tuning the structural parameters, both dispersion as well as mode confinement could be tuned appropriately. As a result, the structure offers single mode guidance over 0.1–3 THz with relatively low dispersion (-0.3 ps/THz·cm above 0.6 THz). The attenuation of a guided mode of the solid-core PCF depends on the field confinement in the core and the core material absorption. It has been shown that the main contribution of the transmission loss is the material absorption loss. The attenuation can be reduced by using material with lower loss or lower refractive index in the terahertz regime.

A Teflon (PTFE) based solid-core (1 mm) microstructured fibre was fabricated and demonstrated for terahertz guidance (over 0.1–1.3 THz) in Figure 2.1(f), whose cladding was formed by arranging air holes in PTFE matrix in a periodic triangular fashion. A $<$ 0.12 cm^{-1} attenuation coefficient over propagation lengths of 10 cm was achieved using polytetrafluoroethylene (PTFE) (Goto *et al.* 2004). As the PTFE is a very cost effective and flexible material, it can be drawn into a longer fibre length as compared to other polymers. Moreover, the refractive index of PTFE is also low ($\eta_{\mathrm{PTFE}} \sim 1.4$–$1.466$) in the terahertz regime (Jin *et al.* 2006, Balakrishnan *et al.* 2009, Islam *et al.* 2020) compared to the HDPE ($\eta_{\mathrm{HDPE}} \sim 1.53$) (Islam *et al.* 2020), which provides lower index contrast for air-Teflon structures and hence, the scattering loss is reduced too. Scattering loss scales as square of the index contrast (Barwicz and Haus 2005).

Although HDPE and PTFE have a low material attenuation ($<$ 0.3 cm^{-1}) compared with conventional polymers used for optical fibres, the absorption coefficient and loss tangent for HDPE and Teflon are relatively higher at high frequencies than Zeonex and Topas (Islam *et al.* 2020). For this reason, extensive research has been carried out to identify polymers with lower loss over a wide range of frequencies in the terahertz regime.

In 2009, a more refined version was later reported by Nielsen *et al.* (2009). The COC (trade name is Topas) material based large mode area ($\sim$ 1.86 mm^2) and small mode area ($\sim$ 0.11 mm^2) solid-core microstructured fibres with common hexagonal array have been fabricated for terahertz guidance along a propagating lengths of 9 cm. Both

of the proposed fibres possess attenuation coeffecient (~ 0.09 cm^{-1}) over 0.35–0.65 THz, and quite low dispersion (< 1 ps/THz·cm) over 0.5–1.5 THz. The reported loss is 5 times smaller than the bulk material loss at the same frequency. Some reduction in loss is expected because a fraction of the guided mode resides in air. Moreover, the high confinement of fibre modes makes them less bend sensitive.

To intoduce birefringence in solid core microstructured fibre, Cho *et al.* broke the symmetry by employing an asymmetric core, consisting of two solid HDPE filaments (Cho *et al.* 2008) in Figure 2.1(h). The two solid HDPE filaments were inserted to create a highly asymmetric refractive index defect. The peak birefringence measured was 0.021 at 0.3 THz. At high frequencies, the THz field is highly confined in the defects, and the field distributions for the two polarizations become almost identical. These type of highly birefringent terahertz birefringent solid core microstructured fibre may find their applications in polarization-sensitive devices such as polarization controllers, filters, and isolators at terahertz frequencies. The power attenuation constant was estimated to be ~ 0.5 and 4 dB/cm at 0.3 and 1 THz, respectively for the 2-cm long fibre. The absorption-limited attenuation in solid core microstructured fibre is high due to the amount of impurities.

Compared to air-core microstructured waveguides, the solid-core waveguides has a broader transition bandwidth since the guiding mechanism is based on total internal reflection and not based on antiresonant or band-gap effects. Thus these waveguides are better suited for the broadband single-mode terahertz guidance. Single mode operation is made easier by the larger step in effective index and can be ensured by appropriate choice of the ratio of hole diameter to pitch. The microstructured cladding controls the dispersion. Solid core microstructured fibres with optimized geometrical parameters are used to minimize group velocity dispersion of the fibre fundamental mode in the 0.2–1.2 THz frequency range (Nielsen *et al.* 2009, Anthony *et al.* 2011a). Dispersion of the fundamental mode was optimized to be less than 1 ps/(THz·cm) in the whole terahertz frequency range.

Indeed, due to guidance in the solid core, losses of such fibres were comparable to that of the bulk attenuation coeffecient of the fibre material ~ 0.1–0.5 cm^{-1}) (increasing towards higher frequencies) (Nielsen *et al.* 2009, Anthony *et al.* 2011a). The material

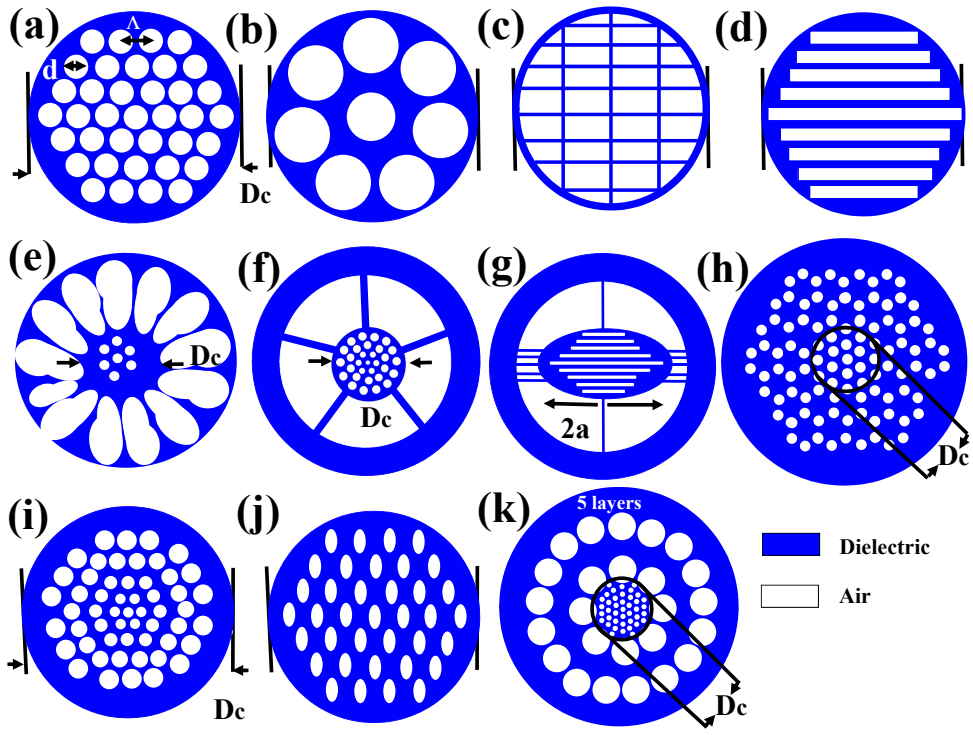

Figure 2.2. TIR and PBG guidance at the porous core in terahertz. (a) Porous subwavelength fibre (Hassani *et al.* 2008a, Hassani *et al.* 2008b, Atakaramians *et al.* 2008, Ma *et al.* 2015); (b) Porous subwavelength fibre (Dupuis *et al.* 2009, Dupuis *et al.* 2010); (c) Rectangular porous fibre (Atakaramians *et al.* 2009a, Atakaramians *et al.* 2009b); (d) Slot-shaped subwavelength porous fibre (Atakaramians *et al.* 2009b); (e) Suspended porous core fibre (Roze *et al.* 2011); (f) Suspended graded-index porous core (Mei *et al.* 2019); (g) Suspended elliptical porous fibre (Faisal and Islam 2018); (h) Porous-core honeycomb band-gap fibres (Bao *et al.* 2012, Nielsen *et al.* 2011, Fan *et al.* 2015, Bai *et al.* 2018, Lu *et al.* 2021); (i) Graded index porous (Ma *et al.* 2015); (j) Subwavelength elliptical porous fibre (Chen *et al.* 2013); (k) Hybrid photonic crystal fibre (Islam *et al.* 2018a).

loss ultimately determines the loss of such solid core waveguides and limits their use to short lengths. Although COC solid-core microstructured waveguides can be bent (90-degree bend) by heating the waveguide, generally they are rigid due to their large dimension (3 mm and more). The low interaction between terahertz waves and material necessary for low-loss propagation requires a large core size (5–10 mm), thus we used a total fibre diameter (1–5 cm), which limited the fibre flexibility.

2.4 Porous core fibres/microstructured-core fibres

The main disadvantage of the rod-in-air subwavelength designs (Chen *et al.* 2006, Lu *et al.* 2008a, Chiu *et al.* 2009, You *et al.* 2009, Chen *et al.* 2009, You *et al.* 2010, Roze *et al.* 2011, Chen *et al.* 2011) is that most of the power is propagated outside of the waveguide core, thus resulting in strong coupling to the environment, which is typically unwanted in power guiding applications. Also, high dispersion at lower frequencies and high propagation loss at higher frequencies present major challenges in the design of a solid-core terahertz fibre.

Inserting a subwavelength-sized air-hole in the middle of an solid dielectric core leads to a significant enhancement of the modal fields in the gas-filled hole, and as a consequence, mitigates the waveguide losses (Nagel *et al.* 2006b). In such a configuration, the discontinuity of the normal component of the electric field at the dielectric interface enhances the field significantly (proportional to the square of the ratio of high and low refractive index) inside the low-index region (here air gap), which results in a lower material loss. The achieved attenuation coeffecient in air-gap silica fibre is quite small (~ 0.12 cm^{-1} below 0.6 THz), however it increases rapidly at higher frequencies. The study also revealed that, with the best possible design, only 26% power can be coupled into the air hole region. Main disadvantage of the subwavelength hole design is that most of the power is still conducted in the high loss material of a core. Also, the mode of subwavelength fibres is significantly affected by its environment thus preventing direct manipulation of such fibres.

Another approach of reducing the length of travelling terahertz waves in a solid lossy material and managing the material loss are to use so-called porous/microstructured-core fibres depicted in Figure 2.2(a–k). This kind of structure is often characterized by its porosity, i.e. the fraction of the air-hole area to the overall core area. By changing the air-hole diameter (and therefore the pitch, namely the distance between the centers of two contiguous air-holes), different porosities are achieved. Therefore, porous fibres have been demonstrated to have lower effective material loss than that achieved in sub-wavelength solid core fibres (Atakaramians *et al.* 2009b).

High modal loss at higher frequencies can be mitigated by using air-clad porous fibres with deeply subwavelength core size. In this case, absorption loss of the porous core

can be made significantly lower than that of the constituent solid material. Additionally, modal group velocity dispersion decreases with lower refractive index contrast between the fibre core and cladding materials. Thus, using porous fibres can help in reducing both loss and group velocity dispersion of the fundamental mode. Porous fibres are similar to sub-wavelength diameter fibres. Sub-wavelength air-clad solid core fibres are also composed of a single rod, cladding in air, and terahertz waves are propagated in weak guiding conditions with a large fraction of evanescent power in air for reducing the attenuation coefficient of the waves. This guiding regime depends on the diameter and on the material refractive index of the fibre. In contrast with subwavelength solid core fibres, the normalized frequency is reduced by introducing air holes into the fibre for decreasing the effective refractive index of the fibre material.

2.4.1 Air-clad dielectric waveguides with subwavelength porous core

The first theoritically proposed subwavelength porous fibres/microstructured-core fibre, which consisted of a micron-scale structured (porous) core with the surrounding air as the cladding (Hassani *et al.* 2008a, Hassani *et al.* 2008b, Atakaramians *et al.* 2008, Atakaramians *et al.* 2009b, Atakaramians *et al.* 2009a, Atakaramians *et al.* 2011); an example is shown in Figure 2.2(a) manages the material loss. The benefit arises from reducing the amount of solid material in the core, owing to the presence of the holes, and hence reducing the material absorption (and also affecting the average refractive index of the core and group velocity of the guided modes). The porous fibre has a lower absorption loss than a non porous fibre of same diameter. Thus, for the same absorption loss as a non-porous fibre, the porous fibre will have a larger diameter. In such a case, it is possible to show that despite the lower index contrast the field of the large diameter porous fibre is more confined when compared to that of the smaller diameter non-porous fibre. Thus it is the porous fibre that has lower bending loss in this case (Hassani *et al.* 2008b). Fundamental mode of a porous fibre is considerably less sensitive to the changes in the air cladding environment than the fundamental mode of a rod-in-the-air fibre (Hassani *et al.* 2008b).

Figure 2.2(a) shows a PMMA porous fibre of 400 μm core diameter, including 37 periodic holes (Atakaramians *et al.* 2008) with maximum achievable porosity of $\sim$ 74%. It is evident that, as the porosity increases, a larger fraction of the power propagates outside the fibre core. The power flow cross section of the fundamental guided mode

2.4.1 Air-clad dielectric waveguides with subwavelength porous core

Porous core fibre	**Material**	**Core size**	**Loss**	**Dispersion**	**Guiding mechanism**
Porous subwavelength fibre (Dupuis *et al.* 2009)	LDPE	Porosity 8–18%; OD = 180, 240, and 325 μm; L = 25 cm	–	–	Single mode
Porous subwavelength fibre (Dupuis *et al.* 2009)	LDPE and PMMA (sacrificial polymer)	Porosity 29–45%; OD = 285, 310, 380 μm, L = 29 cm	0.01 cm^{-1} at 0.3 THz for 380 μm	–	Single mode
Porous subwavelength fibre (Dupuis *et al.* 2010)	LDPE and PMMA (sacrificial polymer)	Porosity 35%; OD = 450 μm; Pitch = 0.60; L = 38.5 cm	0.022 $\pm$ 0.014 cm^{-1} at 0.234 THz	–	Single mode
Porous subwavelength fibre (Dupuis *et al.* 2010)	LDPE and PMMA (sacrificial polymer)	Porosity 86%; OD = 775 μm; Pitch = 0.93; L = 38.5 cm	0.012 $\pm$ 0.010 cm^{-1} at 0.249 THz	–	Single mode
Spider-web porous fibre (Atakaramians *et al.* 2009a, Atakaramians *et al.* 2011)	COC	Porosity 57%; OD = 600 μm	0.08 cm^{-1} at 0.2–0.35 THz	-1.3 and -0.5 ps/m/μm for 0.2 < f < 0.35 THz	–
Rectangular porous fibre (Atakaramians *et al.* 2009a)	COC	Porosity 65%; OD = 350 μm; L = 30.0, 34.1 and 38.2 mm	–	–	–

Table 2.4. Air-clad dielectric waveguides with subwavelength porous core in terahertz. The used materials, the core dimension, the associated guiding mechanism and other optical properties of the porous core fibre is tabulated.

for two porosities (37% and 58%, respectively) has been calculated by using a Finite Element Method software. The widening of the power distribution with porosity is confirmed. Both power fraction and losses are studied in detail by Atakaramians *et al.* (2008).

The fabrication of porous core fibre is quite promising. In 2009 and 2010, Dupuis *et al.* report three strategies for the fabrication of simple porous subwavelength fibres, sketched Figure 2.2(b) using low density Polyethylene (PE) plastic for low-loss terahertz light transmission applications (Dupuis *et al.* 2009, Dupuis *et al.* 2010). The first method is the standard tube stacking technique. Porous PE fibres with average OD = 180, 240, and 325 μm made by stacking PE tubes. Using this fabrication method the porous microstructure was clearly achieved, however, the hole collapse was significant resulting in thick material veins. The second method for the fabrication of porous PE fibres is a subtraction technique where a part of a drawn all-solid fibre is dissolved in order to form air holes (Dupuis *et al.* 2009, Dupuis *et al.* 2010). In that case PMMA acts as a a sacrificial polymer as it can be easily dissolved in the tetrahydrofuran (THF) solvent while leaving the PE plastic intact. Porous PE/PMMA fibres with average OD = of 285, 310, 380 μm made by dissolving PMMA rods after drawing. The authors fabricated a PE rod with one layer of circular air holes. The lowest fibre attenuation coeffecient measured in this work is ~ 0.01 cm^{-1} in the vicinity of 0.3 THz and it is exhibited by the 40% porous subwavelength fibre of diameter 380 μm. For comparison, the loss of a rod-in-the-air subwavelength fibre of a similar diameter was measured to be ~ 0.01 cm^{-1}, while the bulk attenuation coeffecient of a PE plastic used in the fabrication of such fibres is ≥ 1 cm^{-1}. Although air-holes are preserved in the sacrificial polymer technique method, the fabrication process is very lengthy and the choice of material is limited in terms of dissolving solvent and melting temperature differences between the materials. Large melting temperature differences can result in material degradation. Moreover the maximum porosity achieved is 29–45%. By better controlling the fabrication process of porous fibres it should be possible to reduce the amount of fibre defects and, thus, reduce the radiation loss contribution. The third technique employed for fabrication of porous fibres utilises casting of the PE preform into a structured glass mold. The glass rods are pulled out from the preform and any residual glass is etched away before pulling into fibre. Then the resultant PE preform is drawn down using active-pressurisation. The pressurisation is implemented not only

to prevent the hole closure, but also to inflate the holes in order to increase the porosity. A drawback of this approach is that the active-pressurisation severely deforms the fibre cross-section. High porosity (85%) is achieved due to inflation of the holes during the drawing process. Creating fibres with different sized air holes and also fibres with a very large air fill fraction is a manufacturing challenge. When the holes have different sizes, the interaction between the holes during manufacturing is asymmetric, causing the smaller holes to deform.

In their latter work, Atakaramians *et al.* claimed that the extrusion technique is better suited than the stacking technique, sacrificial polymer technique, molding technique and drilling technique for the fabrication of porous fibre (Atakaramians *et al.* 2009a). Because, firstly, microstructured fibres made up of soft glass and polymer with a large air fraction and holes of 1–2 μm in diameter have been successfully fabricated though the extrusion technique (Ebendorff-Heidepriem and Monro 2007), indicating that the fabrication process of terahertz porous fibre (with hundreds of microns in diameter and features in the tens of microns range) is easier to implement than the optical counterpart. Secondly, it has also been shown that it is possible to fabricate non-circular airholes in microstructured optical fibres made up of polymer and soft glasses through the extrusion technique (Ebendorff-Heidepriem and Monro 2007), indicating that the fabrication of the proposed exotic structures are feasible. The preforms are extruded by heating up a bulk polymer/glass billet to a temperature where the material gets soft. Then the soft material is forced through an extrusion die using a ram extruder at a fixed speed. The die exit geometry determines the preform cross-section in Figure 2.2(c). The rectangular fibre preform of 10 mm diameter and 180 mm length is drawn down to three different sets of outer diameters (350–400, 450–500, and 550–600 μm). A birefringence of 0.012 at 0.65 THz is achieved for the rectangular porous fibre. The rectangular porous fibre leads to a 71% porosity. The porosity of the fabricated fibres is measured to be 65% for rectangular structure using electron microscopy, due to the effect of rounding of corners and thickening of the struts.

2.4.2 Microstructured waveguides with subwavelength porous core

In 2011, Nielsen *et. al.* numerically modeled a PBG terahertz fibre type known as honeycomb fibre, which combines PBG guidance with the concept of porous waveguides shown in Figure 2.2(h). Basically the hollow-core of PBG terahertz fibre is replaced

Porous core fibre	Material	Core size	Loss	Dispersion	Guiding mechanism
Porous-core honeycomb band-gap fibre (Bao *et al.* 2012)	TOPAS	D_c = 0.8 mm; Porosity 45%; OD = 3.65m; L = 15 to 5 cm (2.5 cm in steps) cm	1.5 dB/cm at 0.75–1.05 THz	–	PBG
Graded index porous-core fibre (Ma *et al.* 2015)	PE	Porosity = 43%; OD = 1.4 mm, L = 18.45, 12.77 and 8.28 cm	0.025 cm^{-1} at 0.3 THz to 0.15 $^{-1}$ at 1.5 THz	< 1 ps/(THz·cm)	TIR, Single moded below 0.35 THz

Table 2.5. Microstructured dielectric waveguides with subwavelength porous core in terahertz. The geomatrical and optical properties of the porous core subwavelength fibre is also summarized.

with a porous core (Nielsen *et al.* 2011). This allows PBG guidance, while still retaining loss low due to the porous core. Due to the increased effective index of the core, the honeycomb PBG structure allows broad band-gaps (Knight *et al.* 1998). The porous-core fibre is less dispersive than the hollow-core fibre, and they also show that the porous-core fibre has a wider transmission window than the hollow-core fibre. Honeycomb band-gaps are relatively larger than triangular band-gaps, and at comparable structure sizes the honeycomb band-gap operates at lower frequencies than the triangular band-gap (Broeng *et al.* 1998), which can be exploited to make a thinner fibre. The thickness of the fibre is one of the factors limiting the applications of terahertz fibres. Several other proposals have been made in the literature on porous-core honeycomb band-gap terahertz fibre (Fan *et al.* 2015, Islam *et al.* 2017a, Bai *et al.* 2018, Lu *et al.* 2021), however they exhibit relatively narrow spectra and strict periodicity needs to be maintained to satisfy the Bragg conditions.

The fabrication of the first porous-core honeycomb band-gap terahertz fibre was reported in 2012 by Bao *et al.* (2012). The fibre is made of the polymer TOPAS with a D_c = 0.8 mm and confirm that it allows to fabricate long lengths of fibre with a near-perfect periodic structure and thus very clear band-gap guidance. The porous core structure

was drilled into the preform and then drawn to the final diameter. Initially the fibre length was 15 cm, sequentially cut shorter in steps of 2.5 cm to have 5 cm length for reference measurement. The fundamental band-gap at 0.75–1.05 THz is found to have losses lower than 1.5 dB/cm, whereas the loss is below 1.0 dB/cm in the reduced band-gap 0.78–1.02 THz. The particular fibre has an OD = 3.65 mm, air-hole diameter = 165 μm, and pitch = 360 μm, and is thus mechanically flexible.

The guidance of microstructured dielectric waveguides with subwavelength porous core can be PBG or TIR. To support the TIR (index guiding) mechanism, the air-filling fraction of the core was chosen to be lower than that of cladding (Uthman *et al.* 2012). A graded index porous-core fibre (Ma *et al.* 2015) is made from polyethylene plastic and features a non-uniform array of variable size subwavelength holes positioned at subwavelength separations with respect to each other, thus resulting in a graded refractive index effective medium in Figure 2.2(i). The outer diameter of the fibre is $\sim$ 1.4 mm and the L = 18.45, 12.77 and 8.28 cm. The air filling fraction of fabricated GI-mPOF and mPOF are 43.3%. The fibre has a single mode below 0.35 THz, while at higher frequencies it operates in a few-mode regime. Due to high porosity, fibre absorption loss is only a fraction of the bulk absorption loss of polyethylene, and in the whole operation range it varies from 0.025 cm^{-1} at 0.3 THz to 0.15 cm^{-1} at 1.5 THz. Modal group velocity dispersion of the individual modes is reduced below 1 ps/(THz·cm) in the whole operational range due to the use of porous materials and due to the relatively large core size. The authors experimentally demonstrated that graded index porous fibres exhibit smaller pulse distortion, larger bandwidth, and higher excitation efficiency when compared to fibres with uniform porosity. Both the graded index porous fibre and uniform porosity microstrucred fibre are fabricated with the drilling method.

Several other proposals have been made in the literature on porous-core index guiding fibres, such as randomly porous fibre with improved properties (Bai *et al.* 2011), porous-core fibre with elliptical holes with high birefringence ($\sim$ 0.0445) (Chen *et al.* 2013), rotated porous-core microstructured fibre (Islam *et al.* 2015), dispersion-flattened photonic crystal fibre (Islam *et al.* 2016, Islam *et al.* 2017b), circular hybrid core PCF (Islam *et al.* 2018a), diamond core kagome lattice PCF (Sultana *et al.* 2019b) etc.

Both in solid core and porous fibres, group velocity dispersion can be very large at low frequencies due to rapid change in the modal confinement, while dispersion can decrease by more than an order of magnitude at higher frequencies (strong confinement limit) (Dupuis *et al.* 2010, Nielsen *et al.* 2009, Anthony *et al.* 2011a). At higher frequencies, however, the fibre can become multimode and one has to worry about the effect of the intermodal dispersion. Although, subwavelength porous waveguide consisting of air-clad would be an advantage in some sensing applications, they are sensitive to external perturbations.

2.5 Hollow core fibres

There is much research invested in lowering the loss by forcing a large part of the radiation to propagate in air while still being confined to a waveguide, i.e., first way is based on subwavelength solid fibre (Chen *et al.* 2006, Roze *et al.* 2011, Chiu *et al.* 2009, Chen *et al.* 2009, Chen *et al.* 2011, Lu *et al.* 2008a, You *et al.* 2009, You *et al.* 2010), and subwavelength porous fibres (Hassani *et al.* 2008a, Hassani *et al.* 2008b, Atakaramians *et al.* 2008, Atakaramians *et al.* 2009a, Atakaramians *et al.* 2009b, Dupuis *et al.* 2009, Dupuis *et al.* 2010, Ma *et al.* 2015). The guiding mechanism in sub-wavelength solid fibres is based on total internal reflection. The core dimension of the subwavelength type fibre is much smaller than the wavelength. Therefore, the guided mode field extends far into the surrounding air, thus low loss can be obtained due to the small overlap of the propagating mode and the lossy fibre material, has high power fraction outside the core. Severe cross-talk might also be encountered if two such waveguides are placed closely (Chen *et al.* 2009). Further reduction of propagation loss can be achieved by inserting a porous structure into the solid core. However, both solid-core and porous-core subwavelength fibres are very sensitive to external perturbations and bending, which is a challenge in many applications.

The second way of beating these limits is by confining the electromagnetic field in a hollow core. Hollow-core fibre surrounded by a structured cladding, confines/traps most of the power within the air-core region. As a result, hollow-core fibres minimize the outside interference. In the design of hollow-core fibres the main challenge is to ensure high reflection efficiency at the core–cladding interface. Various dielectric cladding structures have been applied, such as the simple tube waveguides

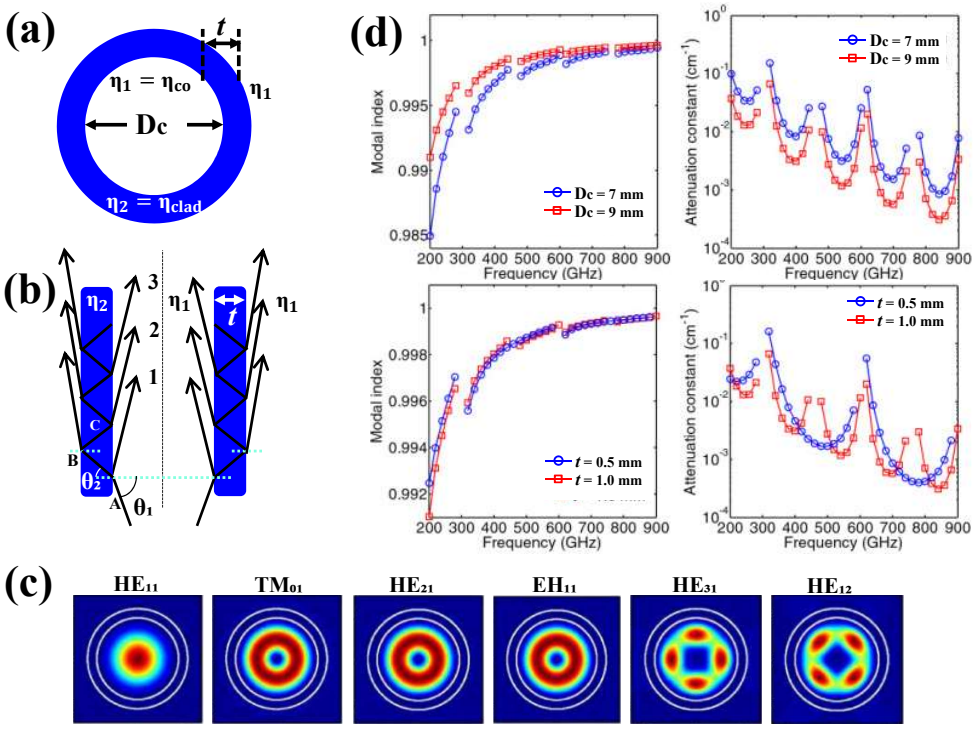

Figure 2.3. Hollow core pipe waveguide. (a) Profile of the pipe waveguide, where $\eta_1 = \eta_{co} = 1$, $\eta_2 = \eta_{clad}$; (b) Fabry-Pérot etalon of the dielectric cladding for thickness t; (c) Vectorial modal intensity distributions (Lai *et al.* 2010); (d) Modal indices and attenuation constants of the fundamental core mode of the pipe waveguide by varying the D_c and t (Lai *et al.* 2009, Lai *et al.* 2010).

(Bowden *et al.* 2008b, Bowden *et al.* 2008a, Lai *et al.* 2010, Bao *et al.* 2015), the kagome waveguides (Lu *et al.* 2008b, Anthony *et al.* 2011b, Yang *et al.* 2016, Li *et al.* 2017a), the tube lattice fibres (Setti *et al.* 2013, Vincetti and Setti 2013, Van Putten *et al.* 2018, Xiao *et al.* 2019, Ankan *et al.* 2020, Mollah *et al.* 2020a), the hollow-core band-gap fibre (Vincetti 2009a, Vincetti 2009b, Wu *et al.* 2011b), and Bragg fibres (Skorobogatiy and Dupuis 2007, Ponseca Jr *et al.* 2008, Dupuis *et al.* 2011, Ung *et al.* 2011). With regard to the antiresonant reflecting mechanism, terahertz fibres widely adopt the simple tube waveguide, kagome waveguide and the tube lattice fibres.

2.5.1 Pipe waveguides

Hollow core pipe waveguides are analagous to hollow-core photonic crystal fibres with a kagome lattice (Benabid *et al.* 2002) and the simplified version of tube lattice (Gérôme *et al.* 2010) in the optical regime. Low-index hollow core pipe waveguide (Annular core fibre) is very simple and it is only a pipe consisting of a thin dielectric tube

Hollow core pipe waveguide	Material and size	Loss	Dispersion	Guiding mechanism
Pipe waveguide (Lai *et al.* 2009)	Teflon pipe; D_c = 9 mm; t = 0.5 and 1 mm; L = 3 m	attenuation constant as low as 0.0008 cm^{-1}	–	ARROW; HE_{11} mode
Tube fibre (Chen and Chen 2010)	PTFE pipe; D_c = 600 μm; OD = 1200 μm	–	–	ARROW; HE_{11} mode
Pipe waveguide (Nguema *et al.* 2011)	Silica pipe; OD = 5 mm; t = 250 and 155 μm; L = 40 cm	0.03 cm^{-1} at 1 THz	–	ARROW
Pipe waveguide (You *et al.* 2012)	Polyethylene (PE) pipe; D_c = 5.57 mm ; t = 1.17 mm; L = 30 cm	five resonant dips at 0.201, 0.266, 0.326, 0.392 and 0.452 THz respectively	–	ARROW
Pipe waveguide (Mazhorova *et al.* 2012b)	Chalcogenide glass pipe; OD = 0.95 mm; t = 98 μm; L = 50 cm	58– 93 dB/m between 0.1–2.5 THz	–	ARROW; HE_{11} mode
Pipe waveguide (Mazhorova *et al.* 2012b)	Chalcogenide glass pipe; OD = 0.95 mm; t = 18μm; L = 50 cm	$<$ 0.05 cm^{-1} (19 dB/m) at 0.75 THz; Bandwidth = 0.5–0.9 THz	–	ARROW; HE_{11} mode
Pipe fibres (Xiao *et al.* 2013)	PMMA pipe; D_c = 3.8 mm; t = 200 μm; L = 0.11, 0.2, 1.37 and 1.2 m	$<$ 7.55 $\pm$ dB/m at 3.1 THz	–	ARROW; HE_{11} mode
Tube waveguide (Bao *et al.* 2015)	PMMA pipe and 1.7-mm thick water layer; D_c = 4 mm; t = 1.29, 1.97, 2.95 mm; L = 5, 20, 40 cm and	0.05–0.5 cm^{-1} in 0.3–1 THz	$<$ 10 ps/(THz·cm)	ARROW

Table 2.6. Hollow core pipe waveguides in terahertz. Indicating the size, material used and other optical properties.

(Lai *et al.* 2009, Lai *et al.* 2010, Lu *et al.* 2010, Chen and Chen 2010, Nguema *et al.* 2011, Mazhorova *et al.* 2011, Mazhorova *et al.* 2012b, You *et al.* 2012, Xiao *et al.* 2013, Lai *et al.* 2014, Bao *et al.* 2015) that guides the terahertz waves using anti-resonant reflections (Haus 1984, Litchinitser *et al.* 2002) from its walls to confine the light in the hollow core with a leaky nature. Fig. 2.3(a) shows the cross section of a dielectric tube waveguide. It has an air-core with diameter D_c surrounded by a dielectric cladding layer with thickness t. Pipe waveguides are different from the air-core terahertz waveguides with high reflection materials (Harrington *et al.* 2004, Hidaka *et al.* 2005, Skorobogatiy and Dupuis 2007, Bowden *et al.* 2007, Themistos *et al.* 2007, Ito *et al.* 2007) or periodic, multilayered dielectric structures (Yu *et al.* 2007a, Lu *et al.* 2008b, Hassani *et al.* 2008a, Hassani *et al.* 2008b, Atakaramians *et al.* 2008, Bai *et al.* 2011, Chen *et al.* 2013, Islam *et al.* 2015, Islam *et al.* 2016, Islam *et al.* 2017b, Islam *et al.* 2018a) to provide high cladding reflection. The pipe waveguide is also different from the one utilizing low-index discontinuity (Nagel *et al.* 2006b), in which a subwavelength air core as well as a small air-core-diameter to cladding-thickness ratio are assumed and the terahertz waves are guided by the mechanism of total internal reflection (TIR). Guiding mechanism of the pipe waveguide is similar to that of the ARROW (Duguay *et al.* 1986), but is realized with a single low-index dielectric layer. The ARROW was first developed by Duguay *et al* for guiding light in planar optical waveguides, composed of one or several dielectric layers. The ARROW guidance is distinctly different from the total internal reflection (TIR) guidance mechanism employed by the subwavelength-sized low-refractive-index discontinuity waveguides (Nagel *et al.* 2006b).

2.5.2 Guiding mechanism of the core modes

The ARROW mechanism can be briefly described by viewing the cladding of the pipe waveguide. For hollow-pipe fibres, the dielectric layer of the pipe acts as a Fabry-Pérot resonator and it is well known that a Fabry-Pérot etalon behaves like a resonator (Haus 1984). A cross section along the tube waveguide is shown in Fig. 2.3(b), where θ_1 and θ_2 are angles of inclined wave vectors with respect to the interface normal in media 1 and 2, respectively. The light propagates at an angle θ_1, defined by the following equation, with respect to the normal of the core-cladding interface:

$$\sin\theta_1 = \frac{n_{\text{eff}}}{n_{\text{core}}}. \tag{2.1}$$

Both reflection and transmission occur at the interface between the core and cladding. The reflected part of the light continues to propagate in the core. The part of the light transmitted into the cladding bounces back and forth between the outer and inner interfaces of the cladding. The bouncing cladding field passes through the more lossy cladding material and thus less power is transmitted back to the core to interfere with the direct transmitted field. In the following, the light that always propagates inside the core referred as the first order pulse. The light that experiences a single Fabry-Pérot reflection in the cladding is referred to as the 2^{nd} order pulse, and higher-order reflections from the cladding that experience n Fabry-Pérot reflections is defined as the pulse of order (n-1) (Bao *et al.* 2015). Therefore, only a few percent of the power is guided in the material and most of the guiding is in the air.

The attenuation in the transmission bands usually is remarkably lower than in the bulk material. For example, in silica pipes (Nguema *et al.* 2011) at terahertz frequencies, the attenuation coefficient can be lower than 0.03 cm^{-1}, whereas silica attenuation coeffecient is around 2 cm^{-1}. The pipe waveguide supports cladding modes for which fields are confined within the cladding region. These modes are guided based on TIR owing to the higher refractive index of the cladding. However, the cladding modes attenuate rapidly since high material absorption losses are encountered. Alternatively, the pipe waveguide also supports core modes with fields confined in the air-core region. As the refractive index of the core is less than that of the cladding, fields of the core modes will oscillate and radiate through the cladding, making the core modes leaky with the propagation constants being complex. However, as the core modes suffer lower material absorption losses than the cladding modes, they are the dominant modes in the pipe waveguide.

The transmission spectrum is periodic and transmission windows are delimited at which the etalon resonates. The frequencies corresponding to the minimum transmission coefficient are referred to as resonant frequencies, and the frequencies corresponding to high transmission parts of the spectrum are called antiresonance frequencies. At or near the resonance frequencies (f_m) the light couples to the cladding of the terahertz pipe waveguide, nearly no reflection takes place at the core-cladding interface and thus fields can hardly exist inside the core region. On the other hand, under the antiresonant conditions of the cladding, i.e., at the frequencies away from the resonant ones,

considerable reflections at the core-cladding interface cause the core modes to appear resulting from the fact that waves bounce back and forth inside the core region. The guiding mechanism in such pipe waveguide has been well described by Nguema *et al.* (2011), Chen and Chen (2010), Mazhorova *et al.* (2012b), Bao *et al.* (2015).

Transmission windows are delimited by the resonant frequencies that can be accurately predicted. Resonance frequencies (f_m) of the cladding depends on the cladding tube thickness t (Vincetti 2009b) or η_{clad} and are given by (Haus 1984, Litchinitser *et al.* 2002):

$$f_m = \frac{mc}{2t\eta_{clad}\cos\theta_2} \tag{2.2}$$

where η_{clad} represents the refractive index of the cladding material. The η_{co} indicates the refractive indices of the core material, c is the speed of light in vacuu and m is an integer, representing the order of resonance. In the regime where the core modes are with glancing reflections, $\theta_1 \sim 90°$. Applying Snell's law and after some manipulations, Eq. 2.5.2 becomes:

$$f_m = \frac{mc}{2t\sqrt{\eta_{clad}^2 - \eta_{co}^2}}. \tag{2.3}$$

A low-index pipe waveguide was proposed and experimentally demonstrated for terahertz waveguiding (Lai *et al.* 2009) using a Teflon air pipes up to 3 meters long with a hollow-core, D_c = 9 mm and a dielectric layer thickness t = 0.5 and 1 mm. It was experimentally confirmed that terahertz waves can be successfully guided in the central air core with excellent mode qualities, high coupling efficiency (as high as 84%), controllable bandwidth, while the measured attenuation constants can be as low as 0.0008 cm^{-1}, and and a bandwidth over 200 GHz for t = 0.5 mm under a straight condition. The effect of material absorption from the dielectric layer is rather small due to the confinement of the waves in the air-core with low penetration in the dielectric layer. The pipe waveguide with 0.5 mm cladding thickness has better mode confinement and wider spaced transmission windows than the 1 mm as the pipe waveguide with thinner cladding thickness suffers lower guiding loss at the antiresonant frequencies as shown in Fig. 2.3(d). Hence, in a ARROW fibre, in order to obtain the widest transmission windows between two resonant frequencies it is necessary to have the thinnest possible wall, often below sub-millimeter dimensions. Also, the size of the core has a strong

effect on the attenuation coefficient of the modes, shown in Fig. 2.3(d). The attenuation constant decreases as D_c increases. Owing to the structure simplicity and excellent performance, after the pioneering Teflon pipe, various pipe waveguides have been reported for terahertz transmission, being made of polytetrafluoroethylene (PTFE) tube (Chen and Chen 2010, Dupuis 2010), polyethylene (PE) tube (Dupuis 2010), silica tube (Nguema *et al.* 2011), polypropylene (PP) tube (You *et al.* 2012), chalcogenide glass tube (Mazhorova *et al.* 2011, Mazhorova *et al.* 2012b), and polymethylmethacrylate (PMMA) tube (Xiao *et al.* 2013, Bao *et al.* 2015). The fundamental (HE_{11}) mode is investigated (Lai *et al.* 2009, Lai *et al.* 2010, Vincetti and Setti 2010, Lu *et al.* 2010, Mazhorova *et al.* 2012b, Xiao *et al.* 2013, Lai *et al.* 2014).

Later, the theoretical aspect of the terahertz pipe waveguides were illustrated with the guiding mechanism and providing the detailed modal analysis (Lai *et al.* 2010, Xiao *et al.* 2013). High-order modes are propagated into the large hollow core along with the fundamental mode as shown in Fig. 2.3(c). It shows the first six vectorial mode representations through the hollow core. The modes propagated in the air-core by the antiresonant reflecting guiding mechanism are not pure modes. They are leaky modes in nature. In contrast, the modes based on the TIR guiding mechanism exhibit propagation losses, and they do not have a cutoff frequency. In consequence, couplings between the fundamental mode and higher order ones are more likely to occur with larger core size leading to multimode propagations and additional losses from intermodal couplings. Modal indices and attenuation constants of the leaky core modes are calculated for various core diameters, cladding thicknesses, and cladding refractive indices. Results are compared with the resonance-frequency formula derived from the Fabry-Pérot etalon and the antiresonant reflecting guiding mechanism is theoretically indentified (Lai *et al.* 2010, Xiao *et al.* 2013, Bao *et al.* 2015).

The group velocity dispersion (GVD) is obtained from the effective refractive index (η_{eff}) by the following equation (Bao *et al.* 2015):

$$\beta_2 = \frac{f\frac{\partial^2 n_{\text{eff}}}{\partial f^2} + \frac{2\partial n_{\text{eff}}}{\partial f}}{2\pi c}. \tag{2.4}$$

Since the calculation of β_2 involves the second derivative of the effective index, the calculated results are sensitive to experimental noise. The group-velocity curve is also

affected by strong drops of the velocity at the resonant frequencies (Nguema *et al.* 2011, Bao *et al.* 2015). The effective refractive index of the terahertz wave guidance through the air-core is < 1. The GVD of the HE_{11} mode propagated into the air channel of a thin PE pipe (t = 143 μm, η_{mat} = 1.45, D_c = 6 mm) is strongly affected by the degradations of the guiding conditions close to the resonant frequencies leading to sharp variations of the GVD from negative to positive values (Nguema *et al.* 2011). The GVD is smaller in the second transmission windows. At larger frequencies, the size of the core compared to the wavelength size is larger. As a result, the HE_{11} mode could propagate more parallel (to the propagation axis) with a larger distance between two consecutive reflections at the dielectric layer interface, leading to properties closer to the ones of a wave propagating in air. The GVD is below $\pm$2 ps/(THz·m) in a broader frequency range, in the second window (from 1.2 to 1.9 THz) than in the first one (from 0.7 to 0.86 THz). Hollow pipe waveguides (D_c = 4 mm, OD = 6.58 mm and t = 1.29 mm) allows the dispersion < 10 ps/THz·cm) in the 0.3–1 THz range (Bao *et al.* 2015).

In practical applications, waveguides often suffer from bending. The general trend is that the bend loss increases with decreasing bend radius. The case of bending loss of leaky-mode pipe waveguides has been investigated for different frequencies, polarizations, core diameters, cladding thicknesses, and cladding materials (Lu *et al.* 2010, Xiao *et al.* 2013, Lai *et al.* 2014). For hollow-core pipe waveguides (D_c = 9 mm and t = 0.5 mm), bend losses are experimentally reported with 0.006 cm^{-1} at 420 GHz for a bend radius of 60 cm (Lu *et al.* 2010). However, it is found that the simulated attenuation constant of the y-polarized mode is less than that of the x-polarized one, and the difference between the two polarizations is accentuates with decreasing bending radius (Lai *et al.* 2014). This phenomenon is quite different from that observed in the TIR-based waveguides, such as for conventional step-index fibre. For the step-index fibre, bending losses of the x- and y-polarized HE_{11} modes are the same (Marcuse 1976, Schermer and Cole 2007). With the same bend radius of 200 cm, simulated results indicate severe deformation in the field profile with the larger core diameter of the pipe waveguide (Lai *et al.* 2014). Although large core size is helpful for reducing transmission loss, it leads to difficulties in fibre bending (Lai *et al.* 2009, Lai *et al.* 2010). For hollow-core pipe waveguides (D_c = 4 mm, OD = 6.58 mm and t = 1.29 mm, L = 30 cm), bend losses are experimentally reported < 0.2 cm^{-1} for a bend radius of 10 cm (Bao *et al.* 2015). Losses are higher for the parallel polarization than for the perpendicular one, with the higher frequencies being more sensitive to bending than the lower

frequencies.

A hollow-core terahertz pipe fibre has been successfully integrated into a reflective terahertz fibre-scan imaging system for in situ and dynamically monitoring the chemical reaction of hydrochloric acid (HCl) and ammonia (NH_3) vapours to generate ammonium chloride (NH_4Cl) aerosols in a sealed chamber (You and Lu 2016). The bending capability of the reflective terahertz pipe fibre-based scan system has been demonstrated by imaging and identifying an array of tablets. Applications of hollow-core terahertz pipe fibres have been also demonstrated for high-performance sensing by tracking the shift of the resonant frequencies, when various subwavelength-thick molecular layers adhered on the inner surface of the dielectric (You *et al.* 2010), when various powders are loaded on the outer surface of the pipe (composed of an absorptive layer), or when different vapours are inserted into the air channel of the pipe (You *et al.* 2012).

A thick silica tube was inflated and drawn to thin-wall pipes with diameter and thickness accuracy better than 1% with the help of the optical fibre fabrication facilities at the XLIM research institute (Nguema *et al.* 2011). Most of the tube waveguides are fabricated from the commercial tube by inflating and drawning method (Xiao *et al.* 2013). The chalcogenide glass ($As_{38}Se_{62}$) capillaries can act as efficient waveguides in the whole midinfrared–terahertz spectral range (Mazhorova *et al.* 2012b). The capillaries are fabricated using a double crucible drawing technique. The double crucible setup is used to draw step index fibres in which both volumes of the double crucible contain core and clad glasses with different refraction indices. At the tip of the double crucible, a drop of glass is formed and as it goes down by gravity, the fibre is drawn like in a conventional fibre drawing tower. As soon as the drop reaches the tractor, it is pulled down with a controlled speed; meanwhile, the pressure in the core crucible is increased in order to form a capillary. By varying the drawing conditions, such as tractor speed and pressure in the core, numerous dimensions of capillaries and wall thicknesses have been obtained. This technique allows production of glass capillaries with wall thicknesses in the range of 12 to 130 μm.

The pipe fibre offers lower loss over the solid polymer fibre and other advantages such as improved confinement, the ease of fabrication, and large mode area (Chen and

Chen 2010).

Although, low loss has been successfully achieved near to antiresonant frequency regions, the transmission bandwidth is limited by the spacing of the resonance frequencies, which is proportional to the refractive index and inversely proportional to the cladding thickness. Note that a thick cladding wall narrows the transmission bandwidth. One way to improve the transmission bandwidth is to reduce the cladding thickness (Nguema *et al.* 2011). Higher inner pressure helps to realize a thinner wall thickness, however, it is at the cost of mechanical strength reduction and increases the probability that the pipe is factures during the fabrication process. In addition, a uniformly thin cladding is in practice difficult to fabricate and cleave due to its low mechanical strength. Moreover, tube waveguides with thin walls are fragile and sensitive to external perturbation, as the propagating mode extends significantly outside the cladding (Lai *et al.* 2009, Lai *et al.* 2010). In addition, guiding eventually fails with diminishing frequency as the grazing incidence approximation breaks down and the reflectivity becomes small with the thin cladding thickness. Large core size in pipe waveguide is helpful for reducing transmission loss, at the same time, a large core leads to difficulties in fibre bending (Lai *et al.* 2009, Lai *et al.* 2010). All these issues are limiting factors aspects for many practical applications.

2.5.3 Kagome hollow core photonic crystal fibres

Kagome hollow-core PCFs are analogous to hollow-core pipe fibres. They have been intensively developed in the optical domain for exploiting their broadband transmission capability. The wider transmission bandwidth makes the kagome hollow-core PCF waveguides an appealing option. The kagome fibres consist of a kagome lattice ('eye of the basket') of thin struts with a large pitch around the hollow core. The appearance of von Neumann-Wigner quasibound states within a continuum allows terahertz propagation in kagome hollow-core microstructured waveguides (Couny and Benabid 2006, Vincetti 2009b) and the cladding does not support photonic band-gaps. Light is confined and propagates along the hollow core via the ARROW guiding mechanism with inhibited coupling due to the low density of cladding modes and small spatial overlap of cladding modes with core modes (Argyros and Pla 2007). The high air-filling fraction in the cladding region results in a low density of guided modes. Consequently, weak coupling between the core and cladding modes is possible, allowing

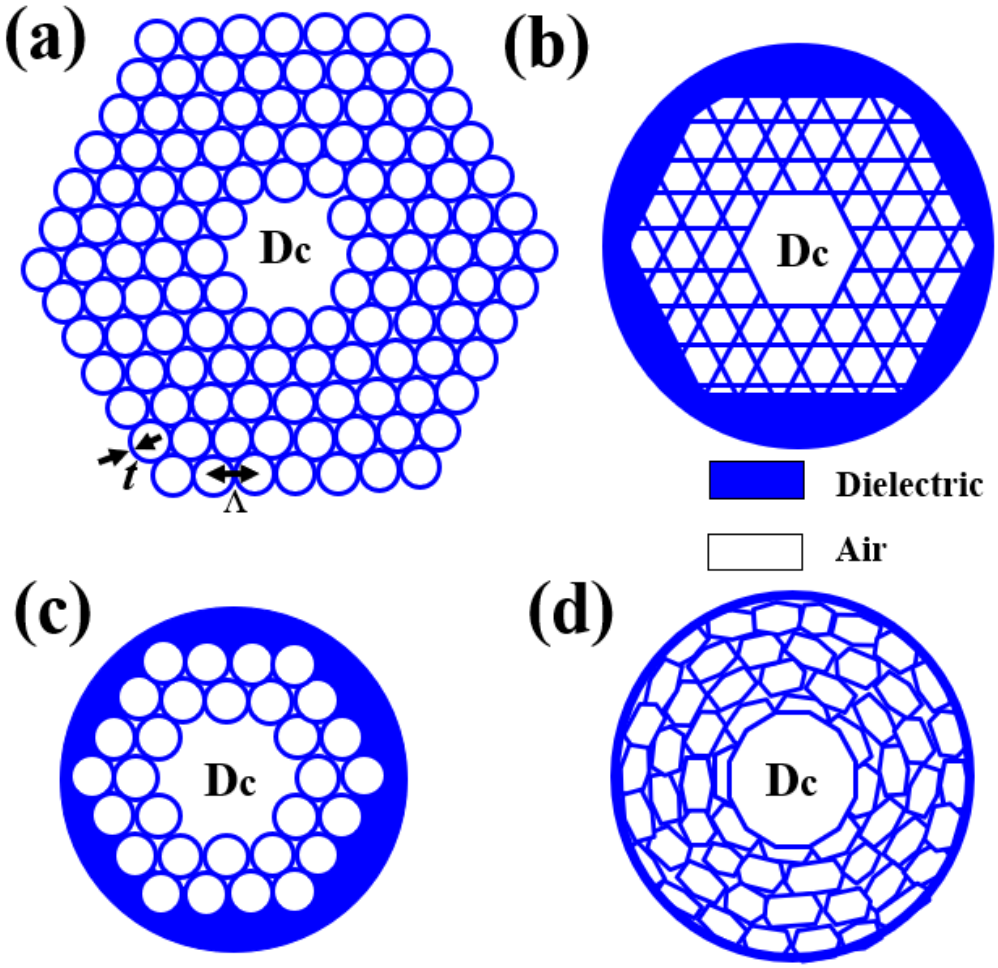

Figure 2.4. kagome structured fibre in terahertz. (a) Air-core microstructure fibre (Lu *et al.* 2008b) (b) Kagome fibre (Vincetti 2009b) (c) Triangular tube lattice hollow-core fibre (Vincetti 2009b, Vincetti 2010, Yang *et al.* 2016, Li *et al.* 2017a) (d) Kagome hollow-core microstructured fibre (Anthony *et al.* 2011b).

propagation in the core with low losses and in broad spectral bands. Because impact of antiresonance on the kagome lattice, the wave guided modes are restricted to the hollow core and are stopped from proficiently coupling to the cladding.

Both the core and the microstructured cladding support propagating modes, but they do not couple to each other owing to the anti-resonance effect. Only, the core mode may couple to cladding modes when the two are resonant, and this is most pronounced at the cut-off frequencies of the cladding modes, resulting in high transmission loss. In other words, the supporting thin walls add some parasitic couplings between the core

2.5.3 Kagome hollow core photonic crystal fibres

Hollow core kagome fibre	Material	Core size	Loss	Dispersion	Guiding mechanism
Air-core microstructure fibre (Lu *et al.* 2008b)	Teflon (PTFE)	D_c = 3, 3.5, 4, 5.5 mm; OD = 8.5, 9.8, 11.45, 16 mm L = 20 cm	0.01 cm^{-1} over the 0.2–0.8 THz (0.002 cm^{-1} at the 0.77 THz) for 5.5 mm core diameter	–	–
Kagome hollow-core microstructured fibre (Anthony *et al.* 2011b)	PMMA	D_c = 1.6 and 2.2 mm; OD = 5 and 6.8 mm, L = 15–45 mm, and 20–45 mm for 1.6 and 2.2 mm core diameter	1 cm^{-1} over 0.75–1.0 THz and 0.6 cm^{-1} over 0.65–1.0 THz for 1.6 and 2.2 mm	Low	Single mode
Kagome photonic crystal waveguide (Yang *et al.* 2016)	VeroWhitePlus polymer	D_c = 9 mm; OD > 16.4 mm, L = 10–30 cm	0.02 cm^{-1} for 0.2–1.0 THz (the minimum is about 0.002 cm^{-1} at 0.75 THz)	–	–

Table 2.7. Kagome hollow core photonic crystal fibres in terahertz. Summarizes the used material, the guiding mechanism, size, and other optical properties.

mode and cladding modes that perturb the attenuation spectrum with high attenuation peaks. Therefore, inhibited coupling usually shows abrupt transmission dips within the transmission band caused by the weak but finite coupling between core modes and cladding modes due to the antiresonant effect. The antiresonant reflecting optical waveguide (ARROW) model (Litchinitser *et al.* 2002) can be used to predict the frequency of the high loss regions, as they occur at the cut-off frequencies for the modes supported by the solid struts in the cladding of the fibre (Pearce *et al.* 2007, Argyros and Pla 2007). It should be mentioned the properties of kagome hollow-core PCF are similar to the hollow-core pipe fibres. The attenuation spectrum is smaller than the hollow-core pipe, due to the addition of at least one antiresonant layer (i.e., a thin hexagonal layer) (Pearce *et al.* 2007).

The aspect of the kagome lattice that contributes to the inhibited coupling mechanism is the thickness of the struts and not the pitch. Therefore, the transmission windows are limited by the strut thickness. This means that the overall diameter of the waveguide can be reduced by reducing the pitch, whilst keeping the strut thickness constant. However, this may come at the cost of reducing the core size and increasing the loss as a result, and a study of this trade-off was reported by Wu *et al.* (2011a). It is not necessary to have many layers at the lattice surrounding the core as the dominant loss mechanism in inhibited coupling fibres is coupling to cladding modes, and not tunnelling through the cladding as in band-gap fibres. Tunnelling can be reduced by extending the cladding outwards from the core, however, as this is not relevant to inhibited coupling fibres, where the overall cladding can be minimised to just a few layers (Argyros and Pla 2007, Wu *et al.* 2011a). A simple and useful analytical model has been developed to understand guidance mechanism and to predict high loss band frequencies in the optical regime (Couny *et al.* 2007, Pearce *et al.* 2007).

Experiments on terahertz kagome fibre (Lu *et al.* 2008b, Anthony *et al.* 2011b, Yang *et al.* 2016), the cladding can be seen as composed of an array of hollow tubes with different shapes. The kagome fibre with a cladding formed by a periodic arrangements of circular tubes in a triangular lattice were reported by Lu *et al.* (2008b) and Anthony *et al.* (2011b) by stacking them together as shown in Figure 2.4(a) and (d), respectively. Teflon tubes are stacked together by hand to form a triangular lattice and seven Teflon tubes have been removed from the center to create a 3, 3.5, 4, and 5.5 mm hollow-core (Lu *et al.* 2008b) in Figure 2.4(a). In simulations, both the single layer and three-layer kagome lattice show similar frequency dependent behaviors, revealing that the guiding mechanism may be just like the ARROW, and the waveguide is dominated by the first cladding layer and the increase of the ring number has little influence on the modal properties of the waveguides. Also, the simulated modal pattern shows that most terahertz field is concentrated inside the central hollow air core and is guided without outside interference, which has high potential for guiding intense terahertz waves with minimized loss. The fabricated kagome fibre with a five-layer cladding and a length of 20 cm shows less than 0.01 cm^{-1} (0.9 dB/m) attenuation at 0.77 THz.

2.5.3 Kagome hollow core photonic crystal fibres

An inhibited coupling waveguide using PMMA was also reported (Anthony *et al.* 2011b) and Figure 2.4(d) shows the geometry. This was of a kagome lattice waveguide with a relatively short lattice pitch and thick struts, a core diameter of 1.6 and 2.2 mm and an overall diameter of 5 and 6.8 mm, respectively. The average power attenuation coefficient is about 1 cm^{-1} over 0.75–1.0 THz for 1.6 mm core diameter. A transmission loss below 0.6 cm^{-1} ($\sim$ 80 dB/m) was measured between 0.65 and 1 THz using a 2.2 mm core diameter, which was approximately 20 times below the material loss of PMMA. It is justified that spatial overlap is reduced in large core diameter as the struts surrounding the core are farther from the center of the core and the field is less intense at the core boundary than the 1.6 mm core. The near field of the output was also characterised to show single-mode operation.

The 3D printing technique will be a promising solution to fabricate terahertz kagome waveguide with controllable characteristics at low cost. Due to the layer-by-layer printing nature of this technique, the fabrication is very convenient, accurate, mass-production capable, and highly flexible. Yang *et al.* have fabricated a kagome photonic crystal waveguide in polymer material by 3D printing (PolyJet-printed) (Yang *et al.* 2016) shown in Figure 2.4(c). The fibre is composed of a hollow-core of 9 mm diameter surrounded by two layers of air holes with a diameter of 3 mm and a wall thickness of 0.35 mm. The maximum fibre length is 30 cm. The cladding design is more a triangular lattice of connected capillaries than a kagome lattice. The kagome type waveguide exhibits a broader bandwidth, which has an average propagation loss of 0.02 cm^{-1} (8.7 dB/m) between 0.2 and 1.0 THz, especially a minimum propagation loss of 0.002 cm^{-1} (0.87 dB/m) at 0.75 THz. Even if the kagome-lattice cladding protects the waves guided in the core to external perturbations, the large outer diameter of such fibre could be reduced since most of the confinement is realized by the two first layers as shown on Figure 2.4(c).

For this prospect, Wu *et al.* have proposed a numerical study on the reduction of the overall fibre diameter by eliminating the outermost cladding layers for the resulting fibres to be practical and flexible (Wu *et al.* 2011a). Several other proposals have been made in the literature on terahertz kagome lattice PCF (Vincetti 2009b, Vincetti 2010, Vincetti and Setti 2012a, Li *et al.* 2017a) shown in Figure 2.4(b–c). Theoretical investigations of these waveguides reveal that the transmission spectrum exhibits an alternation

of low loss and high loss bands. The minimum loss in each low loss region depends on the tube diameter, while the frequency ranges of low loss and dispersion is depend on the thickness of the tubes (Vincetti 2009b).

A group velocity dispersion (β_2) stays relatively small in the high-transmission windows, typical of hollow-core fibres. The low β_2 values exhibited by these fibres are comparable to that of the experimentally achieved low dispersion waveguides (Mendis and Grischkowsky 2001b, Wang and Mittleman 2004, Han *et al.* 2002, Jin *et al.* 2006, Ponseca Jr *et al.* 2008, Anthony *et al.* 2011a). Numerical results suggest that in the fabricated fibres low loss regions can be tuned just by modifying tube thickness t, while the outer diameter can be used to choose the core size and the minimum loss (Vincetti 2009b). In each low loss region, dispersion curve shows a S-shape due to anticrossing with cladding modes at the resonance frequencies. The increment of the tube diameter leads a lower and more flattened curve due to the wider core. In some cases dispersion curve is perturbed approaching low loss regions edge due to weak resonances with other cladding modes, whose effects have already observed in propagation loss spectra.

These hollow-core structures are representative of two most promising fabrication techniques applied to terahertz optical fibre manufacture. The first technique (stack and draw) allows obtaining flexible single-mode waveguides and the second technique (additive manufacturing by 3D printing in polymer) open the possibility to fabricate special designs that are impossible to by prepare with any other manufacturing technique.

When compared with the Bragg waveguide, kagome lattice waveguide offers three times wider transmission band (Wang *et al.* 2011). But the losses due to absorption are eight times higher in kagome-lattice waveguide in comparison to the Bragg waveguides.

A significant downside of kagome waveguides is their large size and lack of flexibility. As an example for the seven ring microstructure fibre proposed by Lu *et al.* (2008b), the total fibre diameter ranges from 16 to 8.5 mm for the commercially available Teflon tubes with the outer/inner diameters of 1.68/2.08 mm, and 0.81/1.11 mm; $>$ 16.4 mm for Yang *et al.* (2016) and 5 mm by Anthony *et al.* (2011b). Therefore, analysis of the

bending loss is not possible to consider. Another disadvantage of these fibres is that they are multimode due to the large core diameters. It has been shown that reducing the core size leads to single mode propagation at the expense of high fundamental mode propagation losses and dispersion. In each low loss region, the dispersion curve shows a S-shape due to anticrossing with cladding modes at the resonance frequencies. Another downside of inhibited coupling usually shows abrupt transmission dips within the transmission band caused by the weak but finite coupling between core modes and cladding modes due to the antiresonant effect.

2.5.4 Tube lattice hollow core fibres

Tube lattice hollow core fibres are the latest simplified version of the kagome waveguides based on antiresonance guiding mechanism with inhibited coupling between the core and cladding modes (Vincetti 2010). The hollow core of the tube lattice fibre is separated from the outer jacket by a cladding formed with layers of triangle tubes arrangement. The simplified structure features an on-node/node-less core boundary, a negative/planar core curvature and a single tube cladding layer as shown in Figure 2.5. Adding a second layer of tubes in a triangular lattice can reduce leakage a little more but adding even more layers has negligible effect (Vincetti 2010). Also, the numerical simulation of kagome type fibre, with a periodic cladding structure demonstrates that the optical properties of the antiresonant fibre largely depend on the first air cladding layer surrounding the air-core. Prior published experimental (Setti *et al.* 2013, Lu and Argyros 2014, Lu *et al.* 2015b, Lu *et al.* 2015a, Cruz *et al.* 2017, Nazarov *et al.* 2018, Stefani *et al.* 2018, Van Putten *et al.* 2018, Li *et al.* 2019, Yang *et al.* 2020, Sultana *et al.* 2020c, Islam *et al.* 2021, Talataisong *et al.* 2021, Yang *et al.* 2021, Sultana *et al.* 2022) and numerical works (Vincetti and Setti 2010, Vincetti *et al.* 2010, Yan *et al.* 2018, Hasanuzzaman *et al.* 2018, Sultana *et al.* 2019c, Yan and Li 2019, Sultana *et al.* 2020b, Mollah *et al.* 2020b) based on single layer tube lattice are the main concern in this section as well as in the following chapters also. Tube lattice fibres (Setti *et al.* 2013, Lu *et al.* 2015b, Nazarov *et al.* 2018) are also referred as hollow core antiresonant photonic crystal fibre (HC-ARPCF) (Cruz *et al.* 2017, Stefani *et al.* 2018, Talataisong *et al.* 2021) from their antiresonant guidance mechanism or negative curvature fibre (Cruz *et al.* 2015) as curves facing the interior of the core.

Hollow core tube lattice fibre	**Material**	**Core size**	**Loss**	**Guiding mechanism**
Circular tube lattice fibre (with node) (Setti *et al.* 2013)	PMMA	D_c = 3.24 mm; D = 1.99 mm; t = 0.252 mm; OD = 9.6 mm; L = 10 and 20 cm	0.25–1.00 (2 transmission window) 0.3 dB·cm^{-1} at 0.375 THz and 0.16 dB·cm^{-1} at 0.828 THz	Inhibited coupling
Circular tube lattice fibre (with node) (Lu *et al.* 2015b)	Zeonex	D_c = 3.84 mm; D = 2.4 mm; t = 0.378 mm	0.1–1.2 (3 transmission window); 1 dB/m at 1 THz	Inhibited coupling
Circular tube lattice fibre (with node) (Lu *et al.* 2015a)	Zeonex	D_c = 3.3, 4 and 3.8 mm; t = 0.092, 0.220 and 0.378 mm; L = 20 cm	0.1–1.5 (3 transmission window); 1 dB/m in 0.55–0.7 and 0.95–1.05 THz and is lower than 5 dB/m for lower frequencies around 0.35 THz	Inhibited coupling, single mode
Circular tube lattice fibre (with node) (Nazarov *et al.* 2018)	PP	D_c = 1.3 mm; D = 0.8 mm; t = 0.06 mm; OD = 3.0–5.3 mm; L = 20–30 cm	0.5–2.5; 7 dB/m in 2–2.2 THz	Inhibited coupling, single-moded
Ice-cream cone shape negative curvature fibre (with node) (Cruz *et al.* 2015)	ABS	D_c = 8.40 mm; D = 10.52 mm; t = 0.54 mm; OD =25 mm; L = 10 cm	0.1–1.1 THz	Antiresonant effect
Fan-shaped negative curvature fibre (with node) (Li *et al.* 2019)	PLA	t = 0.79 mm; L = 14–89 cm	0.015 cm^{-1}	Antiresonant effect

2.5.4 Tube lattice hollow core fibres

Hollow core tube lattice fibre	Material	Core size	Loss	Guiding mechanism
Double pentagon nested fibre (with node) (Yang *et al.* 2020)	Resin	D_c = 9.94 mm; t = 0.96 mm; OD = 17 mm; L = 15 cm	0.11 cm^{-1} in 0.22–1.0 THz (3 transmission window); 0.012 cm^{-1} at 0.922 THz	Antiresonant effect
Circular HC-ARPCF (node-less) (Sultana *et al.* 2022)	Resin	D_c = 5; t = 0.72±0.11 mm; L = 0.8–5 cm	0.21 dB/mm at 0.90 THz; 1.16–1.34 THz	Inhibited coupling and Antiresonant effect
Antiresonant fibre (node-less) (Stefani *et al.* 2018)	PU	D_c = 3 mm; t = 0.4 mm; L = 10–20 cm	0.1–1.1 THz; 10 dB around 0.8 THz for the 10 cm fibre	Antiresonant effect
Circular HC-ARPCF (node-less) (Sultana *et al.* 2022)	Zeonex	D_c = 5; t = 0.73±0.05 mm; OD = 11.8 mm; L = 0.8–5 cm	0.56 dB/mm at 0.63 THz; 0.59–0.74 THz	Inhibited coupling and Antiresonant effect
Semi-elliptical fibre (node-less) (Van Putten *et al.* 2018)	PC	D_c = 6, 6, 10 mm; t = 0.6, 0.6, 1.2 mm; L = 8.7 cm	0.15–0.6 THz	Antiresonant effect
Circular HC-ARPCF (node-less) (Sultana *et al.* 2020c)	Zeonex	D_c = 5; t = 0.45 mm; D = 2.45 mm; OD = 11.8 mm; L = 0.8–5 cm	0.24–1.00 THz	Inhibited coupling and Antiresonant effect

Table 2.8. Tube lattice hollow core fibres in terahertz. Indicating the geometrical and optical properties.

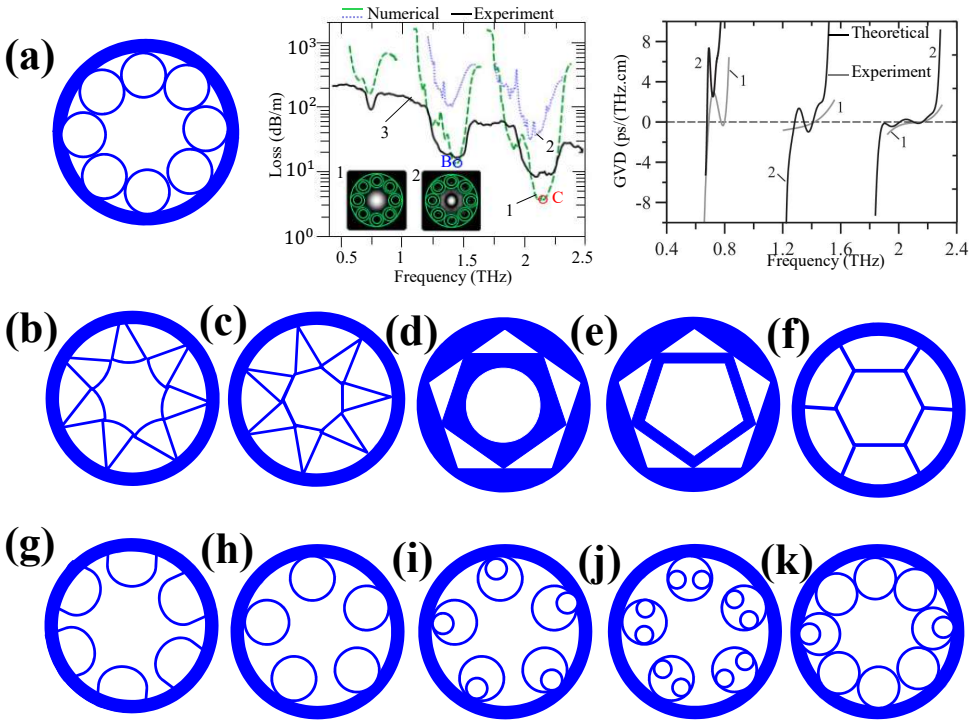

Figure 2.5. Antiresonant structured HC-ARPCF in terahertz regime. (a) Flexible tube lattice fibre with loss and dispersion curve as a function of terahertz frequency (Setti *et al.* 2013, Lu *et al.* 2015b, Lu *et al.* 2015a, Nazarov *et al.* 2018, Stefani *et al.* 2018); (b–c) Ice-creame cone shaped and planar boundary HC-ARPCF (Cruz *et al.* 2015, Li *et al.* 2019); (d–e) Double pentagon nested HC-ARPCF (Yang *et al.* 2020); (f) Patterned hexagonal HC-ARPCF (Islam *et al.* 2021, Talataisong *et al.* 2021); (g) Half-elliptical HC-ARPCF (Cruz *et al.* 2017, Yang *et al.* 2021, Van Putten *et al.* 2018); (h) Regular HC-ARPCF (Sultana *et al.* 2020b); (i) Nested HC-ARPCF (Hasanuzzaman *et al.* 2018, Sultana *et al.* 2020b); (j) Adjacent nested HC-ARPCF (Sultana *et al.* 2020b); (k) Polarization maintained HC-ARPCF (Yan *et al.* 2018, Mollah *et al.* 2020b).

The guiding mechanism of the tube lattice fibres are similar to the ones of the pipe waveguides or kagome hollow-core PCF. The transmission windows are limited by sharp propagation losses at the resonant frequencies where the core modes coupled to leaky cladding modes. The resonant frequencies are well approximated by one of the single tube from the cladding arrangement that is defined by its refractive index, wall thickness, and external diameter (Vincetti and Setti 2010). As for a pipe or a kagome fibre, the transmission windows depend on the wall thickness of the tubes that form the cladding. On other hand, wider transmission windows in the tube lattice fibres are obtained for a tube with a thin wall and a large diameter (Sultana *et al.* 2019c, Sultana *et al.* 2020b, Sultana *et al.* 2022). A thorough theoretical investigation of tube lattice

fibres for terahertz regime has shown them to have potentially broadband transmission windows with multiple transmission windows, low power overlap with the absorbing material region, low dispersion and low loss levels (Vincetti 2009b, Vincetti *et al.* 2010, Vincetti 2010, Sultana *et al.* 2019c, Sultana *et al.* 2020b). Moreover, the cladding tubes provide resonant coupling to core higher order modes (HOMs) to provide HOM suppression (Vincetti *et al.* 2010, Sultana *et al.* 2019c, Sultana *et al.* 2020b, Sultana *et al.* 2022). The difference of propagation loss between the fundamental and the higher order core modes can be increased by a proper choice of cladding features, thus allowing microstructured fibres to be effectively single mode. The cladding tube presents another interest for reducing the propagation losses. The individual tubes contribute to lower the loss as compared to a usual kagome lattice, which consists of straight segments in the cladding (Vincetti and Setti 2012a).

Following the developments of simplified structure, Setti *et al.* (2013) fabricated a hollow core circular tube lattice terahertz fibre, including a comprehensive study of bending. The external diameter of the tube lattice fibre is 9.6 mm. The cladding is a collection of eight hollow dielectric PMMA tubes placed in a circle with an average tube wall thickness around 252 μm and an external tube diameter of about 1.99 mm, leading to a core size around 3.24 mm. Two consecutive tubes in the cladding have no adjacent gap (with node) as shown in Figure 2.5 (a). Cladding tubes were drawn from commercially available PMMA tubes and the structure was assembled manually in such a way as to keep the waveguide flexible. Small pieces (L = 5 mm) of jacket (PMMA tubes) have been added each 10 cm and 20 cm on the fibre structure for ensuring its mechanical stability and flexibility. They have measured two transmission windows extending from 0.29–0.47 THz and from 0.29–0.47 THz for the fundamental core mode. High loss peaks due to the coupling between the core mode and cladding modes separate the different transmission windows at the two resonant frequencies. Comparing the experimentally measured loss of the circular tube lattice fibre and the material absorption of the PMMA, a reduction of 31 times (α_{mat} = 0.3 dB/cm) at 0.375 THz and 272 times (α_{mat} = 16 dB/m) at 0.828 THz were obtained. Theoretical analysis predicts that the loss can be lower than 10 dB/m, but despite the hollow core this was limited by absorption of the PMMA used for the cladding tubes. The reduction of the attenuation coefficient was realized by replacing the PMMA tubes with Zeonex polymer tubes in a subsequent study (Lu and Argyros 2014, Lu *et al.* 2015b, Lu *et al.* 2015a). Lu *et al.* reported a Zeonex based fibre with the lowest loss of 1 dB/m at 1 THz for

the core diameter and the tube thickness of 3.84 mm and 0.378 mm respectively. The transmission spectrum ranges between 0.1–1.2 THz with three transmission windows. Cladding tubes were drawn first and stacked manually. The lowest reported loss in this frequency range makes the tube lattice hollow-core terahertz fibres one of the best terahertz fibres. In 2018, Nazarov *et al.* (2018) demonstrated the possibility of manufacturing a single-mode flexible waveguide, with a loss of 7 dB/m within 1.9–2.2 THz for 1.3 mm core diameter.

A hollow core ice-cream cone shape negative curvature antiresonant tubes was experimentally demonstrated by Cruz *et al.* (2015), Li *et al.* (2019), where the guidance of electromagnetic waves is supported by the antiresonant effect. As shown in Figure 2.5 (b–c), this fibre was fabricated with ABS polymer via Fused Deposition Modeling (FDM) technology (Cruz *et al.* 2015). The experimental results showed a propagation loss of 0.3 dB/cm at 0.47 THz, and three low-loss transmission windows were observed between 0.1–0.21, 0.3–0.4, and 0.5–1.1 THz. Furthermore, this hollow-core structure exhibited several surface modes, due to the low resolution of the FDM 3D printer. The numerical comparison between planar boundary and negative curvature core is also remarkable. An experimental demonstration of the planar boundary, shown in Figure 2.5 (d–e) added in (Yang *et al.* 2020) using double pentagon nested fibre based on SLA printing. Experimental results show an average attenuation coeffecient of 0.11 cm^{-1} in the three consecutive transmission window in the range of 0.2 to 1 THz. A patterned nozzle (Islam *et al.* 2021, Talataisong *et al.* 2021) can reduce the amplitude of the undesired corrugations than the 3D printed structure, making the material wall more uniform and fabricate the antiresonant fibre in Figure 2.5 (f) using single step fabrication process. The fibres (Setti *et al.* 2013, Lu and Argyros 2014, Lu *et al.* 2015b, Lu *et al.* 2015a, Cruz *et al.* 2015, Yan *et al.* 2018, Nazarov *et al.* 2018, Li *et al.* 2019, Yang *et al.* 2020, Islam *et al.* 2021, Talataisong *et al.* 2021) are examples of with-node antiresonant negative curvature fibres as the two consecutive tubes touch and create a node around the hollow core. These negative curvatures minimize the spatial overlap between the core modes and the cladding modes (in the tube lattice) leading to a better confinement and lower attenuation coefficient of the core modes.

2.5.4 Tube lattice hollow core fibres

The negative core curvature is found to enhance the inhibited coupling between the core and cladding modes (Cruz *et al.* 2015), while the node-less core boundary helps to reduce the loss caused by Fano-resonance (Vincetti and Setti 2012b). Node-less core boundary means that the tube elements do not touch. The concept of node-less half-elliptical tube cladding was first explored and modelled in terahertz spectrum using FDM and SLA method (Cruz *et al.* 2017, Van Putten *et al.* 2018, Yang *et al.* 2021), sketched in Figure 2.5 (g), arise from the fact for further lowering transmission loss. The open structure at the cladding jacket allows the fibre to perform as a pressure sensor (Cruz *et al.* 2017). The thicker ABS polymer regions (0.4 mm and 0.2 mm) due to the fabrication methods cause an excessive increase of surface modes. The thickness of the polycarbonate membranes that can be produced in FDM printer by Van Putten *et al.* (2018) is limited to multiples of 0.6 mm with D_c = 6 mm. The resultant effective bandwidth over which useful spectroscopic data can be obtained is in the range of 0.15 THz to 2.0 THz with two consecutive transmission window. A whole FDM printing process from Zeonex filament making to nodeless circular HC-ARPCF is demonstrated by Sultana *et al.* (2020c) and in Figure 2.5 (h). The cross section of the seven-tube HC-ARPCF that used in experiment is of $D_c = 5$ mm, $d_{in} = 1.55$ mm, $t = 0.45$ mm, $w = 1.25$ mm, and $g = 0.811$ mm. The lowest transmission loss of 0.04 dB/mm is obtained from analysing the reference fibre and sample fibre around 0.53 THz. Also, an optimised seven-tube HC-ARPCF can act as a refractometric sensor. A further experiments has extended the deployment of 5 to 7-tubes for different thickness and adjacent gaps based on FDM and SLA method (Sultana *et al.* 2022) in order to analyse the performance in terms of geometrical parameters and type of printing method used. Numerical demonstration for being an effectively single mode fibre has been demonstrated by Sultana *et al.* (2020b), Sultana *et al.* (2022). The tube diameter, wall thickness, adjacent gap between two consecutive tubes, tube number as a function of the core diameter plays an important role for being being an effectively single mode fibre.

Further reduction of the attenuation coefficient is possible to acheive by exploiting advanced design of HC-ARPCF developed by Hasanuzzaman *et al.* (2018), Sultana *et al.* (2020b) referred to as nested and adjacent nested fibre, shown Figure 2.5 (i–k). The simulation based study demonstated that the reduction of the attenuation coefficient is possible by adding one or two tubes within each tube of the cladding with enhanced single-mode operation.

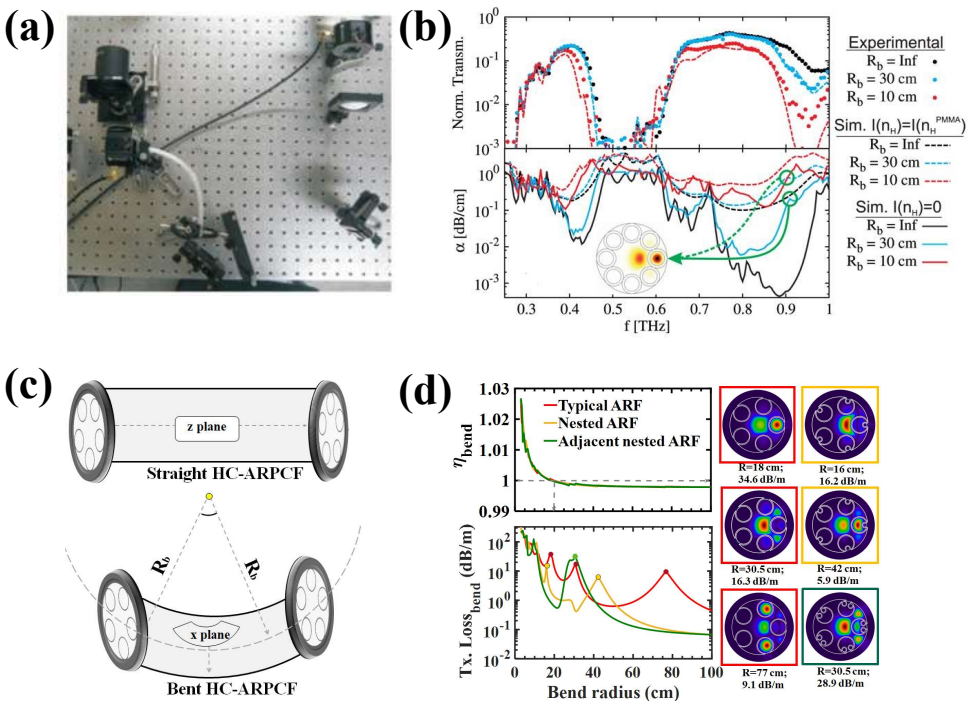

Figure 2.6. Bent structure of HC-ARPCF. (a) Experimental setup of a bent HC-ARPCF, Setti *et al.* (2013) (b) Normalised transmission and propagation loss for different bend radius in simulation and experiment, Setti *et al.* (2013) (c–d) Symbolic representation of straight and bent HC-ARPCFs along with their fundamental mode properties, Sultana *et al.* (2020b).

As previously mentioned, this fibre structure is favorable for broadband transmissions and bending. During the bending loss characterization an external heat-shrink jacket is placed over the 20 cm fibre structure to enhance its mechanical stability (Setti *et al.* 2013) in Figure 3.9 (a–b). The low frequency edges in both transmission windows are substantially insensitive to bending, whereas the high frequency edges shift toward lower frequencies as the bending radius (R_b) decreases from 30 to 10 cm. Bends induce a reduction of the transmission windows by a shift of the higher frequency edges to lower frequency. This shift is induced by a variation of the cutoff frequencies of the cladding modes. Similar experimental demonestration for (R_b) = 30 cm has been performed by Lu *et al.* (2015b) and the loss is still below 5 dB/m. More details regarding analytical and numerical bending loss are discussed by Setti *et al.* (2013), Sultana *et al.* (2020b). The bending loss of a fibre is characterized in two sequential forms: curvature dependent and frequency dependent confinement loss (Sultana *et al.* 2020b). The curvature dependent bending loss starts with the transition of curvature radii (R_b) from zero (and

infinite for straight fibre) to finite (for bent fibre), shown in Figure 3.9 (c–d). The bending of straight fibre, for example towards the x-plane makes the fibre bent and deforms the fundamental air-core index profile towards the cladding tube. This deformation of index profile towards the cladding tube enhances the confinement loss as compared to straight fibre. Smaller bend radius leads to higher refractive index in the outer bent curvature and therefore to smaller cutoff frequencies of the cladding modes that delimit the transmission windows. Furthermore, when the bend radius is small, extra losses due to the resonances between the core mode and cladding modes appear. The refractive indices inside the cladding tubes change according to their relative position along the bend direction and the bend radius. In particular, the effective indices of the hole modes of the tubes increase approaching the one of the core modes until the phase matching condition is reached, causing the extra losses. To increase fibre flexibility, Stefani *et al.* (2018) adopted a mechanically twisted HC-ARPCF, made from polyurethane (PU) dielectric material. This dielectric material allows a 1 cm diameter fibre bent into a 10 cm radius circle, for example. The idea of twisting fibre structures is very interesting because it enables creating modes with an orbital angular momentum (OAM), and controlling the state of polarization and the fibre's optical activity.

A group velocity dispersion (β_2) is influenced by the proximity of modes in the cladding, hence is affected strongly at the edges of the transmission windows, and also by the relative size of the core and wavelength, hence taking larger positive and negative values at lower frequencies (Lu and Argyros 2014, Lu *et al.* 2015b, Lu *et al.* 2015a). In each transmission window, the dispersion is typical of hollow core fibres: below zero at low frequencies, around zero in the middle of each transmission windows, and above zero at high frequencies, shown in Figure 2.5 (a). A group velocity dispersion (β_2) stays strong in the first transmission window at f = 0.76 THz as the core size D_c = 1.3 mm is comparable to the wavelength in this case (Nazarov *et al.* 2018). In particular, β_2 does not exceed 1 ps/(THz·cm) in the frequency range 2–2.2 THz.

Highly birefringent terahertz fibres have potential applications in polarization sensitive terahertz time-domain spectroscopy systems and measurements of biomaterials in terahertz frequency bands (Karpowicz *et al.* 2008, Crowe *et al.* 2004). Based on these requirements, a high-birefringence hollow-core antiresonant terahertz fibre is reported by Yan *et al.* (2018), Mollah *et al.* (2020b) by introducing asymmetry in the cladding.

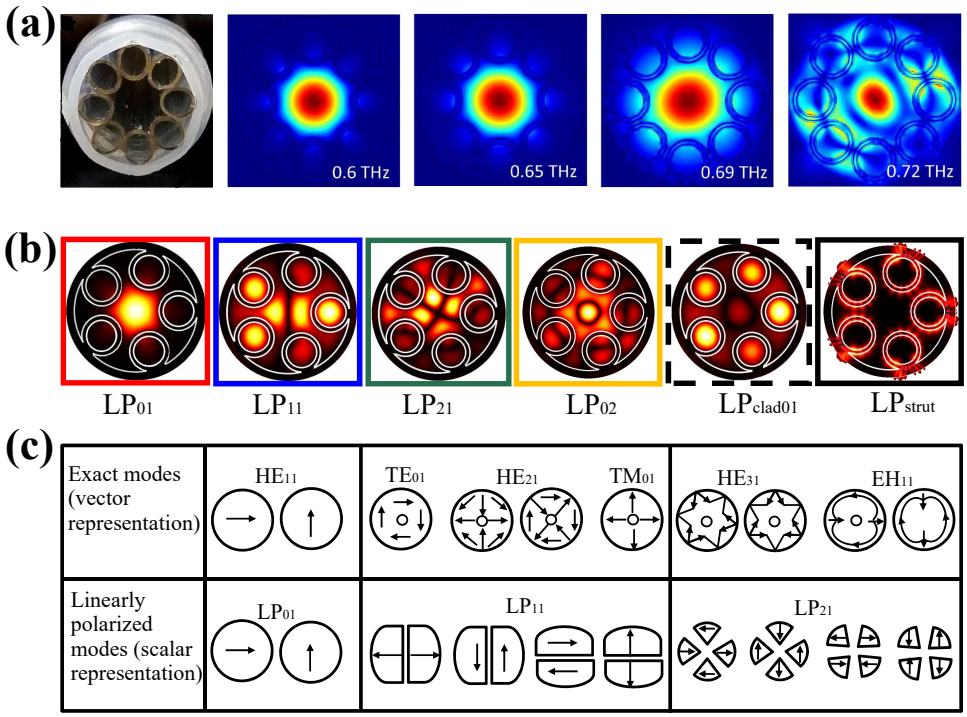

Figure 2.7. Mode profile of HC-ARPCF in terahertz. (a) Mode field distribution of fundamental core mode at different frequencies for HC-ARPCF (Lu *et al.* 2015a) (b) Normalised modal field intensity for core modes and cladding modes through a HC-ARPCF (Sultana *et al.* 2022) (c) The vector and scalar core modes representation of a pipe waveguides (Ma *et al.* 2009).

The simulation results show that the difference between η_{eff} of x- and y-polarization results in a maximum birefringence of 10^{-4}.

The modal analysis of a terahertz wave propagating through the HC-ARPF structure is discussed by Lu *et al.* (2015a), Talataisong *et al.* (2021), Sultana *et al.* (2021). The mode field distribution at four different frequencies can result in low or high loss (Lu *et al.* 2015a). The fundamental core mode is well confined in the hollow core at 0.6 THz, and the fibre loss is very low. As the frequency increases towards the resonance frequency, the fundamental core mode field begins to expand into the cladding, and the loss increases. Around the resonance frequency of 0.72 THz, the fundamental core mode is coupled with the cladding mode, resulting in high loss as expected. The mode field intensities are the Linearly Polarized (LP) modes derived by solving scalar Maxwell's equations under weakly-guided conditions (Gloge 1971) and experimentally characterised by Ma *et al.* (2009). There are two examples of core modes: the fundamental core mode LP_{01}, and the higher order core modes (LP_{11}, LP_{21}, LP_{02}, ...).

2.5.4 Tube lattice hollow core fibres

At the same frequency, there are two kinds of highly lossy cladding modes: the strut modes (LP_{strut}) whose power is mainly located in the dielectric and the cladding modes (LP_{clad01}) whose power is mainly located inside the tubes (Vincetti *et al.* 2010, Sultana *et al.* 2020b, Sultana *et al.* 2020c, Sultana *et al.* 2022). The LP_{clad01} creates a strong resonant coupling with LP_{01} at resonance frequency owing to their phase matched condition ($n_{\text{eff-LP}_{01}} = n_{\text{eff-LP}_{clad01}}$). The vector solutions of Maxwell's equations represents the LP_{01} as HE_{11}.

Single mode regime allows spectroscopy applications, for example of a gas filling the core (Setti *et al.* 2013, Sultana *et al.* 2020c), including nonlinear studies when short intense terahertz pulse will propagate along such a waveguide (Sultana *et al.* 2021). The mechanical flexibility of this kind of fibre has been successfully exploited as a probe in an endoscope geometry and used to guide radiation to and from a sample for enabling terahertz hyperspectral imaging by scanning the end face of the probe in front of the sample (Lu and Argyros 2014, Lu *et al.* 2015a). The results reported herein will potentially contribute to the development of low-loss short-distance terahertz transmission and ultra sensitive water sensing measurements (Islam *et al.* 2021).

The antiresonant fibres of Setti *et al.* (2013), Lu *et al.* (2015b), Nazarov *et al.* (2018) are fabricated by capillary stacking, stack and draw techniques, whereas large-scale fibres are fabricated using 3D printing (Cruz *et al.* 2015, Cruz *et al.* 2017, Van Putten *et al.* 2018, Yang *et al.* 2021, Sultana *et al.* 2020c, Yang *et al.* 2020, Sultana *et al.* 2022). A patterned nozzle with single fabrication method (Islam *et al.* 2021, Talataisong *et al.* 2021) can be used to fabricate the HC-ARPCF to avoid the undesired corrugations.

Tube lattice hollow core fibres dominate the panorama of hollow core fibres as they have a very simple structure, i.e., a circular array of capillaries, allows guidance of very large bandwidths with very low loss, almost independently of the absorption of the material used for the structure (Setti *et al.* 2013, Van Putten *et al.* 2018). Moreover, by tuning the geometrical parameters of this structure, it is possible to obtain single mode operation in large cores (Sultana *et al.* 2020b) and to tune the bending loss of the structure (Stefani *et al.* 2018, Sultana *et al.* 2020b). In the context of terahertz, the realization of such fibres allows reduction of the overall size compared to band-gap or kagome

structures, controlling the modal properties and further reducing the waveguide loss with any material used.

2.6 Comparison between photonic band-gap fibre and negative curvature HC-ARPCF

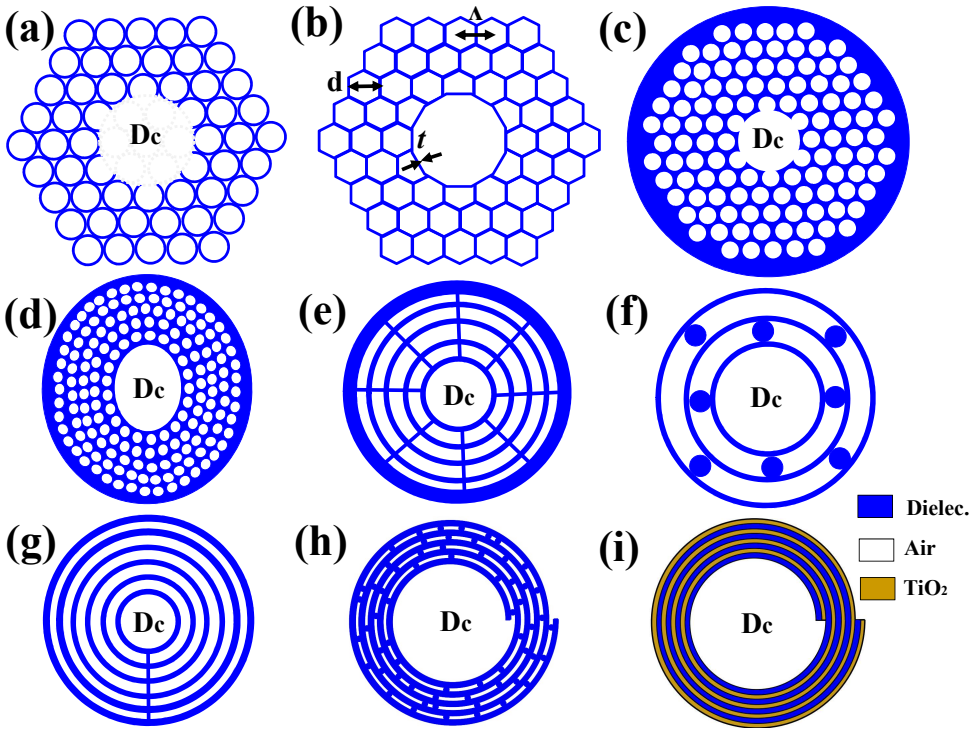

Figure 2.8. Hollow core photonic band-gap fibre in terahertz. Geometry of HC-PBG fibre with (a) Triangular tube lattice (Vincetti 2009a) (b) Hyperuniform disordered dielectric reflectors (Vincetti 2009a, Laurin *et al.* 2014, Ma *et al.* 2016) (c) Electromagnetic band-gap structures (Wu *et al.* 2010, Wu *et al.* 2011b); Geometry of Bragg fibre with (d) Ring-structured (Ponseca Jr *et al.* 2008) (e) Cobweb structure (Yu *et al.* 2007a, Yu *et al.* 2007b) (f–g) Porous structure (Hassani *et al.* 2008b, Cruz *et al.* 2015) (h–i) Rolled structure (Dupuis *et al.* 2011, Ung *et al.* 2011).

This subsection focuses on studying the comparison between two low-index core fibres, such as photonic band-gap (PBG) and negative curvature hollow-core fibres. The band-gap effect occurs in hollow core fibre when the fibre has a microstructured cladding with a periodic distribution of air holes so that the propagation mode field is confined within the core with the help of band-gap reflectors formed by periodic refractive index variation, which prohibit the guided transverse modes from extending

Hollow core photonic band-gap fibre	Material	Core size	Loss	Guiding mechanism
Hollow core PBG fibre (Wu *et al.* 2010, Wu *et al.* 2011b)	UV-curable polymer	D_c = 8.4 mm; D = 3.4 mm; Layer = 5; t = 0.40 mm; L = 5 and 15 cm	0.03 dB/mm at 0.1052 THz	PBG effect
Hollow core PBG fibre (Laurin *et al.* 2014, Ma *et al.* 2016)	ABS	D_c = 5 mm; t = 0.20 and 0.25 mm; OD = 20 mm; L = 2.5 and 10 cm	< 0.10 cm^{-1} at 0.23 THz; Band-gap location = 0.17, 0.22 and 0.29 and 0.38 THz and 0.14, 0.17, 0.23, and 0.29 THz for t = 0.20 and 0.25 mm	Band-gap = 15.3% at 0.29 THz; PBG effect
Ring-structured Bragg fibre (Ponseca Jr *et al.* 2008)	PMMA	D_c = 0.67 mm; OD = 6.3 and 5.6 mm; Layer = 5; L = 1.5 cm	minimum losses to be 1.9 dB/cm at 1.0 THz for fibre 1 and 0.9 dB/cm at 1.3 THz for fibre 2	Band-gap = 50% at 0.29 THz; PBG effect
Rolled Bragg fibre (Ponseca Jr *et al.* 2008)	PTFE	D_c = 6.73 mm; Layer = 5; t = 0.254 mm and 0.150 for PTFE and air; L = 21.4 cm	0.028 cm^{-1} at 0.82 THz	Band-gap = 50% at 0.29 THz; PBG effect
Doped rolled Bragg fibre (Ponseca Jr *et al.* 2008)	PE and TiO_2 powder	D_c = 6.63mm; Layer = 6; t = 0.135 and 0.100 mm for PE and TiO_2 powder; L = 22.5 cm	0.042 cm^{-1} at 0.69 THz	Band-gap = 50% at 0.29 THz; PBG effect
Bragg fibre (Cruz *et al.* 2015)	ABS	D_c = 7.2mm; Layer = 6; t = 0.55 and 0.75 mm for ABS and air; OD = 22.8 mm; L = 9.3 cm	0.1–1 THz	Antiresonant effect at the first polymer ring

Table 2.9. Hollow core photonic band-gap fibres in terahertz.

into the periodic cladding structures over a range of frequencies. The period of such an arrangement and the refractive index variation of the alternative materials together determine a spectral window for which no states are allowed in the cladding, i.e. the photonic band-gap. This removes the condition that the core has a higher index than the cladding, required for total internal reflection as discussed in solid and porous core fibres. The photonic band gap (PBG) type fibre has been well developed and understood in the terahertz regime, shown in Figure 2.8. In these fibres, coupling between core mode and cladding mode is forbidden, thus confining light though the hollow core results negligible transmission losses. In contrast, guidance in kagome/antiresonant fibres is due to the inhibited coupling mechanism, and the cladding does not support band-gaps. Besides, the most common PBG type fibres tend to have spectrally narrow transmission windows due to the formation of frequency dependent photonic band-gaps over a range of frequencies than the inhibited coupled fibre. Depending on the reflector structure, the PBG type fibres can be classified into two categories: (i) PBG fibres with a hexagonal cladding hole structure, shown in Figure 2.8 (a–c) and (ii) an omnidirectional Bragg type cladding with concentric layers of hole structures (Ponseca Jr *et al.* 2008), shown in Figure 2.8 (d–g) or with continuous layers of alternating materials (Dupuis *et al.* 2011, Ung *et al.* 2011), shown in Figure 2.8 (h–i).

In the case of PBG fibres with a hexagonal cladding hole structure (holey reflector), the reflector in the cladding is usually formed of a 2D photonic crystal with periodically positioned holes. In this thesis, this type of fibre is named as photonic band-gap (PBG) fibre. The high-precision hole structure provides very clear band-gap guidance. The band-gap effect at the reflector can only confine and propagate the mode through the core. A polarization-maintaining hollow core PBG polymer fibre is proposed for low-loss terahertz guidance by introducing an asymmetric rectangular core by a periodic arrangement of square holes with round corners in the cladding (Ren *et al.* 2009). Vincetti (2009a) showed in Figure 2.8 (a) that a holey reflector with only three layers of air-holes was sufficient to confine the majority of power in the core, and produced a attenuation coeffecient of 0.0002 cm^{-1} which is negligible compared to material (0.01 cm^{-1}) attenuation coeffecient in the same frequency range.

The fabrication of the first PBG type terahertz fibre was reported by Lu *et al.* (2008b), who stacked 20 cm long Teflon tubes in a close hexagonal structure and used thin

heat-shrinkable polyethylene tubes to keep the Teflon tubes together. To form a central hollow core, seven-Teflon tubes were removed from the structure after stacking. The fibre outer diameters were very large ($\sim$ 20 mm) as no drawing or fusing were used to reduce the preforms diameter. A minimum loss of 0.01 dB/cm was reported with an extremely narrow frequency band less than 20 GHz wide around 770 GHz. In fact no real band-gaps were observed, therefore, the authors instead attributed the guiding mechanism to antiresonant reflecting optical waveguiding (ARROW). In 2011 Wu *et al.* used polymer jetting rapid prototyping to make 5–15 cm long PBG terahertz fibres with a hexagonal cladding hole structure (Wu *et al.* 2010, Wu *et al.* 2011b), sketched in Figure 2.8 (c). A minimum loss of 0.3 dB/cm at 105.2 GHz was reported in a fibre with outer diameter 40 mm, core diameter 8.4 mm, pitch 3 mm, and inner hole diameter 2.6 mm. This special fabrication technique gave perfect hole structures, but imposes a minimum feature size of 0.1–0.15 mm. Due to the huge structure the transmission displayed no real band-gaps, but narrow resonances below 240 GHz. Hollow core PBG waveguides with the optimized hyperuniform disordered dielectric reflectors are fabricated using 3D MultiJet printing (Laurin *et al.* 2014, Ma *et al.* 2016), drawn in Figure 2.8 (b). The diameter of the fabricated hyperuniform waveguides is $\sim$ 20 mm, while the diameter of the hollow core is $\sim$ 5 mm. Experimental results show that the fabricated waveguides featured relatively wide band-gaps (up to $\sim$ 15%) and low attenuation coeffecient (< 0.10 cm^{-1}) within their PBGs. The transmission properties of these waveguides, including the transmission bands and dispersion characters, can be tuned simply by varying the geometrical parameters of the reflector. The main motivation of the hyperuniform disordered reflectors is to explore the possibility of designing hollow-core waveguides that feature spectrally broad band-gaps which are potentially superior to those attainable with purely periodic structures.

The stacking + tubing (Lu *et al.* 2008b) and polymer jetting (Wu *et al.* 2010, Wu *et al.* 2011b, Ung *et al.* 2011, Laurin *et al.* 2014, Cruz *et al.* 2015, Ma *et al.* 2016) techniques provide good periodic (hexagonal) hollow-core PBG structures, but at the expense of very thick reflactor and fibre diameter that do not display broadband, low loss guiding and do not easily allow bending, cleaving and fabrication of long lengths. The demonstrated hole structures were close to perfect, but evidently this type of large diameter PBG fibre is not practical and cannot be cleaved or bent.

Later Ponseca Jr *et al.* (2008) reported the first Bragg-type PBG treahertz fibre (ring-structured) fabricated by drilling one large center hole and consisting of concentric 5-layers of small holes around it into a 7 cm in diameter PMMA polymer rod and drawing it down to a terahertz fibre with approximately 6 mm diameter, shown in Figure 2.8 (d). The ring-structured fibres are the intermediate between 2D bandgap fibres and Bragg fibres. The fibre with the lowest loss of 0.9 dB/cm at 1.3 THz had a core diameter of 670 μm and hole diameters of 65 μm. The reported loss was 1–2 dB/cm (approximately 0.25–0.5 cm^{-1}) at around 1–1.3 THz, a factor of 30–60 times below the PMMA material loss at those frequencies. Importantly, the difficulties in maintaining the preform structure when drawing structures with different sizes of air-holes were very clear. Thus draw-induced deformations resulted in elliptical air-holes in the cladding and not optimised waveguide. Good-quality hollow-core terahertz PBG fibres have so far been difficult to draw due to the different expansion rates of holes of different diameter at elevated temperatures, which leads to deformation of the smaller holes during the drawing process, unless special precautions are taken. The imbalance of hole dimensions can to some extent be alleviated by applying pressure to the holes during drawing. However, such a procedure can only be applied to a limited extent and obviously adds to the complexity of fabrication.

A hollow-core Bragg fibre geometry with cobweb-structure (Yu *et al.* 2007a, Yu *et al.* 2007b) and porous structure (Hassani *et al.* 2008b) were discussed in Figure 2.8 (e–f) with a network of thin material bridges (strips) and of circular bridges (rod), respectively. Both structures are made from a single material. The cobweb-structure Bragg fibre numerically offers lower loss than the ring-structured PBG fibre. For the ring-structured hollow-core fibres, the cladding refractive indices of low and high-layers are of air and host material, respectively. As a result, authors claimed that cladding index contrast of cobweb-structured fibres are higher than the ring-structured fibres due to the larger porosity. Therefore, the ability to confine the transverse leakage of guided wave is better than the ring-structured fibres. However, practical implementation of such a geometry may be challenging (Atakaramians *et al.* 2009a). To reduce the fabrication complexity, in 2008, Hassani *et al.* considered a single material Bragg fibres made of a set of concentric material layers suspended in air by the network of circular bridges (rods). Radiation losses appear from the connecting rods and to reduce the radiation loss material layers need to be increased more than three. Although total modal loss (absorption plus radiation loss) lower than 5 dB/m can be predicted

with 130 dB/m bulk absorption loss of a fibre material, fibre bandwidth was found to be smaller than 0.1 THz. The surface states inhance with the increase of bridges size. Band-gaps of the Bragg fibres with bridges are fractured due to crossing of the core mode dispersion relation with those of the surface states. Parasitic coupling to the surface states of a multilayer reflector facilitated by the material bridges was determined as primary mechanism responsible for the reduction of the bandwidth of Bragg fibre. As a consequence, Cruz *et al.* fabricated a single material Bragg fibre using 3D printing (Cruz *et al.* 2015). Transmission bands were observed spanning 0.12–0.26 THz, 0.32–0.48 THz, and 0.50–1.00 THz. It is noticed a considerable numerical agreement with the measured results in the band-gap regions at low frequencies, but to high frequencies the dips in the transmission appear shifted. However, the terahertz propagation seems to be supported by the anti-resonant effect in the first polymer ring instead of the band-gap effect. Other type of Bragg fibres were subsequently reported in Figure 2.8 (h–i) using continuous layers of alternating materials, TiO_2-loaded HDPE for the high-index layers, and PTFE for the low-index layers (Dupuis *et al.* 2011, Ung *et al.* 2011). These type of Bragg fibres usually feature alternative layers to achieve a periodic variation of the refractive index in the radial direction to produce photonic band-gaps. These multiple layers act as a reflector. An example of such fibres is shown in Figure 10(a). The preform was rolled from thin sheets of polymer and solidified in an oven to give 22.5 cm long fibres with an inner hollow core diameter of 6.6 mm. These had a total diameter of around 12 mm (Ung *et al.* 2011). Several broad transmission bands with loss below 1 dB/cm were observed in the 0.1–2.0 THz regime with the minimum loss being less than 0.12 dB/cm (0.18 dB/cm) for the polymer/air (polymer/polymer) Bragg fibre in the region 0.7–0.8 THz. The rolling + solidification technique (Dupuis *et al.* 2011) can make low loss PBG Bragg fibres, but the fibres are very big and extremely fragile. Besides, it is difficult to find two materials they have larger index contrast, similar thermal and mechanical properties, as well as a compatible processing technique in realizing the structure.

The transmission properties of the PBG type fibre, including the transmission bands and dispersion characteristics, can be tuned simply by varying the geometrical parameters of the reflector. However, high air filling fraction in PBG fibres with a hexagonal cladding hole structure (Vincetti 2009b, Vincetti 2009a, Wu *et al.* 2010, Wu *et al.* 2011b, Ung *et al.* 2011, Laurin *et al.* 2014, Ma *et al.* 2016), or high refractive index contrast in Bragg fibres (Skorobogatiy and Dupuis 2007, Ponseca Jr *et al.* 2008, Dupuis *et al.* 2011,

Ung *et al.* 2011), as well as a strictly periodic cladding structure are needed to obtain an efficient and broad band-gap, which all increase the fabrication complexity.

To enlarge the transmission bandwidth, porous core with various periodic lattices such as, honeycomb (Nielsen *et al.* 2011, Bao *et al.* 2012, Fan *et al.* 2015, Bai *et al.* 2018, Lu *et al.* 2021) and triangular (Liang *et al.* 2013) structure were investigated in the terahertz range at the expense of introducing more material loss. For these fibres, a high refractive index contrast was realized due to ultra-high porosities in the cladding, thus allowing low-loss transmission over a broad spectral range. Reducing the thickness of the struts in the cladding can not only broaden the band-gap width but also flatten the dispersion relation of guided modes with band-gaps.

Although HC-PBG fibres have been studied longer than HC-ARFs, recent theoretical works suggest ARFs can outperform than PBG fibres, when it comes to bandwidth. The simplified HC-ARPCFs have low bending losses and benifit from the same broad bandwidth as kagome-type fibres. Also, antiresonant fibres made from a single layer of stacked tubes have become of prominent interest, as they have an easier fabrication process that requires less tubes in the stack than PBG fibres. As a result, the next section will describe the possible manufacturing techniques of HC-ARPCF in terahertz range.

2.7 Hybrid-clad hollow antiresonant fibre

A slightly different approach is introduced to combine the properties of a metal layer in a dielectric layer of antiresonant waveguide. Each layer has different functionalities, for example, the use of dielectric act as a supporting tube and can introduce the flexibility to deposit metal rod or coating on polymer inner surface. The inner thin metal layer serves as a reflector and maintains the optical properties. The combination of a metal layer of subwavelength-diameter in a dielectric antiresonant cladding provides a specific mode, single-polarization hollow-core terahertz fibre with low-loss for a wider bandwidth (Harrington *et al.* 2004, Bowden *et al.* 2007, Ito *et al.* 2007, Themistos *et al.* 2007, Bowden *et al.* 2008b, Matsuura and Takeda 2008, Bowden *et al.* 2008a). An alternative approach proposed by (Anthony *et al.* 2013, Li *et al.* 2016a, Yudasari *et al.* 2014), is to embed sub-wavelength metal wires within dielectric materials for guiding

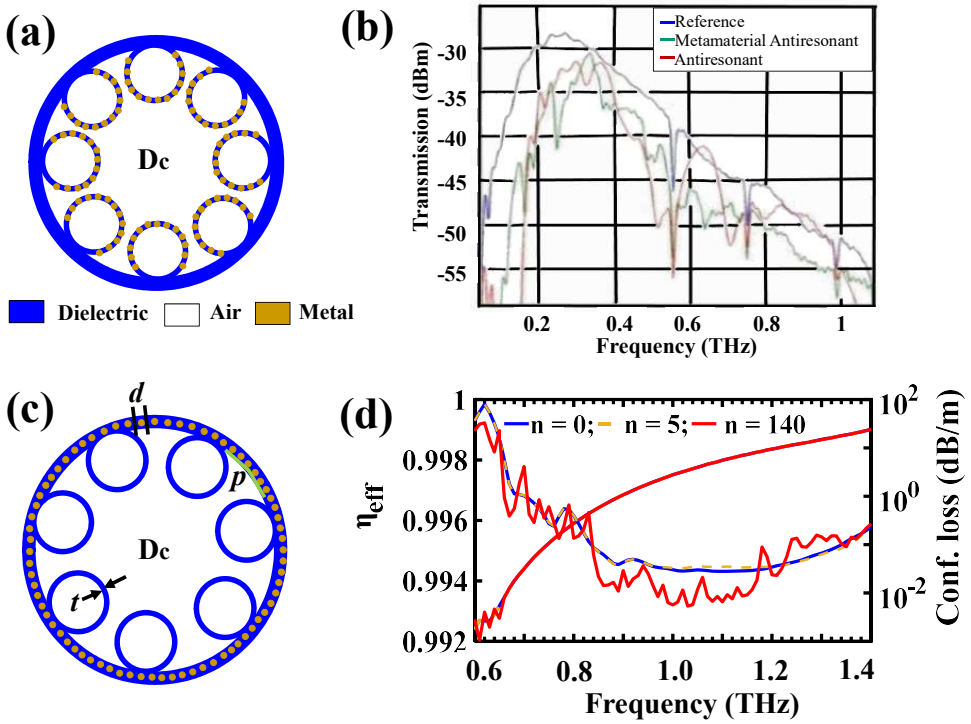

Figure 2.9. Hybrid clad metamaterialHC-ARPCF in terahertz. Geometry and transmission properties of hybrid clad metamaterial HC-ARPCF using embeded metal within (a–b) antiresonat tube (Stefani *et al.* 2009) (c–d) cladding jacket (Sultana *et al.* 2019a, Sultana *et al.* 2020a).

terahertz radiation. If a metal is broken up into subwavelength wires, self and mutual inductance of the wires results in a change to the electrons' effective mass, and the average electron density is reduced in comparison to the bulk metal. These type of waveguides having a minimum of two different layers of materials and refered as hybrid-clad metamaterial waveguide. Metamaterials are man-made composites that obtain their properties from their structure. This structure can be composed of individual meta-atoms, metal-dielectric structures.

We already investigated in previous section that antiresonant cladding structures allow broard band and low loss terahertz propagation through a hollow core when constructive interference occurs in the cladding structure. For further lowering the transmiission in broard bandwidth, the concept to antiresonant fibre by adding sub-wavelength metal wires into the cladding, creating a metamaterial has been applied by Stefani *et al.* (2009), Sultana *et al.* (2019a), Sultana *et al.* (2020a). The fibre by Stefani *et al.* (2009) composed of a layer of eight-tubes without an adjacent node. The 40 metal wires (indium)

of about 100 μm in diameter are embedded in a $\sim$ 400 μm thick and 3 mm diameter of PMMA tube. Total eight of these tubes for 10 cm length have been stacked together to form a hybrid metamaterial antiresonant fibre, depicted in Figure 2.8 (a). The simulated loss obtained at 0.3 THz is as low as 0.3 dB/m. The dielectric HC-ARPCF shows more transmission dips compared to the metamaterial in Figure 2.8 (b).

As a consequence, the idea of adding sub-wavelength metal wires applied into the dielectric jacket (Sultana *et al.* 2019a, Sultana *et al.* 2020a). The reported structure is composed of seven non-touching, circular, dielectric antiresonant tubes, where the cladding dielectric layer contains metal wires, as illustrated in Figure 2.8 (c), employing Zeonex dielectric and aluminum metal. To avoid mode contamination in the air-core and to assist in single mode guidance over a board frequency range, the antiresonant tubes have been tuned with a constant core diameter. The key parameters that determine the performance of the HC-ARPCF with metal-wire inclusions are the innermost dielectric layer thickness p, and diameter d of metal wires. The subwavelength metal wires in a dielectric medium allows the permittivity at a particular frequency to be adjusted by adjusting the size and spacing between the wires in such a subwavelength wire array. Furthermore, such a wire array will have a highly anisotropic permittivity tensor, being described by such a modified Drude model (electric field parallel to the wires). For electric field oriented transverse to the wires, the permittivity will be very close to that of the dielectric medium in which the wires are embedded. Simulation results show that broadband terahertz radiation can be guided with six times lower loss in such hollow core fibres with metallic inclusions, compared to dielectric HC-ARPCF, covering a single mode bandwidth (BW) of 700 GHz in Figure 2.8 (d). A possible fibre fabrication technique is to co-draw metal and dielectrics (Tuniz *et al.* 2012) or via use of printed dielectric waveguides with air holes in the cladding, with later insertion of metal wires into the holes (Yudasari *et al.* 2014).

The following section will highlight the fabrication methodology and corresponding limitations of the HC-ARPCF.

2.8 Fabrication methodologies of HC-ARPCFs

2.8.1 Draw and stack process

Thermal fibre drawing has been widely used for thermoplastic polymers made fibre with the stacking method (Lu *et al.* 2008b, Setti *et al.* 2013, Lu *et al.* 2015a), the drilling method (Ponseca Jr *et al.* 2008, Ma *et al.* 2015), and the extrusion moulding method (Dupuis *et al.* 2010). Fibre drawing entails generally two stages of fabrication. Beginning starts with the construction of a preform which is a scaled-up version of the required diameter. The second stage is the requirement of a polymer drawing tower to drawn a tube (Setti *et al.* 2013, Lu *et al.* 2015a) or a fibre (Nazarov *et al.* 2018). The basic draw process involves heating the preform to a temperature sufficiently larger than glass transition temperature (T_g) to reduce its viscosity so that it can be drawn to a tube/fibre. The heating temperature for PMMA and Zeonex are around 200°C and and 463–443°C, respectively. The T_g that needed to make PMMA and Zeonex soft is around >115°C and 138°C (Argyros 2013, Islam *et al.* 2020). The hole size inside the tube responds to the draw temperature. The two extremes are (i) hole collapse on one side when the temperature is too high and (ii) the fibre material being stretched to the point of fracture due to the expanding holes at low temperatures. Acting on experience the operator of the tower can respond to the fibre behavior by adjusting either the temperature or the draw speed.

The HC-ARPCF (Setti *et al.* 2013) was manufactured from PMMA tubes with 16 mm and 12 mm external and internal diameter respectively. This tube was drawn to an external diameter of 9.6 mm using a polymer fibre drawing tower. Part of it was used for the external jacket, while the remainder was drawn again in order to obtain the cladding tubes with an average thickness of t = 252 μm and an external diameter of about 1.99 mm. Using the drawing method an average thickness of t = 92 μm has been acheived in (Lu *et al.* 2015a) using Zeonex. A details of drawing is discussed in (Arrospide *et al.* 2018). Next, stacking method is applied to form a HC-ARPCF. In stacking method, 20 cm length of the cladding tubes are placed in a circular row at a time to design HC-ARPCF (Setti *et al.* 2013, Lu *et al.* 2015a). They are held by three short jacket rings at either end and in the center of each fibre and a heat shrink tube is used to enhance the mechanical stability, and provide extra protection for ease of handling. The tube stacking method is a handmade process that, on the one hand, makes the method more laborious and complex but, on the other hand, enables the fabrication of some complex preforms for example kagome structure that are not possible to obtain

by using the drilling method. The limitation in the fibre length imposed by the drilling method is possible to overcome. The advantage of this method, although prone to contamination from the larger surface area of the constituent pieces, is that very large air fractions can be achieved by using very thin-walled tubes. Such air fractions cannot be achieved by the other methods and may be necessary for some fibre designs, such as hollow-core optical fibres.

To fabricate HC-ARPCF, Nazarov *et al.* (2018) draws the fibre directly from the stacked preform. The process by Nazarov *et al.* (2018) is similar to Setti *et al.* (2013), Lu *et al.* (2015a) along with additional draw of the preform. The purpose of drawing the fibre directly is to fuse the tube and jacket together that improves mechanical strength, but fibre in this case is not mechanically stable at small bending. The used drawing tower was able to draw the fibre from the PP perform up to 3-m length. At the first stage, the PP tube with outer diameter of 4.3 mm are drawn from the 25 mm and the wall thickness of 4.2 mm by means of the drawing tower. The 50 cm length of eight tubes are tightly stacked along the inner wall of the initial tube of the same length. This scaled-up version of structure is called preform. At the final stage, by varying feed rate of 5–6 mm/min, and the drawing speed of 180–190 mm/min, a HC-ARPCF with outer diameters form 3 to 5.3 mm has been produced. The heating temperature of PP is 245°C and T_g = 180–250°C.

The co-draw technique with metal and dielectrics (Tuniz *et al.* 2012) is the anothe method to fabricate metamaterial structure. In terms of wire metamaterials, PMMA acts as a base material and Indium metal melts at 156.6°C and turns into liquid at the fibre drawing temperatures of approximately 200°C. Indium wire was inserted into PMMA tubes, which were drawn to a smaller diameter. The resulting wires were stacked together inside a larger tube to form the array and drawn a second time to achieve the desired dimensions. Using the fibre co-draw technique, a wire of approximately 8 μm diameter at 100 μm spacing is possible to fabricate. Co-drawing of metal and polymer/glass has been reported to experience difficulties from maintaining the quality and integrity of the multicomponent of the drawn waveguides due to the mismatch in melting temperatures of the metal and polymer/glass (Lee *et al.* 2008). The reported work in Stefani *et al.* (2009), Sultana *et al.* (2019a), Sultana *et al.* (2020a) are the possible example of hybrid clad metamaterial HC-ARPCF. In this respect, this process

of fabrication of metallic-inclusion waveguides is limited to a selection of compatible materials. To overcome the limitation 3D printing can be an alternate option to fabricate metallic-inclusion waveguides.

2.8.2 3D printing

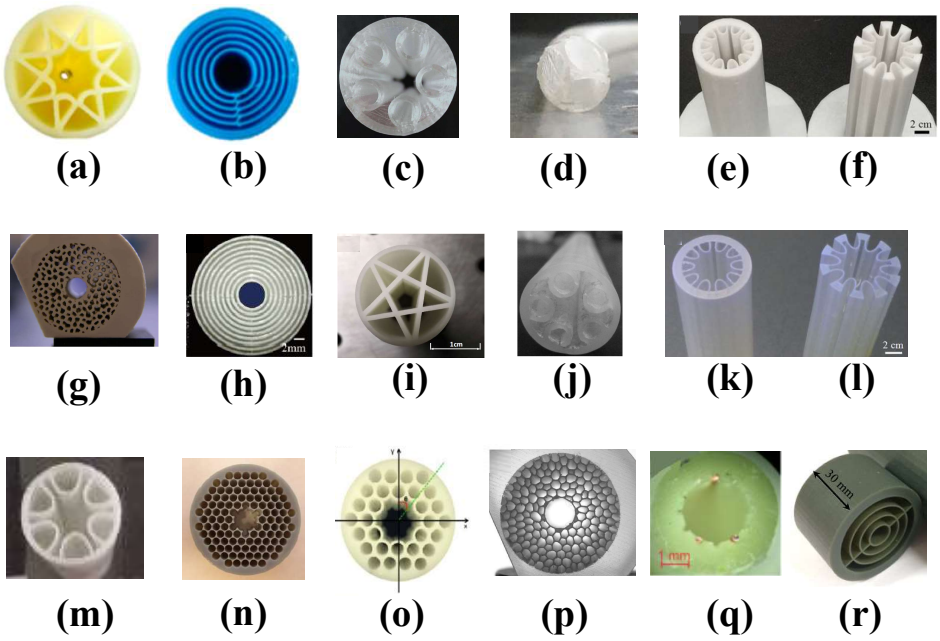

Figure 2.10. The 3D printed fibre in terahertz. The fibre cross-sectional area with (a–f) FDM method (Cruz *et al.* 2015, Sultana *et al.* 2020c, Sultana *et al.* 2022, Xu *et al.* 2021, Cruz *et al.* 2017); (g–m) SLA method (Laurin *et al.* 2014, Li *et al.* 2017b, Yang *et al.* 2016, Sultana *et al.* 2022, Cruz *et al.* 2017, Yang *et al.* 2021); (n–q) Polymer jetting and MultiJet rapid prototyping (Wu *et al.* 2011b, Yang *et al.* 2016, Ma *et al.* 2016, Ma *et al.* 2017, Yudasari *et al.* 2014); (r) Digital Light Processing Rapid Prototyping (Hong *et al.* 2017).

For the 3D printing method, the accuracy of reproducing the optimized design is limited by multiple factors, including the printer specifications, the printing materials, and the complexity of waveguide geometry. The common process of the 3D printing methods is the model design, generally drawn in CAD software, converted to a STL file, and sent to the printer.

The FDM is a well-developed and cost effective 3D technique due to wide adoption of materials and used very widely in a range of industries. The FDM printer worked

under the control of software that converts a 3D model to be printed into a set of G-code commands. The G-code commands provides the option to optimize direction and speed of movement of the nozzle and the printing bed, nozzle temperature, extrusion speed, speed of the cooling fan etc. In the FDM process, thermoplastic filaments are heated, extruded through a nozzle and subsequently deposited on the building bed. A hollow-core fibre with negative curvature core was printed with ABS polymer (Cruz *et al.* 2015) and with PC polymer (Van Putten *et al.* 2018), with Zeonex polymer (Sultana *et al.* 2020c, Sultana *et al.* 2022), and polylactic acid (PLA) (Li *et al.* 2019) via FDM technology. It is also possible to fabricate Bragg waveguide with ABS (Cruz *et al.* 2015, Laurin *et al.* 2014), kagome waveguide with VeroWhitePlus polymer (Yang *et al.* 2016), suspended solid core fibre with PP (Xu *et al.* 2021). One common drawback of FDM printing is that the materials have to be in a filament form to enable the extrusion process. To improve the quality of the filament, the granules can be backed in an oven (Sultana *et al.* 2020c). This assists with the reduction of trapped air bubbles in the filament and increase transparency. In FDM, transparency optimisation of the structures relies on assuring that adjacent threads of plastic filament melt together as much as possible. Normally leaving air voids between the adjacent layers lead to create sources of light scattering. fibres preform manufactured by FDM also require to be annealed to further minimise the light scattering (Cook *et al.* 2015) with much lower temperature (90–170°C). Besides, this hollow-core structure exhibits several surface modes, due to the low resolution of the FDM 3D printer and is intrinsically not well-suited for manufacturing transparent printouts, compared to, e.g., stereolithography. The optimization of printing parameters, practical experience and a post-processing stage mentioned by Sultana *et al.* (2022) play an important role to achieve a good printing quality. The advantage of FDM printing is the potential to allow deposition of single and diverse materials simultaneously. Multiple extrusion nozzles with loading of different materials can be set up in FDM printers, so printed parts can be multi-functional with designed composition. The FDM allows to draw the fibre from the preform (Woyessa 2017) showing no abrupt changes in the response to temperature gradient. It is worth mentioning that printed fibre via FDM can directly be used in terahertz transmission without the need of complex drawing method from preform (Sultana *et al.* 2020c).

In the SLA process, the 3D object is created by curing the liquid photopolymer resin under the influence of an ultraviolet (UV) light. A UV laser beam scans the surface

of a photopolymer resin tank to form each layer of the object. The liquid photopolymer is held in a vat/tank with a built support submerged near the surface of the resin. Then, the built support is re-submerged into the resin and the process is repeated until the 3D object is fully obtained. In the end, a simple cleaning procedure is realized with Isopropyl Alcohol to remove the uncured resin. The most common materials used in SLA is Photosenstive resin (SomosEvoLVe 128) to print Hyperuniform PBG waveguide (Laurin *et al.* 2014), Bragg waveguide (Li *et al.* 2017b), Planner HC-ARPCF (Yang *et al.* 2019), HC-ARPCF with half-elliptical tube (Cruz *et al.* 2017, Yang *et al.* 2021). It is important to obtain the optimal exposure time settings and cure times for avoiding yellowing. Postprocessing techniques such as resin polishing (washing with cleaning agents such as isopropyl alcohol and then dipping the resin part into a liquid clear resin for thinner coating) or spray coating make the printed structure transparent and remove the uncured parts from the structure. At the same time, the post-processing may create some damage in the complex printed parts as it is a manual cleaning and deviate the thickness (shrinkage or swell) (Sultana *et al.* 2022). The UV-curable resins (thermoset polymers) in the SLA cannot be used for fibre drawing as the thermoset polymers cannot be reheated and remoulded. The printed fibre is at a risk of surface warping, due to the unpredictable shrinkage. The layer thickness was affected by the optical parameters of the laser beam (laser power, scanning speed, etc.) and the material properties of the photopolymer (penetration depth and critical exposure).

In the polyjet technique, an inkjet print head deposits thin layers of a UV-curable resin onto a construction tray. UV lamps cure the material as it is being deposited. After cooling and solidifing one cross-section sheet, the print head repeats the jetting process to build another top layer. The advantage of Polyjet over the other methods is its superior spatial resolution of about 100 μm, which depends on the laser spot size. This technique can achieve a fast printing speed with good accuracy and surface finish. One of the challenges using the 3D Polyjet technique is to build longer length structures since the currently available printers have a strict work-volume limitation. Hollow-core fibre with Bragg and kagome structure (Yang *et al.* 2021, Yang *et al.* 2016) via the polyjet technique are the example of polyjet technique.

The Digital Light Processing (DLP) is an improved version of SLA, in which a white light source is used to project the cross-section of the 3D part and for solidification of the photopolymer instead of UV light source with the help of the digital mask. This

process is repeated until the 3D object is completely fabricated. The DLP, as opposed to SLA, is a much faster and cheaper process that has a very high-resolution. At the same time, the main disadvantages of this technology compared to SLA are: parts cannot be left out in the sun or they will degrade; parts overall have worse mechanical properties–they break or crack more easily and are at risk of deteriorating over time; resins are expensive, and the regular replacements of resin tanks and occasionally print platforms also adds up. The loss tangent of the 3D printing material used in the DLP Rapid Prototyping, for example, EnvisionTEC HTM140 is much higher than other low-loss materials commonly used in the terahertz fibres.

In general, for terahertz fibre, the main challenges of using the 3D techniques are to print long length structures.

2.9 Summary and outlook

In this chapter, we reviewed different types of terahertz non-planar dielectric waveguide in terms of guiding mechanism, loss, dispersion, modal analysis, birefringence, bending characteristics, applications and fabrication. The dielectric waveguides discussed in this chapter are divided into three main categories: solid, porous and hollow core fibre. Compared to the hollow core microstructured waveguide, the solid-core microstructured waveguide has a broader transmission bandwidth since the guiding mechanism is based on the total internal reflection and not based on the antiresonant or band-gap effects. Thus these solid core microstructured waveguides are better suited for the broadband single-mode terahertz guidance. Single mode operation is made easier by the larger step in effective index and can be ensured by appropriate choice of the ratio of hole diameter to pitch. Solid core microstructured fibres with optimized geometrical parameters are used to minimize group velocity dispersion of the fibre fundamental mode. Indeed, due to guidance in the solid core, losses of such fibres were comparable to that of the bulk absorption loss of the fibre material and limits their use to short lengths. Also, solid-core microstructured waveguides generally are rigid due to their large dimension (3 mm and more). Although reducing the core size eliminates higher order modes, it increases the attenuation of the fundamental mode.

There are two ways to reduce the transmission loss values: former is subwavelength solid and porous core and later approach is of using hollow core. The air-clad and

Material	Printing technique	Printing structure	Layer thickness (μm)	Refractive index and absorption coefficient	References
ABS polymer	FDM	Negative curvature and planner HC-ARPCF	50–100	1.6	(Cruz *et al.* 2015)
ABS polymer	FDM	Bragg waveguide	–	–	(Cruz *et al.* 2015)
Zeonex polymer	FDM	Negative curvature HC-ARPCF	400	1.529; 5 dB/mm in the 0.1–0.8 THz	(Sultana *et al.* 2020c, Sultana *et al.* 2022)
Polypropylene (PP)	FDM	Suspended solid fibre	–	1.485; 2.36 dB/m	(Xu *et al.* 2021)
–	FDM	HC-ARPCF with half-elliptical tube	–	–	(Cruz *et al.* 2017)
Polycarbonate (PC)	FDM	HC-ARPCF with half-elliptical tube	–	1.6	(Van Putten *et al.* 2018)
Polylactic acid (PLA)	FDM	HC-ARPCF with dodecagon cladding	–	1.58; 5.35 cm^{-1} at 0.1 THz	(Li *et al.* 2019)
ABS polymer	SLA	Hyperuniform PBG waveguide	400	–	(Laurin *et al.* 2014)
Photosenstive resin	SLA	Bragg waveguide	512	1.654; 0.64 cm^{-1} at 0.1–0.3 THz	(Li *et al.* 2017b)

Material	Printing technique	Printing structure	Layer thickness (μm)	Refractive index and absorption coefficient	References
Photosenstive resin (SomosEvoLVe 128)	SLA	Planner HC-ARPCF	–	1.62 in the range of 0.2–2 THz	(Yang *et al.* 2019)
Photosenstive resin (SomosEvoLVe 128)	SLA	HC-ARPCF with half-elliptical tube	–	1.64	(Yang *et al.* 2021)
UV-curable polymer	Polymer jetting rapid prototyping	PBG waveguide	100–150	2.75	(Wu *et al.* 2011b)
VeroWhitePlus polymer	Polymer jetting rapid prototyping	Kagome waveguide	–	–	(Yang *et al.* 2016)
Photoresin (VisyJet Crystal)	MultiJet 3D printer	Hyperuniform PBG waveguide	–	1.67–1.70; 10.43 cm^{-1}	(Ma *et al.* 2016, Ma *et al.* 2017)
UV curable polymer (VisiJet M3)	MultiJet 3D printer	Hybrid clad HC fibre	–	1.50; 7.56 cm^{-1} at 0.3 THz	(Yudasari *et al.* 2014)
EnvisionTEC HTM140 photopolymer	Digital Light Processing Rapid Prototyping	Bragg fibre	400	1.644 in the range of 0.24–0.3 THz; 5 dB/mm from 0.246 to 0.276 THz	(Hong *et al.* 2017)

Table 2.10. The 3D-printable materials within the terahertz spectrum. Indicating the printing technique and optical properties at terahertz.

No.	Stack and draw	3D printing method
1.	It is a tedious and timeconsuming manual technique, requiring much human involvement, then prone to human errors and difficult to transfer to industrial setting	The FDM is mostly an automated process requiring minimal human attendance and can be optimised to yield repeatable results, which makes it easy to apply in industry.
2.	HC-ARPCF stacked together and then further transformed by pressure during drawing may introduce capillary size variation	The FDM and SLA represent very close to the desired structure and ease for customisation.
3.	Requires much time to fabricate	Much shortened delay between design and manufacturing phases.
4.	Drawing/extrusion machines will enable the production of even smaller dimension of terahertz waveguides than the 3D printed fibre	FDM based terahertz fibre can be drawn with expensive drawing tower while SLA based fibre is not possible to draw.

Table 2.11. Comparison between stack and draw technique, and 3D printing method in terahertz HC-ARPCF.

suspended solid core subwavelength fibres are prominent for lowering the loss and rigidity because the guided mode field extends far into the surrounding air, thus low loss can be obtained due to the small overlap of the propagating mode and the lossy fibre material, has high power fraction outside the core. The core dimension of the subwavelength type fibre is much smaller than the wavelength. They are beneficial for terahertz sensing applications specifically for the noninvasive and label-free molecular detection, and gas and liquid spectroscopy. Further reduction of propagation loss can be achieved by inserting a porous structure into the solid core. Severe crosstalk might also be encountered if two air-clad subwavelength waveguides are placed closely. However, both solid-core and porous-core subwavelength fibres are very sensitive to external perturbations and bending, which is a challenge in many applications.

To minimize the outside interference, hollow core fibres can be an alternate option with comparatively lower loss than solid and poroud core fibre. Various dielectric cladding structures have been applied, such as the simple tube waveguides, the kagome waveguides, the tube lattice fibres, the hollow-core band-gap fibre and Bragg band-gap fibres. Among them antiresonant guiding mechanism is followed by the simple tube waveguides (pipe waveguide), the kagome waveguides and the tube lattice fibres (HC-ARPCF) while photonic band-gap guidance is followed by the the hollow-core band-gap fibre and Bragg band-gap fibres. The pipe waveguide is more simplier to fabricate

than the HC-ARPCF. However, thick cladding wall narrows the transmission bandwidth while thinner wall thickness are fragile and sensitive to external perturbation, as the propagating mode extends significantly outside the cladding. Large core size in pipe waveguide is helpful on reducing transmission loss, at the same time, large core leads to difficulties in fibre bending. All these disadvantageous aspects could appear as a limiting factor for many practical applications. The photonic band-gap type fibres offer low loss by sacrificing the transmission bandwidth. The transmission properties of the PBG type fibre, including the transmission bands and dispersion characteristics, can be tuned simply by varying the geometrical parameters of the reflector. However, high air filling fraction in PBG fibres with a hexagonal cladding hole structure or high refractive index contrast in Bragg fibres as well as a strictly periodic cladding structure are needed to obtain an efficient and broad bandgap, which all increase the fabrication complexity. Although HC-PBG fibres have been studied longer than HC-ARPCFs, recent theoretical works suggest ARFs can outperform than PBG fibres, when it comes to bandwidth. The simplified HC-ARPCFs have low bending losses and benifit from the same broad bandwidth as kagome-type fibres. Also, antiresonant fibres made from a single layer of stacked tubes have become of prominent interest, as they have an easier fabrication process that requires less tubes in the stack than PBG fibres. As a result, the aim of this chapter is to provide the technological background of the terahertz dielectric and hybrid clad HC-ARPCFs, including the applications and the available fabrication methods. As discussed, 3D printing seems to be the key enabling technology to advance fabrication of photonic crystal fibre preforms the aim of this thesis is to print HC-ARPCF using the settings of the FDM and SLA process.

In order to find a suitable design, numerical simulations are performed in the next chapter on the attention in HC-ARPCFs with regular circular and nested designs, and novel adjacent nested and hybrid clad designs. Besides, the details performance as a refractive index sensor and ways of creating nonlinearity using a HC-ARPCF are the novel contributions..

Chapter 3

Terahertz antiresonant fibre: Concept, modelling, and nonlinearity

IN the previous chapter we reviewed different types of terahertz hollow core fibres, corresponding guiding mechanisms, fabrication methods and experimental procedures in terms of the applications. In this chapter, we show our contribution to modelling and analysis on a particular new class of hollow core fibre in terahertz named as antiresonant hollow core photonic crystal fibre (HC-ARPCF). Here, a number of regular and novel structures on HC-ARPCFs are created by arranging a set of cladding air tubes around the hollow core. We numerically analyze various hollow-core antiresonant fibres (HC-ARPCFs) for operation at terahertz frequencies. A novel approach for preparing ultrashort pulses from gas-filled HC-ARPCF that has been also presented in this chapter to achieve efficient broadband terahertz generation and detection along with the linear properties of HC-ARPCF.

3.1 Key contributions of terahertz HC-ARPCFs

From the literature review, we find that there is still a lack of suitable terahertz waveguides in terms of low-loss, single-mode guidance, nonlinearity, and simplicity in fabrication. In order to produce practical waveguide structures for terahertz spectrum, it is difficult to find a way of improving the mode confinement while retaining low in material loss. Considering all of these shortcomings, a suitable terahertz HC-ARPCF can be an ideal candidate by exploiting the enhancement of the core guided mode field inside the hollow core. Therefore, we propose some regular and novel HC-ARPCF designs to achieve low transmission loss, together with superior suppression of higher-order modes (HOMs). We analyse the fundamental core mode, cladding mode, core higher-order modes (HOMs), the angle dependency of adjacent tubes and bending loss to find the best design for low loss terahertz transmission. In this chapter, we also apply the novel concept of HC-ARPCF with metal-wire inclusions for low loss and broardband terahertz guidance, creating a metamaterial and compare the terahertz performance against the dielectric HC-ARPCF. We also demonstrate for the first time the mechanism of the nonlinear properties of the HC-ARPCF in terahertz spectrum.

3.1.1 Design, simulation, and signal processing methodology

We use a finite element based "Eigenvalue solver" (COMSOL Multiphysics, version 5.3 and 5.4) to perform the numerical simulations, . For the wave equation, the perfectly-matched layers (PMLs) are notional absorbing layers, outside the fibre domain, that assist in solving the open boundary problems during simulation. This is not just one line, but rather a number of elements or 15 in our case. The simulation window is circular. In order to achieve improved accuracy in simulation, great care is taken in the use of an extremely fine mesh size. We use a non-uniform mesh. We maintain a smaller mesh size in the antiresonant tubes compared to the air region (Poletti 2014, Belardi and Knight 2014, Habib *et al.* 2019). The mesh size in the antiresonant-tubes is chosen at $\sim\lambda/10$, and in the air-region $\sim\lambda/5$, which is an extremely fine mesh size for obtaining accurate results. In all of our HC-ARPCF designs we choose Zeonex (COP) because of its desirable properties at terahertz, the details of materials are fully described by Islam *et al.* (2019), Islam *et al.* (2020).

3.1.2 Synopsis of the numerical method

The higher refractive index of the strut, t acts as a Fabry-Pérot resonator. At some frequencies, the struts reflect the light towards the core, and most of the light is propagated through the core at those off-resonance or antiresonant frequencies. At resonance frequencies (f_{m}), the light couples to the strut and the core mode becomes more lossy. The spectral transmission of antiresonant fibres manifest as multi-band transmissions. The resonance frequency (f_{m}) depends on the cladding tube thickness t (Vincetti 2009b) or η_{clad} or η_{co} and is calculated from the following equation (Lu and Argyros 2014):

$$f_{\mathrm{m}} = \frac{mc}{2t\sqrt{\eta_{\mathrm{clad}}^2 - \eta_{\mathrm{co}}^2}} \tag{3.1}$$

where η_{clad} represents the refractive index of the cladding material, Zeonex, in this work. The η_{co} indicates the refractive indices of the core material and m is an integer, representing the order of resonance.

The loss contribution for HC-ARPCFs in terahertz spectrum is the confinement loss that arises when light from the source is not confined to the core region and leaks out towards the cladding. In fibre geometry, leakage can arise when light is trapped into the polymer webs, or in the small gaps between the tubes and the external fibre jacket. In numerical calculations, confinement loss is proportional to the imaginary part of complex refractive index of the guided mode, which can be calculated by Islam *et al.* (2017b),

$$L_{\mathrm{c}} = \left(\frac{4\pi f}{c}\right) \mathrm{Im}(\eta_{\mathrm{eff}}), \mathrm{cm}^{-1} \tag{3.2}$$

where, L_{c} indicates the confinement loss, f specifies the operating frequency, and $\mathrm{Im}(\eta_{\mathrm{eff}})$ represents the imaginary part of the effective refractive index.

The fraction of power (P) confined in sample area, for example in core or in the bulk material, is used to quantify the amount of overlap between light and material and it follows as (Islam *et al.* 2018c, Cordeiro *et al.* 2006),

$$P = \frac{\int_{\mathrm{sample}} \mathrm{R_e}(E_{\mathrm{x}}H_{\mathrm{y}} - E_{\mathrm{y}}H_{\mathrm{x}})\, dxdy}{\int_{\mathrm{total}} \mathrm{R_e}(E_{\mathrm{x}}H_{\mathrm{y}} - E_{\mathrm{y}}H_{\mathrm{x}})\, dxdy} \times 100 \tag{3.3}$$

where R_{e} denotes the real part, E_{x}, E_{y} and H_{x}, H_{y} are the transverse electric and magnetic field of the guided mode respectively. For the sensing purpose in this chapter,

the integration of the numerator is carried out for the analyte to be sensed in the core region and the integration of denominator is performed over the whole fibre region.

A second loss mechanism in antiresonant fibre is the effective material loss (α_{eff}) that is introduced when guided light is absorbed by the background material (Islam *et al.* 2017b, Chen *et al.* 2013, Snyder and Love 2012), and is given by,

$$\alpha_{\text{eff}} = \sqrt{\frac{\epsilon_0}{\mu_0}} \left(\frac{\int_{\text{mat}} \eta_{\text{mat}} |E|^2 \alpha_{\text{mat}} dA}{|\int_{\text{all}} S_z dA|} \right) = \alpha_{\text{mat}} P_{\text{mat}} \tag{3.4}$$

where, ϵ_0 and μ_0 designates the permittivity and permeability in free space, η_{mat} indicates the effective refractive index of Zeonex and S_z implies the z-component of Poynting vector, $S_z = \frac{1}{2}(\mathbf{E} \times \mathbf{H}^*)z$, here, $\mathbf{E}$ is the electric field component and $\mathbf{H}^*$ is the magnetic field component. The integration in the numerator is only performed over the solid material because the propagation loss of terahertz radiation in air is negligible in comparison. As the material absorption loss is spatially uniform, the α_{eff} is given by the product of material absorption loss and the fraction of power in material (P_{mat}). Here, P_{mat} is calculated with Equation (3.3) considering the sample being the fibre solid material (Zeonex). The material absorption loss (α_{mat}) is linearly proportional to frequency ranges between 0.2 to 1.6 THz for Topas, where the α_{mat} is observed 0.06 cm^{-1} at 0.4 THz and it increases at a rate of 0.36 cm^{-1}/THz (Chen *et al.* 2013). Using the same concept on Zeonex, the α_{mat} is calculated by α_{mat} = 0.36$\times$(f-0.4)+0.06, cm^{-1}, where f is the frequency in THz.

The confinement loss (L_c) is then added to the effective material loss (α_{eff}) to produce transmission loss (Vincetti *et al.* 2010).

$$\alpha_{\text{trans}} = \alpha_{\text{eff}} + L_c. \tag{3.5}$$

To investigate the refractive index sensing performance, it is important to calculate the relative sensitivity. Relative sensitivity measures the amount of light and sample interaction within the core and can be expressed as (Islam *et al.* 2018c, Ademgil 2014),

$$R_s = \frac{\eta_r}{\eta_{\text{eff}}} \times P_{\text{air}} \tag{3.6}$$

where R_s is defined as the relative sensitivity, η_r is the refractive index of the sample that need to be sensed, η_{eff} represents the effective refractive index in wave guide and P_{air} is the percentage of light/gas interaction in hollow core calculated from Equation (3).

From the result of relative sensitivity, refractive index sensitivity (S_f) can be calculated by the following equation (Chen *et al.* 2014),

$$S_f = \frac{\Delta f}{\Delta \eta} \tag{3.7}$$

where, Δf represents the spectral shift of the resonance frequency and $\Delta \eta$ is the change of the analytes refractive index.

Another sensor performance parameter called the Figure of merit (FOM) evaluates the overall sensing performance of a sensor. The FOM implies the detection limit of the refractive index sensor and is defined as (Liu *et al.* 2018, Peng *et al.* 2013, Srivastava *et al.* 2013, Islam *et al.* 2018b):

$$\text{FOM} = \frac{S_f}{\text{FWHM}} \tag{3.8}$$

where, FWHM denotes the full width at half minima of a resonance dip.

The degree of detection of a sensor can also be measured using the quality factor (Q) that is defined as (Yoshie *et al.* 2011),

$$Q = \frac{f_m}{\text{FWHM}} \tag{3.9}$$

where, f_m is the central resonance frequency and calculated from Equation (3.1).

Sensor interaction length is necessary to highlight the sensing performance of a refractive index sensor and is determined from (Islam *et al.* 2018b),

$$L = \frac{1}{\alpha_{trans}} \tag{3.10}$$

L represents the fibre physical length where the input signal will drop to $1/e$ (37%) to its original value, determined from the transmission loss (α_{trans}) using Equation (3.5).

3.1.3 Objective and framework

In Section 3.2, we carry out the observation on dielectric typical, nested, and adjacent nested HC-ARPCFs, based on the tube number, constant and variable tube gap. For the

first time we introduce the adjacent nested HC-ARPCF in terahertz and demonstrate that adjacent nested HC-ARPCF in Subsection 3.2.2 shows closely similar loss characteristics to nested HC-ARPCF with proper optimization. We also analyze the concept of the fundamental mode confinement in-depth for five-tube HC-ARPCFs along with the adjacent nested tube angles and spacings. We expand the simulation for six-tube HC-ARPCFs in Subsection 3.2.3. An extensive analysis of the fundamental core modes, higher-order core modes, and cladding mode is carried out in Subsection 3.2.4 to achieve the information on modal contents of the reported HC-ARPCFs for five and six-tube. We also demonstrate that for the variable tube gap, the five-tube HC-ARPCF leads to better single mode guidance than the six-tube HC-ARPCFs for each designs. Along with the impact of gap variation on five, six and seven-tube HC-ARPCFs, we numerically focus on the constant gap and the impact of the constant gap on tube numbers in Subsection 3.2.5 and compare it between typical and nested HC-ARPCFs. Analysis of the fibre designs shows that the five-tube nested HC-ARPCF exhibits lower transmission loss and superior HOM suppression than the typical and adjacent nested HC-ARPCFs, which is not discussed in the published terahertz fibres literature.

In Section 3.3, we apply the concept to HC-ARPCF by adding sub-wavelength metal wires into the cladding, creating metamaterial properties that we compare against dielectric HC-ARPCF of the same dimensions. The multimode nature of large core diameter terahertz fibres has to be suppressed by tuning the antiresonant tubes to act as a single mode fibre in the whole transmission region. The goal is to effectively confine the guided wave through a large hollow core with lower loss than previously possible. Subsection 3.3.2 and 3.3.3 investigate the effect of metal wires on the confinement loss. We explain and illustrate how the metal inclusions serve to better confine the desired core modes, while minimizing material losses. Numerical study of fundamental and HOMs of the proposed fibre shows a wide-range single mode guidance, strong light confinement and six times lower loss than the dielectric HC-ARPCF. We also address the impact of waveguide modes on transmission characteristics for HC-ARPCF with and without metal wires in Subsection 3.3.4. The results show that the LP_{11} is influenced mostly by changes to the cladding pattern. A summary of this work has published by our group in IRMMW conference (Sultana *et al.* 2019a). The proposed structure with a hollow core is a potential candidate for a low loss terahertz waveguide.

An open research problem is the lack of high power terahertz laser sources that can create linear and nonlinear pulses simultaneously for nonlinear applications such as terahertz supercontinuum generation, terahertz high harmonic generation, etc. In Section 3.4, we model and simulate a simple dielectric terahertz HC-ARPCF, show the linear properties and explore the mechanism of achieving nonlinearity with the established technology when it acts as a fibre-based gas laser. First, the linear properties of HC-ARPCF are discussed in Section 3.4.2 and 3.4.3, and then the nonlinear properties of the same structure are demonstrated as a laser, considering a gas-filled core in the terahertz regime in Section 3.4.4 and 3.4.5.

3.2 Terahertz dielectric HC-ARPCFs

Prior studies have proposed several dielectric fibres for low loss terahertz transmission, including sub-wavelength fibres (Chen *et al.* 2006), porous core fibres (Islam *et al.* 2017c, Islam *et al.* 2016, Hassani *et al.* 2008a) and hollow core fibres (Wu *et al.* 2011b, Nielsen *et al.* 2011, Anthony *et al.* 2011b). The guided mode field in sub-wavelength fibres extends far into the surrounding air to minimize the overlap of the propagation mode and the lossy fibre material, and has high power fraction outside the core. Further reduction of propagation loss can be achieved by inserting a porous structure into the core. However, they are very sensitive to external perturbations and bending (Chen *et al.* 2009), which is very challenging in many applications.

An approach for improving field confinement has been demonstrated in the visible and infrared regime. The concept of the on-node single cladding layer and hexagonal hollow-core HC-ARPCF was first proposed, analyzed, and experimented in the visible-infrared (Gérôme *et al.* 2010). In HC-ARPCFs, light is confined and guided to the air-core due to the weak coupling between core and cladding modes known as inhibited coupling (Argyros and Pla 2007). A number of thin dielectric airy tubes around the air-core have lower refractive index than the core. Therefore, the low density of cladding mode guides light toward the core over a broad frequency range. Low loss region appears due to the inhibited coupling. In some narrow frequency ranges, the core mode couples strongly with cladding when the two modes are resonant and the transmission loss becomes high. The resonance frequency can be assumed from the thin dielectric wall using antiresonant reflecting optical waveguide (ARROW) model.

Sequentially, the simple structure of on-node cladding (Gérôme *et al.* 2010) was advanced to node-free negative curvature cladding pattern (Kolyadin *et al.* 2013, Poletti 2014, Uebel *et al.* 2016, Michieletto *et al.* 2016, Gao *et al.* 2016, Wei *et al.* 2017, Hasan *et al.* 2017) to improve the fibre performance. Different fibre parameters including the number of cladding tubes (Michieletto *et al.* 2016), the gap between cladding tubes (Gao *et al.* 2016, Hasan *et al.* 2017), single nested tubes (Poletti 2014), double nested tube and position of nested tubes (Habib *et al.* 2015) were considered to analyze the transmission loss, bending loss, and higher-order mode suppression capability in the optical regime. The HC-ARPCFs have been widely investigated in the infrared and mid-infrared range. However, there are very few studies in the terahertz regime, this includes circular antiresonant tubes (Vincetti *et al.* 2010, Setti *et al.* 2013, Lu *et al.* 2015b, Nazarov *et al.* 2018), elliptical antiresonant tubes (Van Putten *et al.* 2018), ice-cream cone shape negative curvature antiresonant tubes (Cruz *et al.* 2015), and nested antiresonant node-free fibre (Hasanuzzaman *et al.* 2018).

3.2.1 Fibre geometry

Fig. 3.1 depicts the profile of HC-ARPCFs with three different cladding structures. A regular five-tube HC-ARPCF is shown in Fig. 3.1(a). The nested HC-ARPCF in which a small nested tube with inner diameter, d is shown in Fig. 3.1(b). Fig. 3.1(c) shows an adjacent HC-ARPCF in which two adjacent nested tubes are placed in each antiresonant tube. The core diameter D_c is at the center of the fibre, with the antiresonant tubes of D surrounding the core. The gap, g between two adjacent tubes forms a node-free boundary around the core. Also, the Zeonex tube thickness, t predicts the first transmission spectra centered around 1 THz. Here gray and white colour indicate the dielectric material and air regions respectively. In all of our numerical investigations, we kept $D_c = 3$ mm, $g = 0.99$ mm and $t = 0.09$ mm constant. The node-free core boundary shows comparatively lower and smoother transmission spectra than the on-node core boundary (Wu *et al.* 2011a, Vincetti and Setti 2011, Vincetti and Setti 2012b).

3.2.2 Five-tube based HC-ARPCFs

Initially, the five-tube HC-ARPCFs with three different cladding patterns are taken in consideration to compare the transmission loss spectra and the fundamental mode

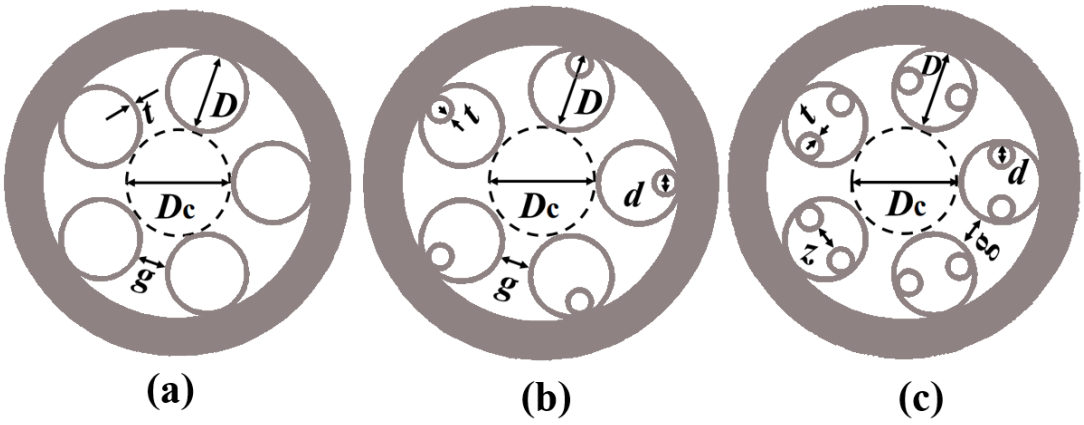

Figure 3.1. Dielectric HC-ARPCF for terahertz transmission. Cross-section of the fibres considered in simulations (a) Typical, (b) Nested, and (c) Adjacent nested HC-ARPCF. Here the optimum dimensions are $D_c = 3$ mm, $D = 2.1$ mm, $t = 0.09$ mm, $g = 0.99$ mm, and $d = 0.54$ mm, Sultana *et al.* (2020b).

profiles, presented in Fig. 3.2(a). In numerical calculations, the effective material loss estimated from the absorbed power in the Zeonex® struts and summed to the leakage loss in order to calculate the transmission loss. The solid red line indicates the transmission loss of a regular HC-ARPCF with a loss level of 0.085 dB/m at 1 THz. The solid blue line is the transmission loss of the nested HC-ARPCF. In this case the transmission loss in nested tubes is of 0.055 dB/m at 1 THz. Finally, the solid green line corresponds to adjacent nested HC-ARPCF with 0.065 dB/m loss at 1 THz with a minimum loss of 0.055 dB/m at 1.05 THz. In these comparisons, the nested HC-ARPCF provides the lower transmission loss than regular HC-ARPCF and a smoother loss curve over the frequency regime than the adjacent nested HC-ARPCF. The small indentation of the adjacent nested tubes form the nodes near the core boundary and induce the loss peak in the transmission band due to Fano resonances (Vincetti and Setti 2011, Vincetti and Setti 2012b) at the lower frequency regime.

The oscillations in transmission band are more obvious when the adjacent nodes are positioned very close to the core boundary as shown in Fig. 3.2(b). The adjacent nested tube position is defined from the angle between the apex of adjacent tube and antiresonant tube as shown inset of Fig. 3.2(b). The adjacent node position of 40° offers improved transmission spectra over 60°, 90° and 120°.

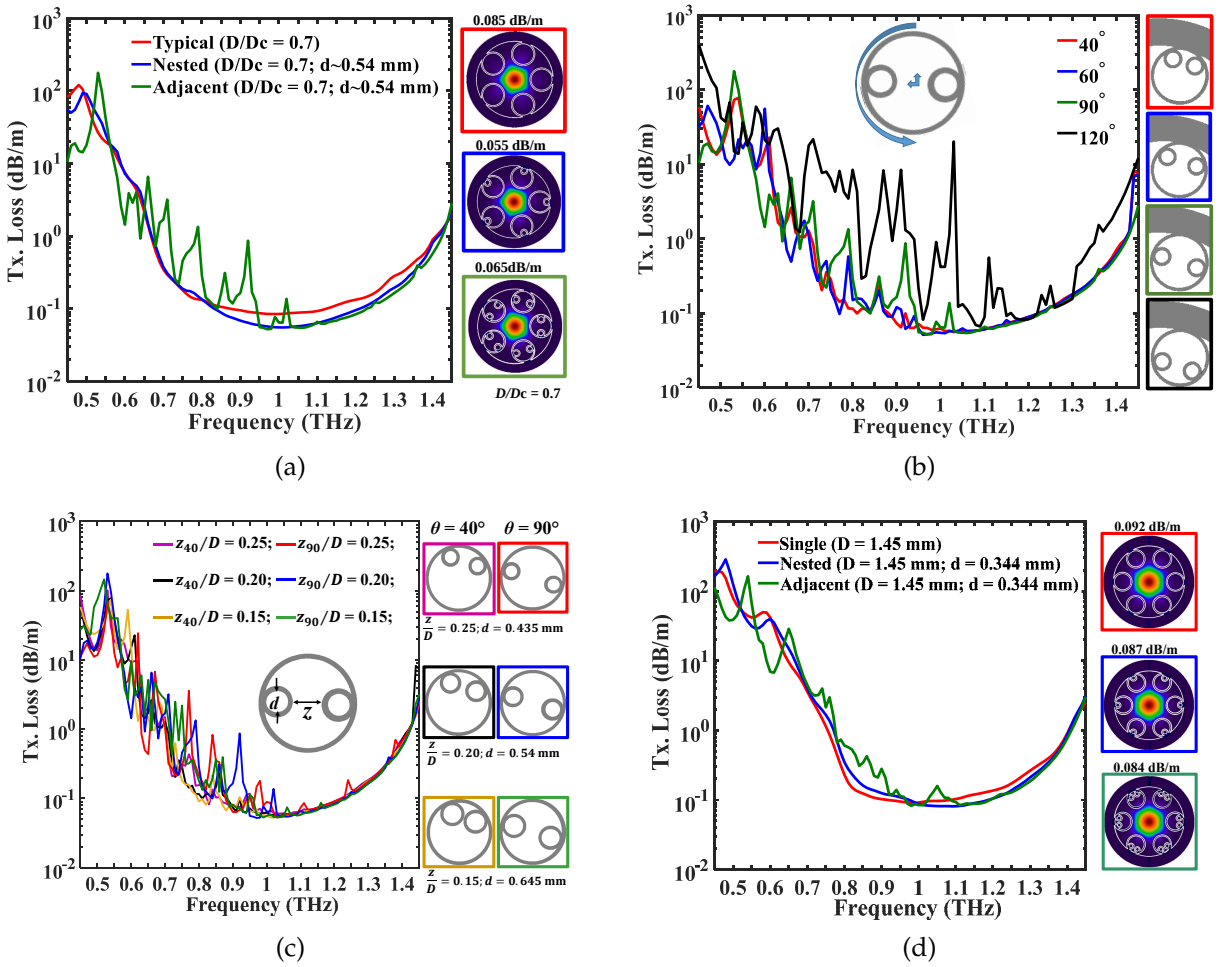

Figure 3.2. Simulated transmission losses for three different HC-ARPCFs. Transmission loss of five-tube based HC-ARPCFs (a) typical, nested, and adjacent nested HC-ARPCF; (b) adjacent nested HC-ARPCF with different nested tube positions (θ); (c) adjacent nested HC-ARPCF with different nested tube positions (θ) and different adjacent tube spacings (z/D). (d) Transmission loss of six-tube based regular, nested, and adjacent nested HC-ARPCF. Here, $D_c = 3$ mm, and $t = 0.09$ mm, Sultana *et al.* (2020b).

Fig. 3.2(c) illustrates that the size and position of the adjacent nested tubes make little difference to the loss spectrum. In this simulation, we scan the distance between the adjacent nested tubes with constant antiresonant tube diameter from $z/D = 0.15$ to 0.25 for the adjacent node position of 40° and 90° and observe a small effect on the loss spectrum. However, the loss peaks are more obvious below 1 THz. The observation on size and position of the adjacent nested HC-ARPCF reduces the fabrication obligation.

3.2.3 Six-tube based HC-ARPCFs

As a comparison, we investigate the simulation results of six-tube HC-ARPCFs. It is important to mention that the previously reported HC-ARPCF have focused on six or more antiresonant tubes (Van Putten *et al.* 2018, Vincetti and Setti 2010, Vincetti *et al.* 2010, Setti *et al.* 2013, Lu *et al.* 2015b, Nazarov *et al.* 2018, Cruz *et al.* 2015). Fig. 3.2(d) displays the calculated transmission loss spectra for the single, nested, adjacent nested six-tube HC-ARPCF. The red solid line indicates the single HC-ARPCF with a minimum loss of 0.092 dB/m. Blue and green lines are for the nested and adjacent nested HC-ARPCFs showing minimum transmission losses values 0.087 dB/m and 0.084 dB/m, respectively. All the losses are calculated at 1 THz. Fig. 3.2(d) demonstrate that the regular six-tube HC-ARPCF provides wider transmission spectra than the similar six-tube nested and adjacent nested HC-ARPCFs. The six-tube nested and adjacent nested HC-ARPCF maintain the similar transmission spectra above 1.1 THz. Below 1.1 THz, the six-tube adjacent nested HC-ARPCF with node position of 40° provides a very small oscillation in the transmission spectra due to reduced Fano resonances. This Fano-induced oscillation is comparatively lower than the five-tube adjacent nested HC-ARPCF with node position of 90°, as previously demonstrated in Fig. 3.2(a)–3.2(b). Moreover, the six-tube fibres with three different configurations show comparatively higher transmission loss and narrower transmission spectra than their equivalent five-tube geometries, as shown in Fig. 3.2(a).

3.2.4 Higher-order mode extinction ratio

In this subsection, the modal properies of HC-ARPCFs are numerically analyzed with a fixed D_c, while the cladding tube diameter is varied over a range where the HOMs are suppressed at $f = 1$ THz. At this frequency, the lowest mode LP_{01} shows the smallest transmission loss and has become the dominant mode in HC-ARPCFs in this thesis. In Fig. 3.3 and Fig. 3.4, the LP_{11a} and LP_{11b} shows similar refractive indices, therefore can be considered as first set of HOM, where modal intensity distribution are also identical. They are distinguished by electric field distribution as LP_{11a} and LP_{11b} (not shown in the Figure).

In order to investigate the coupling mechanism between the core and cladding modes, we carry out simulations as a function of D/D_c with constant D_c. Fig. 3.3 shows the

3.2.4 Higher-order mode extinction ratio

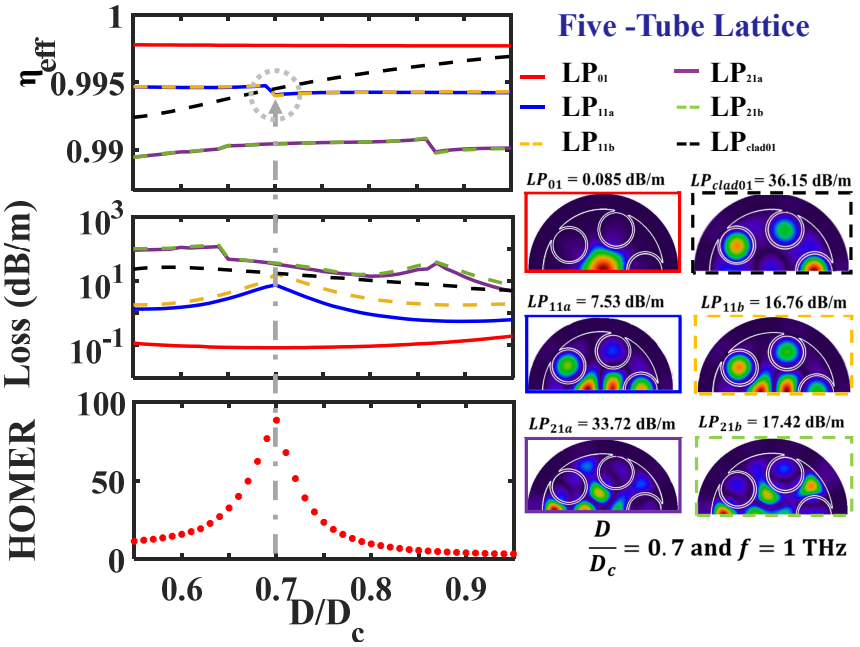

Figure 3.3. Higher-order mode extinction ratio for typical five-tube HC-ARPCF. The effect of changing inner tube diameter D on η_{eff}, loss, HOMER and mode field pattern for five-tubes. The fibre have the same core diameter, $D_c = 3$ mm and uniform Zeonex strut thickness, $t = 0.09$ mm and $g = 0.99$ mm, Sultana *et al.* (2020b).

characteristics of a five-tube lattice HC-ARPCF where it can be seen that the effective mode indices (η_{eff}) remains almost unchanged for all the core modes as a function of D/D_c. Interestingly, for a narrow range ($0.64 \leq D/D_c \leq 0.76$) the loss remains 0.09 dB/m, whereas D dominates the HOMs losses. The FM loss increases with D beyond $D/D_c \geq 0.77$. At $D/D_c = 0.7$, the modes (cladding and HOMs) strongly couple with each other, therefore the higher-order mode extinction ratio (HOMER) is obtained. Note that, the HOMER is used to quantitatively measure fibres single mode performance. It is defined as the ratio of core HOMs loss and FM loss (Habib *et al.* 2015, Habib *et al.* 2019).

A similar calculation for the six-tube fibre, Fig. 3.4, shows that the FM loss can also be similar to the five-tube fibre however within a comparatively broader range ($0.55 \leq D/D_c \leq 0.76$) than that of five-tube fibre for the sack of lower HOMER. The maximum HOMs loss for LP_{11a} and LP_{11b} are obtained when $D/D_c \sim 0.68$. However, the LP_{21a} shows comparatively lower loss than the LP_{11} group from the range of $0.59 \leq D/D_c \leq 0.74$. As a result, a maximum HOMER of ~ 11 is obtained at $D/D_c = 59$ and 75 respectively, that is lower than the five-tube fibre. However, a small separation (for

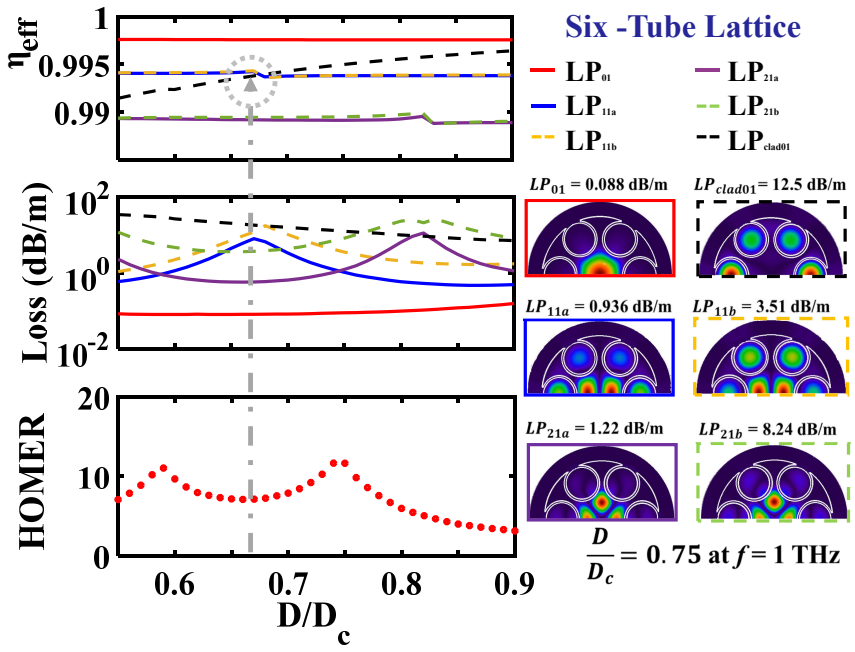

Figure 3.4. Higher-order mode extinction ratio for typical six-tube HC-ARPCF. The effect of changing inner tube diameter D on η_{eff}, loss, HOMER and mode field pattern for six-tubes HC-ARPCF. The fibre have the same core diameter, $D_c = 3$ mm and uniform Zeonex strut thickness, $t = 0.09$ mm and $g = 0.99$ mm, Sultana *et al.* (2020b).

example $D/D_c = 59$) between the antiresonant tubes leads to challenging fabrication of the fibre.

For further understanding the modal characteristics of the nested HC-ARPCF we show the transmission losses and HOMER by contour plottings that are shown in Fig. 3.5, from where it is possible to determine the single mode and low loss operating region of the fibre. Fig. 3.5(ii), showing that, within $0.7 \leq D/D_c \leq 1.2$ and $0.3 \leq z/D \leq 0.73$ the loss of the FM maintains 0.05 dB/m. Fig. 3.5(iii) indicates that maintaining the FM loss below 0.05 dB/m, the loss of HOMs can be high as 7.3 dB/m for $D/D_c = 1.09$ and $z/D = 0.34$. The loss in HOMs is high because of the strong coupling between the core HOMs and cladding modes (Argyros and Pla 2007). Therefore, according to the obtained result it can be said that, by engineering the antiresonant tubes the HOMs can be significantly suppressed.

The HOMER of the nested HC-ARPCFs is also investigated that is shown in Fig. 3.5(iv). This indicates that a maximum HOMER of >140 can be obtained. To our knowledge, this is the highest HOMER value for any kind of terahertz fibre.

3.2.4 Higher-order mode extinction ratio

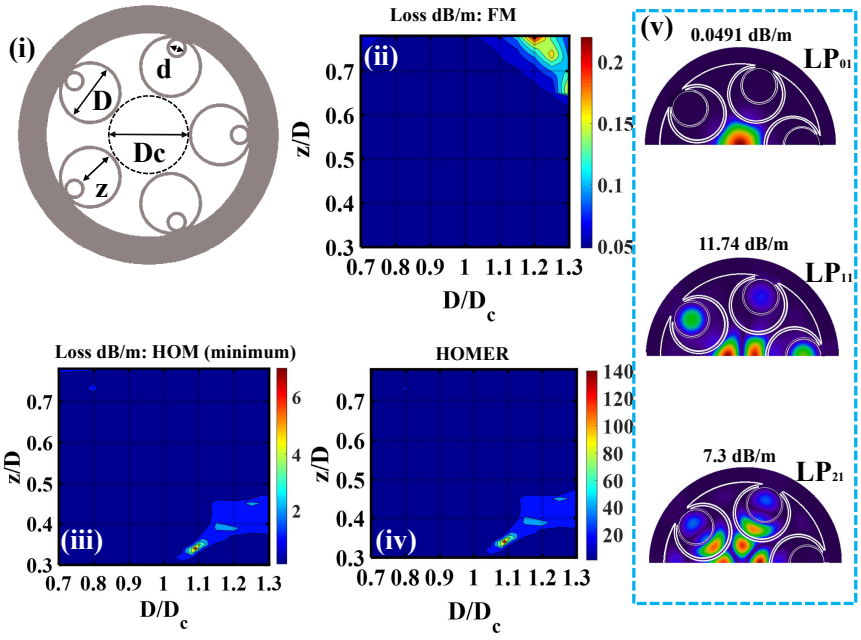

Figure 3.5. Higher-order mode extinction ratio for five-tube nested HC-ARPCF. (i) Cross section of the five-tube based nested HC-ARPCF. The transmission loss of (ii) FM; (iii) HOMs, and (iv) HOMER. (v) Respective mode pattern of LP_{01}, LP_{11}, and LP_{21} at $D/D_c = 1.09$ and $z/D = 0.34$. The simulations to plot this figure are performed at 1 THz, with $D_c = 3$ mm and $t = 0.09$ mm, Sultana *et al.* (2020b).

An extensive analysis of losses (FM and HOMs) and HOMER as a function of D/D_c and z/D for the angular position of their weld point at $\theta = 90^\circ$ is also carried out, Fig. 3.6 that the results pertain to adjacent nested HC-ARPCF. It can be seen that, for a wide range of z/D and D/D_c the FM loss remains constant where the minimum loss is 0.048 dB/m. However, due to relatively weak coupling between the HOMs and cladding modes, the HOMER is relatively small (slightly higher than 97).

The effect of changing adjacent nested tube positions on loss and HOMER is shown in Fig. 3.7. The change in adjacent nested tube position can also introduce the lower LP_{02} mode than LP_{11}, or LP_{21} in very limited cases. We also considered the losses of LP_{02} to calculate the HOMER. The loss and HOMER in calculated by keeping g constant and changing the angular position, θ. We found that at $D/D_c = 0.7$, adjacent nested five-tube HC-ARPCF exhibits higher sensitivity to the modal contamination and behaves as a multimode waveguide. The weld position between 40° and 70° are more sensitive to HOMs and behaves as multi-mode (the ratio $D/D_c = 1.25$, $z/D = 0.2$). The achieved HOMER is ~ 80 at $D/D_c = 1.25$ with weld position, $\theta = 100^\circ$. The weld position $\theta = 90^\circ$ provides HOM suppression of >57, adequate for single mode operation. However,

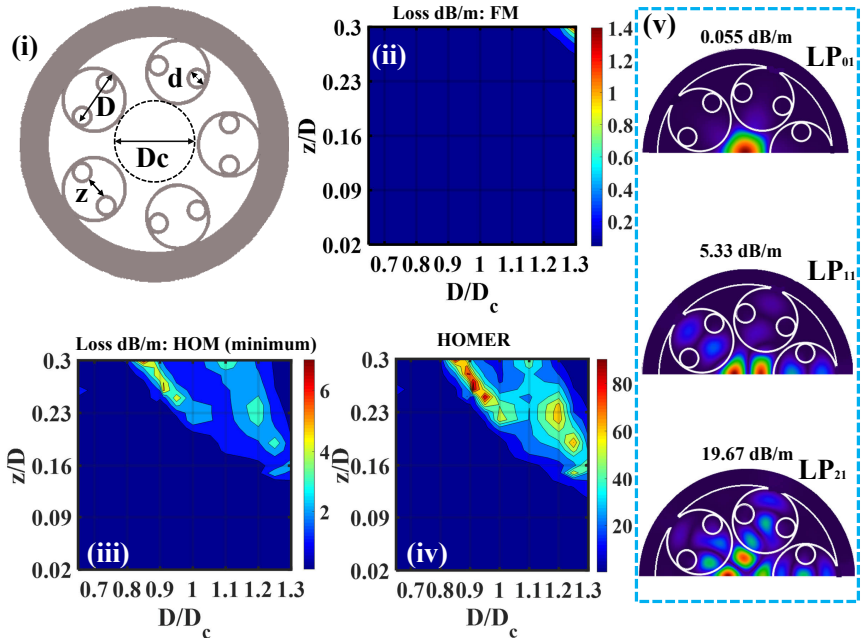

Figure 3.6. Higher-order mode extinction ratio for five-tube adjacent nested HC-ARPCF. (i) Cross section of the five-tube based adjacent nested HC-ARPCF. Calculated total transmission loss of (ii) FM; (iii) HOMs, and (iv) HOMER. (v) Respective mode pattern of LP_{01}, LP_{11}, and LP_{21} at $D/D_c = 0.91$ and $z/D = 0.26$. The simulations to plot this figure are performed at 1 THz, with $D_c = 3$ mm and $t = 0.09$ mm, Sultana *et al.* (2020b).

The position at 40° generates less resonance than 60°, 90° and 120° (see also Fig. 3.2(b)). This is due to the core and nodes between adjacent nested tube in primary capillaries being further away from the core, as shown in Fig. 3.2(b).

3.2.5 Effect of tube number on transmission loss

The effect of antiesonant tube numbers for constant adjacent tube gap on the transmission spectra is studied in this section. Both the nested and the adjacent nested HC-ARPCFs are considered and analyzed for five, six and seven tubes. The transmission losses are shown in Fig. 3.8(a)–Fig. 3.8(b), where it is found that the five-tube nested and adjacent nested HC-ARPCF show similar transmission losses (0.055 dB/m at 1 THz and 0.056 dB/m at 1.03 THz, respectively) and wider transmission bandwidths as compared to the six and seven tubes. This is because of the larger distance from the core to the jacket for five-tube fibres. Generally the size of air regions inside the tube inversely related with the tube numbers. As the tube number increases the

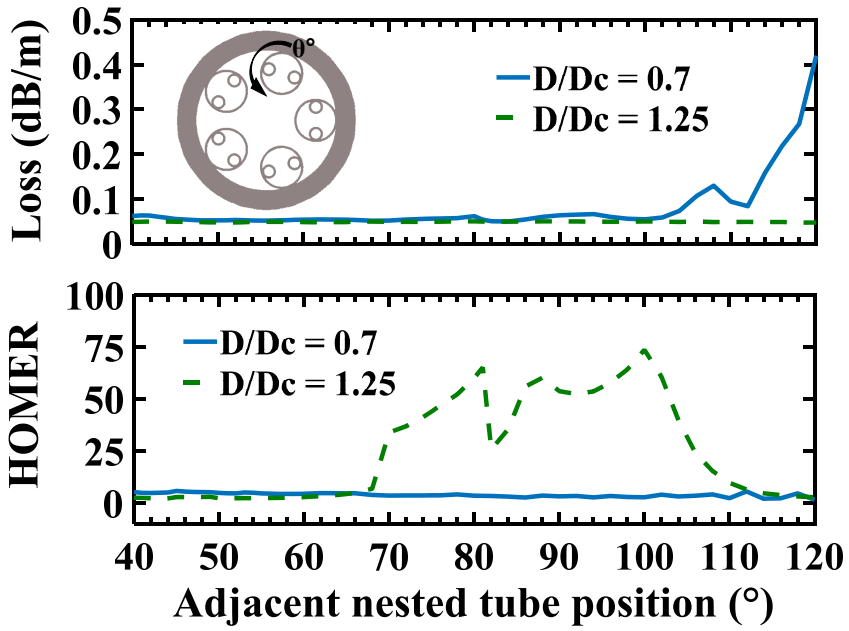

Figure 3.7. Simulated transmission loss spectra and HOMER based on adjacent nested tube positions. Simulated transmission loss spectra and HOMER for five tube adjacent nested tube positions having $D/D_c = 0.7$ and $z/D = 0.2$. The optimum dimensions i.e $D_c = 3$ mm, $t = 0.09$ mm and $g = 0.99$ mm are chosen, Sultana *et al.* (2020b).

size of air regions decreases when the tube-gap is considered fixed. However, all the adjacent nested HC-ARPCFs with weld position 40° are influenced slightly with Fano-induced oscillations in the transmission band.

3.2.6 Bending losses

The total diameter of the proposed five-tube HC-ARPCF is 9.56 mm (when $D/D_c = 0.7$) and can also be considered flexible compared to the flexible terahertz tube lattice fibre (9.6 mm) (Setti *et al.* 2013). The flexible waveguides are deserved for terahertz imaging applications; however, the curvature of the fibre introduces bending loss. The bending loss of a fibre is characterized in two sequential forms: curvature dependent and frequency dependent confinement loss.

The curvature dependent bending loss starts with the transition of curvature radii from zero (and infinite for straight fibre) to finite (for bent fibre). Fig. 3.9 shows the schematic transition of straight HC-ARPCF to bent HC-ARPCF including the corresponding fundamental mode profiles respectively. The light propagates through the z-plane for both

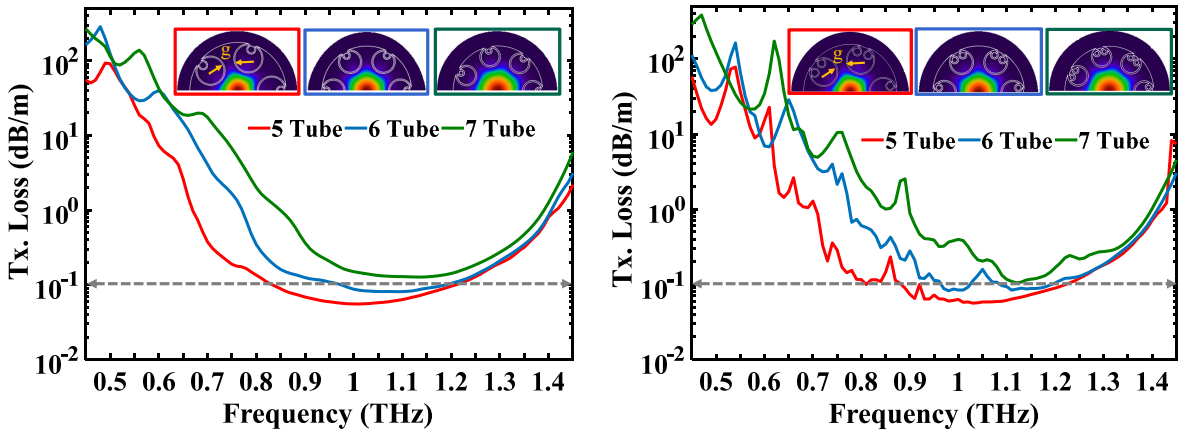

Figure 3.8. Calculated transmission loss based on tube number. Calculated transmission losses of five, six and seven tube based, (a) regular nested and (b) adjacent nested fibres having $D/D_c = 0.7$. Note that, for (a–b) the optimum dimensions i.e $D_c = 3$ mm, $t = 0.09$ mm and $g = 0.99$ mm are chosen, Sultana *et al.* (2020b).

straight and bent fibre. The bending of straight fibre towards x-plane makes the fibre bent and deforms the fundamental air-core index profile LP_{01} towards the cladding tube. This deformation of index profile towards the cladding tube enhances the confinement loss as compared to straight fibre. The air-core index profile for the bent fibre, $\eta_{\mathrm{bend}}(x)$ is quantified using the equation (Setti *et al.* 2013, Bao *et al.* 2015, Li *et al.* 2016a)

$$\eta_{\mathrm{bend}}(x) = \eta(x) \exp \frac{x}{R_{\mathrm{bend}}} \tag{3.11}$$

where $\eta(x)$ denotes a refractive index profile of straight fibre. In simulation, we use $\eta(x) = 1$. Here, x is the bending direction and R_{bend} defines the bend radius.

For analyzing the optical properties of bent fibre in Fig. 3.10(a) as a function of bend radius R_{bend}, we consider the five-tubes HC-ARPCFs with three proposed structures as shown in Fig. 3.1. In Fig. 3.10(a), the optical properties are considered for $D_c = 3$ mm, $D/D_c = 0.7$ and $t = 0.09$ mm at 1 THz. We numerically analysis the η_{bend} and transmission loss of bent fibre by varying the R_{bend} between 3 cm to 100 cm. The smaller the R_{bend} the greater the curvature of the fibre, which highly deforms the desired air-core index profile LP_{01} towards the cladding tube. Light leakages from the air-core through the gap, g and the phase match between LP_{01} and $\mathrm{LP}_{\mathrm{clad01}}$ are responsible for $\eta_{\mathrm{bend}} \geq 1$

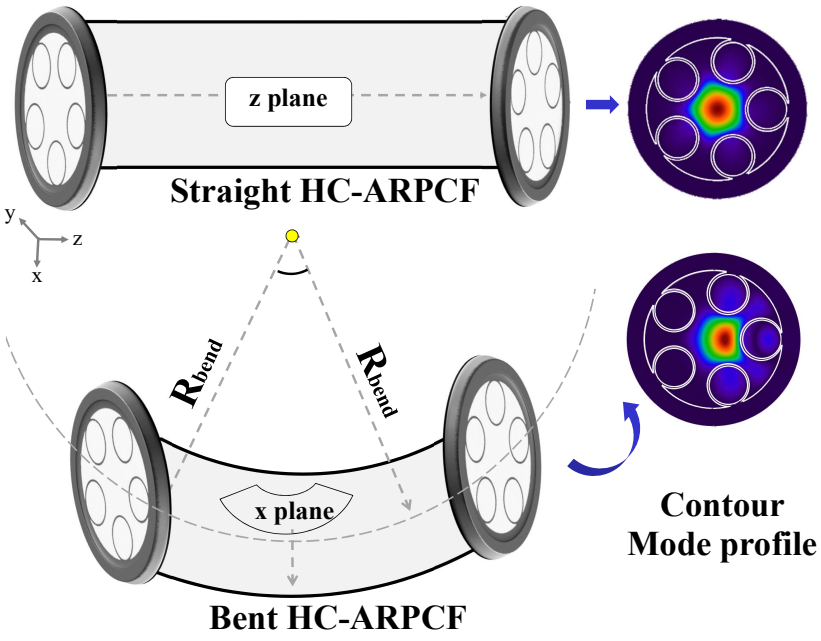

Figure 3.9. Straight and bent HC-ARPCFs. Symbolic representation of straight and bent HC-ARPCFs, and the corresponding LP_{01} modes, Sultana *et al.* (2020b).

when $R_{\text{bend}} \leq 20$.

For ease of visualization, we include the air-core index profile LP_{01} according to the cladding structures in Fig. 3.10(a). Also, we numerically analyze the transmission loss of the bent fibre, which is known to affect bending loss. The bending loss spectra for the three structures introduce undesired high loss peaks over the range of R_{bend}. The high loss peaks arises in bent fibre when higher mode contamination and phase matching between core and cladding modes become dominant. With $D/D_{\text{c}} = 0.7$, the bending losses differ due to the cladding pattern variations. The regular HC-ARPCF shows a higher loss region with more pronounced peaks than nested and adjacent nested fibre. The high loss peaks of 34.6, 16.3 and 9.1 dB/m for regular HC-ARPCFs appear around $R_{\text{bend}} = 18$, 30.5 and 85 cm respectively. The high loss peaks in nested HC-ARPCFs appear around $R_{\text{bend}} = 16$, and 42 cm with the bending loss of 16.2 dB/m and 5.9 dB/m respectively. The adjacent nested HC-ARPCF shows a high loss of 28.9 dB/m around $R_{\text{bend}} = 30.5$ cm. Excluding the high loss peak, adjacent nested HC-ARPCF shows comparatively lower loss between the $R_{\text{bend}} = 3$ and 80 cm than regular and nested HC-ARPCFs. Both the nested and adjacent nested HC-ARPCFs shows similar loss spectra when $R_{\text{bend}} \geq 80$ cm.

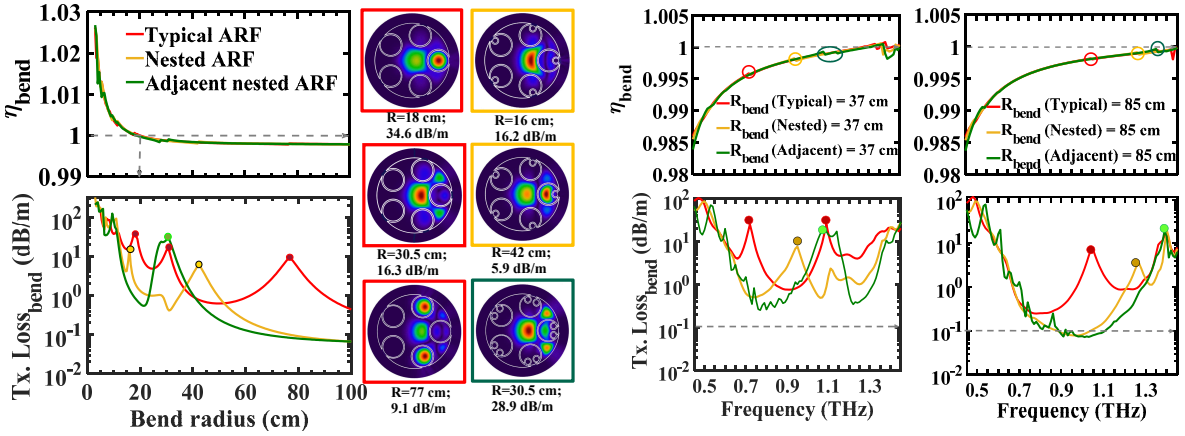

Figure 3.10. Calculated transmission loss for bent HC-ARPCFs. Calculated η_{bend} and transmission losses as a function of (a) bend radius (R_{bend}) at 1 THz and (b) frequency for five-tube typical, nested and adjacent nested HC-ARPCFs. Note that, the optimum dimensions i.e $D_c = 3$ mm, $D/D_c = 0.7$, $t = 0.09$ mm, $d = 0.54$ mm, $z/D = 0.2$, $\theta = 40^\circ$ and $g = 0.99$ mm are chosen, Sultana *et al.* (2020b).

Next, we investigate the frequency dependent refractive indices and bending losses for five-tube HC-ARPCFs; comparatively with small and large bend radius, $R_{\text{bend}} = 37$ and 85 cm as shown in Fig. 3.10(a). The η_{bend} in regular, nested and adjacent nested for $R_{\text{bend}} = 37$ and 85 cm follow the similar trends over the frequency range between 0.45 and 1.45 THz. The disruptions of η_{bend} marked with circles cause high losses peaks. For example, regular HC-ARPCFs with $R_{\text{bend}} = 37$ cm causes high loss peaks of 25 dB/m around 0.72 and 1.09 THz. The adjacent nested HC-ARPCFs with $R_{\text{bend}} = 37$ cm offers a lower loss of 0.26 dB/m at 0.77 THz than the nested fibre. The regular HC-ARPCF suffers from the bending loss and narrower transmission region than the nested and adjacent nested HC-ARPCFs. The adjacent nested and nested HC-ARPCFs carry the same bending loss of 0.07–0.09 dB/m around 1.01 THz for the large bend radius, $R_{\text{bend}} = 85$ cm. Also, the adjacent nested HC-ARPCF shows a slightly broader transmission bandwidth than the nested HC-ARPCF. However, the bending loss curve for adjacent HC-ARPCF is not as smooth as in the regular and nested bending loss curve because of the reduced Fano resonance introduced from the adjacent node of angle 40°. As a comparison between two bend radii, the frequency dependent bending loss for $R_{\text{bend}} = 37$ cm shows more pronounced peaks and higher loss than the $R_{\text{bend}} = 85$ cm in Fig. 3.10(a) due to the small bend radius. The smaller the R_{bend},

the higher the bending loss.

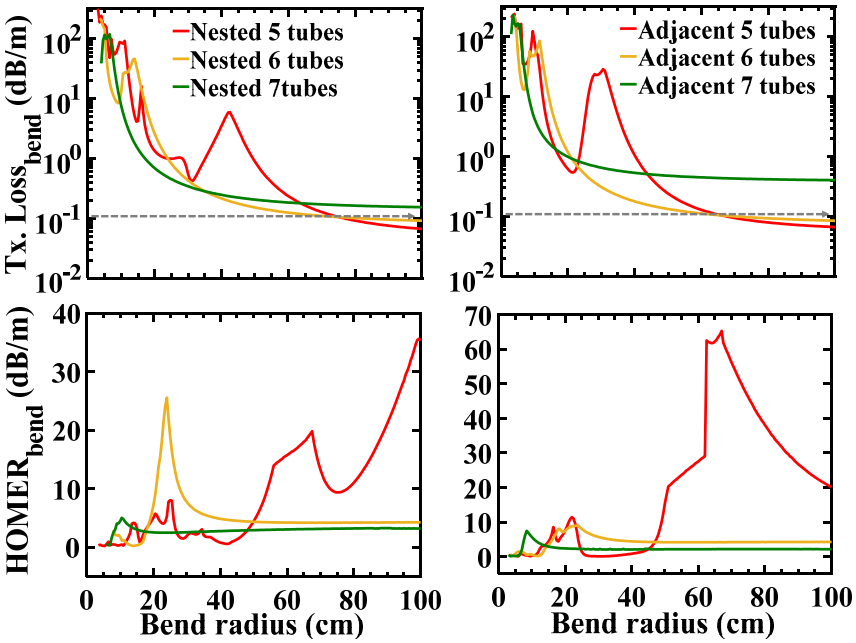

Figure 3.11. Calculated bend radius of HC-ARPCFs. Calculated transmission losses and HOMER of five, six and seven tube based on regular nested and adjacent nested fibres having $D/D_c = 0.7$. Note that, the optimum dimensions i.e $D_c = 3$ mm, $D/D_c = 0.7$, $t = 0.09$ mm, $d = 0.54$ mm, $z/D = 0.2$, $\theta = 40^\circ$, $g = 0.99$ mm and $f = 1$ THz are chosen, Sultana *et al.* (2020b).

Finally, the impact of antiresonant tube numbers using a fixed adjacent gap is analyzed to investigate the bending loss and HOMER as a function of R_{bend} in Fig. 3.11. The effective refractive index for five tubes is higher than six and seven tubes. This results in a small refractive index variation between the LP_{01} and LP_{clad01} of five antiresonant tubes. As a result, when the five-tube HC-ARPCF is bent in the xz plane the LP_{clad01} and LP_{01} are easily phased matched at small bend radii and the higher-order mode becomes dominant. The bending loss for five-tube nested HC-ARPCF is higher than seven tubes and six tubes at $R_{bend} \leq 24$ cm and $24 \leq R_{bend} \leq 75$ respectively. Similar results are obtained for seven and six-tube adjacent nested HC-ARPCF at $R_{bend} \leq 16$ cm and $23 \leq R_{bend} \leq 65$ respectively. Surprisingly, the five-tube nested and adjacent nested HC-ARPCFs at $R_{bend} \geq 75$ cm and $R_{bend} \geq 65$ cm provide lower loss than six and seven-tube HC-ARPCFs. The bending loss for large bend radii and straight fibre maintains a similar concept, for example, five tubes offers lower loss as larger antiresonant tubes allow phase matching between the LP_{clad01} and lowest HOM,

making the LP_{01} dominant. The most achievable lowest HOM includes the LP_{11}, LP_{21}, LP_{02}. The seven tubes in large bend radii and straight fibre provide the highest loss due to the short core-cladding distance using a constant adjacent tube gap.

For bent fibre with nested and adjacent nested tubes, we attempt to show the HOMER (ratio between lowest HOM and LP_{01}) in Fig. 3.11 when the adjacent tube gap, g is constant. The five-tube HC-ARPCFs are bend sensitive than six and seven tubes and can achieve comparatively larger HOMER for large bend radii. The both five and six-tube nested HC-ARPCFs can provide HOMER at large and small bend radius respectively. However, the five-tube adjacent nested HC-ARPCF achieves the highest HOMER of 65 at $D/D_c = 0.7$, $\theta = 40^\circ$ and $f = 1$ THz. The mode contamination appears in six- and seven-tube adjacent nested bent HC-ARPCFs.

3.3 Terahertz HC-ARPCF with metal wire inclusions

Metallic waveguides proposed for terahertz guidance are the scaled-up versions of guiding devices from microwave and radio frequencies. The surface waves supported by metals at terahertz frequencies are experiencing challenges because the waves are typically poorly confined and weakly bound to the metal surface. The terahertz surface modes exist because the metals have a good conductivity and the modes result from the coupling between electromagnetic waves and free electrons at the surface of the conductor. However, the interaction is typically weak because of the repulsion between the valence electrons and the electrons present in the inner shells. That repulsion severely limits the penetration of the electromagnetic fields for example $\sim$ 50–100 nm at the metallic waveguide wall, but extends 100 μm into the dielectric wall. The dominant mode for the hollow metallic waveguide rely on propagation of the electrical field. Therefore, the first downside is that metallic structure weakly guides the terahertz radiation with a low confinement factor. Thus the metallic structure around the hollow core (McGowan *et al.* 1999, Gallot *et al.* 2000, Vitiello *et al.* 2011, Wallis *et al.* 2016, Hidaka *et al.* 2005) only provides guiding boundaries in the teraherz regime. In fact, this problem is not specific to the terahertz regime and it is even more acute at microwave and radio frequencies. Another downside is the resulting high bending loss through such weak guiding waveguides and surface roughness of metals (Nagel *et al.* 2006a, Jeon *et al.* 2005), which limits their applicability. Metallic waveguides suffer from Ohmic losses while dielectric waveguides suffer from the material

absorption loses. Dry air is the best transparent medium for terahertz pulses. Therefore, intelligent design of waveguides are required to over come Ohmic and material loss limitations.

A hollow polymer based inner metal coated waveguide (Harrington *et al.* 2004, Ito *et al.* 2007, Themistos *et al.* 2007, Bowden *et al.* 2007, Bowden *et al.* 2008b, Bowden *et al.* 2008a, Matsuura and Takeda 2008, Tang *et al.* 2009, Markov *et al.* 2012, Navarro-Cía *et al.* 2013, Tang *et al.* 2015) solves these problems having a smooth metal coating inside the thin polymer wall. The waveguide requires fabrication using liquid-phase chemical deposition techniques (Harrington *et al.* 2004, Bowden *et al.* 2008a) to coat the dielectric film over the metal, and a wet chemistry method to deposit the metal film.

To reduce the fabrication complexity, an alternative approach proposed by Mitrofanov and Harrington (2010), Tian *et al.* (2010), Anthony *et al.* (2013), Yudasari *et al.* (2014), Wallis *et al.* (2015), Li *et al.* (2016b) is to embed sub-wavelength metal wires within dielectric materials for guiding terahertz radiation. A possible fibre fabrication technique is to co-draw metal and dielectrics (Tuniz *et al.* 2012) or via use of printed dielectric waveguides with air holes in the cladding, with later insertion of metal wires into the holes (Yudasari *et al.* 2014).

3.3.1 Fibre geometry

The proposed structure can be fabricated with seven non-touching, circular, dielectric antiresonant tubes, where the cladding dielectric layer contains metal wires, as illustrated in Fig. 3.12, employing Zeonex dielectric and aluminum metal. The HC-ARPCF with metal-wire inclusions have a core diameter (D_c) of 3 mm, inner dielectric antiresonant tube diameter (D) of 2.04 mm, and a Zeonex wall thickness (t) of 0.09 mm. A constant core diameter $D/D_c = 0.68$ avoids the mode contamination in the air-core and assists in single mode guidance over a board frequency range. The metal wires are inserted at the optimal distance p from the inside of the 1.5 mm thick Zeonex cladding layer. The cladding layer not only provides mechanical support for the metal wires, but also helps to confine the mode guidance in the air-core. The key parameters that determine the performance of the HC-ARPCFs with metal-wire inclusions are the innermost

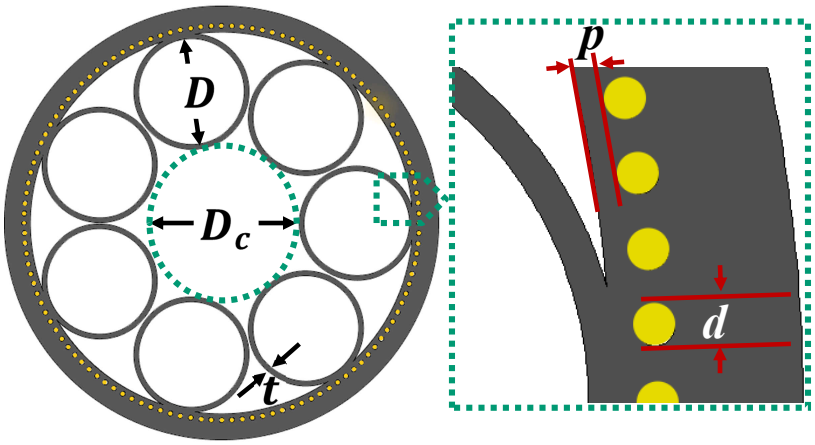

Figure 3.12. Terahertz HC-ARPCF with metal wire inclusions. Schematic of metamaterial cladded AR fibre with an enlarged view of the metamaterial section. The fibre geometry has been set with seven capillary tubes of inner diameter $D = 2.04$ mm, strut thickness of polymer tube $t = 0.09$ mm, core diameter $D_c = 3$ mm and fibre outer diameter OD $= 8.38$ mm. The white, gray and yellow colours indicate air, dielectric and metal regions respectively, Sultana *et al.* (2019a), Sultana *et al.* (2020a).

dielectric layer thickness p, and diameter d of metal wires in Fig. 3.12 illustrating these parameters. The complex refractive index of aluminium at 1 THz is $517.34 - i561.13$.

3.3.2 Effect of metal wire number

The affect of the metal wire number n on the confinement loss of the waveguide is investigated and shown to be critical for design optimization. Fig. 3.13 shows confinement loss of a LP_{01}-like fundamental mode as a function of sub-wavelength metal wire number for the innermost dielectric layer thickness $p = 306$ μm, 288 μm and 270 μm. fibres with a small number of metal wires in the Zeonex cladding, suffer a similar confinement loss to an all-dielectric cladding layer, behaving like dielectric AR fibres. The confinement loss of the LP_{01}-like fundamental mode varies greatly when the metal wire number is more than 100 for each cases ($p = 306$, 288 and 270 μm). The losses are significantly reduced to 0.006 dB/m at 1 THz where there are more than 120 metal-wires of diameter $d = 100$ μm and innermost dielectric layer thickness $p = 288$ μm. However, with the number of metal wires increasing, the cladding becomes more metallic in nature, and the confinement loss increases. The optimized structure has 140 subwavelength aluminum wires as indicated with an arrow in Fig. 3.13.

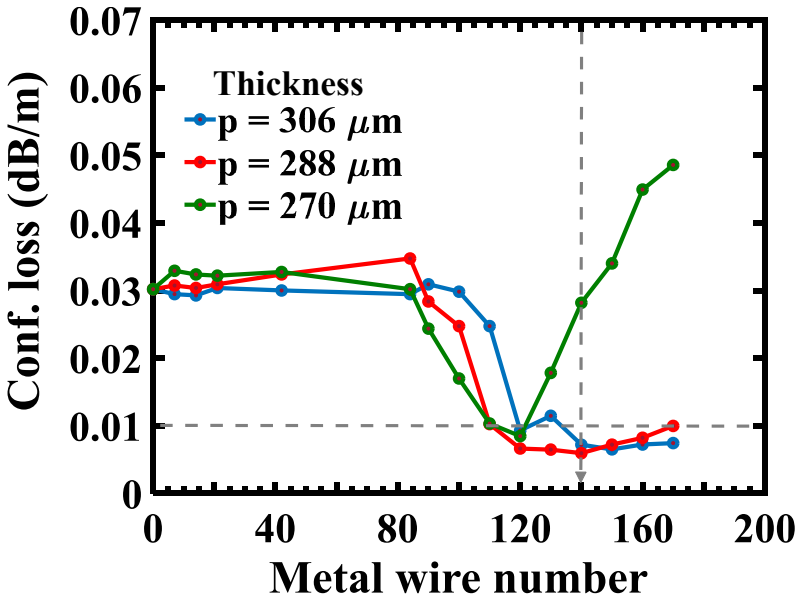

Figure 3.13. Effect of metal wire number in simulation. (a) Simulated loss at 1 THz by varying the aluminum wire number. The fibre has a uniform wire diameter $d = 100$ μm for thickness between the internal side of the metal wire and the inner dielectric cladding layer of $p = 306$ μm, 288 μm and 270 μm, Sultana *et al.* (2019a), Sultana *et al.* (2020a).

3.3.3 Effect of inner cladding dielectric layer thickness and metal wire diameter

The transmission efficiency is optimized with number of metal wires while diameter d is varied between 20 μm and 160 μm, and the innermost dielectric layer thickness, p is varied from 230 to 330 μm, as illustrated in Fig. 3.14(a)–Fig. 3.14(b). It can be seen from Fig. 3.14(a) that the innermost dielectric layer thickness plays an important role in minimizing and maximizing the confinement loss of the LP_{01}-like fundamental mode. The minimum loss of 0.0058 dB/m at 1 THz for the LP_{01}-like fundamental mode can be found at $p = 289$ μm for $d = 100$ μm and $n = 140$. When the innermost dielectric layer thickness p is reduced to less than 270 μm, the confinement loss increases rapidly due to Ohmic loss of the metal, that plays the dominant role in the increase of confinement loss. In that case the HC-ARPCF with metal inclusions behaves like an HC-ARPCF with an internal metal coating.

We also numerically simulate the confinement loss as a function of metal wire diameter d in Fig. 3.14(b) where the metal wire number n = 140 and innermost dielectric

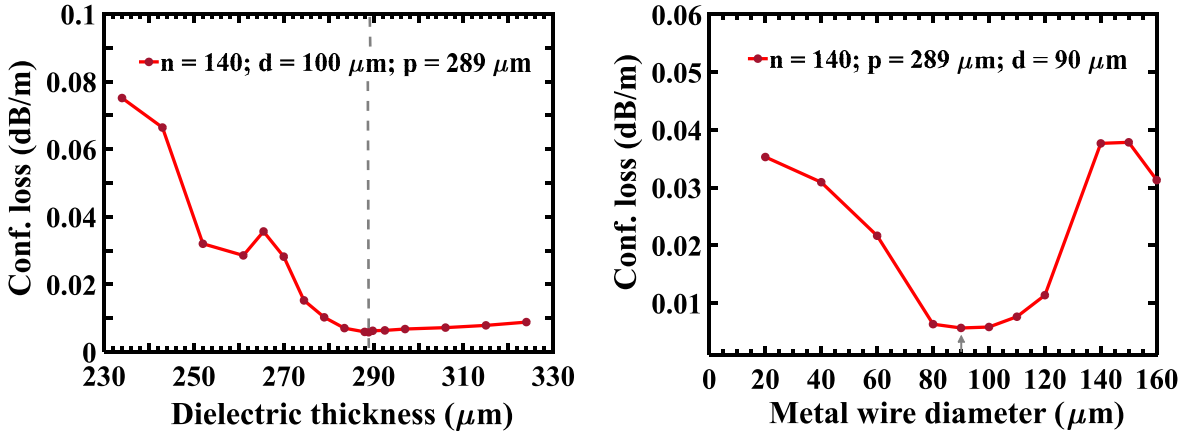

Figure 3.14. Effect of dielectric layer thickness and metal wire diameter in simulation. Simulated loss at 1 THz by varying (a) thickness between the internal side of the metal wire and the inner dielectric cladding layer *p*; (b) the aluminum wire diameter *d*, Sultana *et al.* (2019a), Sultana *et al.* (2020a).

layer thickness $p = 289$ μm. When the d is less than 80 μm, the confinement loss of the LP_{01}-like fundamental mode increases and the fibre behaves like a pure dielectric waveguide. In contrast, when the d is more than 140 μm, the confinement loss of the LP_{01}-like fundamental mode increases due the metal. Based on the above numerical simulation, we consider $n = 140$, $p = 289$ μm and $d = 90$ μm as near optimum, and analyse of the proposed fibre.

3.3.4 Comparison between HC-ARPCF with and without metal wire inclusion

The LP_{01}-like fundamental mode field intensity of HC-ARPCFs with metal-wire inclusions shown rightmost in Fig. 3.15 for metal wire numbers, $n = 0$, 5 and 140. The fibres have a uniform wire diameter $d = 90$ μm and fixed dielectric thickness between the internal side of the aluminium wire and inner surface of dielectric cladding $p = 289$ μm. Fig. 3.15(i) shows the effective refractive index and confinement loss of the LP_{01}-like fundamental mode as a function of frequency. The effective refractive index of the air-core is similar for HC-ARPCF with $n = 0$, 5 and 140 metal-wire inclusions as shown in Fig. 3.15(i). The confinement loss for AR fibres with around 140 metal-wire inclusions shows comparatively lower loss than for lower numbers of metal-wire inclusions. The

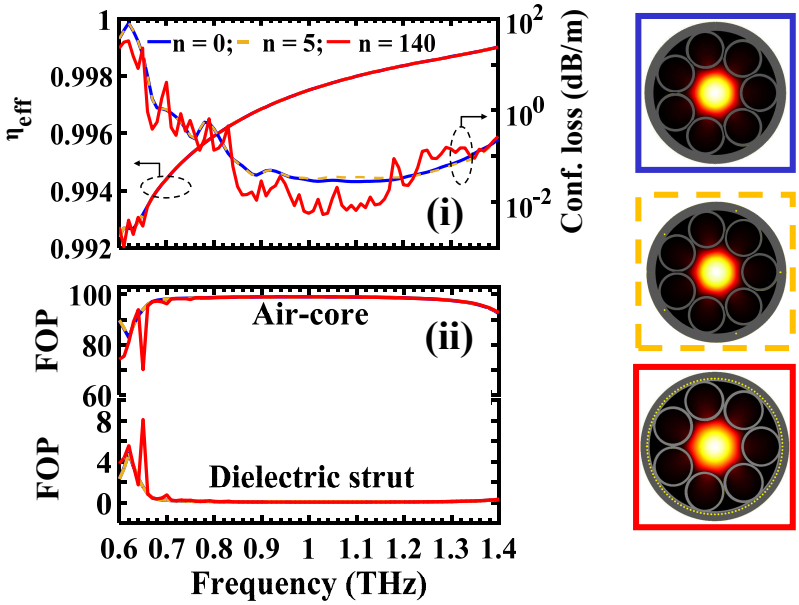

Figure 3.15. Simulated confinement of power comparison between HC-ARPCF with and without metal wire inclusion. Simulated (i) refractive index (η_{eff}) in left axis and confinement loss of LP_{01}-like fundamental mode in right axis; fraction of power in (ii) air core (FOP_{core}) at top and Zeonex strut (FOP_{strut}) at bottom. The simulations are performed by varying the metal wire numbers, $n = 0$, 5 and 140. The fibre has a uniform wire diameter $d = 90$ μm and fixed dielectric thickness between the internal side of the metal wire and the inner dielectric cladding layer $p = 289$ μm, Sultana *et al.* (2019a), Sultana *et al.* (2020a).

blue, yellow and red line indicate the HC-ARPCFs with 0, 5 and 140 metal-wire inclusions respectively. The simulation has been performed within the low loss region around 0.6–1.4 THz with the step size of 0.01 THz. A minimum confinement loss of 0.03 dB/m occurs at 1.03 THz for dielectric HC-ARPCFs ($n = 0$), where HC-ARPCF with 140 metal wire inclusions shows 0.005 dB/m at 1.03 THz, which is six times lower than dielectric HC-ARPCFs. We have shown in Fig. 3.15 that a single layer of optimized sub-wavelength metal wires in a host dielectric environment is sufficient to provide good guidance with the same properties. Fig. 3.15(ii) shows the fraction of power both the air air core and dielectric strut adjacent to the core. Approximately 99% of the power is transmitted through the air-core for all of the HC-ARPCFs with metal-wire inclusions, with less than 0.05% through the antiresonant dielectric struts. Therefore, a very small fraction, less than 0.05% of the power, penetrates through the Zeonex layer to reach the metal inclusions. However, even this small penetration, makes an impact on the loss, for different numbers of metal wires.

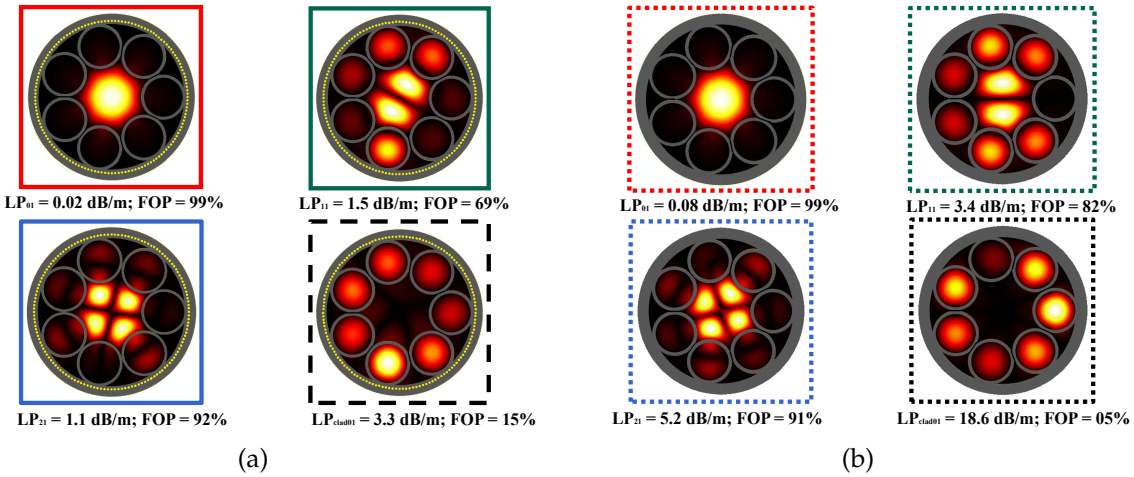

Figure 3.16. Fundamental mode comparison between HC-ARPCF with and without metal wire inclusion. Spatial electric field E distribution for the modes in the (a) HC-ARPCF with metal-wire inclusions and (b) HC-ARPCF without metal-wire inclusions: LP_{01}, LP_{11}, LP_{21}, and LP_{clad01} (from left to right) at 1.03 THz, Sultana *et al.* (2019a), Sultana *et al.* (2020a).

The mode field intensities shown in Fig. 3.16(a)–Fig. 3.16(b) are the Linearly Polarized (LP) modes derived by solving scalar Maxwell's equations under weakly-guided conditions (Gloge 1971) and experimentally characterised by Ma *et al.* (2009). We took four LP group modes and analysed the optical properties on the HC-ARPCF with metal wire inclusions and without metal wire inclusions. Mode field intensity of fundamental core mode (LP_{01}), higher-order core modes (LP_{11}, LP_{21}) and cladding mode (LP_{clad01}) at 1.03 THz are considered. In the HC-ARPCF, the core modes localize in the air-core only where the cladding mode localizes in cladding-air holes or dielectric cladding wall (Vincetti and Setti 2010). In our work, we define the light localisation in cladding–air holes as a cladding mode. It is noted that the true vectorial eigenmode of HE_{11} is in LP_{01} mode. Also, the TM_{01}, HE_{21} and TE_{01} modes are in the LP_{11} mode group. From Fig. 3.16(a)–Fig. 3.16(b), we can see that the HC-ARPCF with metal wire inclusions has a stronger light confinement in the air-core. For LP_{01}, LP_{21} and LP_{clad01} modes, the FOPs in core with metal are higher than that of without metal wire inclusions, however, for the LP_{11}, the result is opposite, 69% for the HC-ARPCF with metal wire inclusions. Because approximately 0.2% of power is absorbed in dielectric strut

which is higher than that of without metal wire inclusions (0.12%). The study also confirms that the overall confinement loss for all four modes decreases with the metal wire inclusions. We consider Fresnel reflection by considering contrast of refractive indices with polymer vs air and metal. The dielectric coating over the metal wire inclusions enhances the reflectivity of the metal-wire inclusions and reduce the loss. Moreover, the LP_{11} mode is also sensitive to the cladding pattern. The LP_{11} provides low loss between the HOMs in HC-ARPCFs without metal-wire inclusions. Only inserting the metal wire inclusion at the cladding, the LP_{21} provides low loss between the HOMs. The single mode guidance ratio are 170 and 112 for HC-ARPCFs with metal-wire inclusions and without metal-wire inclusions respectively. The loss ratio of lowest HOM and the fundamental LP_{01} (the LP_{21}/LP_{01} and LP_{11}/LP_{01} for HC-ARPCFs with metal-wire inclusions and without metal-wire inclusions respectively) results in single mode guidance. The loss ratio increases to maximum at $D/D_c = 0.68$, shown in Fig. 3.3. Here, the metal wire inclusions increase the single mode guidance by a factor of 58 (170–112) as compared to no metal-wire inclusions at 1.03 THz. It is important to note that diameter and position of the metal wire inclusions are optimized.

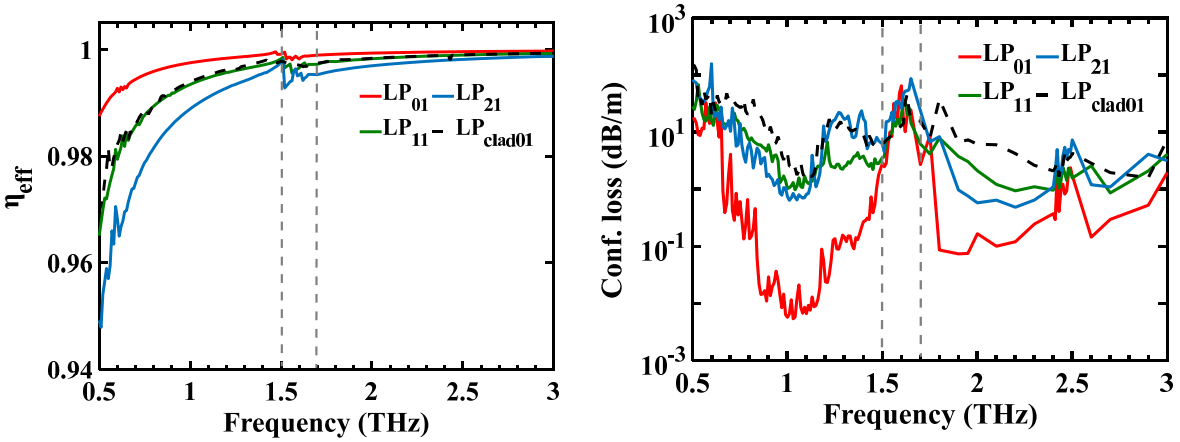

Figure 3.17. Simulated transmission loss comparison between fundamental and higher-order mode in metal wire included HC-ARPCF. Simulated (a) η_{eff}; (b) confinement loss and (c) spatial electric field E distribution of HC-ARPCF for the LP_{01}, LP_{11}, LP_{21}, and LP_{clad01} mode. The fibre has 140 metal-wire inclusions, a uniform wire diameter $d = 90$ μm and fixed dielectric thickness between the internal side of the metal wire and the inner dielectric cladding layer $p = 289$ μm, Sultana *et al.* (2019a), Sultana *et al.* (2020a).

The real part of effective index (η_{eff}) for the LP_{11} and LP_{clad01} in Fig. 3.17(a) maintains the same phase to avoid mode contamination over the frequency range 0.5–3 THz. To precisely evaluate the propagation properties we use a frequency step size of 0.01 THz. Fig. 3.17(b) shows the corresponding simulated confinement loss of the guided modes. The confinement loss difference between LP_{01}-like fundamental mode and lowest HOM defines the single mode operation window between 0.8–1.3 THz. However, from 0.8 to 1.3 THz, the confinement loss is lower than 0.1 dB/m, while for the other frequency ranges (0.5–0.8 THz and 1.3 1.6 THz), the confinement loss is not relatively low. The variation of confinement loss in the single mode operation range is substantial as the innermost dielectric layer introduces an interference peak (Matsuura and Takeda 2008) in the single mode operation range. The resonance frequency lies around 1.55 THz where the LP_{01}-like fundamental mode is coupled to LP_{clad01} and it is difficult to differentiate the LP_{01}-like fundamental mode from the LP_{clad01} mode. Also, around the resonance frequency, mode contamination arises. Above 1.6 THz, mode contamination arises with multi-mode propagation. The simulation also indicates that the minimum confinement loss for the LP_{01}-like fundamental mode is 0.006 dB/m at 1 THz. The LP_{21} provides the lowest HOM confinement loss of 0.75 dB/m at 1 THz. The ratio of higher mode suppression is nearly 130 at 1 THz. The simulation has been performed for a uniform wire diameter $d = 90$ μm and innermost dielectric layer thickness $p = 289$ μm and $D/D_{\text{c}} = 0.68$. A number of HOMs introduced in a large core diameter (3 mm), giving rise to mode contamination.

The fundamental mode field distribution for HC-ARPCF with and without metal wire inclusions are included in Fig. 3.18, for $D/D_{\text{c}} = 0.2$, in order to show the impact of adjacent tube gaps on confinement loss. When the antiresonant tubes are small, such that $D/D_{\text{c}} = 0.2$, light leaks through the large gap between two adjacent antiresonant tubes. The small distance from air-core to cladding wall hence increases the confinement loss to 0.9 dB/m for the LP_{01}-like fundamental mode at 1 THz as shown in Fig. 3.18(a). The metal wires in Fig. 3.18(b) demonstrate very clear influence on the leakage through the gap between adjacent tubes and the cladding structure. It reduces the confinement loss to 0.06 dB/m that is 15 times lower than the dielectric fibre alone.

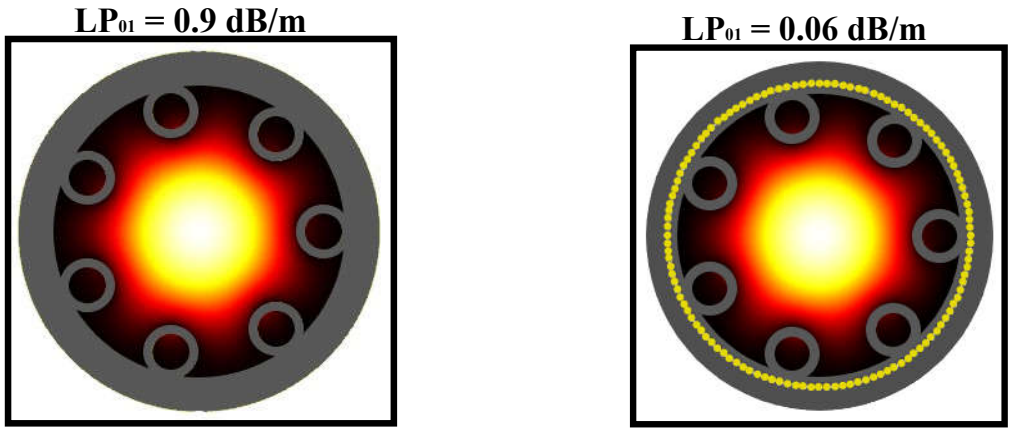

Figure 3.18. Fundamental mode comparison between HC-ARPCF with and without metal wire inclusion. Simulated intensity distributions and confinement loss of the LP_{01}-like fundamental mode in air-core when $D/D_c = 0.2$ for (a) HC-ARPCF with metal wire inclusions; (b) HC-ARPCF without metal wire inclusions at 1 THz. All HC-ARPCFs with 140 metal-wire inclusions have a uniform wire diameter $d = 90$ μm and fixed thickness between aluminium wire and inner dielectric cladding layer $p = 289$ μm, Sultana *et al.* (2019a), Sultana *et al.* (2020a).

3.4 Linearity and nonlinearity of terahertz HC-ARPCF

In nonlinear optics, a major challenge is to maximize the interaction between the light from laser sources and low-density media such as gases. An ultrafast laser beam can be focused to form a highly intense spot over a small concentrated area. The ultrafast laser beam has a short pulse width of less than one picosecond and high peak power in the beam profile illustrated in Fig. 3.19. The beam profile of the laser source describes the energy density and distribution of light, and the beam profile of a laser source is usually affected during the propagation and collimation of the beam. An efficient nonlinear optical sensor also requires high peak power at low energy (low average power) over short duration of laser pulse, a high beam profile and long interaction length. These requirements of a nonlinear optical sensor with low attenuation constant can be achieved in hollow-core photonic crystal fibre (HC-PCF). Gas-filled HC-PCF exhibits optical nonlinearity for an ultrashort temporal and spectral broadening of NIR pulses (Travers *et al.* 2011, Russell *et al.* 2014). The nonlinearity in HC-PCF can be achieved by tuning the gas pressure. Gas-filled HC-PCF nonlinear media are low-cost, replenishable, reconfigurable and exhibit sharp spectral lines (Downer 2002). Linear

and nonlinear responses are also found in other types of optical fibres.

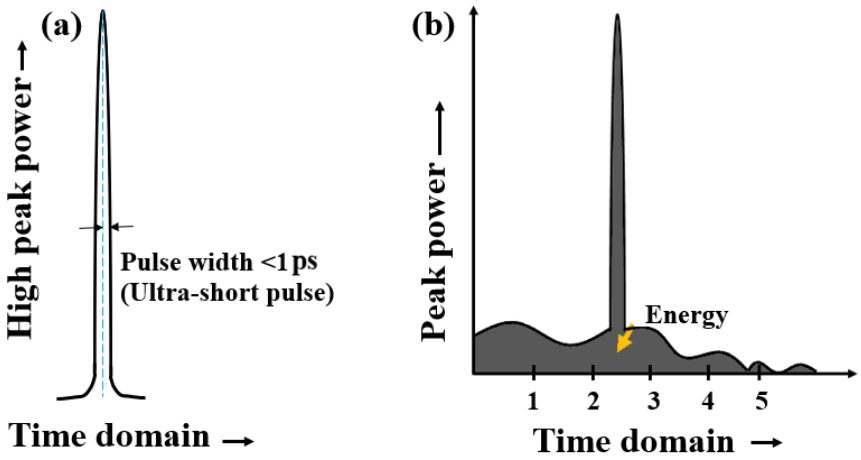

Figure 3.19. Ultrashort laser pulse. (a) An ultrashort pulse with high peak power over a very short duration of pulse width and low average power. The laser has a short pulse width of less than one picosecond and high energy in the beam profile. (b) The graphical representation for power and energy throughout laser pulses. Peak power can be defined as the ratio of single pulse energy and the pulse width. Pulse energy corresponds to the area under the pulse shape. The average power denoted as the multiplication of single pulse energy and repetition time. The short duration of the laser pulse prevents the sensor damage by lowering the average power, Sultana *et al.* (2021).

For example, recently a single-mode fibre (SMF)/multimode fibre (MMF)/SM quasi two-mode fibre was reported for temperature measurements (Olivero *et al.* 2017). Similarly, an optical sensor built as a cascade of SMF/HCF/HC-PCF filled with ethanol can sense the refractive index and temperature of the liquid ethanol simultaneously (Zhao *et al.* 2016), or a cascade of SMF/HCF/No core fibre (NCF)/PCF filled with liquid crystal/NCF/SMF measures the electric field sensitivity with the strain (tension) from the reflection and transmission spectrum (Li *et al.* 2018). For the reported sensors (Olivero *et al.* 2017, Zhao *et al.* 2016, Li *et al.* 2018), a nearly linear relation between the peak wavelength and the temperature or refractive index or electric field intensity was observed. A magnetic field sensor based on a surface plasmon resonance (SPR) has also been reported to detect magnetic fluids (Zhou *et al.* 2018). Using silver as a plasmonic material to coat the fibre, the surface plasmon effect on the fibre surface was

observed. Due to the plasmonic effect, this sensor shows nonlinear sensing characteristics. Graphene has also been used to enhance the sensing performance. Recent work on metal-graphene coated fibre-based SPR sensors was theoretically analyzed for liquid analyte detection (de Melo *et al.* 2018). The reported sensor shows an enhancement in sensitivity when using graphene. Because of the nonlinearity of graphene and metal, this sensor also exhibits nonlinear sensing performance. A range of other nonlinear effects such as supercontinuum generation (Corkum *et al.* 1986), high-harmonic generation (Popmintchev *et al.* 2010), etc. have also been demonstrated in both resonant and antiresonant modes (Allen and Eberly 1987, Reintjes 2012, Lee *et al.* 1990). However, research-based on such nonlinearities in the terahertz regime has not been previously addressed.

3.4.1 Fibre geometry and single mode operation

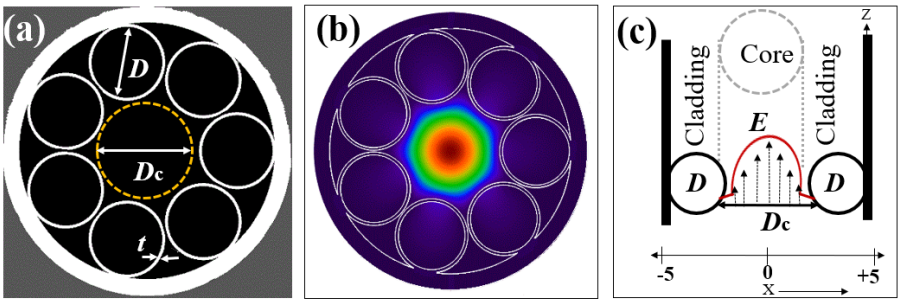

Figure 3.20. Dielectric HC-ARPCF. (a) Cross-section of a proposed HC-ARPCF, showing seven non-touching air holes in the cladding. (b) Modal field intensity of LP_{01}-like fundamental mode at 1 THz. (c) Schematic representation of LP_{01}-like fundamental mode (red curve) and corresponding electric field pattern (dashed arrow), Sultana *et al.* (2021).

The cross-section of the HC-ARPCF shown in Fig. 3.20(a) consists of a single layer of seven anti-resonant cladding tubes (with diameter D and Zeonex web thickness t) surrounding a central air defect. The geometry and corresponding dimensions are as simial as Fig. 3.12. The linearly polarized LP_{01} mode is considered as a dominant and fundamental mode as there is no power degradation. The LP_{01} mode in Fig. 3.20(b) is localized at the central hollow core for the straight fibre. Fig. 3.20(c) shows the schematic of LP_{01} mode using the red curve in the core. The thin membrane of the cladding tube reflects most of the light and confines in the central core. Here, the

dashed arrow inside the red curve exhibits the electric field intensity (E).

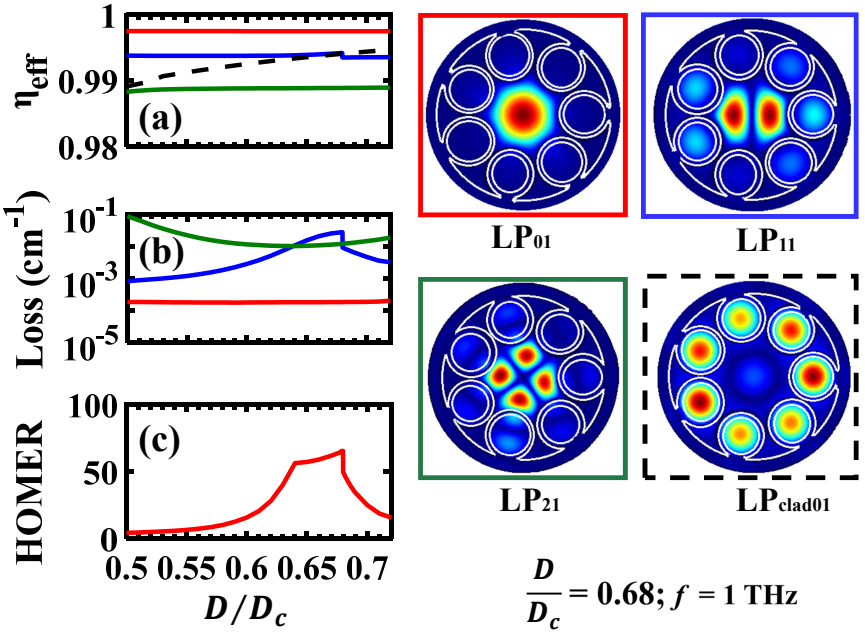

Figure 3.21. Simulated single mode guidance. Effect of changing the inner tube diameter d_{in} on resonant coupling between core modes and cladding mode while core diameter D_c = 3 mm; (a) Effective indices (LP_{01}, LP_{11}, LP_{21} and LP_{clad01}); (b) Transmission loss of core modes and (c) HOMER as a function of D/D_c. The color of the frame corresponds to the color of line of the plot, Sultana *et al.* (2020c).

We analyze the effect of inner cladding tube diameter (D) on resonant coupling in Fig. 3.21. The simulations are performed with fixed core diameter (D_c) while we vary the inner tube diameter (D) as a ratio of D/D_c from 0.5 to 0.72. It assumes in Fig. 3.21(a) that the real part of simulated effective refractive indices of LP_{01}, LP_{11}, LP_{21} are almost identical with the change of D/D_c at 1 THz where LP_{clad01} increases with the increase of D/D_c. The LP_{clad01} creates a strong resonant coupling with LP_{11} at $D/D_c = 0.68$ owing to their phase matched condition ($n_{\text{eff-LP}_{11}} = n_{\text{eff-LP}_{clad01}}$).

As a consequence, strong anti-crossing leads to high transmission loss for LP_{11} mode. Interestingly, the LP_{01} has relatively constant transmission loss with minimum value of 1.86×10^{-4} cm^{-1} over a wide range of D/D_c. The lowest transmission loss of HOMs at $D/D_c = 0.68$ obtained from LP_{21} is of 1.2×10^{-2} cm^{-1} in Fig. 3.21(b). The result indicates that HOM supression is possible with the proper engineering of cladding structure.

In addition, the higher-order mode extinction ratio (HOMER), which is defined as the ratio between the lowest loss of HOMs and the loss of fundamental mode (Habib *et al.* 2015) shown in Fig. 3.21(c), is used to quantify the single mode behaviour and strong modal filtering. For $D/D_c = 0.68$, the HOMER is 66. This assures that 66 times lower loss is achieved for LP_{01} as compared to the lowest loss of core HOM (LP_{21}) when the HC-ARPCF is kept straight.

Tab. 5.1 highlights the optical properties obtained for different modes of the proposed HC-ARPCF. It indicates that the maximum achievable HOMER is 66 with $D/D_c = 0.68$ with obtainable minimum loss of 1.86×10^{-4} cm^{-1} including material loss.

Property	**Seven tube HC-ARPCF**
Anti-crossing point	$D/D_c = 0.68$
Trans. loss of LP_{01}	1.86×10^{-4} cm^{-1}
Trans. loss for LP_{21}	1.2×10^{-2} cm^{-1}
HOMER	66
Optimized trans. loss	1.86×10^{-4} cm^{-1}

Table 3.1. Optical properties for seven tube HC-ARPCF at 1 THz.. Showing the HC-ARPCF transmission performance, Sultana *et al.* (2020c).

3.4.2 Linear properties of HC-ARPCF: Transmission loss spectra

Fig. 3.22(a) indicates that the effective refractive index (η_{eff}) of the LP_{01}-like fundamental mode increases linearly with the frequency. The mode field profile of the LP_{01}-like fundamental mode in Fig. 3.22(c) indicates the strong field confinement inside the core, which is desirable for obtaining low transmission loss at 1 THz frequency. Also, the LP_{01}-like fundamental mode indicates the effect of cladding resonance at 1.6 THz, as power couples between the core mode and the surrounding thin Zeonex webs.

The degree of transmission loss is fully dependent on the core size and thickness of the cladding web. The obtained loss in the fundamental mode is illustrated in Fig. 3.22(b). The physics of the resonance peaks (high leakage loss) obtained in Fig. 3.22(b) can be recognized as the radial resonances of light with the concentric Zeonex structure. There is the coupling of power between the core modes and the Zeonex webs.

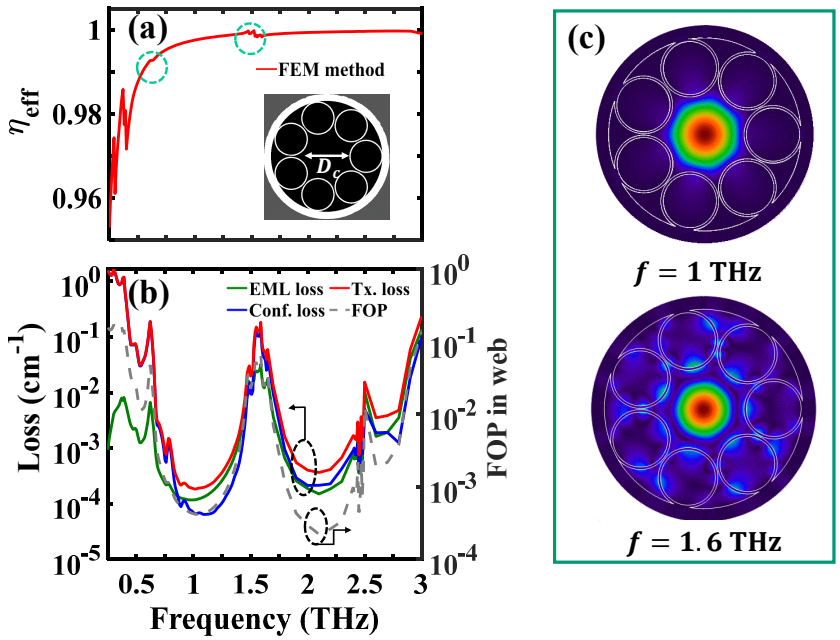

Figure 3.22. Development of dielectric HC-ARPCF for terahertz transmission in simulation. Effective refractive index (η_{eff}) of LP_{01}-like fundamental mode, (b) effective material loss (EML), confinement loss, transmission loss (left) and fraction of power (FOP) in polymer web (right) of an evacuated HC-ARPCF with a 3 mm core diameter, and 0.09 mm polymer web; (c) Mode field intensity plots of two computed modes at 1 THz (on antiresonance) and 1.6 THz (on-resonance), Sultana *et al.* (2021).

The fraction of power (FOP) in the polymer web indicates a significant increase of FOP at cladding resonances, $\sim$ 1.6 THz, 2.5 THz, etc. where light from the core strongly couples with the polymer web. There is very low power coupling (0.01%) to the surrounding polymer web. The FOP in the polymer web is used to calculate the EML. The material absorption loss (α_{mat}) of Zeonex is linearly proportional with frequency (Islam *et al.* 2019, Nielsen *et al.* 2009, Chen *et al.* 2013, Sebastian *et al.* 2017). At higher frequencies, the dielectric losses of transparent polymer increases due to polarization relaxation (Fedulova *et al.* 2012, Levitskaya and Sternberg 2019). Hence, the effect of EML is not significant in the lower frequency region (e.g., lower than 0.9 THz) and as the frequency increases, the increment in EML will be significant at higher frequencies. Fig. 3.22(b) clearly shows that the transmission loss is unaffected by EML in the frequency range between 0.5–0.9 THz. In the first transmission spectrum, a low loss region appears around at 0.9–1.3 THz and minimum loss of 1.86×10^{-4} cm^{-1} obtained

at 1 THz at a transmission bandwidth of 0.5–1.5 THz. The EML is then added to leakage loss and this yields the total propagation loss. Apart from the resonance peaks, the HC-ARPCF provides broadband guidance (0.62–1.60 THz).

3.4.3 Linear properties of HC-ARPCF: Performance as a refractometric sensor

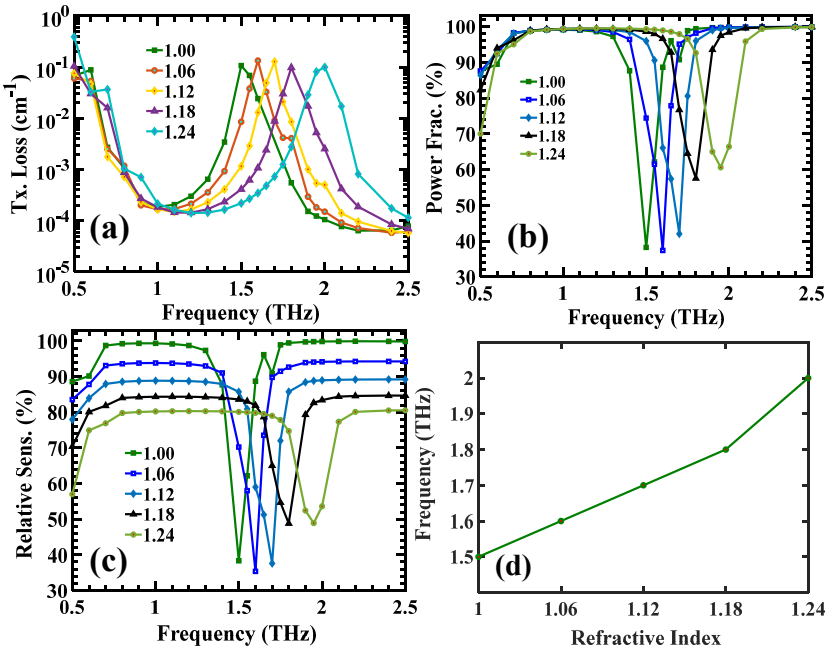

Figure 3.23. Simulated refractometric sensing performance. (a) Transmission loss spectra with different variation of analyte RI. (b) Core power fraction for different analytes of the proposed gas sensor; (c) Relative sensitivity of the proposed gas sensor. (d) Change of resonance frequency with the change of refractive index, Sultana *et al.* (2020c).

On the basis of guiding properties Fig. 3.22(a), we numerically show the HC-ARPCF sensing performance by changing the refractive indices (RI) from 1.0 to 1.24 in the core at Fig. 3.23(a). At the resonance frequency (f_{m}), the effective refractive indices between $\mathrm{LP}_{\mathrm{clad01}}$ and LP_{01} create a resonant coupling and LP_{01} experience enhanced leakage through the high indexed Zeonex layer. The theoretical $f_{\mathrm{m}} = 1.446$ THz is estimated from Equation (3.1) at $m = 1$. The simulated f_{m} is at 1.5 THz shows blue-shift relative to the corresponding theoretical value. The blue shift of the resonance frequency can be explained by the mode field distribution (Liu *et al.* 2015). More frequently, changes in real part of RI for LP_{01} is sensed via resonance peak shifts (Senlik *et al.* 2010).

Fig. 3.23(a) indicates that when the refractive index of the hollow core is changed and loaded with the refractive index of 1.06, 1.12, 1.18 and 1.24, the resonance dips from 1.5 THz change their positions and shift towards 1.6 THz, 1.7 THz, 1.8 THz and 2 THz respectively. These resonant shifts are the signature of refractive index variation inside the fibre core, demonstrating how the fibre can potentially be an effective and sensitive refractive index transducer. Fig. 3.23(b) shows the amount of light and analyte interaction of the fundamental LP_{01} mode within the guided hollow core for different analytes as a function of frequency, obtained from eigenmode solver using Equation (3.3). The numerical simulation reveals that more than 98% of power concentrates within the hollow core for this propagation mode around 1 THz. The increase of n_{co} reduces the difference between the n_{clad} and n_{co}, which in turn disturbs the guidance of light using antiresonant reflecting optical waveguide (ARROW) model and may suppress the resonant properties of the fibre. In this case, most of the light will be guided through the core due to small index variations between core and cladding and the core power fraction may gradually increase with the analyte refractive index at the resonant frequency. The modal power distributions by means of different effective refractive indices of the core filled with analytes correspond to the spectral characteristics of analytes. Fig. 3.23(c) represents the relative sensitivity calculated from Equation (3.6) of the refractive-index sensor and relative sensitivity relative to the refractive index of the sample that need to be sensed. Specifically, transmission dips are considered for analyte species characterization because it is rarely affected by the analyte pressure, analyte temperature nor system's dynamic range as is the absorption strength. Relative sensitivities of the proposed terahertz refractive index sensor are 38, 35, 37, 48, 49 at the transmission dips for an analyte refractive index of 1.00, 1.06, 1.12, 1.18, and 1.24 respectively.

Fig. 3.23(d) illustrates the relationship between the analyte RI and the corresponding resonant frequency. In this simulation, the transmission dip goes to higher frequencies with increase in analyte refractive index. In other words the relationship between the small change of refractive index in the core and slight shift of resonance frequency is linear to a first order approximation. In our analysis, the resonance frequency is at 1.5 THz for RI of 1.0 and the FWHM of the resonant peak is about 0.1 THz. For the next step, the analyte RI of 1.0 is replaced with 1.06, 1.12, 1.18 and 1.24 and the corresponding FWHM are 0.06 THz, 0.062 THz, 0.09 THz and 0.13 THz respectively. The increase in resonance bandwidth (FWHM) can be used to detect higher refractive indices. As

can be seen from Fig. 3.23(d) that the simulated refractive index change of $\Delta\eta = 0.06$ results in a resonance frequency shift of $\Delta f = 100$ GHz for refractive indices between 1.00 and 1.18 and 200 GHz for refractive indices from 1.18 to 1.24. The constant spectral shift $\Delta f = 100$ GHz for the constant refractive index variation $\Delta\eta = 0.06$ results in the relative sensitivity 1670 GHz/RIU, as shown in Fig. 3.23(d). However, the change in spectral shift $\Delta f = 200$ GHz at 1.24 has doubled the relative sensitivity. The unspecified mode confinement at resonance frequency can create impact on the transition of resonant frequency towards 2 THz with spectral shift $\Delta f = 200$ GHz and doubles the theoretical refractive index sensitivity $S_f = 3333$ GHz/RIU for 1.24.

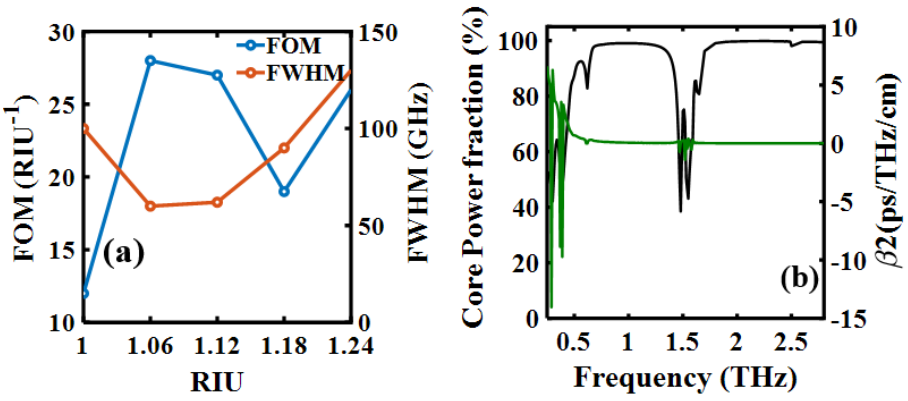

Figure 3.24. Simulated sensing performance. (a) FOM and FWHM with RI variation. (b) Calculated group velocity dispersion (GVD) of an evacuated HC-ARPCF with a 3 mm core diameter, and 0.09 mm polymer web (green curve), Sultana *et al.* (2020c), Sultana *et al.* (2021).

From Equation (3.7) the theoretical refractive index sensitivity (S_f) for the proposed sensor is from 1670 to 3335 GHz/RIU (refractive-index-unit). The proposed sensor shows FOMs of 17, 28, 27, 19 and 13 respectively. The highest FOM is obtained for the refractive index of 1.06, shown in Fig. 3.24(a) as the resonance bandwidth (FWHM) is comparatively sharper than at this value. A high quality factor (Q) sensor implies high sensitivity and a narrow FWHM (Yoshie *et al.* 2011). The Q values of the proposed refractive index sensor are 15, 27, 27.5, 20 and 16 respectively.

Sensor length is also an important parameter that is determined from the inverse of the transmission loss. As the transmission loss characteristics in HC-ARPCF varies with

different refractive indices, the sensor lengths also varies accordingly. The transmission losses at resonant points are 0.11 cm^{-1}, 0.13 cm^{-1}, 0.13 cm^{-1}, 0.1 cm^{-1}, and 0.1 cm^{-1} for refractive indices of 1.00, 1.06, 1.12, 1.18 and 1.24 respectively. At the resonance frequencies, maximum fibre operating lengths range between 7.7 cm to 10 cm.

For the variation of analyte refractive indices, Tab. 3.2 shows the performance metrics of the proposed terahertz refractive index sensor that indicate that with the change of refractive index the proposed sensor can attain a maximum spectral sensitivity of 3335 GHz/RIU and maximum quality factor and FOM of 27.5 and 28 respectively. In this subsection, our proposed seven tube HC-ARPCF can numerically detect the analyte with the RI ranges ranges between 1.00–1.24 is in the group of vapour as considered in (You *et al.* 2012). The resultant refractive index sensitivity, quality factor, and FOM are ranging from 1670–3335 GHz/RIU, 15–27.5, and 17–28 RIU^{-1}.

Analyte RI variation	**Resonant peak (THz)**	**Relative sensitivity (S_f)**	**RI sensitivity (GHz/RIU)**	**FWHM (GHz)**	**Quality factor**	**FOM (RIU^{-1})**	**Length (cm)**
1.00–1.06	1.5	38	1670	100	15	17	9.4
1.06–1.12	1.6	35	1670	60	27	28	7.7
1.12–1.18	1.7	37	1670	62	27.5	27	7.7
1.18–1.24	1.8	48	1670	90	20	19	10
1.24	2.0	49	3335	130	16	26	10

Table 3.2. Terahertz sensing performance of the proposed antiresonant fibre. Showing the HC-ARPCF transmission performance, Sultana *et al.* (2020c).

The performance of the proposed sensor as compared with the prior sensors reported for terahertz sensing is shown in Tab. 3.3. Based on the average sensitivity, quality factor, and FOM the proposed sensor shows improved performance.

The group velocity dispersion (GVD) and the power flow through the core are shown in Fig. 3.24(b). We can see that over 99.99% of the light can be guided through the core region. The cladding resonance disrupts the transmission and therefore has very little impact on the GVD. The low dispersion slope implies that even though the material

Reference	Sensor structure	RI	RI sensitivity (GHz/RIU)	Q-factor	FOM (RIU^{-1})
(Cruz *et al.* 2013)	Core-less wave guide	1.4–1.5	5	–	–
(Cruz *et al.* 2017)	Hollow pipe wave guide	1.0–1.44	972	–	–
This Paper	Seven tube HC-ARPCF	1.00–1.24	from 1670 to 3335	from 15 to 27.5	from 17 to 28

Table 3.3. Comparison of the proposed refractive index sensor with priors sensor in the terahertz regime. Showing the HC-ARPCF transmission performance, Sultana *et al.* (2020c).

nonlinearity for Zeonex is relatively weak, the nonlinear contribution to the phase-matching is significant. It displays almost flat and zero GVD for the LP_{01}-like fundamental mode. With the advantage of having a much lower transmission loss, an HC-ARPCF is linear with a zero dispersion for the entire frequency range which is verified through FEM simulation shown in Fig. 3.24(b) (green curve). The shallow and flat GVD slope changes rapidly at resonance frequencies where the refractive index of the core mode and cladding mode matches and causes strong coupling between them. Although a HC-ARPCF exhibits zero dispersion, it has a close to zero nonlinear coefficient because of its low FOPS ($\ll 0.01\%$) in the material; however, there are ways to create nonlinearity in the terahertz regime. HC-ARPCFs provide anomalous dispersion which is suitable for chirped pulse compression by self-phase modulation (SPM). This facilitates linear or near-linear dispersive compression, analogous to what can be acquired through bulk diffraction gratings, in an all-fibre system at pulse energies where standard fibres would be strongly nonlinear. The GVD plays the central role in controlling the nonlinear dynamics, the dispersion properties of which can be

extensively engineered by varying the gas species or the gas pressure–this has become the dominant approach for exploring the nonlinear effect in gas-filled HC-ARPCF.

3.4.4 Comparison between linear and nonlinear properties of HC-ARPCF

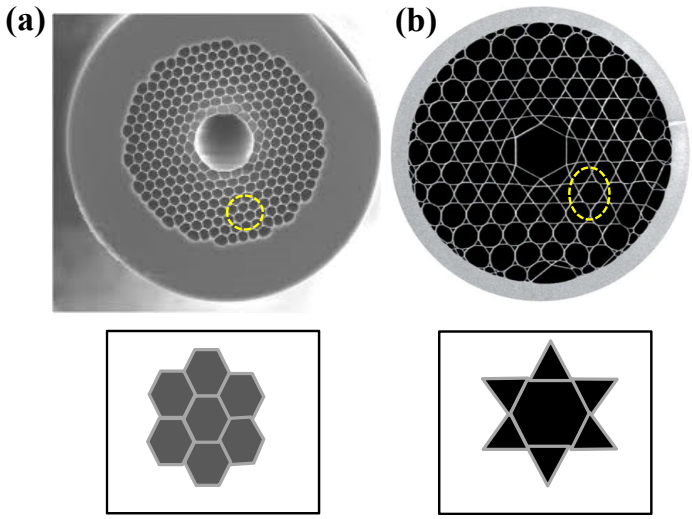

Figure 3.25. The nonlinearity in HC-PCF. Cross-section of HC-PCF in (a) photonic bandgap style (Travers *et al.* 2011) and (b) kagome style (Russell *et al.* 2014) with their corresponding enlarged cladding patterns.

In this subsection, we outline the linear and nonlinear properties of different HC-PCF and determine the best candidate for nonlinear fibre sensing. Based on guiding mechanisms, HC-PCF comes in two main varieties. The first is a photonic bandgap (PBG) fibre as shown in Fig. 3.25(a) that exhibits low loss, confines light strongly, and the GVD has a steep slope that makes it suitable for spectral filtering (Travers *et al.* 2011).

The second type of HC-PCF has a kagome lattice cladding as shown in Fig. 3.25(b) that can exhibit ultra-broadband guidance of light with extremely low loss and displays weak anomalous GVD over the entire transmission window employing a low dispersion slope. The kagome-lattice fibre can also include the anticrossing due to the coupling between fundamental core mode and cladding mode at a resonant frequency. These cladding resonances are quite narrow and disrupt the transmission window,

therefore, they have very little impact on dispersion properties (Russell *et al.* 2014). Note that the dispersion properties of kagome cladded PCF in Fig. 3.25(b) and the HC-ARPCF in Fig. 3.20(a) are similar however the transmission losses of these two are different. At the same core diameter, the kagome cladded fibre exhibits significantly lower loss than the HC-ARPCF. However, considering fabrication feasibility, capillary cladded fibre is simpler than the kagome fibre. Therefore, it is more practical to use capillary cladded fibre for any nonlinear applications.

3.4.5 Ways to create nonlinearities in HC-ARPCF

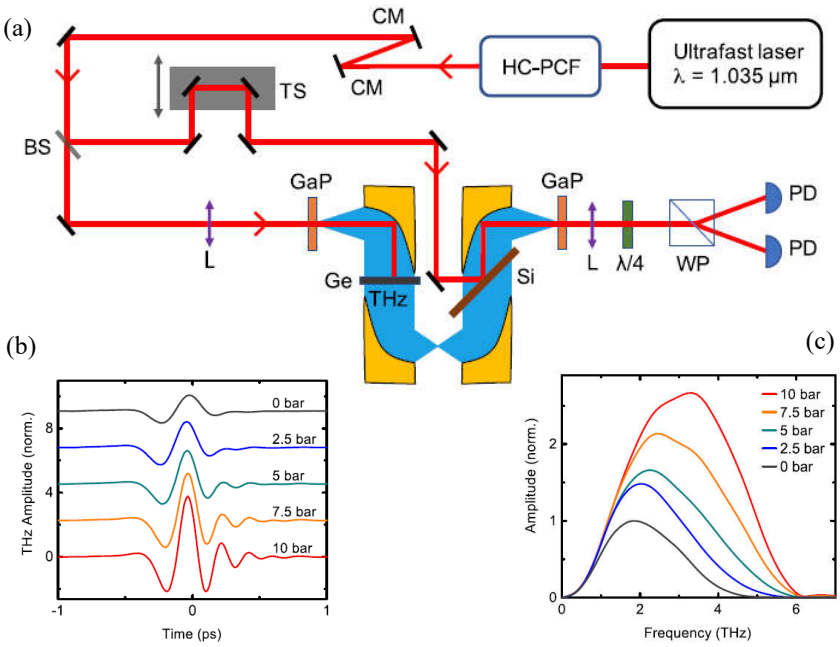

Figure 3.26. Broadband terahertz generation and detection mechanism. (a) Schematic of the experimental setup to achieve broadband terahertz generation and detection. CM: chirped mirror; BS: beam splitter; TS: translational stage; L: lens, GaP: ∠110⟩ oriented 220 μ-thick gallium phosphide crystal; Ge: germanium wafer; Si: silicon wafer; $\lambda/4$: quarter-wave plate; WP: Wollaston prism; PD: photodetector; (b) Temporal amplitude recorded with terahertz lock-in amplifer prepared in the HC-PCF at different Ar pressures; (c) Corresponding THz spectral amplitude, Cui *et al.* (2018).

In a hollow core terahertz fibre, the possible nonlinearities can be obtained following the experimental setup proposed by Cui *et al.* (2018). In a gas-filled environment, the HC-ARPCF can be used to broaden the terahertz spectrum. The proposed terahertz system setup can be used with a stable MHz laser that can deliver pulses of

sub-microjoule energy and duration of a few hundred femtoseconds.

A Yb:KGW ultrafast laser amplifier propagates near-infrared (NIR) pulses as an optical source in Fig. 3.26(a). The HC-ARPCF in a gas-filled environment can be used to compress the NIR pulses for efficient broadband terahertz spectrum by varying the gas pressure. Here, the linear and nonlinear properties of the HC-ARPCF can be controlled by controlling the gas pressure that also permits the optimization of pulse spectral broadening.

To compensate for the positive chirp induced from self-phase modulation (SPM), a pair of identical chirped mirrors can be placed after the HC-ARPCF. A beam splitter divides the NIR pulses into linear pump pulse and probe pulse where two nonlinear gallium phosphide (GaP) crystals are used for terahertz generation and detection respectively based on optical rectification. The emitted terahertz pulses from GaP are collected and focused on the identical detection crystal (GaP) using parabolic mirrors. The terahertz pulse in detection crystal and the pump pulse together allow coherent detection. When the terahertz electric field penetrates along the one axis of the nonlinear detection crystal, the variations in crystal refractive index create birefringence in the terahertz electric field, which is assumed linearly polarized at the beginning. A quarter-wave plate has two perpendicular axes and decomposes the electric field as E_x and E_y. When the quarter-wave plate is not oriented at 45°, to the elliptically polarized electric field, it adds $\pi/2$ dephasing for both components. A suitably oriented Wollaston prism (two triangular birefringent prisms interfaced together) provides the intensities for both orthogonal components, labelled as "WP" in Fig. 3.26(a). The intensity mismatch is measured using two photodetectors. This detection procedure known as electro-optic sampling has been applied for coherent pulse detection to accurately recover the phase difference and amplitude of two orthogonal components. The nonlinear crystal modifies the polarization state of the terahertz electric field and by resolving the change in polarization it is possible to directly map the terahertz electric field. As the gas pressure increases from 0 to 10 bar, the peak terahertz amplitude increases due to temporal compression of the NIR pulses, leading to higher peak powers and, consequently, to more efficient nonlinear frequency down-conversion, illustrated in Fig. 3.26(b). The corresponding terahertz spectral amplitudes are shown in Fig. 3.26(c). The development of an efficient terahertz system with a broadband spectral window can allow access to molecular resonance for sensing applications.

3.5 Chapter summary

We propose three different dielectric cladding structures with typical, regular nested, and adjacent nested HC-ARPCFs. We find that the five-tube HC-ARPCF exhibits lower loss and wider transmission bandwidths as compared to six and seven tube designs. Also regular nested HC-ARPCF are not susceptible to Fano resonances as is the case for adjacent nested HC-ARPCFs, and provide a superior HOM suppression of 140. It is important to note that the five-tube HC-ARPCFs are bend sensitive and suffer from higher bending loss for small bend radii than six and seven tubes. Also, a small bend radius shrinks the transmission window.

Next, we optimize a novel seven-tube HC-ARPCF with metal-wire inclusions. The HCARPCF with optimized metal-wire inclusions exhibits six times lower loss, covering a single mode bandwidth (BW) of 700 GHz. This fibre also increased single mode guidance by a factor of 58 compared with a pure dielectric HC-ARPCF, making it promising for terahertz transmission.

Finally, a novel approach for preparing ultrashort pulses from gas-filled HC-ARPCF has been presented to achieve efficient broadband terahertz generation and detection. The linear properties of an evacuated waveguide become nonlinear by tuning the gas pressure, creating a broadband terahertz spectrum due to SPM. The approach is extremely interesting due to the low cost of the technology and the simplicity of the waveguide architecture. The development of effcient terahertz systems with broadband spectral window can allow the access of molecular resonances for ultrasensitive sensing applications.

In the following chapter, we discuss a 3D fabrication procedure to fabricate seven-tube HC-ARPCF for terahertz transmission. The fabrication technique is suitable for fabrication of any kind of complex terahertz fibres. The experimental analysis of the fibre is also carried out and discussed considering transmission loss and coupling loss for five different fibre lengths.

Chapter 4

Dielectric antiresonant fibre: Design, fabrication, and characterisation

A hollow core antiresonant photonic crystal fibre (HC-ARPCF) is fabricated by fused deposition modeling (FDM) of 3D printing technology. The experimental analysis is carried out using terahertz time domain spectroscopy (THz-TDS), and supports our numerical findings, illustrating how the proposed fibres can be used for low loss transmission of terahertz waves. The simplicity of the proposed fibre structures facilitates fabrication for a number of different transmission and sensing applications in the terahertz range.

4.1 Introduction

Out of many ways of fabricating optical waveguides, recent attention has been directed towards 3D printing with its ability to produce different symmetric and asymmetric fibre structures, owing to continuous improvements in manufacturing technologies. The idea of 3D printing fibre first emerged in 2016 (Zubel *et al.* 2016) where the authors presented the potential of drawing a fibre cane from a 3D printed fibre preform using a PMMA filament. In 2017, the first drawn HCF cane was demonstrated (Marques *et al.* 2017), however no optical guiding was observed.

There are different 3D printing methods for polymers including Stereolithography Apparatus (SLA) and Fused Decomposition Modelling (FDM), that constrains the types of base materials that the printer can use. Due to the photo curing process, SLA printing is used for thermoset polymers, while FDM uses thermoplastics such as Zeonex. In 2016, Yang investigated 3D printed terahertz hollow waveguide based on a kagome photonic structure using the *Objet30 Prime* printer, which is an SLA printer. The lowest reported loss thorough this fibre was 0.002 cm^{-1} (0.868 dB/m) at 0.75 THz (Yang *et al.* 2016). The core Yang *et al.* (2016) is massive at 9 mm, with the lengths of 10 cm, 20 cm and 30 cm. However, thermoset polymers cannot be remelted, and therefore SLA is not a suitable choice for drawing the fibre. Note that FDM methods work for thermoplastic polymers, with a wider variety of available polymer.

As the FDM technique is suitable for fabrication with a wider range of polymers, it is selected for the fabrication of our Zeonex based fibre samples. The FDM technique is also the most commonly used and low-cost technique. It relies on a polymer filament fed through a nozzle depositing molten polymer that cools and hardens after deposition (Talataisong *et al.* 2018, Van Putten *et al.* 2018).

4.1.1 Objective and framework

We fabricate a Zeonex based node-less single layer negative curvature HC-ARPCF using the FDM technique. The aim is to introduce inhibited coupling between core and cladding mode for low loss terahertz guidance, and resonant coupling between HOM and cladding modes for single mode guidance. The fibre can then efficiently transmit

terahertz waves with low propagation loss and improved core power fraction, applicable for transmission and sensing in the terahertz regime. We organize the work as follows, in Section 4.2, we discuss in details about the filaments making, 3D fabrication process, printed fibre geometry and for the first time we measure effective material loss on printed Zeonex; Section 4.3 introduces the experimental setup with terahertz time domain spectroscopy (THz-TDS) for transmission, while Section 4.4 highlights the experimental analysis on the transmission and coupling loss using THz-TDS.

4.2 The FDM based 3D printing

4.2.1 Methodology of filament making

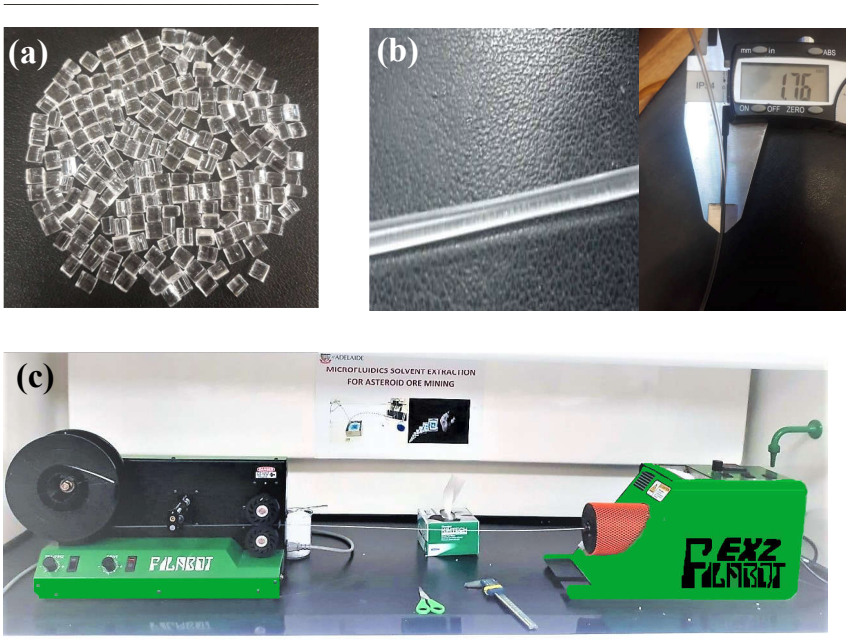

Figure 4.1. Preparation of filament and 3D printed fibre using that filament. (a) Zeonex granules (480R) manufactured by Zeon corporation; (b) Zeonex filament of 1.75 mm diameter made by *Filabot EX2 Filament Extruder*; (c) A 3D filament extruder: *Filabot EX2 Filament Extruder*, Sultana *et al.* (2020c).

The procedure for 3D printing can be divided into three main steps. In the first stage, the sample filament is made from Zeonex granules. Second, the 3D printed fibre is made with a 3D printer using those filaments. Finally, fibre drawing is performed on the 3D printed fibre to obtain the required thickness. The final "fibre drawing" step is optional and is possible to avoid by using a 0.1 mm nozzle diameter delivering a

20 μm layer thickness, even with higher quality printing resolution as mentioned in (Köhler *et al.* 2016). Due to the larger wavelength in the terahertz regime compared to visible and infrared, the dimensions of the fibre are much larger. As a result, some of the fibres for short-range terahertz applications can be printed directly using the FDM printer, which can reduce the cost of requiring a drawing tower.

To improve the quality of the filament and fibre, we bake the Zeonex granules in Fig. 4.1(a) at 78°C over 24 hours in an oven. This assists with the reduction of trapped air bubbles in the filament. During heating, air bubbles can expand and create filament deformation and sudden breakage. Additionally, trapped air bubbles can also expand in the fibre during the printing process and degrade the fibre quality. A 3D filament extruder *Filabot EX2 Filament Extruder* in Fig. 4.1(c) is used to extrude the granules to a 1.76 $\pm$ 0.01 mm Zeonex filament in Fig. 4.1(b) at 198 celsius, that is compatible with the employed 3D printer. In this way, we are able to make pure transparent Zeonex filaments without air bubbles as shown in Fig. 4.1(b).

4.2.2 Methodology of 3D printing

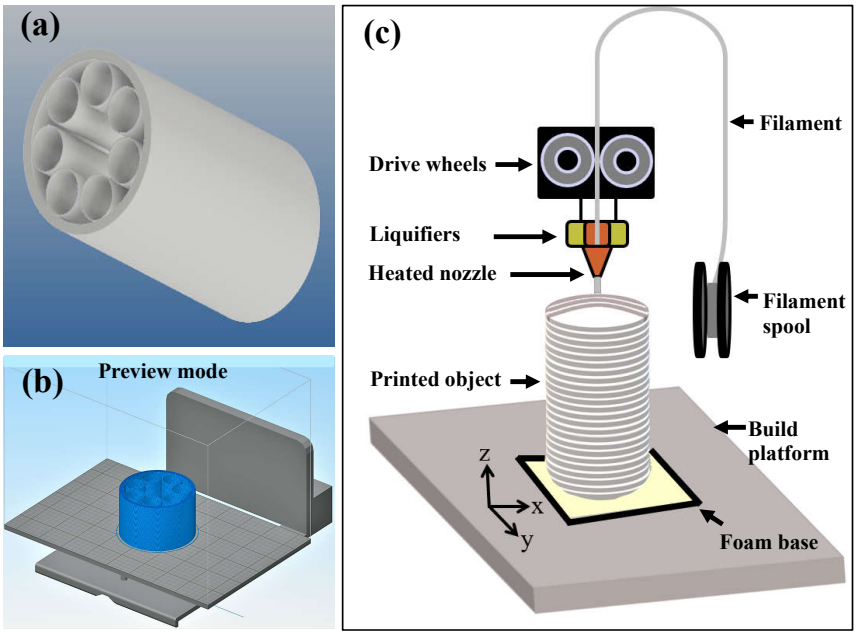

Figure 4.2. Preview model and 3D printer. (a) The 3D model designed with *Autodesk Inventor* Professionals 2019 software; (b) The STL file format for 3D printing preview model; (c) A sketch of FDM based *Flashforge Creator Pro* 3D printer.

The 3D model of the proposed HC-ARPCF fibre is designed using *Autodesk Inventor* Professionals 2019 software, shown in Fig. 4.2(a) and is ported into a stereolithography (STL) file format, shown in Fig. 4.2(b). The fibre is printed using a *Flashforge Creator Pro* shown in Fig. 4.2(c), with a minimum vertical feature size of 0.4 mm and a maximum height of 150 mm and 0.1 mm horizontal resolution. The fibre transparency is optimized by ensuring that the adjacent printed lines are fused with minimal air trapping. To reduce air-gaps, the amount of trapped air, and the size distribution of the air bubbles from the adjacent printed lines, the infill is set to 100% and the layer height is reduced to as small as possible—rather than using a few larger layers of plastic, we use many smaller but much more tightly packed together layers. The temperatures and speeds that we use are a product of vigorous trial and error. The final temperatures that are settled-on are chosen as they produce the best quality and most consistent prints. For the best results a nozzle temperature of 273°C is used as well as setting the platform temperature to 125°C. The parts are printed at the slow speed of 8 mm/s to gain the fastest and decent adhesion between the adjacent layers, whereas typical printing speeds are usually in the range of 70–100 mm/s. The HC-ARPCF fibre is then cleaved by using heated razor blade from the 3D printer.

4.2.3 Fibre geometry

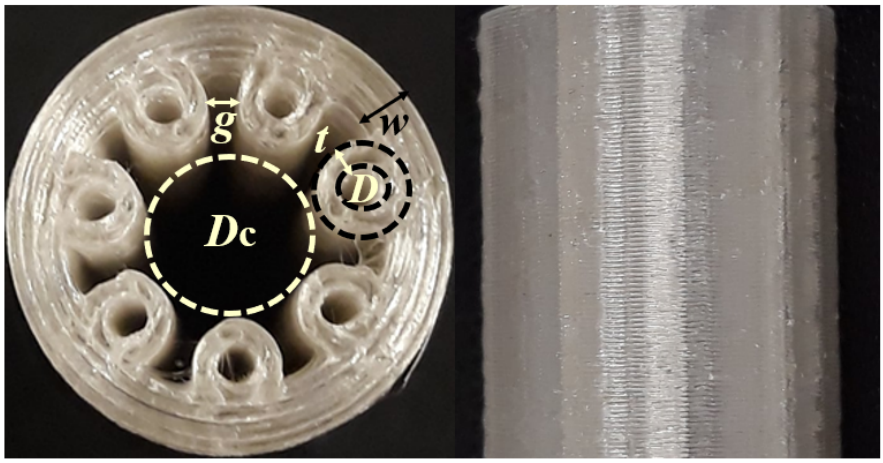

Figure 4.3. The FDM printed seven-tube HC-ARPCF. Top and side view of the 3D printed Zeonex based HC-ARPCF (from Left to right), Sultana *et al.* (2020c).

The 3D printed HC-ARPCF's top and side views is presented in Fig. 4.3. We use this fibre as a HC-ARPCF directly for experimental measurement. The cross section of the

fibre that used in our experiment is of $D_c = 5$ mm, $D = 1.55$ mm, $t = 0.45$ mm, $w = 1.25$ mm, and $g = 0.811$ mm. In this chapter, we carry out the measurements directly on 3D printed fibre samples for the lengths of $L = 8$ mm, 20 mm, 30 mm, 40 mm, and 50 mm, due to the low resolution of employed 3D printer. The final stage of fibre drawing remains open for future study, to obtain the numerically optimized dimensions (described in Section 3.3 and 3.4). The deposition of heated liquid Zeonex may vary the tube thickness a little along its axial direction due to the fluid properties and movement of the nozzle creates unexpected tiny threads near the adjacent gaps and inside the tubes, which need to be cleaned.

4.2.4 3D printed material loss

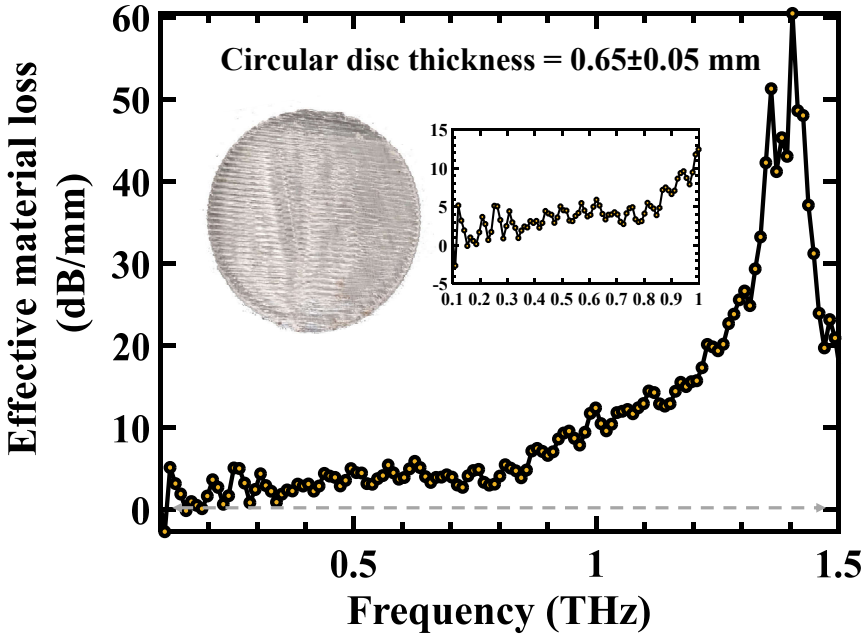

Figure 4.4. Effective material loss for printed Zeonex. Effective material loss measured on a circular disc with a thickness of 0.7 mm and a diameter of 24 mm in the 0.1–1.5 THz, Sultana *et al.* (2020c).

To measure the effective material loss of the Zeonex polymer, a circular disc with an uneven thickness of 0.65±0.05 mm and a diameter of 24 mm is printed, as shown at the inset of Fig. 4.4. Fig. 4.4 shows the measured effective material loss in the 0.1–1.5 THz range. The measured effective material loss of the printed Zeonex is about 5 dB/mm, in the 0.1–0.8 THz range, and this increases gradually to 26 dB/mm for 1.3 THz. The unpolished 3D printed solid surface, which is not fully transparent for terahertz transmission, increases the effective material loss as compared to the transparent Zeonex

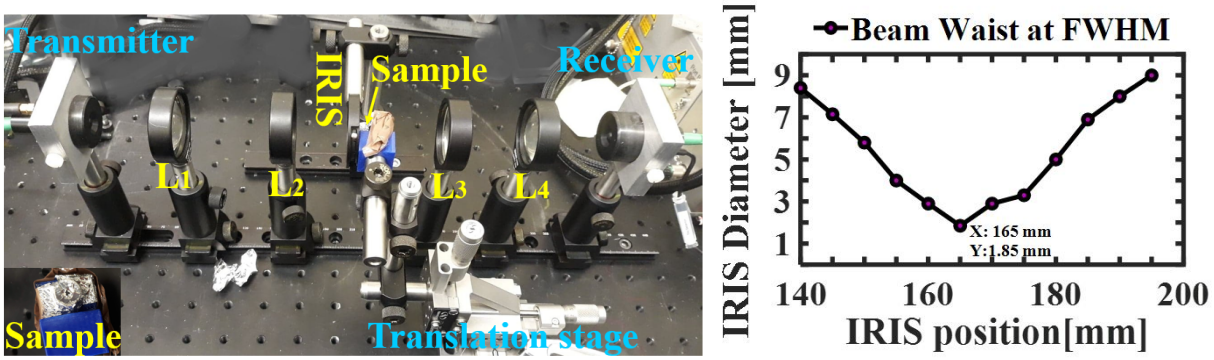

(a) (b)

Figure 4.5. Terahertz time-domain spectroscopy system. (a) Setup for the terahertz experiment: terahertz transmitter, L_1, L_2, Iris diaphragm, fibre under test, L_3, L_4, terahertz detector (from left to right in bottom). Terahertz time-domain spectrometer here: Menlo system (TERA K15 Terahertz Kit); (b) Beam diameter between L_2 and L_3, measured with iris diaphragm, Sultana *et al.* (2020c).

disc (Islam *et al.* 2020) due to the surface scattering loss arising from the coarseness of the printed disc. The measurement details are discussed in Section 4.4.

4.3 Experimental setup

A terahertz time-domain spectroscopy (THz-TDS) system with photoconductive antennas as transmitter and receiver, and four plano-convex, aspheric lenses made of TPX polymer (System n.d.a, System n.d.b) are used for fibre characterization. We perform the transmission measurements of Zeonex based seven-tube HC-ARPCF using a commercial fibre coupled THz-TDS system (Menlo) with an effective spectral range of 0.1–2.0 THz. The diagram for terahertz fibre transmission using Menlo system is shown in Fig. 4.5(a). The THz-TDS system consists of three main parts: (1) optical source (2) delay line controller and (3) terahertz wave path. The laser beam generated from "T-light" (Optical Source) is split into a strong pump beam for the generation of the terahertz radiation and a weak probe beam for the detection. The terahertz pulse, generated from the LT-GaAs-based photoconductive antenna, is collimated by an on-axis plano-convex lens (L_1) to produce a nearly parallel beam with Gaussian FWHM of 25 mm. Another plano-convex lens (L_4) is used to focus the collimated terahertz beam on the terahertz detector antenna.

The detector antenna is gated by the optical probe beam, and the current, which is proportional to the incident terahertz field, is recorded using a lock-in amplifier as a function of the temporal delay between the pump and probe beams. An acousto-optic modulator allows the pump beam to be modulated at a frequency of 10 kHz, where the system has the highest signal-to-noise ratio. Prior to the HC-ARPCF loss measurement another pair of on-axis plano-concave lenses (L_2 and L_3) with the focal length of 50 mm are placed between the collimated terahertz beam to couple the beam waist into the hollow core of HC-ARPCF, which is important for fundamental mode matching. The plano-convex lenses (L_2 and L_3) focus the beam to a 1.85 mm waist verified by an iris diaphragm, shown in Fig. 4.5(b). These two plano-convex lenses are separated by 100 mm, as the focal lengths are 50 mm. The spectrometer is set to operate in rapid scan mode, with a lock-in time constant of 300 μs for observing alignment and signal properties during the measurement set-up. Then a lock-in time constant of the 10 ms is selected for collecting the data for later analysis. Fig. 4.5(a) indicates the experimental alignment of terahertz wave path. There are two types of reference signals: (i) no fibre and (ii) with shortest length of fibre. The 'no fibre' reference signal is measured without the HC-ARPCF while the sample fibre scan is taken after inserting the fibre sample between the pair of plano-convex lenses (L_2 and L_3) as shown in Fig. 4.5(a). Here, the iris diaphragm is used to mark the position of beam waist and block any unwanted signal passing through the fibre core.

The transmitted terahertz signal from HC-ARPCF is again collected from another plano-convex lens (L_4) and coupled into a photoconductive detector for terahertz wave measurement. Both the emitter and detector is pumped with T-light fibre coupled femtosecond fibre laser. The printed fibre is mounted on an automated xyz-translation stage for mapping the fibre modes. Finally, data acquisition is carried out with "K15 TeraScan Mark II 1.31" software from Menlo. This software provides the temporal and power spectra of the signals for further signal characterization.

4.4 Experimental results: Effect of fibre length

The experiment is performed with $t = 0.45$ mm as *Flashforge Creator Pro* can print with a minimum vertical feature size of 0.4 mm. A more optimized fibre (described in Section 3.3 and 3.4) can be prepared by drawing the printed fibre (Talataisong *et al.* 2018,

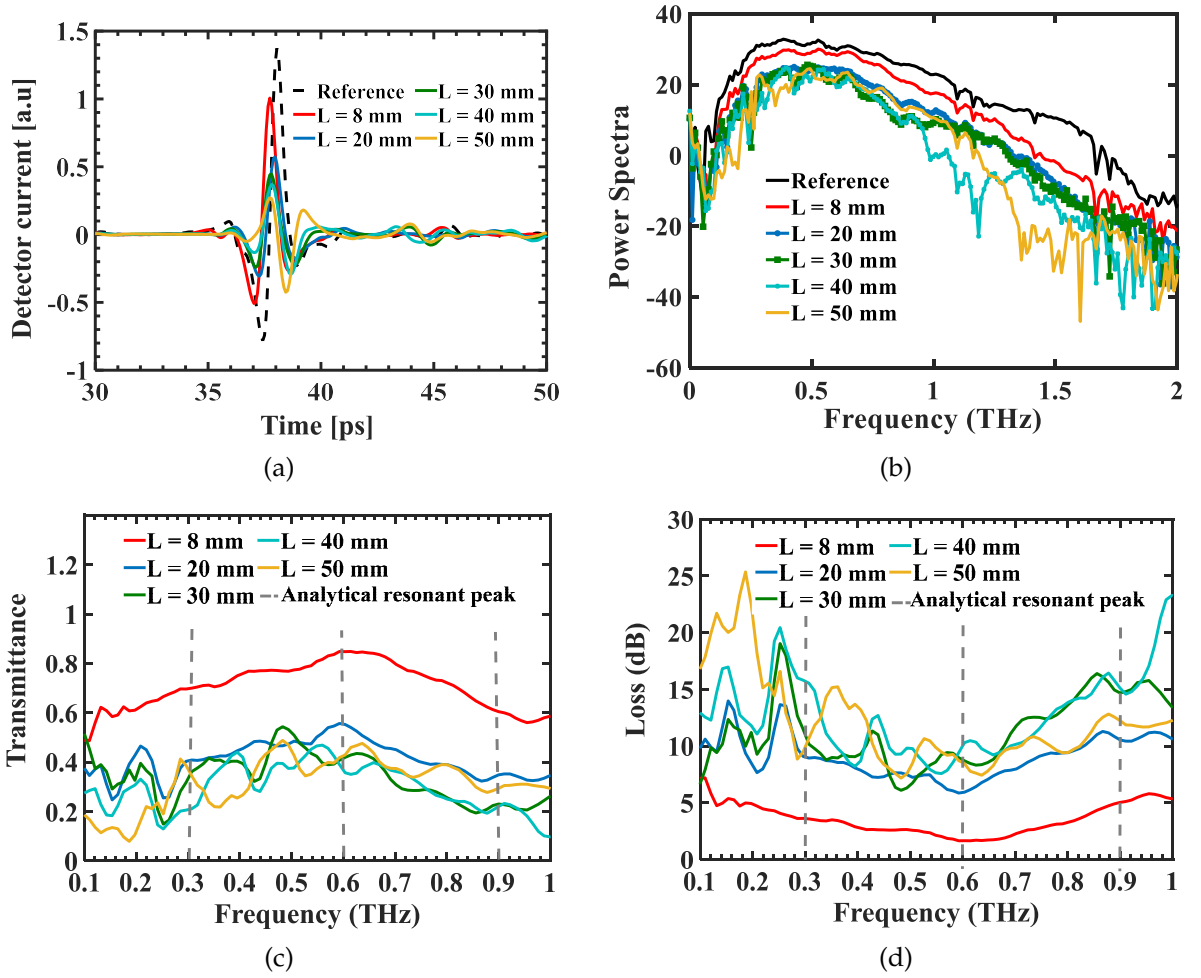

Figure 4.6. Temporal and FFT signal through a printed fibre. (a) Temporal signals as measured by the lock in amplifier for the reference pulse and sample pulses of the seven tube HC-ARPCF for the length of $L = 8$ mm, 20 mm, 30 mm, 40 mm, and 50 mm; (b) Corresponding power spectra; (c) Measured transmittance of terahertz HC-ARPCF; (d) Loss measurement of terahertz HC-ARPCF. Vertical grid lines in (c) and (d) denote the theoretical resonance frequencies. All the samples are printed with same capillary thickness and gap between two capillaries of $t = 0.45$ mm and $g = 0.811$ mm, Sultana *et al.* (2020c).

Talataisong *et al.* 2019). Drawing the fibre to obtain proposed numerical dimensions can be our future work for the application of analyte sensing.

The 3D printed seven tube HC-ARPCF and corresponding resulting waveforms are shown in Fig. 4.3 and Fig. 4.6 respectively. To characterize the fibre transmission and coupling loss individually, loss measurement is performed using a cutback technique. The cutback technique involves comparing the transmitted power through a longer piece of fibre to the power transmitted through a shorter piece of the fibre. Without changing the input end arrangement of the fibre, the output end of the fibre need to be cleaved to acheive a shorter length and measure the transmitted power from the output end. The procedure can be repeated for different lengths. Since the fibre is cut from the output end, this method is called the cut-back method. However, it is not possible to cut the printed fibre length during the measurement without changing the coupling conditions as the air holes may collapse during the cutting and need a very high pressure air purger to remove the obstacles. To avoid this difficulty, we print different lengths (L = 8, 20, 30, 40 and 50 mm) of fibres with the same cross-section. For guiding the light through the core only, we wrap the individual fibre with aluminum foil with a hole diameter of approximately 5 mm to the input and output waveguide end, shown at the left bottom in Fig. 4.5(a). We place each length of fibre consecutively in the sample holder, and compare and analyse the effect of length on the terahertz transmission spectrum. Therefore, we cannot assure the coupling loss is constant. Humidity in the air can create water lines in the signal, which decreases terahertz transmission (Taherkhani *et al.* 2019). To study the individual fibre performance accurately, measurements are made in a nitrogen environment with negligible humidity. Also, five scans are performed for each fibre in situ and then averaged.

Fig. 4.6(a)plots the temporal signal of the reference scan and sample scans. The peak of the detector current for reference signal at maximum ranges from -0.78 to +1.37 a.u. It decreases gradually from +1.0, +0.58, +0.45, +0.37 and +0.27 a.u with increasing the terahertz fibre lengths of L = 8 mm, 20 mm, 30 mm, 40 mm and 50 mm respectively. The propagation loss introduced by each length of terahertz fibre results in a reduction of peak amplitude of detector current. As seen in Fig. 4.6(a), the reference signal peak leads by 0.32 ps with respect to the signals through the hollow core fibres. Any small change in alignment can make a difference of arrival time of the transmitted signal

through the hollow core. Here, the arrival time difference can arise as we move L_3 toward L_4 to place the fibre end at the probable focal spot of L_4. Also, the time difference may arise from the unexpected webs at the gap between the two adjacent tubes introduced by the FDM printing. This small variation of time delay confirms that most of the terahertz signal passes through the air core with proper alignment.

The power spectra calculated by fast Fourier transform (FFT) determines the transmission properties of the fibre in Fig. 4.6(b). The Fourier transform of the recorded detector current of the reference (without the sample) and that through the fibres are used to measure the power spectra for the fibres in each case. We found that there are sudden peaks in samples for $L = 20$ mm, 30 mm, 40 mm and 50 mm correspond to the $L = 8$ mm. The fibre of $L = 8$ mm carry the similar behaviour of reference signal due to the short fibre length and rarely showing the antiresonant characteristics. Therefore, it is important to have a longer fibre length in order to achieve the characteristics of the fibre and stable mode distribution.

The transmittance of the fibre measured is determined from the absolute ratio (sample and reference) of the complex modulus of the transformed data for different fibre lengths. The measurements on transmittance are taken by comparing the transmitted terahertz waveforms with and without the sample in Fig. 4.6(c) at the terahertz beam path. The $L = 8$ mm fibre is too short to be called a fibre. A fibre length of 8 mm is not sufficient to draw any conclusions as it is far too short to achieve a stable mode distribution or eliminate others spurious effects. To be clear, the lens focal length is 50 mm maximum. The distance between L_3 toward L_4 is not large enough to place a fibre of $L = 50$ mm while maintaining the proper coupling at the end facet at $L = 50$ mm. Therefore, leaving out the experimental results for $L = 50$ mm may alleviate the coupling problem. However, avoiding $L = 8$ and 50 mm also would mean not giving the full picture regarding the transmission. Fig. 4.7(d) shows the measured loss. This can be seen clearly in Figs. 4.6(c) + 4.7(d) where $L = 8$ mm seems to be an outlier, when compared to all the other lengths. The $L = 50$ mm fibre is used with a different alignment. By looking at the results of the 3 remaining fibres, there is hardly any recognizable trend.

To assist rigor in the data processing, we attempt to separate the fibre transmission loss from the coupling loss as a combination of different fibre lengths in Fig. 4.7. In

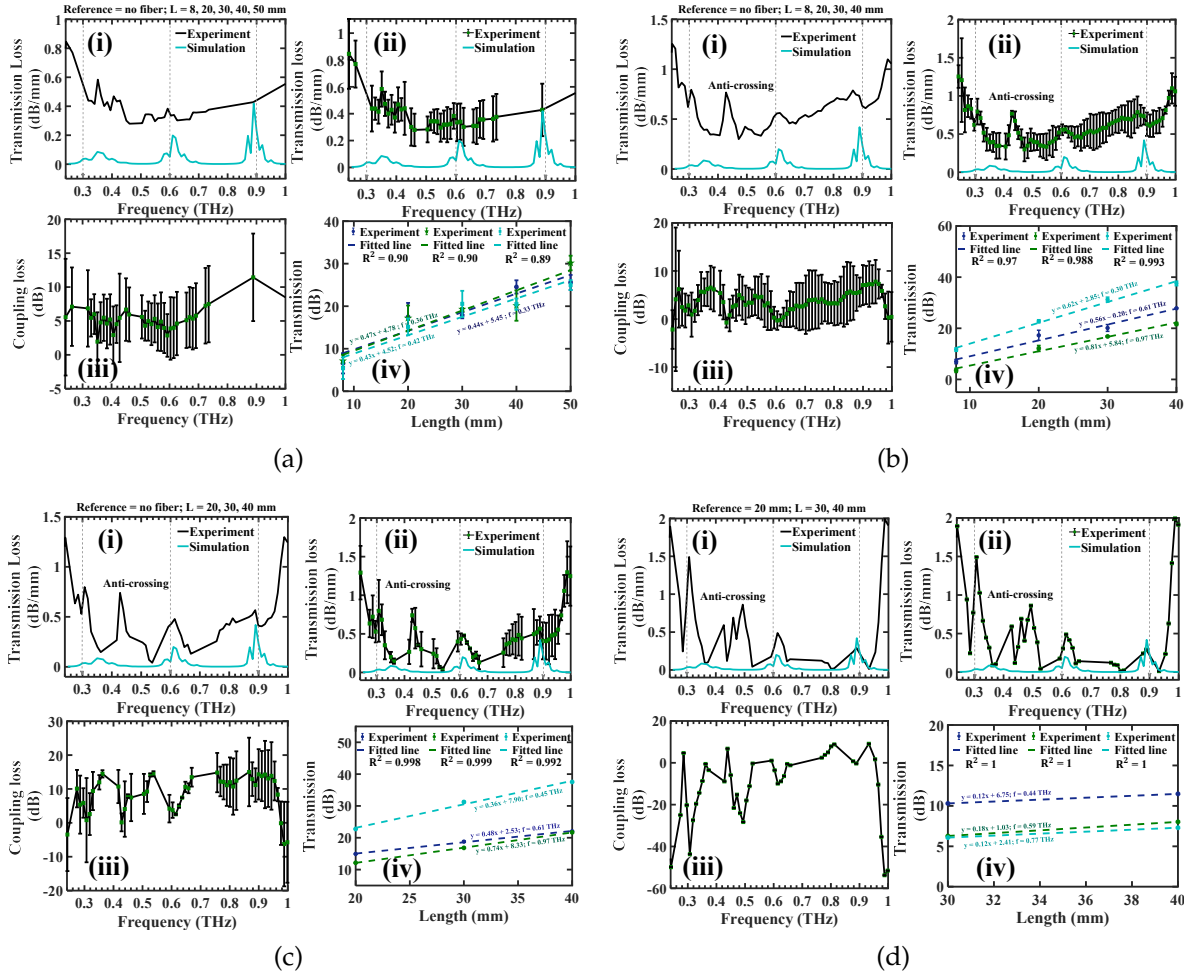

Figure 4.7. Transmission and coupling loss in 3D printed fibre. (a–d) (i) Frequency dependent experimental and simulated transmission loss; (a–d)(ii) Frequency dependent experimental and simulated transmission loss with their corresponding errors. Vertical grid lines in (i) and (ii) are the indication of the theoretical resonance frequencies of the seven tube HC-ARPCF for the different length combinations. (a–d)(iii) Frequency dependent measured coupling loss with corresponding errors; and (a–d)(iv) Length dependent transmissions through the HC-ARPCFs. The solid markers indicate the measured transmission while the dashed lines denote the best-fit lines at different frequencies. All the samples are printed with same capillary thickness and gap between two capillaries of $t = 0.45$ mm and $g = 0.811$ mm respectively, Sultana *et al.* (2020c).

addition, using the 'no fibre' measurements as a reference can assist with a mixture of coupling efficiency and fibre losses. The 8 mm fibre length is far too short as stated above. The use of a 20 mm long section as a reference and comparing this with other fibre lengths, thereby may eliminate the coupling loss. The combination of cases that have been chosen are:

(a) $L = 8$, 20, 30, 40 and 50 mm; reference = no fibre,

(b) $L = 8$, 20, 30 and 40 mm; reference = no fibre,

(c) $L = 20$, 30 and 40 mm; reference = no fibre and

(d) $L = 30$ and 40 mm; reference = 20 mm.

In all cases, the fibres are short due to the experimental setup limitation where we were able to measure fibres no longer than 50 mm. To obtain a stable mode distribution inside the fibre considering the excitation of HOMs, it is necessary to have a longer fibre so that the mode distribution can stabilize.

From the transmission loss spectra in Fig. 4.7, (i) we can observe that case (a) does not provide the resonance properties at higher frequency. The high and low loss regions can easily be obtained in cases (b-d). The analytical resonance peaks for $t = 0.45$ mm appear at $\sim$0.30 THz, $\sim$0.60 THz, and $\sim$0.90 THz, using Equation (1) and the vertical grid lines are the indication of the analytical resonant properties in fibre. The measured resonance peaks for Fig. 4.7(b-d), (i) appear at 0.31 THz, 0.61 THz, and 0.99 THz, which are almost similar to the analytical results. Moreover, the simulation of the scaled-up fibre is compared here with the measured transmission loss in Fig. 4.7(a-d), (i). There are some additional losses such as water absorption loss and scattering loss, in addition to the transmission loss, which are introduced during experiments, whilst neglected during simulations. The low loss of 0.3 dB/mm at 0.47 THz is obtained with case (b). The lowest transmission loss of 0.04 dB/mm is obtained from cases (c-d) around 0.53 THz. Fig. 4.7(c-d), (i) shows a similar trend between simulated and measured transmission loss. We hypothesize that the anti-crossing between fundamental and HOMs may cause high loss peak in the low loss regions and they are more pronounced at lower frequency around 0.44 THz.

Fibre type	**Material printing**	**D_c, t and OD (mm)**	**THz**	**Trans. loss**
Kagome hollow core (Yang *et al.* 2016)	VeroWhitePlus (SLA)	D_c = 9; t = 0.35	0.2–1.0	0.02 cm^{-1} (average)
Pentagram hollow core (Yang *et al.* 2019)	Photosensitive resin (SLA)	t = 1; OD = 21	0.5–2.0	0.025 cm^{-1} (1.94 THz)
6-tube Half-elliptical (Van Putten *et al.* 2018)	Polycarbonate (FDM)	D_c = 6, 6, 10; t = 0.6, 0.6, 1.2	0.15–0.6	–
10-tube Elliptical (Cruz *et al.* 2017)	ABS polymer (SLA, FDM)	t = 0.4, 0.2; OD = 8.3	–	–
8-tube Cone shaped (Cruz *et al.* 2015)	ABS polymer (SLA)	D_c = 8.4; t = 0.54; OD = 25	0.1–0.5	–
7-tube Circular (Sultana *et al.* 2020c)	Zeonex (FDM)	D_c = 5; t = 0.45; OD = 11.8	0.24–1.0	0.04 dB/mm (0.53 THz)

Table 4.1. 3D printed HC-ARPCF. Characteristics of terahertz HC-ARPCF based on 3D printing techniques, Sultana *et al.* (2020c).

To quantitatively assess the data, we use the linear coefficient errors for transmission and coupling loss based on using the coefficient of determination (R^2) in Fig. 4.7(a-d) (ii and iii). We plot the coupling and transmission loss when R^2 is higher than 0.6 to obtain reliable data. It is apparent from Fig. 4.7(a-d) (iii) that the coupling losses vary for different length combinations as the fibres are independent during the measurement. Therefore, it is difficult obtaining constant coupling loss as it ranges from -53 dB to 15 dB from sample to sample, in the 0.3 to 1.0 THz. The differences in coupling losses come from the focal spot size mismatch between the fibre front-end facets and adjacent lens due to the consecutive placement of fibres. However, with the help of xyz-translation stages, the radial and lateral displacement has been tried to mitigate. The linear curve fitting over the experimental data in Fig. 4.7(a-d) (iv) for a few frequencies differentiate the good from poor data. Note that some of the non-idealities in the experimental results are obviously due to the surface roughness of the fibre produced during 3D printing.

Table B.1 shows in detail the characteristics comparison of the proposed HC-ARPCFs and investigates the variation in optical performances with prior established results. On the basis of fabrication feasibility, small core size, broad transmission window, and low transmission loss the obtained results are comparable with the prior results.

4.5 Discussion

The experimental validation of the HC-ARPCF is carried out using THz-TDS where five different fibre lengths and considered to achieve the antiresonant properties. It is found that printed fibres with different fibre length combinations show improved antiresonant effects and the analytical resonance frequencies are ideally matched with the numerical analysis of scaled-up fibre. Note that, there are imperfections in the obtained results that are due to the surface roughness in fibre fabrication. The simplicity in fibre design and appropriate optical properties of the fibre makes it a suitable candidate for short distance terahertz transmission and further can be used for refractometric sensing.

In the following chapter, the effect of 3D printing on the surface roughness, transparency and thickness variation is discussed. The discussion is followed by two different 3D printing method for various optimized HC-ARPCF design in the terahertz regime. The performance analysis of all the fibres are carried out and fabricated a simplified fibre that can be used for further refractometric sensing analysis.

Chapter 5

SLA and FDM printed fibres: Simulation, fabrication, and experiment

RESEARCH on fibres operating in the terahertz frequency range is rapidly growing with numerous potential applications. However, designing a terahertz fibre with controllable and desirable transmission characteristics is a challenging problem due to the complex cladding structure. We present a hollow-core antiresonant fibre (HC-ARPCF) patterned with a set of simple antiresonant cladding tubes exhibiting extraordinary control of terahertz transmission. With variations in the cladding-tube number and strut thickness for fixed adjacent tube-gap, we report a controllable cladding field that controls the low and high loss spectra, corresponding bandwidths, electric mode field, and mode interference in the core. Furthermore, we present two different 3D printing approaches for fabricating the HC-ARPCF with appropriate dimensions and compare printing accuracy, surface quality, together with the corresponding controllable transmission properties due to the imperfections in the tube boundaries. This study has broad interest and direct relevance to the material science, optics and photonics, and the manufacturing industry. Since the hollow core is bounded with a set of antiresonant cladding tubes, the printed fibres successfully maintain low loss and reflection properties across the 0.4–1.0 THz frequency range. The experimental results confirm the simulation and analytical results for transmission and extinction.

5.1 Introduction

With the advantage of anomalous dispersion, high core power fraction, low loss transmission, broad bandwidth, and simple geometry, HC-ARPCFs opened up the possibility of supercontinuum generation driven by gas-filled HC-ARPCF (Sollapur *et al.* 2017, Adamu *et al.* 2020), high power beam delivery (Michieletto *et al.* 2016), bio-molecule sensing (Giovanardi *et al.* 2019), liquid-based sensing (Nissen *et al.* 2018), and gas sensing (Nikodem *et al.* 2019) in the optical regime.

Terahertz applications based on HC-ARPCF are still limited in terms of signal transmission (Van Putten *et al.* 2018, Cruz *et al.* 2015, Setti *et al.* 2013, Sultana *et al.* 2020c), spectroscopic studies (Lu and Argyros 2014) and sensing (Ankan *et al.* 2020, Sultana *et al.* 2020c) due to the challenging fabrication procedure. Thus, reliable additive manufacture of these waveguides is a valuable new contribution. Fused Decomposition Modelling (FDM) and the Stereolithography Apparatus (SLA) are very well-known 3D techniques in terahertz. Fabrication of optical terahertz devices via 3D printing is cost effective and ideal for rapid prototyping. However, because of theoretical and experimental performance inconsistencies, 3D printing has shortcomings for widespread adoption in terahertz systems. No studies have compared these techniques and the corresponding impact on terahertz performance.

5.1.1 Objective and framework

For the first time we consider the thickness variation, roughness and transparency of the printed object, quantify the thickness variation as a function of antiresonant tube number for a constant adjacent gap, and measure the performance based on the printing method, thickness variation and antiresonant tube number. Also, for the first time we study printing parameters for Zeonex, including nozzle temperature, and extrusion velocity and investigate their impact on optical performance in the terahertz regime. Our goal is to develop low-loss, low-cost and versatile terahertz fibres, in particular for scientific and commercial applications that can be easily fabricated via 3D printing technology.

With a constant cladding gap, we analyze the transmission properties as a function of material absorption coefficient (α_{mat}) in Subsection 5.3.3, antiresonant tube sector angle in Subsection 5.3.4, and antiresonant tube strut thickness in Subsection 5.3.5. The purpose of these investigations is to provide a deeper understanding of the guiding mechanism for HC-ARPCF, evaluation of single-mode behaviour, and reflection capabilities of the cladding strut. Furthermore, we consider a five, six, and seven-tube HC-ARPCF to find the optimized transmission properties as a function of the antiresonant tube number in Subsection 5.3.6.

To explore the findings in practice, we fabricate the fibres with two well-known 3D printing techniques, using two different materials in Subsection 5.4.1. The reasons for using two different fibre printing methods is to compare their printing quality and accuracy (Subsection 5.4.2), and transmission performance with a constant gap for different strut wall thickness (Subsection 5.5.1–5.5.2) and cladding-tube numbers (Subsection 5.5.3). Terahertz fibres have such large dimensions that they can be printed directly without additional expensive and complex drawing procedures (Sultana *et al.* 2020c). Note that bending characterization cannot be measured due to limited ability to bend the fibres as a result of the larger outer diameter and short length of the printed fibres.

5.2 Material and geometry

Zeonex offers low material loss of 0.184 cm^{-1}, and carries the required thermal and chemical stability (Islam *et al.* 2019, Islam *et al.* 2020) in the terahertz band. Zeonex filaments are made in-house with a *Filabot EX2 Filament Extruder*, discussed by Sultana *et al.* (2020c) and the filament is compatible with the Fused Decomposition Method (FDM) for 3D fibre printing. For the first time we use Zeonex filaments for FDM printing and carry out optimization of the printing parameters according to the material properties (Sultana *et al.* 2020c). A different 3D printing method, the Stereolithography Apparatus (SLA) technique, uses UV-resin (Li *et al.* 2017b) rather than Zeonex. The material loss for UV-resin is 16 cm^{-1} (Islam *et al.* 2019, Islam *et al.* 2020), which is quite high. However, we compare their terahertz transmission properties in a HC-ARPCF as there is no material in the core. We characterize the fibre properties with two different materials and printing mechanisms. The real parts of the complex refractive indices are 1.529 and 1.69 for Zeonex and UV-resin, respectively (Islam *et al.* 2019, Islam *et al.* 2020).

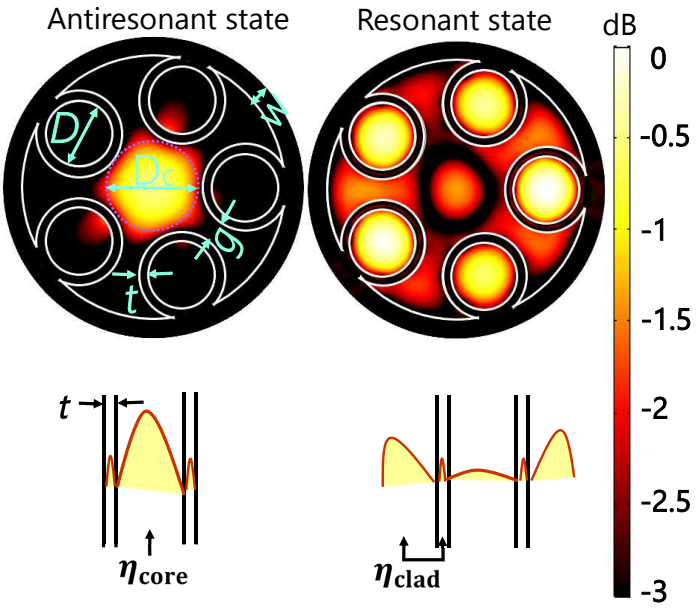

Figure 5.1. Five-tube dielectric HC-ARPCF. Logarithmic mode field intensity and schematic of ARROW guiding principle based on the antiresonant and resonant state of HC-ARPCF.

A single hollow-core with diameter $D_c = 5$ mm is surrounded by a layer of five-antiresonant tubes, which act a cladding layer as shown in Figure 5.1. The antiresonant tube diameter is D, strut thickness is t and the shortest adjacent tube gap is $g = 1.11$ mm. The antiresonant tubes are supported by a protective jacket of thickness $w = 1$ mm to ensure mechanical stability. The material regions are defined with w, and t, while the air regions are denoted by D_c, D, and g.

5.3 Simulation results with straight HC-ARPCF

5.3.1 Guidance in the HC-ARPCF

When $t = 0.5$ mm, and for $m = 1$ to 5, $f_{1...} = 0.26, 0.52, 0.78, 1.04, 1.3...$ THz and $f_{1...} = 0.22, 0.44, 0.766, 0.88, 1.1...$ THz for Zeonex and UV-resin fibres, respectively. The guidance mechanism of the HC-ARPCF (Debord *et al.* 2017), as well as the kagome fibre (Russell *et al.* 2014), can also be explained due to the inhibited coupling guidance (coupling between core and cladding mode is forbidden in guidance), where the cladding mode (LP_{clad01}) maintains a lower density of states (η_{eff}) than the fundamental core mode (LP_{01}). To analyze the inhibited guidance, fundamental core mode (LP_{01}), cladding mode (LP_{clad01}), and strut mode (LP_{strut}) are considered as a function

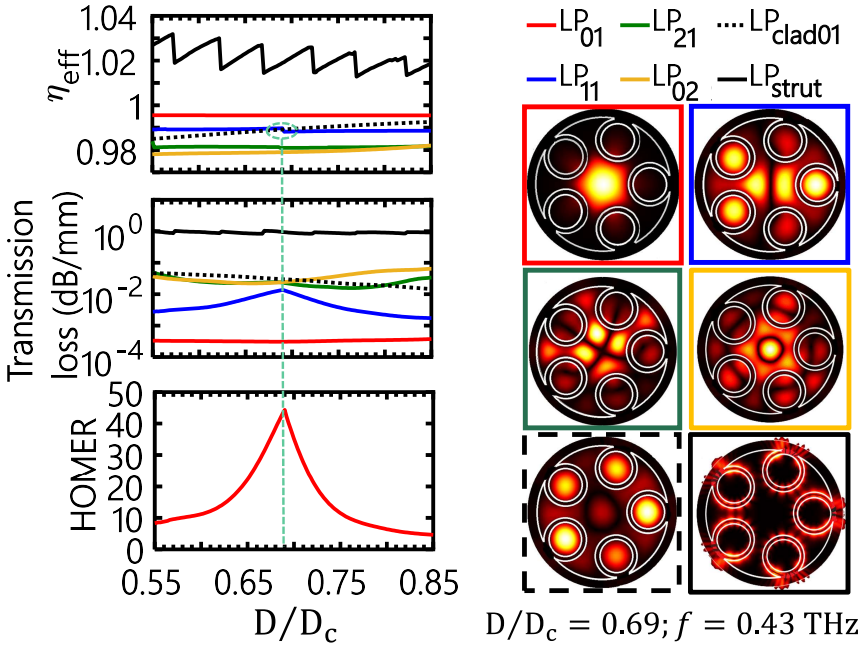

Figure 5.2. Principle of simulated inhibited guidance in HC-ARPCF. Simulated effect of changing the D on effective refractive index, transmission loss and higher-order mode suppression while the D_c is constant. Linear mode field profiles of the first three core guided modes are shown at the right-hand side for $D/D_c = 1.38/2$. The colour of the frame corresponds to the colour of the line of the plot. The proposed core diameter is $D_c = 5$ mm with antiresonant-tube thickness $t = 0.5$ mm, and adjacent tube gap $g = 1.11$ mm.

of D/D_c in Figure 5.2 with $D_c = 5$ mm. At a specific frequency $f = 0.43$ THz, an increase of D enhances the cladding refractive index ($\eta_{\text{clad01)}}$ and the increased η_{clad01} tends to match the constant core refractive index (η_{LP01}) due to the high density of $\text{LP}_{\text{clad01}}$ mode. Core-cladding phase matching is inhibited at a specific frequency for low loss transmission. Therefore, $\eta_{\text{LP01}} > \eta_{\text{clad01}}$ has been analyzed as a function of D/D_c in Figure 5.2. The separation of antiresonant tubes assists in inhibited coupling with proper optimization and eliminates the loss introduced from the adjacent connecting nodes. The modes of the fibre are hybrid and weakly coupled as shown in Figure 5.2, with a field parallel to the fibre. Therefore, the transverse field pattern evolves along the length of the fibre. There is no transverse asymmetry when we consider the length of the fibre.

5.3.2 Optimization of the antiresonant tube diameter

We have also considered higher order core modes (HOMs) named as LP_{11}, LP_{21}, LP_{02} to check how closely the fibre achieves single-modeness in Figure 5.2. The core LP_{11} mode phase match with the cladding LP_{clad01} mode (η_{LP11}=η_{clad01}) when at $D/D_c = 0.69$ making the fibre effectively single-mode. The LP_{11} mode has been chosen due to its lower transmission loss among other HOMs such as LP_{11}, LP_{21}, LP_{02}. The transmission loss takes into account both the confinement loss and the material loss (Vincetti *et al.* 2010). For the normalized value of at $D/D_c = 0.69$, transmission loss for the LP_{01} mode is about 1.55×10^{-4} dB/mm, while the highest loss of the LP_{11} mode is about 1.30×10^{-2} dB/mm. The higher-order mode extinction ratio (HOMER) defined as the degree of mode suppression for the proposed fibre is approximately 44 at $D/D_c = 0.69$. The HOMER is defined as the ratio of lowest HOM (i.e., LP_{11}) to the LP_{01}. HOMER for four sector angles. The proposed core diameter is $D_c = 5$ mm, inner antiresonant tube diameter $D = 3.45$ mm with antiresonant-tube thickness $t = 0.5$ mm, and adjacent tube gap $g = 1.11$ mm.

5.3.3 Imaginary refractive index of cladding material

The frequency-dependent imaginary refractive index of the dielectric cladding material, $\kappa(f)$ demonstrates the effect of fibre transmission loss for different modes. The $\kappa(f)$ can be expressed in terms of the material absorption coefficient (α_{mat}) as $\kappa(f) = \left(\frac{c}{4\pi f}\right)\alpha_{mat}$ (Vincetti 2009b, Islam *et al.* 2020). Figure 5.3 illustrates the dependence of $\kappa(f)$ on frequency for the LP_{01} mode with $\alpha_{mat} = 0.02$, 0.04, 0.08, 0.12, and 1.6 mm^{-1}. The changes in η_{clad} (solid and dashed curves separately are for Zeonex and UV-resin) cause the resonant frequency shift in η_{eff} as well as in transmission loss as shown in Figure 5.3, which can be analytically explained by Equation 3.2. At the same time, the $\kappa(f)$ has been used to simulate the $Im(\eta_{eff})$ for LP_{01} mode. We should note that the transmission losses in Figure 5.3 have been simulated with $\kappa(f) = 0$. The high value of α_{mat} not only suppresses the resonant properties but increases the transmission losses both for Zeonex and UV-resin as shown in Figure 5.3.

5.3.4 Impact of antiresonant tube shape on light propagation

To understand the light guidance with the assistance of antiresonant tubes, we have considered four different sector angles in antiresonant tubes as shown in Figure 5.4(a).

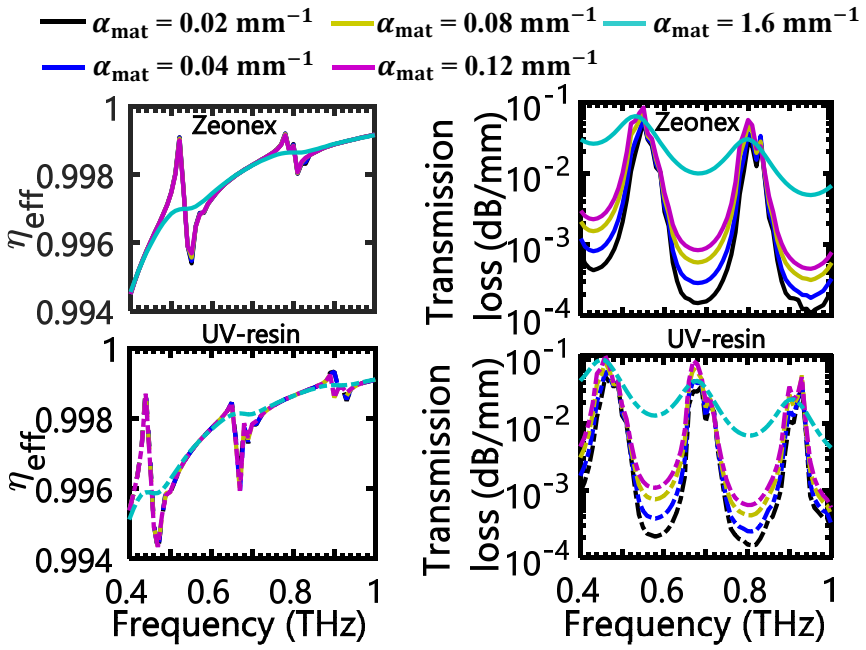

Figure 5.3. Material variations in simulated HC-ARPCF. Effective refractive index, and transmission loss for α_{mat} = 0.02, 0.04, 0.08, 0.12, and 1.6 mm^{-1} based on frequency-dependent imaginary refractive index. The solid and dashed curves indicate the Zeonex and UV-resin respectively. The proposed core diameter is D_c = 5 mm, inner antiresonant tube diameter D = 3.45 mm with antiresonant-tube thickness t = 0.5 mm, and adjacent tube gap g = 1.11 mm.

The grey colour is for material and the white colour defines the air region. Although, the sector angles, $\theta = 90°$, 180° and 270° are not practically possible to fabricate in this form, but they can initiate the idea of new cladding pattern for HC-ARPCF. Also, different states of the sector angles highlight the importance of well-formed antiresonant tube in light confinement. The parameters used in Figure 5.4(a) are the same except the sector angle. The fibre with $\theta = 360°$ is our proposed HC-ARPCF as shown in Figure 5.1. The yellow, green, purple, and blue solid lines represent the LP_{01} mode for $\theta = 90°$, 180°, 270°, and 360° respectively in Figure Figure 5.4(b). The investigation on effective refractive indices (η_{eff}) for the LP_{01} mode as a function of terahertz frequency show similar behaviour for different sector angles. Due to the incomplete quarter cladding pattern in the antiresonant tube at $\theta = 90°$, most of the light is trapped on the cladding strut, depending on the nature of light propagation and the LP_{01} mode offers higher transmission loss than the LP_{strut} mode. The part of the antiresonant tube around the core is similar and the same amount of the Zeonex material around the core has maintained the similarities in material absorption loss for different sector angles.

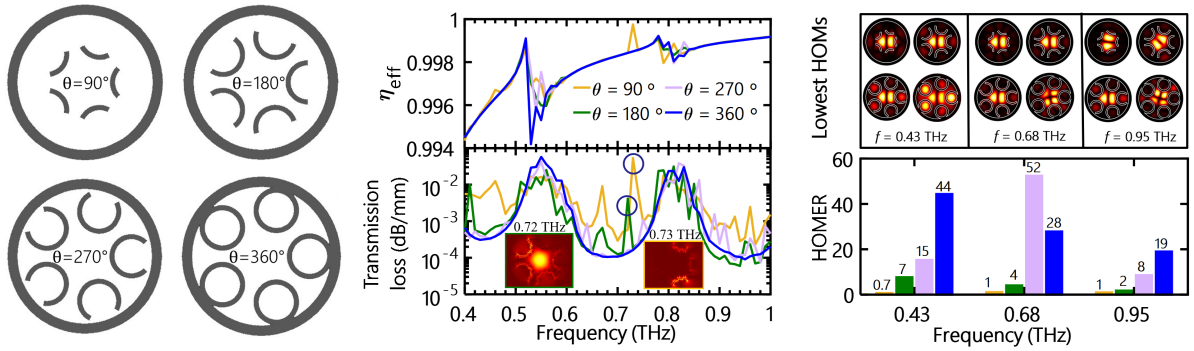

Figure 5.4. Antiresonant tube shape in simulation. (a) Cross-section of five-tubes HC-ARPCF with sector angles of $\theta = 90°$, 180°, 270°, and 360°; (b) The corresponding effective refractive indices (η_{eff}) and transmission losses of LP_{01} mode for different sector angles between the frequency ranges of 0.4–1 THz. (c) The corresponding higher-order mode extinction ratio (HOMER) at 0.43, 0.68, and 0.95 THz. The mode field patterns for the lowest HOMs are in the top to observe the single-mode guidance of HC-ARPCF with the variation of sector angles. Four different colour bars represent the HOMER for four sector angles. The proposed core diameter is $D_c = 5$ mm, inner antiresonant tube diameter $D = 3.45$ mm with antiresonant-tube thickness $t = 0.5$ mm, and adjacent tube gap $g = 1.11$ mm.

However, the tangents of light flow at $\theta = 90°$, 180° and 270° spreading around the supporting cladding, w, and create undesired high loss peak in material and confinement loss calculations. As a result, the transmission loss curves for $\theta = 90°$, 180° and 270° fluctuates widely. The $\theta = 360°$ offers a smooth curve shown in blue over the frequency 0.4–1 THz with multiple bandwidths. The hollow core with $\theta = 360°$ provides minimum transmission losses of 1.55×10^{-4} mm, 8.75×10^{-5} mm, and 1.06×10^{-4} mm at 0.43, 0.68, and 0.95 THz, respectively. The HOMERs for the $\theta = 90°$, 180°, 270°, and 360° have been calculated at 0.43, 0.68, and 0.95 THz, respectively in Figure 5.4(c). The corresponding lowest HOMs are included at the top. The HOMER = 0.7, 7, 15, and 44 at $f = 0.43$ THz for the $\theta = 90°$, 180°, 270°, and 360°, respectively.

5.3.5 Impact of strut thickness

By varying the t of antiresonant tubes, we calculate the transmission losses and HOMERs in the range between 0.4–1 THz, shown in Figure 5.5(a). The increase of $t = 0.45$, 0.50, ... 0.85 mm in Figure 5.5(a) decreases the $D = 3.55$, 3.45, ... 2.75 mm, respectively to

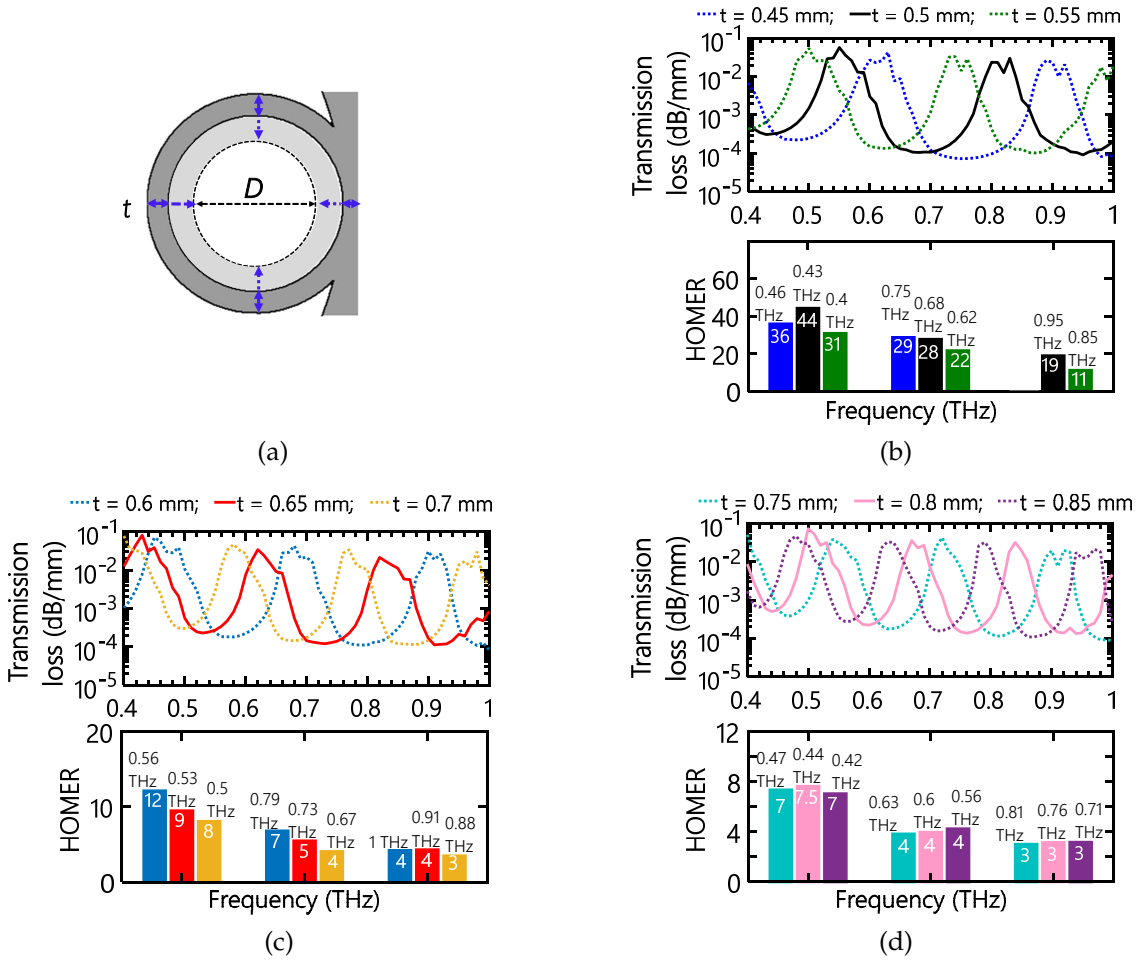

Figure 5.5. Strut thickness of simulated HC-ARPCF. (a) Axial image of antiresonant tube diameter, D as a function of t. The D decreases with the increase of t. Transmission loss and HOMER for (b) $t = 0.45$, 0.50 and 0.55 mm; (c) $t = 0.60$, 0.65 and 0.70 mm; (d) $t = 0.75$, 0.80 and 0.85 mm. The proposed core diameter is $D_c = 5$ mm, and adjacent tube gap $g = 1.11$ mm.

keep g constant. Also, depending on t, Equation 3.1 analytically calculates the high loss resonant frequency, while $m = 1, 2, ...$ defines the order number. The first observation from Figure 5.5(b)–5.5(d) is that the increase of t slightly narrows the transmission bandwidths. Secondly, as most of the light propagates through the hollow core, the transmission losses increase slightly with t. Thirdly, the HOMERs decrease gradually with the increase of t. The increase of t decreases D, therefore, η_{clad01} decreases while η_{HOM} remains constant. When $\eta_{\text{clad01}} < \eta_{\text{HOM}}$ the fibre is unable to make the coupling between the two modes. Hence, the mode of contamination increases gradually. The same concept is applied for $\eta_{\text{clad01}} > \eta_{\text{HOM}}$. The larger $\text{LP}_{\text{clad01}}$ from $D = 3.45$ mm

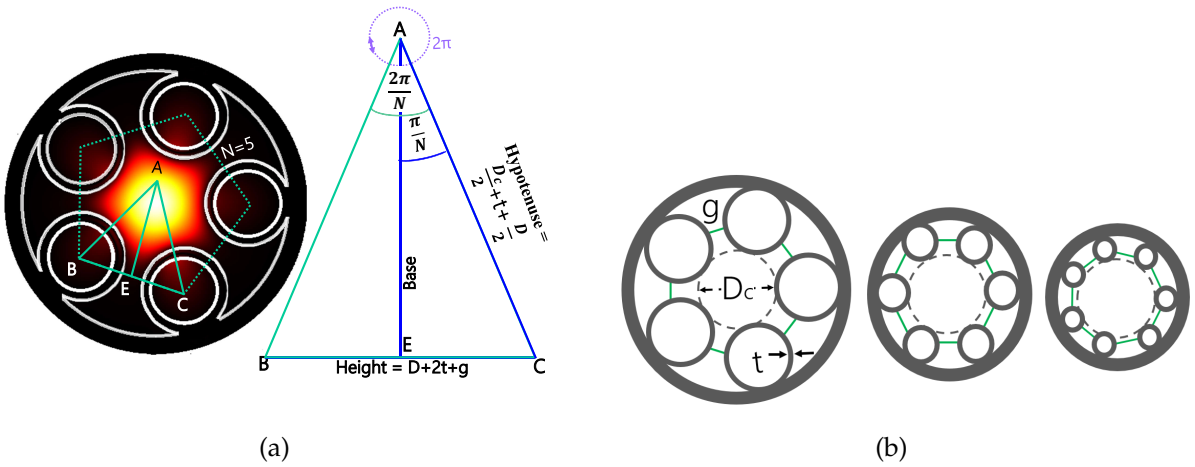

(a) (b)

Figure 5.6. The cladding-tube numbers with constant gap. (a) Trigonometrical representation of the HC-ARPCF as a function of antiresonant tube numbers with a constant g. (b) Axial images for five, six, and seven-tube HC-ARPCF with constant g. The variations in cladding-tube numbers create changes in the d, and outer fibre diameter. The simulations are performed for constant $D_c = 5$ mm, $t = 0.50$ mm, and $g = 1.11$ mm.

with $t = 0.45$ mm reduces the desired HOM coupling than the optimized $D = 3.45$ mm and makes the HOMER smaller than when $t = 0.5$ mm.

5.3.6 Impact of cladding-tube numbers with constant gap

To obtain the minimum adjacent gap, g, we consider the trigonometrical representation of five-tube HC-ARPCF as shown in Figure 5.6(a). The centre to centre distances $(D + 2t + g)$ in adjacent cladding tubes are equal and form a pentagon. The centre of the pentagon A is surrounded by five arms, $N = 5$. From the trigonometric identities, we know,

$$\begin{aligned} \mathrm{EC} &= \mathrm{AC}\sin(\frac{\pi}{N}); \\ \frac{D+2t+g}{2} &= (\frac{D_c}{2}+t+\frac{D}{2})\sin(\frac{\pi}{N}); \\ g &= (D_c+2t+D)\sin(\frac{\pi}{N}) - (D+2t) \end{aligned} \tag{5.1}$$

where $N = 5$ indicates the arms of the five-tube HC-ARPCF for $D_c = 5$ mm, $D = 1.38 \times \frac{D_c}{2}$ mm, and $t = 0.5$ mm. The D for six and seven-tube HC-ARPCFs are calculated from Equation (5.1) with $N = 6$, and 7, respectively and with constant $g = 1.1$ mm.

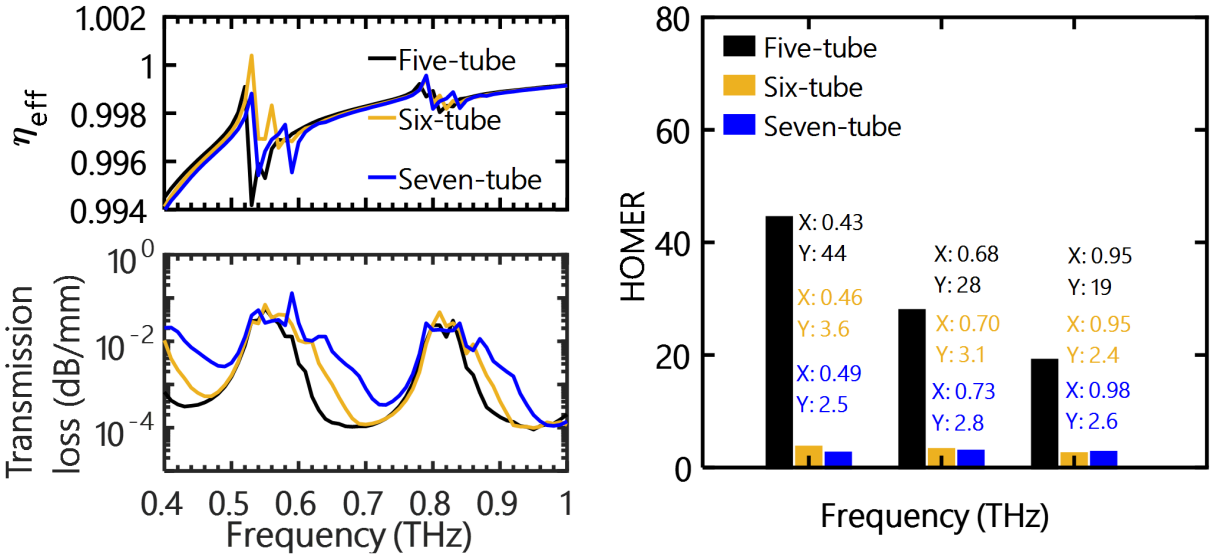

Figure 5.7. Simulated transmission loss and HOMER based on the cladding-tube numbers with constant gap. (a) The η_{eff} and transmission loss for five, six, and seven-tube HC-ARPCF with constant g. (b) The corresponding HOMERs. The simulations are performed for constant $D_c = 5$ mm, $t = 0.50$ mm, and $g = 1.11$ mm.

$$D[1-\sin(\frac{\pi}{N})] = (D_c+2t)\sin(\frac{\pi}{N}) - (g+2t);$$
$$D = \frac{(D_c+2t)\sin(\frac{\pi}{N}) - (g+2t)}{1-\sin(\frac{\pi}{N})}. \tag{5.2}$$

The increase in cladding-tube numbers decreases the cladding tube diameter as well as fibre outer diameter for constant g compared to the five-tube HC-ARPCF as shown in Figure 5.6(b). The distance between the core and cladding-tube diameter ($\frac{D_c}{2}+2t+D$) in five-tube HC-ARPCF are larger and confines more light in the core than six and seven-tube HC-ARPCFs. Therefore, there are differences in the η_{eff} and transmission losses for five, six, and seven-tube HC-ARPCFs, as illustrated in Figure 5.7(a). The five-tube performs better with lower loss and broader band transmission. Again, with five-tubes design each tube is bigger for a constant gap, that is advantageous from the fabrication perspective. Since g is constant, the leakage through the adjacent gap should be the same for all three designs. The increased cladding-tube numbers narrow the transmission regions and broaden the high loss area for six and seven-tube HC-ARPCF due to the leakage from the core with minimum cladding-tube distance. It should be noted that the high loss resonant frequencies can easily be tuned by varying

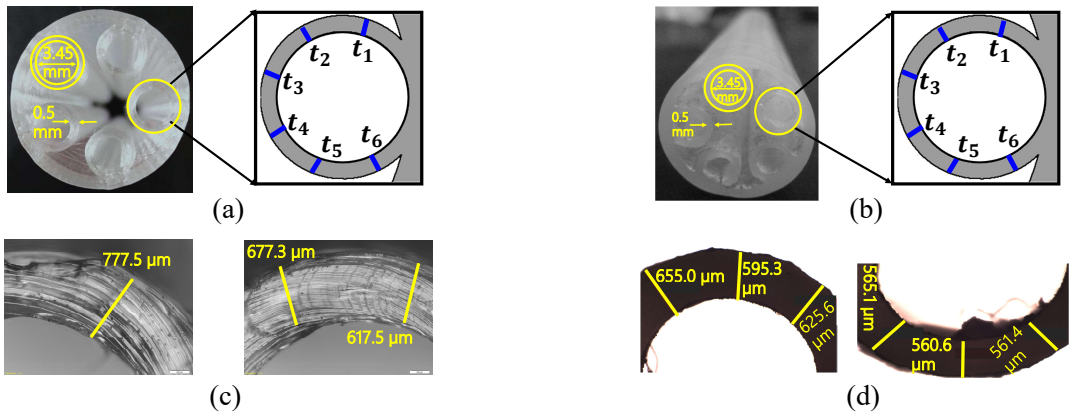

Figure 5.8. The FDM and SLA printed cross section. (a-b) Cross-section of FDM and SLA printed five-tube HC-ARPCF, and enlarged single antiresonant tube (nominal value is 0.50 mm); (c-d) Corresponding microscopic view for antiresonant tube thickness variation. The scale bar in the bottom right hand corner of each micrograph is 200 μm.

the cladding-tube number with constant g. The reduced cladding tube diameter in six and seven-tube HC-ARPCFs not only reduces the transmission performances, but also suppresses the coupling between cladding and HOM. As a result, maximum HOMER is less than 4 for six and seven-tube HC-ARPCFs as shown in Figure 5.7(b). From the above discussion with constant g, five-tube HC-ARPCF offers lower loss, broadens transmission bandwidth, and shows better single-mode behaviour than six and seven-tube designs. However, we should also be concerned about the poor inhibited coupling between core and cladding for resulting in poorer transmission when $N \leq 4$.

5.4 Fabrication method

5.4.1 Fabrication of HC-ARPCF using 3D printing

Additive printed layers are the fundamental principle of 3D printing technology. Based on the deposition technique, two of the most common 3D printing approaches, (i) the Fused Decomposition Modelling (FDM) technique (Van Putten *et al.* 2018, Sultana *et al.* 2020c, Talataisong *et al.* 2020) and (ii) the Stereolithography Apparatus (SLA) technique (Cruz *et al.* 2015, Ma *et al.* 2016) have been chosen in this section to demonstrate how efficiently and accurately the fibres can be printed.

5.4.2 Comparison between the FDM and SLA printed terahertz HC-ARPCF

The FDM printer is the Flashforge Creator Pro, model 1. The printing features and mechanism are discussed in (Sultana *et al.* 2020c) in detail. Figure 5.8(a) adds the axial image for FDM printed HC-ARPCF made of Zeonex. Our nominal five-tube HC-ARPCF has an antiresonant inner tube diameter $D = 3.45$ mm with minimum adjacent tube gap $g = 1.1$ mm, and strut thickness $t = 0.5$ mm for a core diameter $D_c = 5$ mm. Each antiresonant tube-wall is measured at six different locations assigned from t_1 to t_6 to accurately measure tube thickness. The two microscopic images in Figure 5.8(c) show the printed thicknesses of tube 1 which confirm variation in strut for each tube. With a nozzle diameter of 0.4 mm, the achievable average tube thickness is 0.73 ± 0.05 mm as shown in Table 5.1. The measured average tube thickness variation is 46% thicker than the nominal value (0.50 mm). The increase in thickness is due to die swell, a well-known phenomenon for polymers (Koopmans 1999).

During printing, the melted polymer flows out from the reservoir through the conical capillary die to free space. As the melted polymer is a viscoelastic liquid it stores the elastic energy while traveling through the conical capillary die. The transition from the confined flow to free-flow releases the stored elastic energy that swells the extruded polymer and creates the material density variation at the nozzle point (confined inner nozzle and free space nozzle outlet). Die swell depends on feed speed, viscosity as a function of temperature, force, stick-slip behaviour, non-Newtonian flow, etc. The free extrusion force and the extrudate diameter need to be adjusted against different working temperatures and extrusion velocity on a trial and error basis. For optimization, the changes in extrusion velocity with constant temperature or vice versa are controlled by software that is also connected to the extruder controller board. We note that the FDM printing method leaves a longitudinal groove corresponding to each deposited layer, which results in longitudinal corrugations in the fibre, as evident in Figure 5.9(a), and increases with the layer thickness. The staircase effect that happens due to the layer-by-layer deposition in the FDM method results in the corresponding grooves and causes the surface roughness (Wickramasinghe *et al.* 2020). The minimum layer height, finer wall thickness, cooling-heating cycle between two layers, print temperature, print speed, print acceleration and flow rate, higher layer deposition resolution, and skilled nozzle positioning repeatability can reduce the staircase effect and improve surface

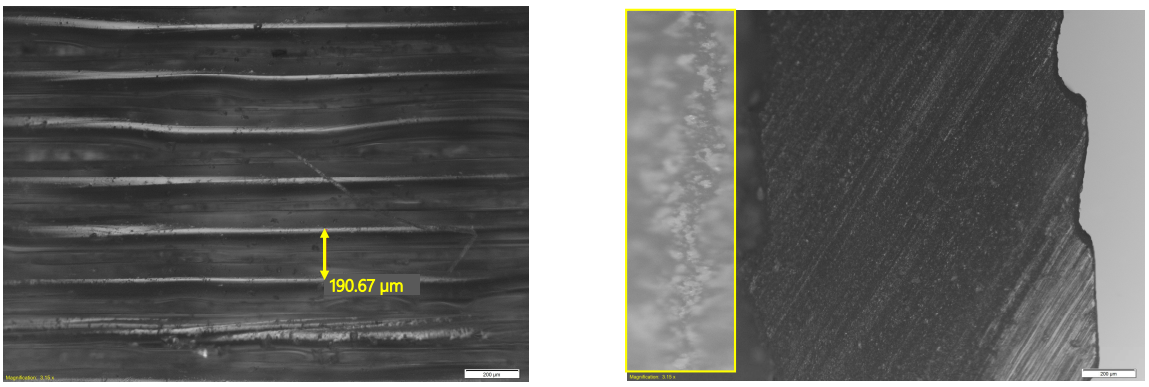

(a) (b)

Figure 5.9. The FDM and SLA printed surface. The microscopic outer surface profile of (a) FDM printed fibre shows 190.67 µm distance from layer to layer and (b) SLA printed fibre shows comparatively smother surface than the FDM. The yellow box shows a zoomed in region of the SLA printed outer surface. The scale bar in the bottom right hand corner of each micrograph is 200 μm and the zoom factor is 3.15.

quality. Also, post processes can further reduce the surface roughness remarkably (Wickramasinghe *et al.* 2020). The SLA printing method, on the other hand, is based on a UV laser that scans a liquid resin following the object design. The SLA printing method is carried out using the FormLabs, model 1+. The cured resin becomes solid and each vertical layer of the fibre is then formed. In the end, a simple cleaning procedure is realized with Isopropyl Alcohol to remove the uncured resin. Figure 5.8(b) adds the axial image for SLA printed HC-ARPCF made of UV-resin. Some damage to the antiresonant tube is noticeable. The cleaning agents tend to attack solidified shapes during manual removing the supporting material. Also, unoptimized thinner layers can give lower accuracy and damage some of the printed parts. The two microscopic images in Figure 5.8(d) show the printed thicknesses of tube 1 that confirms the variation in strut thickness for each tube. Post-cure exposure to Isopropyl Alcohol may cause some materials to change dimensions (swell or shrink). The achievable average tube thickness based on the SLA technique is 0.72 ± 0.11 mm as shown in Table B.1. The standard deviation (± 0.11) shows the large uncertainty of the measured average value (0.72 mm). The measured average tube thickness is $\sim 44\%$ thicker than the nominal value. The average adjacent gaps g in antiresonant tubes are 0.93 mm. Mechanical control for the galvanometer, mirrors, and build platform in SLA may diminish over time that refers to the precision in movement, and determines the accuracy in printing.

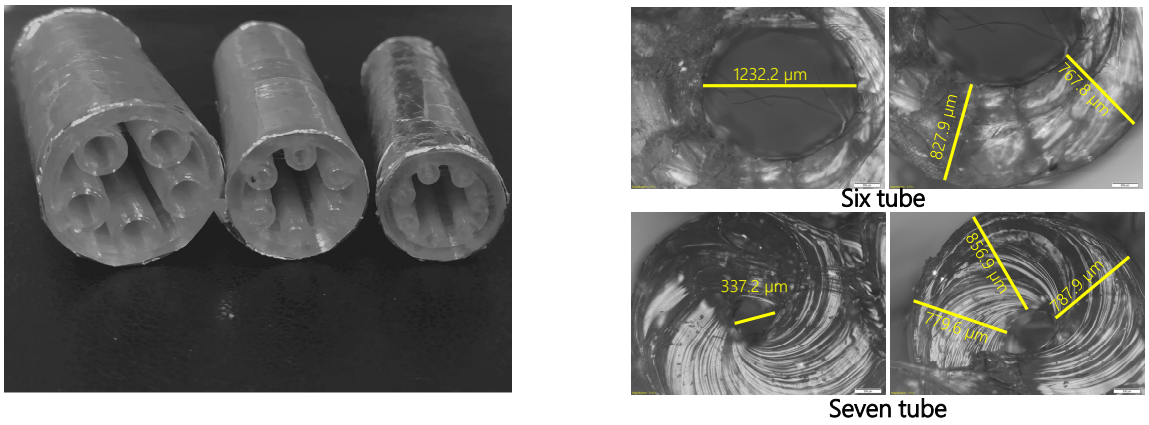

(a) (b)

Figure 5.10. The FDM based antiresonant tube and thickness variation. (a) Axial image for five, six, and seven-tube HC-ARPCF with constant g based on FDM. (b) Microscopic detail (D and t) of one tube from FDM printed six and seven-tube HC-ARPCF. The scale bar in the bottom right hand corner of each micrograph is 200 μm.

Figure 5.9(a) shows the outer surface of the fibre, which is comparatively smoother than the FDM method as the SLA is a nozzle-free method. However, overexposure to UV light commonly makes the clear resin print parts yellow and non-transparent. Exposure time is the UV light exposure duration for a single layer of the printed part that solidifies from the liquid resin. The SLA-printed parts have isotropic mechanical properties because a single UV laser pass does not fully solidify the liquid resin. To enhance the layer adhesion, further UV laser passes assist previously solidified layers to fuse them. The laser power intensity and spot diameter, scan speed, curing or the exposure time, printing resolution, layer thickness, and lift speed of the build plate have an impact on the surface quality and dimensional accuracy (Cho *et al.* 2005).

Next, we compare printing accuracy in FDM and SLA method based on the tube numbers. In this consideration, the increase in tube number causes a decrease in D, outer tube diameter, and fibre outer diameter, based on constant g. The FDM based five, six, and seven-tube HC-ARPCF maintains the average strut thicknesses $t = 0.73 \pm 0.05$ mm from the microscopic measurement as shown in Figure 5.10(a), while keeping $g = 1.1$–1.2 mm. The 46% extension in thickness has reduced $D = 1.79/1.23$ and $0.88/0.34$ mm (nominal/printed) for six and seven-tube HC-ARPCF in Figure 5.10(b). Slight ellipticity in seven-tube HC-ARPCF is noticeable due to the reduced tube dimensions. The

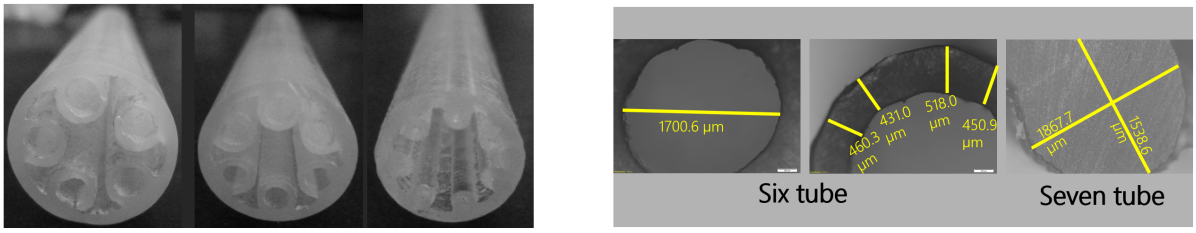

(a) (b)

Figure 5.11. The SLA based antiresonant tube and thickness variation. (a) Axial image for five, six, and seven-tube HC-ARPCF with constant g based on SLA. (b) Microscopic detail (D and t) of one tube from SLA printed six and seven-tube HC-ARPCF.

undesired corrugations and spikes are present throughout, including the inner antiresonant tubes due to the staircase effect that occurs due to the layer-by-layer deposition in the FDM method results.

Figure 5.11(a)–5.11(b) focuses on SLA printed five, six, and seven-tube HC-ARPCF. There is variation in average strut thicknesses from the microscopic measurements, for example, $t = 0.72 \pm 0.11$ mm for five-tube, $t = 0.49 \pm 0.07$ mm for six-tube, and $t = 0.90 \pm 0.04$ mm for seven-tube HC-ARPCF. From the microscopic measurement, it is observed that 20%–44% thickness for five-tube or 74%–88% thickness for seven-tube has extended from the nominal thickness. The SLA printing not only expands the thickness, but also 0.20%–19% shrinkage is achieved for six-tube from the nominal thickness. The nominal/printed $D = 1.79/1.7$ mm in the six-tube HC-ARPCF maintains the $g \sim 1.05$ mm. The reduced D in the SLA printed seven-tube HC-ARPCF is collapsed and the thickness extends to 88% during printing in Figure 5.11(b). The nominal/printed $D = 0.88/0$ mm maintaining the $g \sim 1.13$ mm.

5.5 Results: Terahertz performance and comparison with simulations

5.5.1 Terahertz transmission analysis in THz-TDS

We perform terahertz time-domain spectroscopy (THz-TDS) measurement to characterize the HC-ARPCFs manufactured by FDM and SLA, using TERA K15 from the Menlo system (Sultana *et al.* 2020c). The T-Light femto-second laser is a diode pumped fibre with a center wavelength at 1550 nm, a total average power $>$ 80 mW at a

100 MHz repetition rate, and a pulse length $<$ 90 fs (with a 1 m patch cord), used to drive the PCA receiver and transmitter antennae in the terahertz system. The terahertz bandwidth of the measurement system lies in 0.1–2 THz band. The terahertz detector currents $\rightarrow E(t)$ (sometimes known as temporal signals) are detected at terahertz receiver and recorded with a lock-in amplifier. Measurements are carried out with (i) the free space with focused lenses and (ii) the fibres of five different lengths, L = 20, 25, 30, 40, and 50 mm with same focused lenses in a dry-air environment. The results in Figure 5.12(a)–5.12(c) shows the terahertz detector current for nominal/printed t = 0.45/0.68, 0.50/0.73, 0.55/0.78 mm, respectively, where the D is decreased as t is increased. The detector currents as a function of time have not shifted significantly with different lengths of fibre compared to free space, as the beam spot size of 1.85 mm travels through a 5 mm hollow core. Also, with the increase of fibre lengths, detector currents decrease as additional propagation loss is introduced along the terahertz path. Fourier transform of the temporal detector current provides the transmission spectra, absorption coefficient, dispersion (Nielsen *et al.* 2009, Bao *et al.* 2015, Anthony *et al.* 2011a), effective refractive index (Anthony *et al.* 2011a, Yang *et al.* 2016), material loss (Nielsen *et al.* 2009, Bao *et al.* 2015, Islam *et al.* 2019, Islam *et al.* 2020), coupling loss (Bao *et al.* 2012), and transmission loss (Nielsen *et al.* 2009, Yang *et al.* 2016).

Tube number	t_1 **(mm)**	t_2 **(mm)**	t_3 **(mm)**	t_4 **(mm)**	t_5 **(mm)**	t_6 **(mm)**	**Avg. (mm)**
1	0.777	0.732	0.655	0.617	0.677	0.665	0.687
2	0.715	0.749	0.737	0.681	0.704	0.706	0.715
3	0.755	0.696	0.650	0.731	0.711	0.778	0.720
4	0.781	0.759	0.734	0.738	0.70	0.793	0.751
5	0.778	0.762	0.792	0.830	0.796	0.768	0.787
Avg. (mm)	0.761	0.739	0.713	0.719	0.717	0.742	0.732

Table 5.1. Antiresonant tube thickness: FDM based five-tube HC-ARPCF.

The cut back loss measurement is a well-known procedure in which the sample power for a long fibre is ratioed against the reference power from the shortest segment of the same fibre (Harrington *et al.* 2004). The complex transmission is

$$\mathrm{T}(\omega, L) = \frac{\mathrm{P}_{\mathrm{sample}}}{\mathrm{P}_{\mathrm{reference}}} \tag{5.3}$$

5.5.1 Terahertz transmission analysis in THz-TDS

Tube number	t_1 (mm)	t_2 (mm)	t_3 (mm)	t_4 (mm)	t_5 (mm)	t_6 (mm)	Avg. (mm)
1	0.665	0.726	0.592	0.550	0.620	0.491	0.607
2	0.811	0.885	0.574	0.573	0.522	0.754	0.687
3	0.883	0.914	0.857	0.653	0.576	0.547	0.738
4	0.798	0.832	0.873	0.632	0.789	0.619	0.757
5	0.800	0.825	0.909	0.713	0.780	0.874	0.817
Avg. (mm)	0.791	0.836	0.761	0.624	0.657	0.657	0.721

Table 5.2. Antiresonant tube thickness: SLA based five-tube HC-ARPCF.

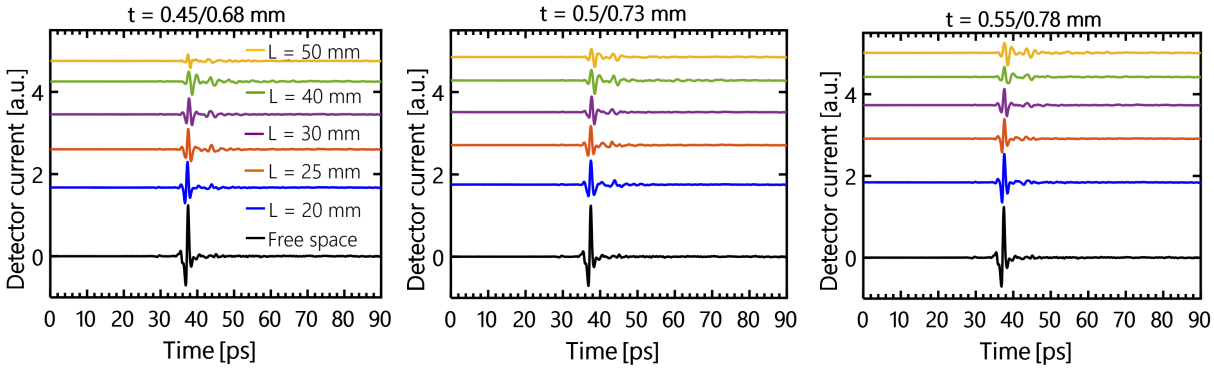

Figure 5.12. The FDM based measured terahertz time-domain signal. Measured terahertz time-domain signal over three different propagation lengths of five-tubes HC-ARPCF (D_c = 5 mm, L = 25, 30 and 40 mm) with the nominal/printed antiresonant tube thickness for (a) HC-ARPCF$_1$ ($t = 0.45/0.68$); (b) HC-ARPCF$_2$ ($t = 0.50/0.73$); and (c) HC-ARPCF$_3$ ($t = 0.55/0.78$) using 20 mm propagation length as a reference.

where, $P_{sample} = \int E^2(t)\, dt$ is the terahertz power signal as a function of the fibre length L. The $E(t)$ is the terahertz detector current as a function of delay time for individual fibre length. The reference power signal, $P_{reference}$ can be the free-space signal without fibre (Dupuis *et al.* 2010, Wu *et al.* 2011b, Anthony *et al.* 2011b, Bao *et al.* 2012, Anthony *et al.* 2013, Yudasari *et al.* 2014, Ma *et al.* 2016, Li *et al.* 2017b, Van Putten *et al.* 2018, Talataisong *et al.* 2020) or the shortest segment of fibre (Harrington *et al.* 2004, Bowden *et al.* 2008b, Bao *et al.* 2015, Yang *et al.* 2016, Wallis *et al.* 2016) at the coupling position.

The frequency dependent fibre loss is extracted from the complex transmission $\mathrm{T}(\omega, L)$ of each fibre length (Nielsen *et al.* 2009)

$$\alpha(\omega, L) = -\frac{10}{L}\log(\mathrm{T}), \mathrm{dB/mm} \tag{5.4}$$

where, L is in mm. The slope and intercept of the linear fit correspond to the frequency-dependent transmission loss (dB/mm) and coupling loss (dB), respectively. In this way, the coupling loss (not shown in this manuscript) is separated from the measured transmission loss.

In this chapter, a similar approach of the cut back method uses different length segments of fibre that provide an individual measurement of the transmission loss. Printing a new fibre is easier and less time consuming than repeatedly cutting a thick fibre without disturbing its entrance tip alignment. Therefore, we produce individual fibres of different lengths and aligned each at the focal plane, to obtain the results considered in this manuscript for terahertz loss measurement. This alignment approach is consistent with Bao *et al.* (2012), Bao *et al.* (2015), Yang *et al.* (2016), Ma *et al.* (2016), Li *et al.* (2017b), Van Putten *et al.* (2018) in THz-TDS research.

In the case of very short fibre (less than 10 mm), a significant amount of light may not be coupled into the waveguide and can reach the detector. To avoid the probable problems of the free space signal, the shortest segment of fibre length (20 mm) is considered as the reference, to calculate the fibre transmission loss.

5.5.2 The FDM printed HC-ARPCF: Transmission loss analysis based on strut thickness

The black solid line in Figure 5.13(a)–5.13(c) averages the experimented transmission loss over the propagation length of $L = 25$, 30, and 40 mm using the 20 mm as a reference for FDM based fibre. The $L = 50$ mm has not been considered for transmission loss measurement due to the setup limitation. In Figure 5.13(a)–5.13(c) the frequency-dependent terahertz transmission losses have been calculated for nominal/printed $t = 0.45/0.68$, $0.50/0.73$, $0.55/0.78$ mm with five-tube HC-ARPCF. The gradual increases in tube thickness decrease the inner tube diameter D only while assuming the

5.5.2 The FDM printed HC-ARPCF: Transmission loss analysis based on strut thickness

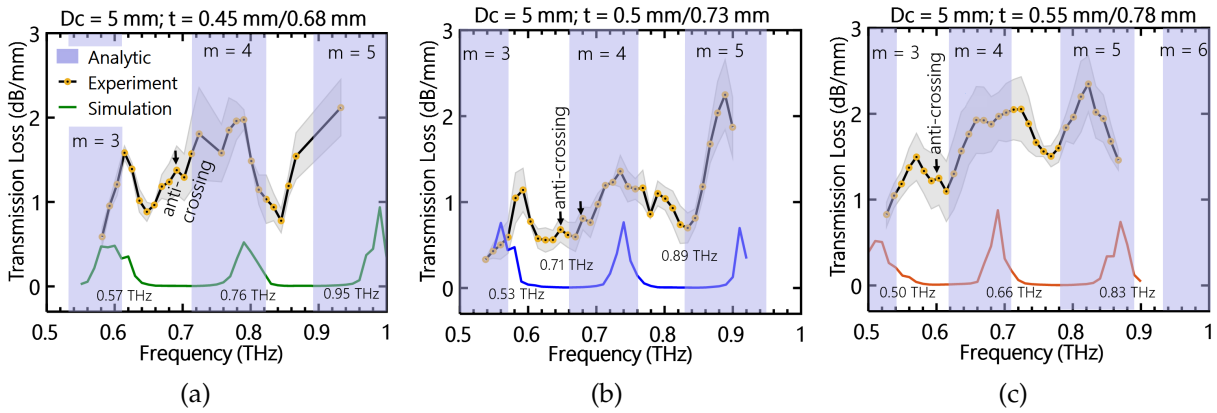

Figure 5.13. The FDM based measured terahertz transmission loss. Transmission loss (black solid line) averaged over three different propagation lengths of five-tubes HC-ARPCF (D_c = 5 mm, L = 25, 30 and 40 mm). The nominal/printed antiresonant tube thicknesses for five-tubes are (a) HC-ARPCF$_1$ (t = 0.45/0.68); (b) HC-ARPCF$_2$ (t = 0.5/0.73); and (c) HC-ARPCF$_3$ (t = 0.55/0.78) using 20 mm propagation length as reference. The grey shades represents the standard deviation error using the coefficient of determination ($R^2 \geq 0.9$). The dark green, blue, and orange curves indicate the FEM simulation for the printed t and the light blue rectangular boxes are the indication of analytical high loss resonance frequency for the printed $t \pm 0.05$ mm.

$D_c = 5$ mm, g, outer tube diameter and fibre outer diameter are constant. For each frequency, we plot the loss (dB) versus fibre length and apply a linear fit. If the coefficient of determination (R^2) of the linear fit is ≥ 0.9 we obtain the slope of the linear fit that is the loss per length (dB/mm) and its standard deviation. The shaded grey regions represent the standard deviation error using $R^2 \geq 0.9$.

The observed minimal transmission loss of 0.88 dB/mm (at 0.65 THz), 0.56 dB/mm (at 0.63 THz), and 1.1 dB/mm (at 0.61 THz) appears for t = 0.68, 0.73, and 0.78 mm, respectively with orders m = 3, and 4. The simulation results are obtained for ideal fibre where the water absorption loss and scattering loss from the longitudinal groove are excluded. The FDM method leaves longitudinal grooves corresponding to each deposited layer, as evident in Figure 5.9(a), which likely results in significant scattering and possibly explains the discrepancy between the FEM and experimental results. The anti-crossing indicates the core modes interference, highlighted in the low loss region for Figure 5.13(a)–5.13(c) due to the discrepancy between experiment and simulation results. The fibre modal properties can be predicted from the Figure 5.5(c)–5.5(d), where the HOMER ranges between 3–9 for t = 0.60–0.85 mm. The analytical resonant

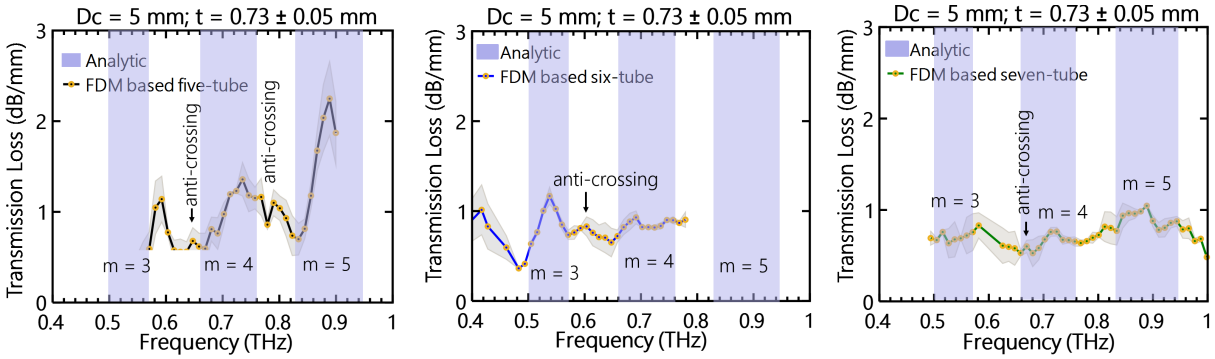

Figure 5.14. The FDM based measured terahertz transmission loss. Measured transmission loss for (a) five (b) six and (c) seven-tube HC-ARPCF based on FDM method and constant g. The measured transmission losses are averaged over three different lengths ($L = 25$, 30, and 40 mm) while $L = 20$ mm is the reference. The nominal/printed $t = 0.50/0.73$ mm is based on the capabilities of present-day FDM. The grey shaded region in (a–c) represents the standard deviation error using the coefficient of determination ($R^2 \geq 0.9$) while the light blue vertical bars represent regions of high resonant loss, from analytical calculations for the printed t.

frequencies for $m = 3$, 4, and 5 using Equation (3.1) are at 0.57, 0.76, and 0.95 THz (for $t = 0.68 \pm 0.05$ mm), at 0.53, 0.71, and 0.89 THz (for $t = 0.73 \pm 0.05$ mm), and at 0.50, 0.66, and 0.83 THz (for $t = 0.78 \pm 0.05$ mm), respectively. The simulation and experiment results are in agreement with the analytic calculations of the low-loss regions around 0.50–1.00 THz for the five-tube HC-ARPCF.

5.5.3 The FDM and SLA printed HC-ARPCF: Terahertz transmission comparison based on tube number

The frequency-dependent transmission losses of the FDM printed HC-ARPCFs are illustrated in Figure 5.14(a)–5.14(c) based on the tubes number. The light blue vertical bars are for analytical high loss resonance frequency with printed $t \pm 0.05$ mm. The analytic high loss regions at $m = 3$–5 coincide perfectly with the experimented high loss regions. The experimentally measured transmission loss minima appear at 0.56 dB/mm (at 0.63 THz), 0.65 dB/mm (at 0.65 THz), and 0.53 dB/mm (at 0.68 THz) for FDM based five, six and seven-tube HC-ARPCF, respectively. All the above discussions in Figure 5.10(a)–5.10(b), Figure 5.13 and Figure 5.14(a)–5.14(c) are associated with FDM printed fibre, and are summarized in Table B.2.

5.5.3 The FDM and SLA printed HC-ARPCF: Terahertz transmission comparison based on tube number

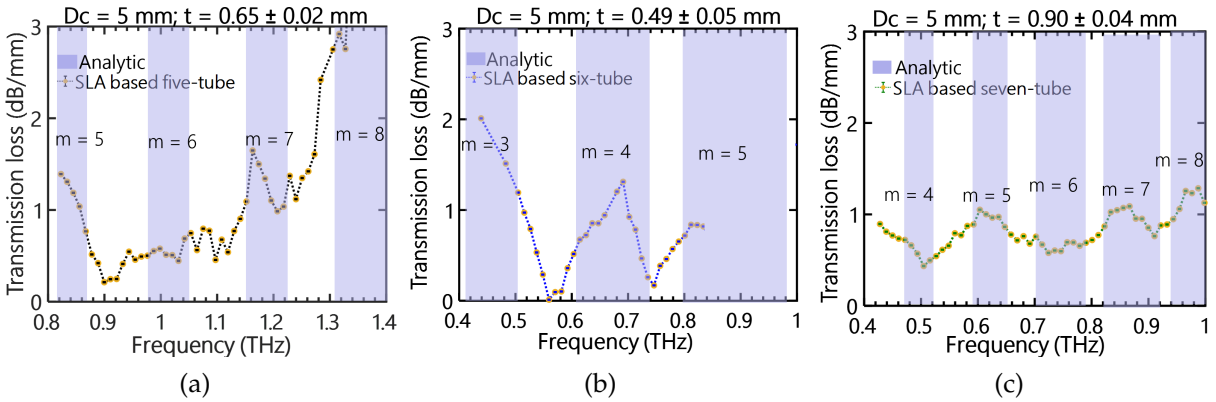

Figure 5.15. The SLA based measured terahertz transmission loss. Measured transmission loss for (a) five (b) six and (c) seven-tube HC-ARPCF based on the SLA printed fibres with constant g. The measured transmission losses are averaged over two different lengths, $L = 27$, 33 mm with the reference $L = 22$ (five-tube), $L = 28$, 32 mm with the reference $L = 23$ (six-tube) and $L = 23$, 31 mm with the reference $L = 15$ (seven-tube). The nominal/printed $t = 0.5/0.72$ mm (five-tube), 0.5/0.60 mm (six-tube) and 0.5/0.65 mm (seven-tube) is printed using SLA. The grey shaded region in (a–c) represents the standard deviation error using the coefficient of determination ($R^2 \geq 0.9$) while the light blue vertical bars represent regions of high resonant loss, from analytical calculations for the printed t.

The SLA-based 100 mm of fibre is cut into three different segments to characterize the transmission properties. For SLA printed five-tube HC-ARPCF, the experimental transmission losses have been averaged over two propagation lengths, $L = 27$, and 33 mm using the 22 mm as a reference in Figure 5.15(a). The lower order transmission with $m \leq 4$ has not been established in the transmission spectrum. The high loss frequency at $m = 6$ has also not formed. The suppressed resonant properties at $m = 6$ may arise from a broken antiresonant tube and also from the nontransparent printed structure. The transmission loss spectrum ranges between 0.8–1.4 THz with analytic order, $m = 5$–8. Given the large standard deviation in average strut thickness ($t = 0.72 \pm 0.11$ mm for five-tube), the high loss resonant frequencies of the analytic results are reasonably consistent with $t = 0.65 \pm 0.02$ mm in Figure 5.15(a). The low loss transmission of 0.17 dB/mm at 0.75 THz lies in $m = 5$–6 region. The propagation lengths are $L = 28$, and 32 mm (for six-tube HC-ARPCF) and $L = 23$, and 31 mm (seven-tube HC-ARPCF) with constant $g \sim 1.05$ and ~ 1.13 mm, and with corresponding reference fibre lengths are 23, and 15 mm, respectively. The low loss of 0.01 dB/mm at 0.56 THz and 0.44 dB/mm at 0.5 THz appears in $m = 3$–4 in Figure 5.15(b) and

Figure 5.15(c). The high loss resonant frequencies of the analytic results are reasonably consistent for $t = 0.49 \pm 0.05$ mm and $t = 0.90 \pm 0.04$ mm in Figure 5.15(b) and Figure 5.15(c). Table B.2 summarizes the transmission properties of the SLA printed HC-ARPCFs.

Printing type	**Tube number**	**Nominal t (mm)**	**Printed t (mm)**	**Trans. loss (dB/mm)**	**Trans. windows (THz)**	**Order m**
FDM	5	0.45	0.68 ± 0.05	0.88; 0.65 THz	0.61–0.72	3–4
FDM	5	0.50	0.73 ± 0.05	0.56; 0.63 THz	0.59–0.74	3–4
FDM	5	0.55	0.78 ± 0.05	1.10; 0.61 THz	0.57–0.66	3–4
FDM	6	0.50	0.73 ± 0.05	0.65; 0.65 THz	0.54–0.69	3–4
FDM	7	0.50	0.73 ± 0.05	0.53; 0.68 THz	0.58–0.71	3–4
SLA	5	0.50	0.72 ± 0.11	0.21; 0.90 THz	1.16–1.34	5–6
SLA	6	0.50	0.49 ± 0.07	0.01; 0.56 THz	0.50–0.68	3–4
SLA	7	0.50	0.90 ± 0.04	0.58; 0.72 THz	0.60–0.83	4–5

Table 5.3. Summary of measured results for FDM and SLA based HC-ARPCFs.

We have used ordinary, low-cost, 3D printers in both cases those may affect the printings as well as transmission performances. The damaged (broken and fused) SLA antiresonant tubes, the minimum sample length difference with the shortest segment of ($L \leq 20$) reference fibre, and the large deviation in average strut thickness (± 0.11), non-transparency encourage to consider only the experiment and corresponding analytic results in Figure 5.15. The two different printing methodologies result in significant variations, especially in D, g and t for five, six, and seven-tube HC-ARPCF in Figure 5.8–5.11. These factors likely explain the discrepancies between Figure 5.14 and Figure 5.15.

In FDM printing, the main challenges come from the (i) thickness deviation from the nominal design due to die swell effect and (ii) material density variation or corrugations due to staircase effect. It is not possible to avoid the die swell in the nozzle-based printing, but it can be counterbalanced by appropriate process conditions and die design. Future work may focus on managing the die swell effect by maintaining the feed speed, viscosity of Zeonex as a function of temperature, force, stick-slip behaviour, non-Newtonian flow, etc during printing. Suitable post-processing studies

need to investigate the reduction of the staircase effect that leaves the grooves along with the printed parts. Post-processing heat curing, for example, CO_2 laser treatment or annealing is a potential way to improve the surface quality of the 3D printed fibre (Wickramasinghe *et al.* 2020). Another post-processing technique is chemical exposure by using a vapor smoothing station that improves the surface finish of the FDM-based parts to nano-level with negligible dimension deviations (Wickramasinghe *et al.* 2020). A patterned nozzle (Talataisong *et al.* 2020, Islam *et al.* 2021, Talataisong *et al.* 2021) can reduce the amplitude of the undesired corrugations from the structure, making the material wall more uniform.

Although the SLA is also a layer by layer deposition technique, the staircase effect is negligible due to the nozzle free method compared with the FDM method. However, the challenges arise from the (i) non-transparent structure, (ii) broken and collapsed tube, and (iii) thickness variation. The faster scanning speed lowers the accuracy and the slower scanning speed over-cured the printed parts. It is important to obtain the optimal exposure time settings and cure times for avoiding yellowing. Post-processing techniques such as resin polishing (washing with cleaning agents like Isopropyl Alcohol and then dipping the resin part into a liquid clear resin for thinner coating) or spray coating make the printed structure transparent and remove the uncured parts from the structure. At the same time, the post-processing may create some damage in the complex printed parts as it is a manual cleaning and deviate the thickness (shrinkage or swell). The laser power intensity and spot diameter, scan speed, curing or the exposure time, printing resolution, layer thickness, and lift speed of the build plate have an impact on the surface quality and dimensional accuracy (Cho *et al.* 2005) and need to be optimized for the clear resin.

In simulation and experiment, we have not analysed the bending properties because of the large outer diameter. The bent fibres can be printed with different bending radii, which will add a new dimension to investigate the bending loss properties for both the FDM and the SLA printed macro structured fibre.

5.6 Discussion

The HC-ARPCFs with strut thicknesses variation ranging between 0.45–0.85 mm have been analyzed numerically to examine the reflection properties from strut and transmission loss of the corresponding fibres, provided in Section 5.3. The thickness variations with the constant gap reduce the antiresonant tube diameters and provide the corresponding mode interference behaviour. Furthermore, the changes in antiresonant tube numbers with a constant gap are also considered in simulation to investigate the transmission properties and modal behaviour of HC-ARPCF.

To validate the numerical observations in the experiment, we have used the FDM and SLA printed HC-ARPCF. As the fibre has a hollow core, the materials depending on the printing mechanisms show less impact on the terahertz transmission. The purpose of using two different mechanisms of fibre printing is to investigate the printing quality and accuracy. The FDM extends the strut thickness by 46% due to the die swell, a well-known phenomenon for polymer and prints the strut thicknesses with 0.68–0.78 mm when nominal thickness varies between 0.45–0.55 mm. To minimize the gap between expectation and actual strut thickness, the die swell would be constant for a constant set of conditions, which explains the good consistency of the thickness increase. The positive aspect of FDM is that the method maintains similar strut thicknesses like 0.73 ± 0.05 mm with the antiresonant tubes number variations for a constant gap. Also, the actual gap ranges between 1.1–1.2 mm which is consistent with the nominal design values. The coarse layers and corrugations due to the staircase effect result in significant scattering and possibly explain the discrepancy in transmission between the FEM and experimental results. Post-processing chemical treatment, CO_2 laser treatment, or annealing process is a potential way to improve the surface quality of the FDM printed fibre. The high loss regions in the terahertz spectrum are sensitive to the strut thickness variations and tube number, follow similar trends with the analytic and simulated resonant frequency. Low loss terahertz transmission and multispectral behaviour are also remarkable results in FDM.

Depending on the tube numbers, the SLA method extends the strut thickness 20%–88% for the nominal thickness of 0.50 mm. The standard deviation in average strut thickness is ±0.11 which is higher than that of the FDM method. Also, the SLA printed HC-ARPCF using UV-resin are not very transparent due to the overexposure time and

has created damage in antiresonant tubes, resulting in inconsistent transmission loss with the analytic results. Because of these phenomena (i.e. loss sensitivity to thickness variation, nontransparent structure, broken and collapsed tubes, short segment of the sample, and reference fibre), the SLA fibres are not as good as the FDM fibre. The advantage of the SLA-printed fibres is comparatively smoother than FDM-printed. The laser power intensity and spot diameter, scan speed, curing or the exposure time, layer thickness, and lift speed of the build plate improve the surface quality and dimensional accuracy. The high and low loss regions in the terahertz spectrum using the two printing methods are different due to the thickness and dielectric refractive indices variations. The optimization in printing parameters and further post-processing can improve printing quality and accuracy.

Conclusion and future remarks

THIS chapter concludes the work presented in this thesis. Chapters 1 and 2 contains the relevant background information, thesis outline and a brief review of terahertz optical fibres. This covers the motivation behind the studies, the frequency of interests, the materials used to design the photonic devices, and the waveguiding, simulation, fabrication, and experimental methodologies of terahertz optical fibre. Chapters 3 to 5 describe the original contributions to the design and realization of 3D printed terahertz waveguides. Lastly, an outlook for future research on 3D printed terahertz antiresonant fibres is presented.

6.1 Thesis overview

The overview of the thesis including the motivation each study, the methodology, the obtained results, and the future directions are discussed in this chapter.

6.2 Chapter 2: Review of terahertz waveguides

6.2.1 Aim

Terahertz hollow core fibres are essential for developing the full potential of complex terahertz systems. In Chapter 2, we aim to combine the recent development of hollow core terahertz optical fibres with different geometries and guiding mechanisms, the background materials, the fabrication and measurement techniques, and potential applications.

6.2.2 Methodology

We examine various optical fibre types including tube fibres, solid core fibre, hollow-core photonic bandgap, antiresonant fibres, porous-core fibres, metamaterial-based fibres, and their guiding mechanisms. The past and present trends of fabrication methods, including drilling, stacking, extrusion and 3D printing, are elaborated.

6.2.3 Results

The work on terahertz optical fibre discussed throughout Chapter 2 provides a comprehensive review of various geometry including the microstructured photonic crystal fibre, the hollow-core fibre, the antiresonant fibre and the metamaterial-based fibres; the guiding mechanism of each type of fibres; an analysis of different methodology of fibre fabrication and characterization.

From the discussion, it can be noted that every fibre has some advantages and disadvantages and there is a trade-off between low loss, bandwidth and fabrication feasibility. For example, hollow-core fibre can provide low loss terahertz guidance and comparatively simple fabrication at the expense of low bandwidth of operation. On

the other hand, porous fibre can provide larger bandwidth but with higher loss and increased fabrication complexity as compared to hollow-core fibres. Metamaterial-based waveguides are still in their infancy by comparison.

The various fabrication methodologies discussed indicate the possibilities of fabricating various geometries of terahertz optical fibres. For example, the drilling method is suitable for fabricating circular hole patterns only, whereas the extrusion and 3D printing techniques can fabricate any type of complex and asymmetric fibre geometries. The most common method for terahertz fibre characterization is the use of THz-TDS where different optics setups can be used to focus signal onto the fibre core. Among the various terahertz applications short-range high throughput transmission, gas, and chemical sensing and imaging show significant promise.

6.2.4 Future direction

Free-space terahertz wave propagation is still widely used, but terahertz waveguides and, in particular, optical fibres are gaining increasing attention. Their importance is related to the concept of developing complex terahertz configurations that potentially combine sources and detectors with a reliable and simple way of terathertz transmission. Antiresonant fibres stand out among other hollow-core fibres, due to their robustness to fabrication tolerances, geometrical simplicity, and hence fabrication feasibility. Combining simplicity and low attenuation with high bandwidth, single-mode guidance, and low dispersion is, for most applications, the main target. Fibres possessing composite cladding, with metamaterial inclusions, better confine the terahertz signal (Li *et al.* 2016a), and fibres that are helically twisted to guide modes with orbital angular momentum are two of the most exciting directions for actual and near future investigations.

Different manufacturing techniques are being used to produce such fibres, but 3D printing technology represents a clear advantage in terms of cost, time, easiness, and potential for manufacture of speciality fibres (Cruz *et al.* 2018) already integrated with other components required for a particular application. The whole fibre cross-section can be produced simultaneously (Atakaramians *et al.* 2009a)—this is different from 3D printing or stacking-and-draw, for example. Simple and complex waveguides can be

obtained by carefully designing the extrusion die, ram speed and furnace temperature profile. Extrusion of fibre projects with intrinsic low confinement loss due mostly air guidance, and while using low terahertz loss materials, is an interesting route to be wider explored.

Due to their large overall dimensions, with external diameters as large as 10 mm in some situations (Yang *et al.* 2016, Lai *et al.* 2009), some terahertz fibres are not mechanically flexible and this reduces the practical interest in applications requiring long waveguide lengths. Investigating ways of producing flexible fibres via selection of the required mechanical properties the fibre material and the fibre geometry, such as fibres with high air filling fraction and thin external jackets, as well as studying waveguide curvature loss will help develop this field further. Combining special coatings such as graphene (Mittendorff *et al.* 2017) could extend the functionalities of terahertz fibres and will likely be a hot topic in this vibrant research area.

6.3 Chapter 3: Terahertz antiresonant fibre: Concept, modelling, and nonlinearity

6.3.1 Aim

After a brief review of terahertz optical fibre, the aim of Chapter 3 is to design, simulate, and analyse various terahertz optical fibre to get an optimal fibre for terahertz transmission. The goal is to achieve low transmission loss, low and flat dispersion, and non-linearity in a fabrication friendly terahertz optical fibre.

6.3.2 Methodology

The design and simulation of all the contributed waveguides are carried out using the full vector Finite Element Method (FEM) method based on commercially available software COMSOL multiphysics. The *Electromagnetic Waves, emw* solver with a *Physics-controlled mesh* sequence having an *Extremely fine* mesh element size is used to get high accuracy output from the simulation software. A perfectly matched layer (PML) boundary condition is considered at the outer surface to make the computational region finite. In all the simulations we used Zeonex because it offers low material loss of

0.184 cm^{-1}, and carries the required thermal and chemical stability (Islam *et al.* 2019, Islam *et al.* 2020) in the terahertz band.

6.3.3 Results

To achieve the goal, we design and investigate antiresonant terahertz optical fibre that can be easily fabricatable using 3D printing technology. Besides achieving low transmission loss we also achieved high HOMER with low transmission transmission loss. All the fibres are possible to print either by polymer materials and/or resin materials.

6.3.4 Future direction

Further simpler terahertz waveguides can be designed for both transmission and sensing. Moreover, new composite materials can be built that can create plasmons in the material surface. 3D printing using the composite material could provide improved transmission and sensing. In other words, the surface of the 3D printed fibre could be coated with plasmonic material such as graphene and that could provide improve confinement of the electromagnetic field and create plasmons on the fibre surface.

The content of Chapter 3 is published in *IEEE Access*, *Fibers*, *IEEE Instrumentation & Measurement Magazine*, *IEEE Transactions on Terahertz Science and Technology*.

6.4 Chapter 4: Dielectric antiresonant fibre: Design, fabrication, and characterisation

6.4.1 Aim

The aim of Chapter 4 is to explore the fused deposition modeling (FDM) of 3D printing technology to fabricate HC-ARPCF. The further aim is to characterize the fibre using terahertz kit for transmission measurement.

6.4.2 Methodology

Prior to 3D pringing polymer filament was made using a tabletop filabot extruder. The materials used here is Zeonex because of its attractive optical properties in the terahertz

band. The filaments are then used to print the antiresonant fibres of various lengths. The printed fibres are then characterized using our Menlo system.

6.4.3 Results

The experimental validation of the HC-ARPCF is carried out using THz-TDS where five different fibre lengths and considered to achieve the antiresonant properties. It is found that printed fibres with different fibre length combinations show improved antiresonant effects and the analytical resonance frequencies are ideally matched with the numerical analysis. Note that, there are imperfections in the obtained results which are due to the surface roughness in fibre fabrication. Various lengths of the optimized antiresonant fibre was printed and the results indicate that fibres with shorter length provides improved transmission properties over longer length fibre. The propagation distance is countable is this regard.

6.4.4 Future direction

In this chapter we found that printing using FDM technology provides improved transparency however that comes with improper surface roughness. Further 3D printing methodologies such as advanced nanoprinting technology could be used to improved the surface roughness. Moreover, printing using UV-resin material in the SLA printing technology can be used to obtain an improved surface roughness over the FDM technology.

The content of Chapter 4 is published in *IEEE Transactions on Terahertz Science and Technology*.

6.5 Chapter 5: SLA and FDM printed fibres: Simulation, fabrication, and experiment

6.5.1 Aim

Our goal is to develop low-loss, low-cost and versatile terahertz fibres, in particular for scientifc and commercial applications that can be easily fabricated via 3D printing technology.

6.5.2 Methodology

To achieve the goal, for the first time we consider the thickness variation, roughness and transparency of the printed object, quantify the thickness variation as a function of antiresonant tube number for a constant adjacent gap, and measure the performance based on the printing method, thickness variation and antiresonant tube number. Also, for the first time we study printing parameters for Zeonex, including nozzle temperature, and extrusion velocity and investigate their impact on optical performance in the terahertz regime.

To explore the findings in practice, we fabricate the fibres with two well-known 3D printing techniques, using two different materials. The reasons for using two different fibre printing methods is to compare their printing quality and accuracy, and transmission performance with a constant gap for different strut wall thickness, and cladding-tube numbers.

6.5.3 Results

Terahertz fibres with large dimensions can be printed directly without additional expensive and complex drawing procedures (Sultana *et al.* 2020c). The thickness variations with the constant gap reduce the antiresonant tube diameters and provide the corresponding mode interference behaviour. Furthermore, the changes in antiresonant tube numbers with a constant gap are also considered in simulation to investigate the transmission properties and modal behaviour of HC-ARPCF. Note that bending characterization cannot be measured due to limited ability to bend the fibres as a result of the larger outer diameter and short length of the printed fibres. To validate the numerical observations in the experiment, we have used the FDM and SLA printed HC-ARPCF. As the fibre has a hollow core, the materials depending on the printing mechanisms show less impact on the terahertz transmission. The purpose of using two different mechanisms of fibre printing is to investigate the printing quality and accuracy. The FDM extends the strut thickness by 46% due to the die swell, a well-known phenomenon for polymer and prints the strut thicknesses with 0.68–0.78 mm when nominal thickness varies between 0.45–0.55 mm. To minimize the gap between expectation and actual strut thickness, the die swell would be constant for a constant set of conditions, which explains the good consistency of the thickness increase. The

positive aspect of FDM is that the method maintains similar strut thicknesses like 0.73 ± 0.05 mm with the antiresonant tubes number variations for a constant gap. Also, the actual gap ranges between 1.1–1.2 mm which is consistent with the nominal design values. The coarse layers and corrugations due to the staircase effect result in significant scattering and possibly explain the discrepancy in transmission between the FEM and experimental results. Post-processing chemical treatment, CO_2 laser treatment, or annealing process is a potential way to improve the surface quality of the FDM printed fibre. The high loss regions in the terahertz spectrum are sensitive to the strut thickness variations and tube number, follow similar trends with the analytic and simulated resonant frequency. Low loss terahertz transmission and multi-spectral behaviour are also remarkable results in FDM. Depending on the tube numbers, the SLA method extends the strut thickness 20%–88% for the nominal thickness of 0.50 mm. The standard deviation in average strut thickness is ± 0.11 which is higher than that of the FDM method. Also, the SLA printed HC-ARPCF using UV-resin are not very transparent due to the overexposure time and has created damage in antiresonant tubes, resulting in inconsistent transmission loss with the analytic results. Because of these phenomena (i.e. loss sensitivity to thickness variation, nontransparent structure, broken and collapsed tubes, short segment of the sample, and reference fibre), the SLA fibres are not as good as the FDM fibre. The advantage of the SLA printed fibres is comparatively smoother than FDM printed. The laser power intensity and spot diameter, scan speed, curing or the exposure time, layer thickness, and lift speed of the build plate improve the surface quality and dimensional accuracy. The high and low loss regions in the terahertz spectrum using the two printing methods are different due to the thickness and dielectric refractive indices variations. The optimization in printing parameters and further post-processing can improve printing quality and accuracy

6.5.4 Future direction

Further simpler terahertz waveguides can be designed for both transmission and sensing. Moreover, new composite materials can be built that can create plasmons in the material surface. Note that 3D printing using the composite material can provide improved transmission and sensing. In other words, the surface of the 3D printed fibre

could be coated with plasmonic material such as graphene and that could provide improve confinement of the electromagnetic field and create plasmons on the fibre surface.

The content of Chapter 5 is submitted for publication at *Journal of Lightwave Technology*.

Simulation procedure in COMSOL Multiphysics

The goal of Appendix A is to outline the modeling procedure in COMSOL's Wave Optics Module that was adopted in this thesis study.

A.1 Computer simulation

Computer simulation has become an essential part of science and engineering. Today a broad spectrum of options for simulation is available. Each technique has its own unique attributes. All share a common concern: Can we rely on the results? A computer simulation environment is simply a translation of real-world physical laws in their virtual form. It would be ideal to have a simulation environment that included the possibility to add any physical effect to the model.

Three popular computational electromagnetic methods are used to simulate the wave propagation and to numerically configure the geometries and boundary conditions for practical problems: finite-difference method (FDM), finite-volume method (FVM), and finite-element methods (FEM). Each method has its own advantages and disadvantages depending on the specific problems. Based on these methods, many commercial software packages are available, such as FDTD solutions, CST, HFSS, COMSOL®, IE3D and FEKO.

A.2 Finite Element Method

The description of the laws of physics for space- and time-dependent problems are usually expressed in terms of Partial Differential Equations (PDEs). For the vast majority of

geometries and problems, these partial differential equations (PDEs) cannot be solved with analytical methods (separation of variables, Green functions, method of characteristics, Laplace and Fourier transforms). Instead, an approximation of the equations can be constructed, typically based upon different types of discretizations (small area). These discretization methods approximate the PDEs with numerical model equations, which can be solved using numerical methods, for example, Finite Element Method (FEM) (1D, 2D, and 3D), Finite Difference Method (FDM), Finite Boundary Element.

The finite element method (FEM) is a popular technique for numerically solving differential equations in engineering and mathematics. The classic domains of structural analysis, heat transfer, fluid flow, mass transport, and electromagnetic potential are typical issue areas of interest. In two or three spatial variables, the FEM is a generic numerical approach for solving partial differential equations (i.e., some boundary value problems). The FEM breaks a big and continuous physical model into smaller, simpler sections called finite elements in order to solve a problem, shown in Figure A.1(a) and laws of nature are applied on the generic element. This is accomplished by a specific space discretization in the space dimensions, which is performed through the creation of an object mesh: the numerical domain for the solution, which has a finite number of points, shown in Figure A.1(b). The results are then recombined to represent the continuum.

One of the benefits of using the FEM is that it offers great freedom in the selection of discretization, both in the elements that may be used to discretize space and the basis functions. It is possible to select test and basis functions that are supported over a very small geometrical region. Analogous to the idea that connecting many tiny straight lines can approximate a larger circle, FEM encompasses all the methods for connecting many simple element equations over many small subdomains, named finite elements, to approximate a more complex equation over a larger domain. As a result, FEM has advantage in complex and inhomogeneous problems. Another benefit of the finite element method is that the theory is well developed. It uses variational methods to minimize an error function and produce a stable solution. For instance, the theory provides useful error estimates, or bounds for the error, when the numerical model equations are solved on a computer. Furthermore, The FEM is a frequency domain method which makes it efficient in dealing with narrow-band problems. The weakness

for FEM is that the whole domain must be mashed and the open structure creates radiation and scattering.

A.2.1 Solving a PDE through FEM

- Specify the types of solver: stationary, time-dependent, eigenvalue, parametric.
- Specify the domain of the equation.
- Specify the boundary conditions.
- Create a mesh (divide the domain into finite elements).

A.2.2 Finite Elements

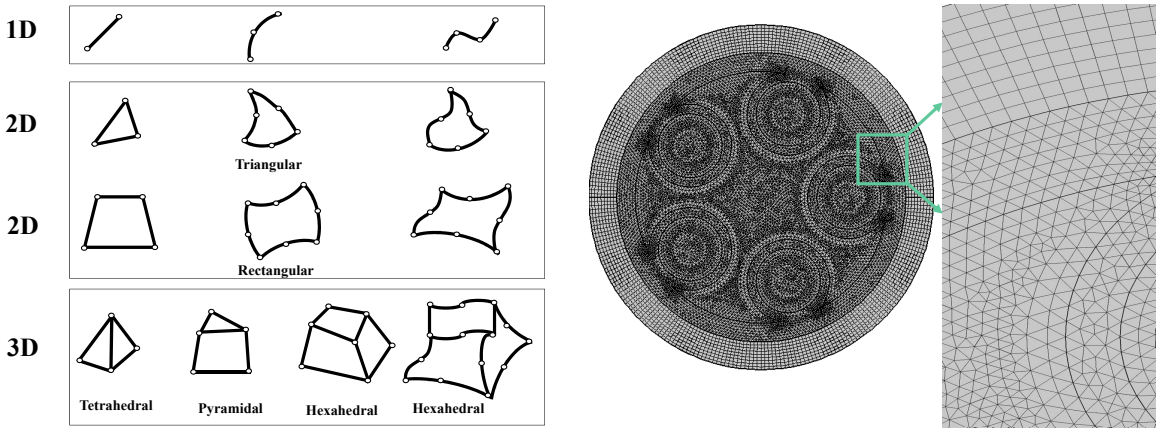

Figure A.1. Finite Element and 2D mesh. (a) Finite Element; (b) 2D mesh in a fibre geometry.

- Defined by dimensiones (1D, 2D, and 3D).
- Defined by Nodes.
- Defined by Geometry.
- Defined by Degrees of Freedom (vertices).
- Defined by Nodal forces.

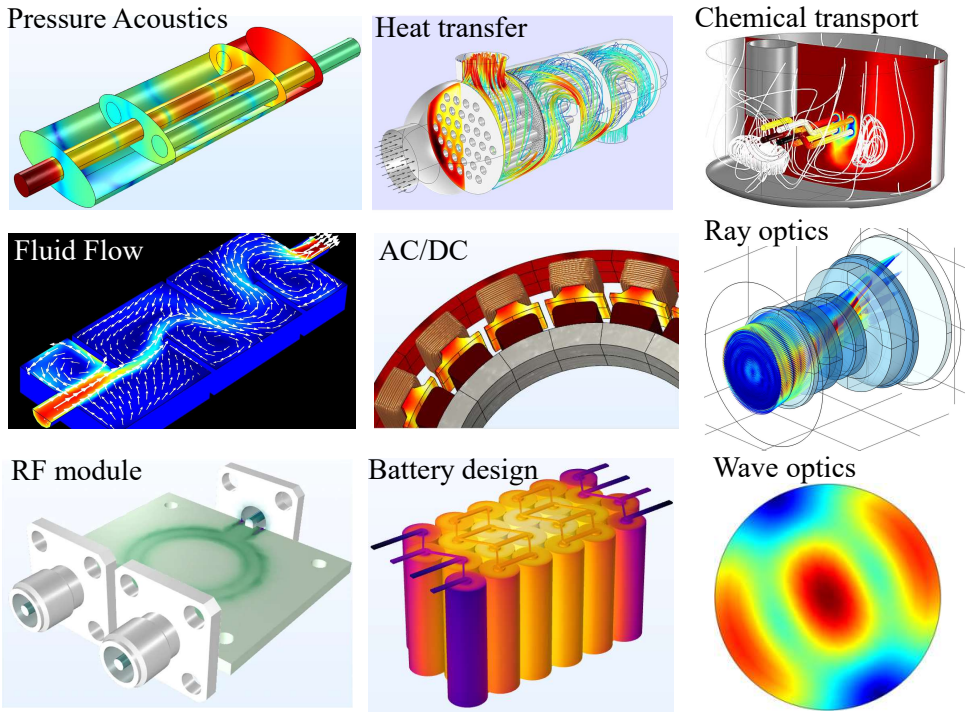

Figure A.2. Application fields. Application fields in COMSOL Multiphysics®

A.3 COMSOL Multiphysics®

COMSOL Multiphysics® is a finite element analysis, solver and Simulation software package for various physics and engineering applications, shown in Figure A.2, especially coupled phenomena, or multiphysics. COMSOL Multiphysics® software design devices and process the calculations according to the modelling workflow—from defining geometries, material properties and the physics that describe the specific phenomena for producing the accurate and trustworthy results based on the FEM method.

The advantages of COMSOL Multiphysics® is custom made simulation tools that contain all the benefits of a model built with the Model Builder, without the extraneous information. COMSOL Multiphysics® also offers an extensive interface to MATLAB (hence, also Octave), computer aided design (CAD) programmes, and its toolboxes for a large variety of programming, preprocessing and postprocessing possibilities. With a COMSOL Server license, an application can be run in major web browsers on platforms such as Windows®, macOS, iOS, Linux®, and Android™. In addition to conventional physics-based user interfaces, COMSOL Multiphysics® also allows for entering

coupled systems of partial differential equations (PDEs). For example, COMSOL Multiphysics® can couple simulations with heat transfer, structural mechanics, fluid flow formulations, and other physical phenomena.

A.4 Finite Element Method in COMSOL Multiphysics

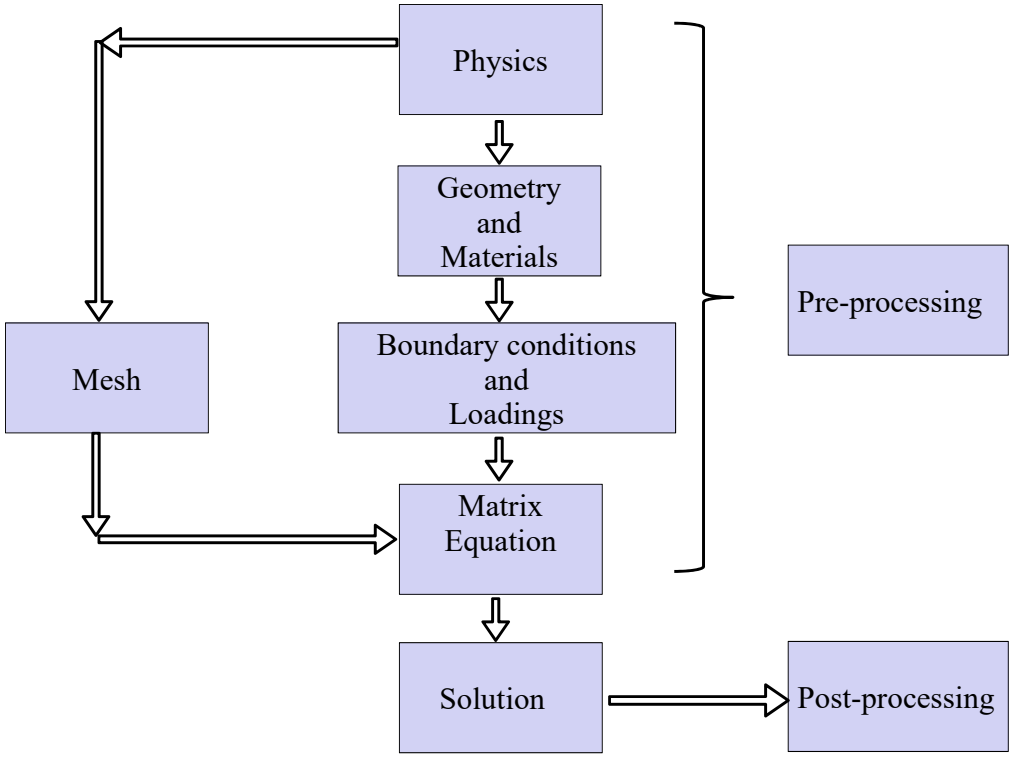

Figure A.3. Step by step COMSOL Simulation procedure. Basic steps to perform a finite element analysis in COMSOL Multiphysics®.

The application of FEM for the modeling and simulation of different physical phenomena in interconnect structures by using COMSOL Multiphysics® is discussed here. The finite element analysis in COMSOL Multiphysics® is performed by following a procedural flow, as depicted in Figure A.3. The method can be split into three basic steps [38]:

- **Pre-processing**: The pre-processing step enables the user to build the model. Since it contains all the information regarding the FEM application for interconnect study, it is convenient to divide it into smaller sub-steps. The first sub-step involves the creation of the interconnect geometry (1D, 2D, or 3D) to represent the domain under study, and assign the material properties to the domain. Then,

the physical environments of the problem under investigation are generated by assigning the underlying physics (or multiphysics), mathematical equations, and finite element formulation to the model. Typically, the latter is hidden among the core of the commercial software. After that, the application of appropriate loadings, boundary and initial conditions to the domain under study, as well as its discretization into finite elements, determines the matrix equation governing the model, in a similar form of the one presented in equation.

- **Solver**: This step is followed by solving the set of algebraic equations, which provides the physics-related nodal solutions of the model. COMSOL Multiphysics mainly employs two methods to obtain the model solution, namely segregated step and fully coupled method. The segregated step method generates the set of algebraic equations for every physical model under consideration and calculates the resulting solutions for each of those models by following a sequence specified by the user. The fully coupled method generates the single set of algebraic equations for all the involved physical models and implements them in a single iteration scheme which is repeated until convergence is reached.
- **Post-processing**: Once the solutions of the problems are determined, the post-processing step enables the user to evaluate the results of the finite element analysis by means of plotting and data exporting tools.

A.5 Pre-processing

A.5.1 Model Wizard

These instructions are for the user interface on Windows but apply, with minor differences, also to Linux and Mac. Figure A.4 shows the precise initial steps:

1 To start the software, we click the **COMSOL icon** on the desktop. When the software opens, there is an option to choose the Model Wizard to create a new COMSOL model or Blank Model to create one manually. For this waveguide design, we click the **Model Wizard.mph** button. If COMSOL is already open, anyone can start the Model Wizard by selecting New from the File menu and then click Model Wizard. The Model Wizard guides through the first steps of setting up a model. The next window lets select the dimension of the modeling space.

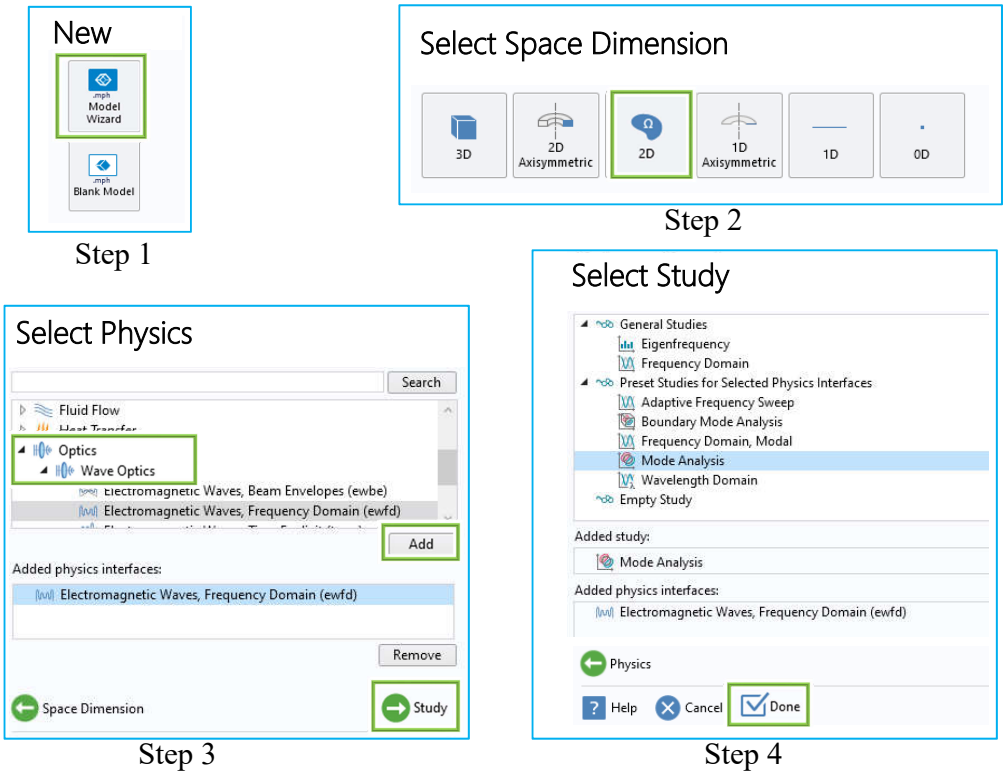

Figure A.4. First sub-steps in COMSOL. The 2D geometry interconnection.

2 In the **Select Space Dimension** window click **2D**. If it is possible it is recommended to solve the problem in 2D because the necessary approximations are small, the solution is more accurate in 2D. This is because 3D models often require more computer power, memory, and time to solve as a much denser mesh can be used.

3 In the **Select Physics** tree under **Optics⇒Wave optics** click the **Electromagnetic Waves, Frequency Domain (*ewfd*)**.

- The **Select Physics** interface tree can process the results for any engineering field such as AC/DC, Acoustics, Chemical Species Transport, Fluid Flow, Heat Transfer, Optics, Structural Mechanics and Mathematics, shown in Figure A.2.

- The **Optics** interfaces may be used for electromagnetic modeling of nano-optical and plasmonic devices, gratings and metamaterials, waveguides and couplers, optical scattering phenomena, and nonlinear optics.

- The **Wave Optics** interfaces are based upon Maxwell's equations together with material laws. Wave optics used for time-harmonic and transient electromagnetic modeling, respectively of the above mentioned devices or system. The Wave Optics interfaces are used to compute electromagnetic fields and waves in optical applications. Typical frequencies for optical applications are of the order of hundreds of terahertz.
- The **Electromagnetic Waves, Frequency Domain (*ewfd*)** interface (2D only) solves time-harmonic wave equation for the electric field. Press the **Add** button to add the physics interface then click the Study. This physics interface supports the study types Frequency Domain, Eigenfrequency, Mode Analysis, and Boundary Mode Analysis and is used primarily to model electromagnetic wave propagation in different media and structures.

4 In the **Select Study** tree under Preset Studies for Selected Physics Interfaces, click the **Mode Analysis**. The Mode Analysis study is used to compute the propagation constants or wave numbers as well as propagating mode shapes at ports and waveguide cross section, for a given frequency for the 2D only. Press **Done** to finish the initial setup.

The all steps for antiresonant waveguide modelling is shown in Figure A.5 and described in details in Subsection A.5.2–Section A.5.4.

A.5.2 Model Builder

There are two types of builder windows: Application Builder Windows, and Model Builder Windows. As we do not have any need of input port, buttons and programming environment, here, we use **Model Bulider** instead of Application Builder to carry out the waveguide simulations.

Parameters

Parameters are defined under the **Global Definitions** node to control the settings of a model and are user-defined constant scalars that are usable throughout the Model Builder. First, a set of parameters is defined in the Setting Window for creating the geometry and defining the material. The SI units are used to describe the relevant properties, parameters, and dimensions along with other unit systems.

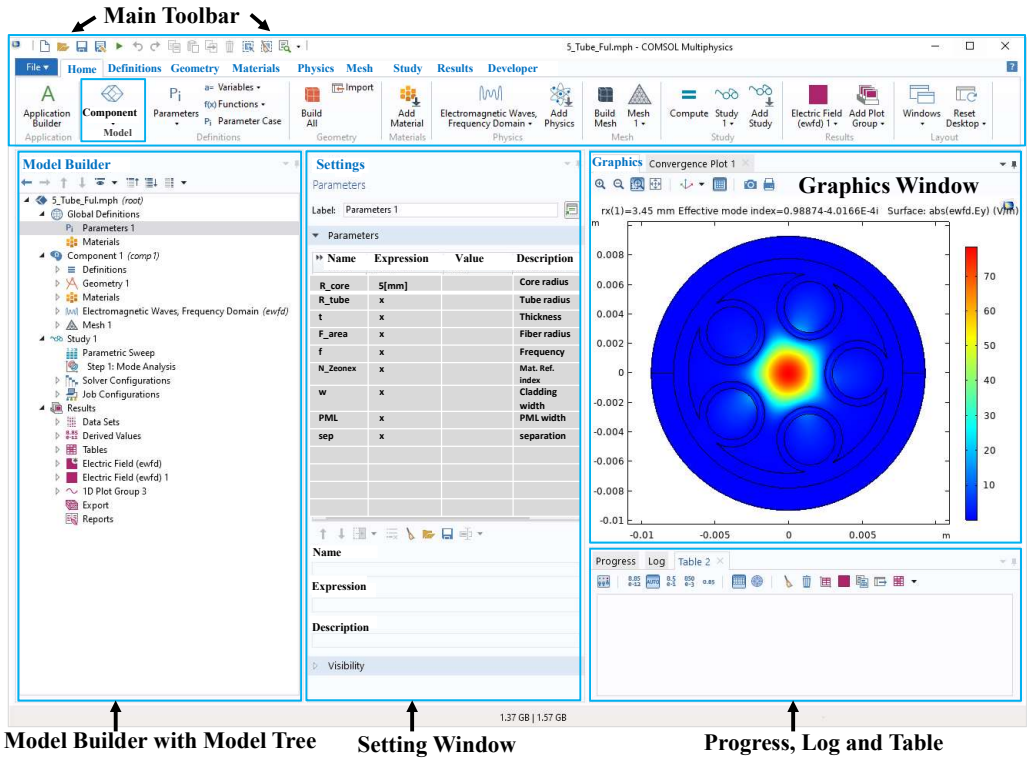

Figure A.5. Step by step COMSOL Simulation procedure. Basic steps to perform a finite element analysis in COMSOL Multiphysics®.

Variables

Variables can be defined in the **Component 1** node. A globally defined variable can be used throughout a model. Variables can be used for spatially or time-varying expressions, including dependent field variables for which you are solving.

Geometry 1

Geometry 1 are defined under the **Component 1** node in the Model Builder tree. Using a parametrized geometry it is easy to experiment with different dimensions for the waveguide structure. Draw or import the model geometry in the Geometry branch.

Materials

Now, add **Materials** under the **Component 1** node in the Model Builder tree for the cladding and the core of the waveguides.

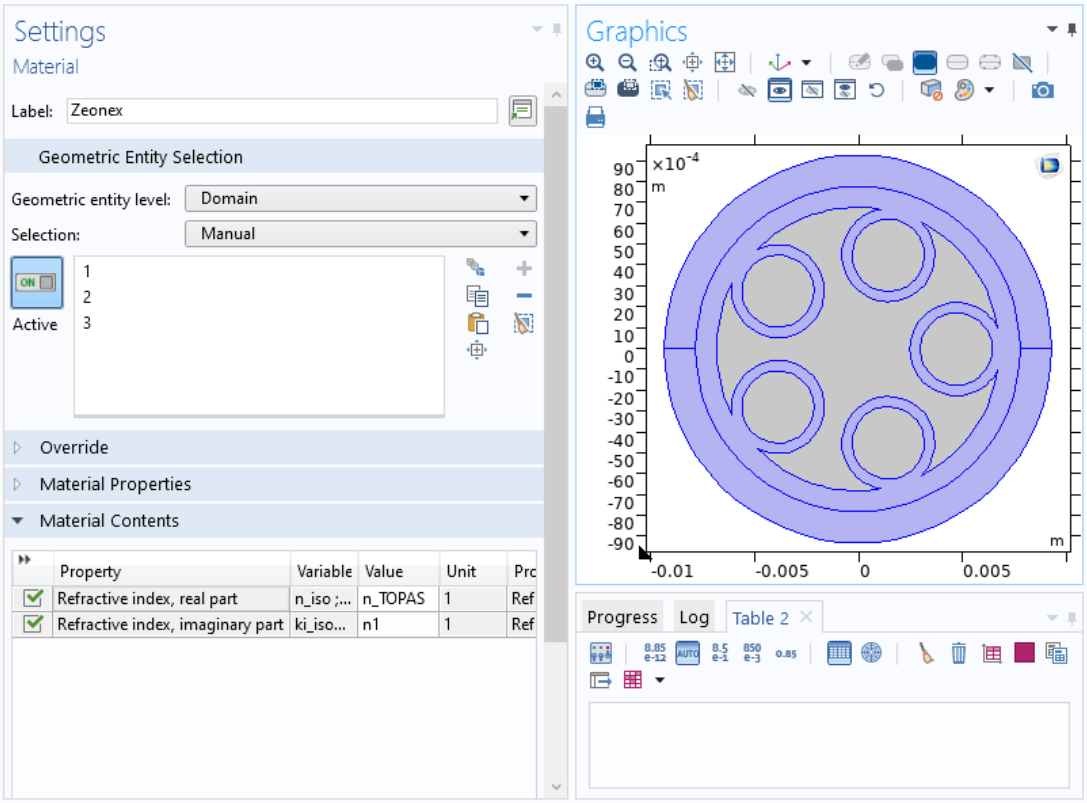

Figure A.6. Material definition in COMSOL. Showing the COMSOL window after defining a material.

- First add the waveguide cladding material. By default, the first material will be assigned to all domains. **Geometric Entity Selection** will be Domain and Manual in the material Setting Window.

- For this waveguide structure, **Blank Material** is labled as Zeonex in the Model Builder tree and used as cladding material.

- In the second step, it is required to define the waveguide core domain.

- The process will be repeated for the core material which is air.

- In the material Setting Window for the Zeonex, assign the **Materials Properties⇒Electromagnetic Models⇒Refractive Index (Real and Imaginary)**. Material properties include inhomogeneous and fully anisotropic materials, media with gains or losses, and complex-valued material properties.

- Check the **Material Contents** for including the the real and imaginary reftractive index and assign the Apperance as Plasctic for Zeonex.

Mesh 1

The **Mesh 1** is under the **The Electromagnetic Waves, Frequency Domain interface (*ewfd*)**. The Mesh Settings Sequence is **User-controlled** mesh. When selected, this invokes a parameter for the maximum mesh element size in free space. The **Physics-controlled mesh** automatically scales the maximum mesh element size as the frequency changes in different dielectric and magnetic regions. If the model is configured by any periodic conditions, identical meshes are generated on each pair of periodic boundaries. Perfectly matched layers are built with a structured mesh, specifically, a swept mesh in 3D and a **mapped mesh in 2D**. We callibrate the **element size** in the Setting Window for **General physics** and predefined as **Extremely fine**. **Resolution** of narrow regions is chosen maximum of 1.

Efficient Boundary Conditions: PMLs

Add **PMLs (perfectly matched layers)** to simulate electromagnetic waves that propagate into an unbounded domain. The PMLs are layers that absorbs all radiated waves with small reflections. The simulation domain is delimited by boundary condition feature nodes. The default boundary condition feature for the Electromagnetic Waves, Frequency Domain (*ewfd*) physics interfaces in the Wave Optics Module is the **Perfect Electric Conductor feature**.

A.5.3 Solver

Study 1

A **Study** node is added to the Model Builder including a corresponding study steps. For the waveguide model, special plots are generated by enabling the check box for the **generation of the default plots** and **convergence plots** in the setting Window. A study step Settings window has a Physics and Variables Selection section where inclusion and exclusion of physics interfaces and variables can be adjusted and set. Add a **Mode Analysis** study under the Study node to compute the propagation constants and mode shapes at waveguide cross sections. The Mode Analysis study step performs eigenvalue analyses on the 2D transverse cut cross section of a waveguide or a transmission line to compute the resonant modes and to find allowed propagating modes. As we are dealing with the air (real η_{core}=1) in the core, the **search for mode around**

for the fundamental mode in our cases is 0.999 in the Study Setting Window. **Transform** is selected for **Effective mode**, **Mode serach** will be **manual**, **Desired number of modes** is enabled for 4 to minimize the computation time for the fundamental mode for a paticular Mode analysis frequency. Solver Configurations contain nodes that define variables to solve for the solvers and settings, and additional sequence nodes for storing the solution. Press the **Compute** in the setting window to compute the mode analysis.

A.5.4 Post-processing

Results

In the Model Builder under Electric Field, click Surface 1. From the Settings window for Surface node enter *abs(ewfd.Ey)* in the Expression text field and the unit is V/m, to plot the mode field polarized in the y (or x) direction. From the Effective mode index list, choose the effective index for the fundamental mode and desired modes. To copy the effective indices for the different modes select **Global Evaluation** under **Derived Values**. From the Expression section in the Derived Values Settings window enter *ewfd.neff* and *imag(ewfd.neff)* to have the real and imaginary refractive index in a particular frequency for the our model. Click the **Evaluate** button to have the results in the **Progress** window and mode is visualized in the **Graphics** window.

Even after a model is defined, we can edit input data, equations, boundary conditions, geometry (Davidson 2010, Dickinson *et al.* 2014).

In summary, in this Appendix we present the step by step procedure of COMSOL Multiphysics® simulation. In the next Appendix we will present the required MATLAB coding to obtain the optical properties of 2D materials, graphene and black phosphorous. The MATLAB coding for obtaining the the property of an optical fibre from the experimental data will also be presented.

Appendix B

Equipment and arrangement in terahertz experiments

The material characterisation and fibre measurement in this thesis are performed in "TERA K15" Time-Domain Terahertz Spectrometer. The terahertz generation and detection antennas of the setup are not altered during the measurements, only their position and the optical path between the two units was altered. The equipment used to carry out terahertz measurements in Chapter 4, and Chapter 5 is listed in this appendix.

B.1 Terahertz setup

Table B.1 highlights the major equipment used at the University of Adelaide to carry out terahertz measurements for freespace in Fig. B.1, material characterisation in Fig. B.2 and transmission through the printed fibre in Fig. B.3.

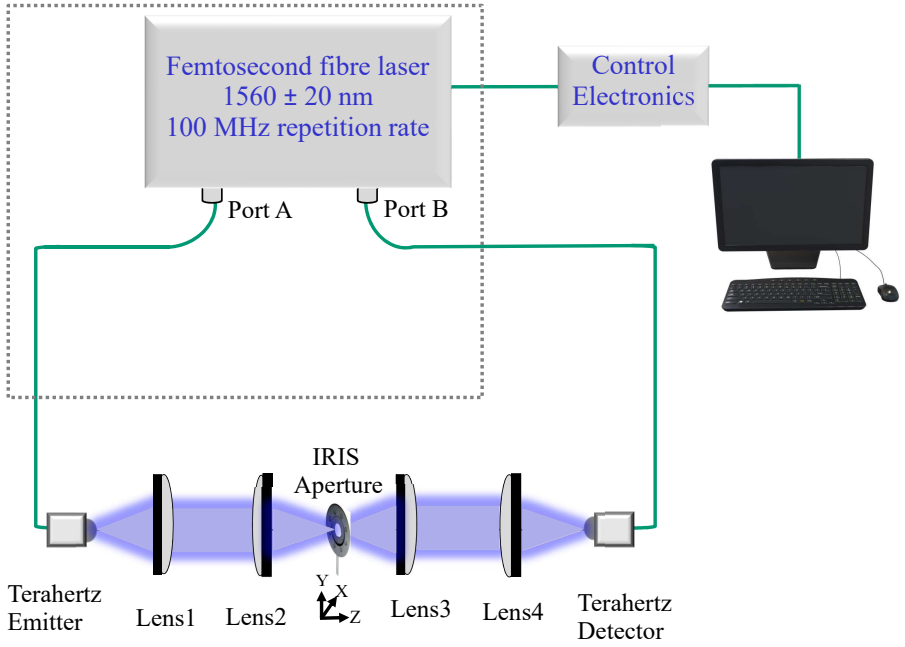

Figure B.1. The experimental setup for freespace measurement. The setup encompasses a femtosecond (fs) laser, a terahertz emitter, L_1, L_2, Iris diaphragm, L_3, L_4, terahertz detector (from left to right). Beam diameter between L_2 and L_3 is measured with iris diaphragm to measure the beam-waist of the freespace terahertz signal. The whole system is enclosed in a purge box containing dry air, Sultana *et al.* (2020c).

The transmission THz-TDS setup used in this work is a commercial system from Menlo Systems (System n.d.a, System n.d.b). The THz-TDS system (TERA K15, Terahertz Kit) with 1560 ±20 nm wavelength femtosecond laser is using fibre coupled, high-resistivity InGaAs/InAlAs multi-layer photo-conductive antennas for terahertz generation and detection, and TPX polymer lenses for focussing at the sample. Antennas and lenses are flexible and easy to operate. The alignment of the terahertz path can be reconfigured between transmission and reflection geometry.

The THz-TDS system consists of four main parts: (1) Optical source (2) Optical delay line controller and (3) Terahertz emitter and recevier (4) Terahertz optics. The laser beam generated from "T-light" (Optical Source) is split into a strong pump beam for

Purpose	Material	Equipment type	Manufacturer	Model
Menlo Systems Femtosecond fibre Laser	Ultra-fast Erbium doped	All fibre coupled laser	GmbH (Menlo system)	T-light
Terahertz generation	LT InGaAs/InAlAs-based	Photoconductive antenna, Strip Line 25 μm	GmbH	TERA 15-TX/RX-FC
Terahertz detection	InGaAs/InAlAs-based	Photoconductive antenna, Dipole 25 μm; gap 10 μm	GmbH	TERA 15-TX/RX-FC
Plano-convex TPX50, aspheric lenses	TPX polymer	THORLABS Inc.	–	–
Phase sensitive detection	Analog Lock-in Amplifier	–	–	–
xyz-translation stage	–	–	–	Home-made
IRIS diaphragm	–	THORLABS Inc.	–	–

Purpose	Material	Equipment type	Manufacturer	Model
PC and Software Package for Measurement and Data Analysis	K15 TeraScan Mark II 1.31 software	–	–	Compitable with T-light

Table B.1. List of equipment used at University of Adelaide. The Table includes the major equipment used commercial set up model "TERA K15" from the Menlo System at The University of Adelaide for material characterisation and fibre transmission in Chapter 4, and Chapter 5.

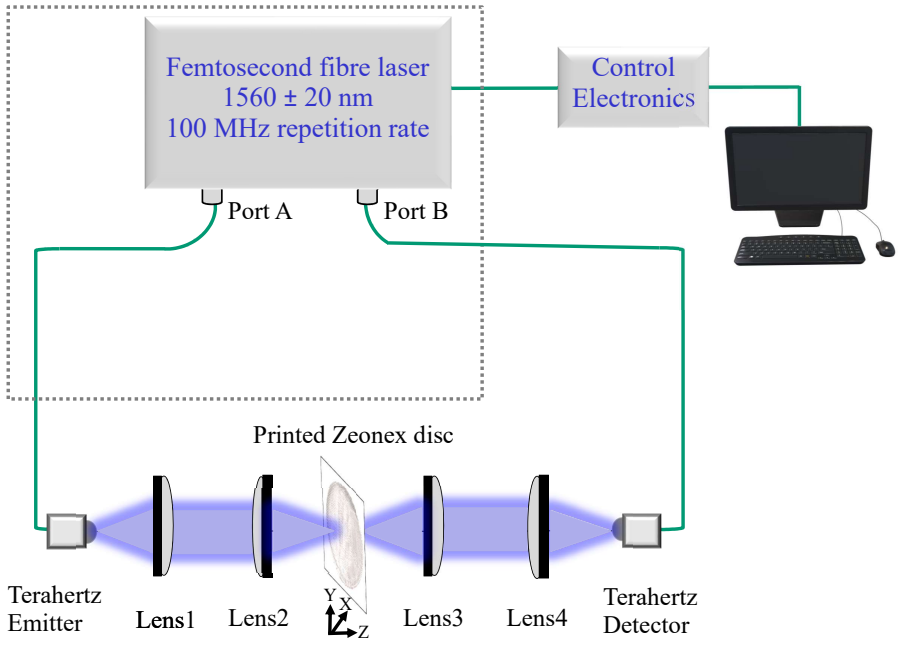

Figure B.2. The experimental setup for material characterisation. The setup is as similiar as Fig. B.1 except the Iris diaphragm is replaced with the printed Zeonex sample to characterise the material Sultana *et al.* (2020c).

the generation of the terahertz radiation and a weak probe beam for the detection. One beam travels through the beam splitter, folded by two mirrors, and then focuses onto the surface of the photoconductive antenna (terahertz emitter/receiver), to pump the semiconductor materials in order to generate and detect terahertz signal. The terahertz

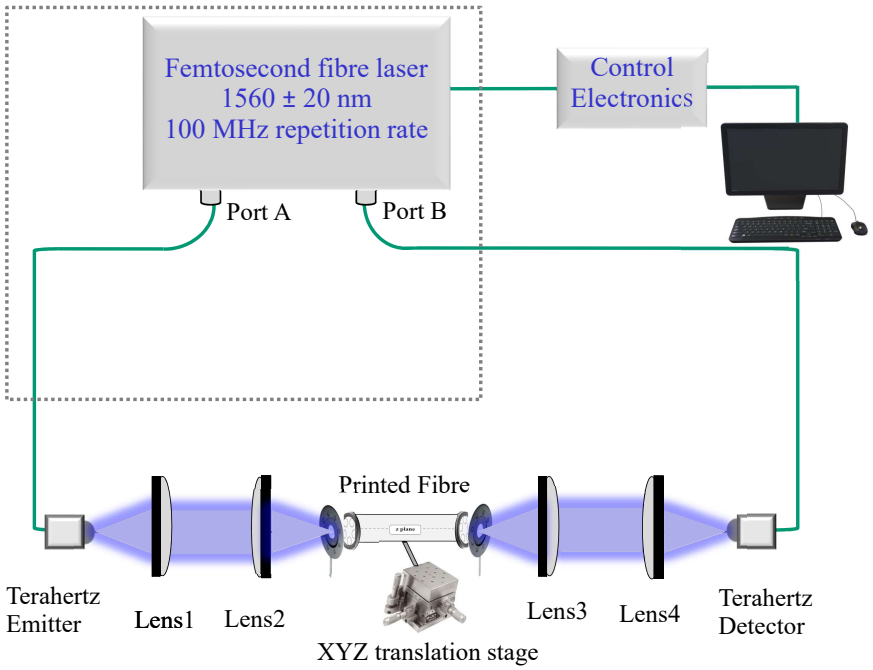

Figure B.3. The experimental setup for printed fibre transmission. In this setup we place a the printed fibre at the focal points of L_2 and L_3. The terahertz generation and detection antennas of the setup are not altered during the measurements, only the position and the optical path between the two units was altered. A xyz-translation stage with sample holder precisely changes the sample position in any directions, Sultana *et al.* (2020c).

pulse, generated from the LT InGaAs/InAlAs-based photoconductive antenna, is collimated by an on-axis plano-convex lens (L_1) to produce a nearly parallel beam with Gaussian FWHM of 25 mm. Another plano-convex lens (L_4) is used to focus the collimated terahertz beam on the terahertz detector antenna.

The modulated photocurrent ($\pm$10 V, 10 kHz, square wave) in the terahertz emitter is measured using a lock-in amplifier where the system has the highest signal-to-noise ratio and the teraherz pulse waveform was obtained by performing a Fourier transform of the varying time delay due to actuation of the translation stage. All measurements were performed at normal incidence.

Prior to the freespace loss measurement another pair of on-axis plano-concave lenses (L_2 and L_3) with the focal length of 50 mm are placed between the collimated terahertz beam to couple the beam waist as shown in Fig. B.1. The plano-convex lenses (L_2 and L_3) focus the beam to a 1.85 mm waist verified by an iris diaphragm. These two

plano-convex lenses are separated by 100 mm, as the focal lengths are 50 mm. The spectrometer is set to operate in rapid scan mode, with a lock-in time constant of 300 μs for observing alignment and signal properties during the measurement set-up. Then a lock-in time constant of the 10 ms is selected for collecting the data for later analysis. There are two types of reference signals: (i) no fibre and (ii) with shortest length of fibre. The 'no fibre' reference signal in Fig. B.1 is measured without the HC-ARPCF while the sample fibre scan is taken after inserting the fibre sample between the pair of plano-convex lenses (L_2 and L_3) as shown in Fig. B.3. The 'no fibre' reference signal in this thesis is considered only to characterise the printed Zeonex in Fig. B.2. Here, the iris diaphragm is used to mark the position of beam waist and block any unwanted signal passing through the fibre core. The printed fibre is mounted on an automated xyz-translation stage for mapping the fibre modes. Finally, data acquisition is carried out with "K15 TeraScan Mark II 1.31" software from Menlo. This software provides the temporal and power spectra of the signals for further signal characterization.

B.2 T-light: 1560 nm femtosecond fibre laser

B.2.1 System components

- Optical Breadboard with terahertz Emitter and Receiver Modules
- Optical Delay Line
- THz Optics
- Femtosecond Laser Source

B.2.2 Control electronics

- TC1550 Control Electronics for the Laser Head
- HVG110 Electrical Chopper for Emitter Antenna, 0.1–75 kHz, up to $\pm$60 V
- Control Electronics for the Delay Line
- Data Acquisition Platform, 16-Bit, 250 kS/s
- Analog Lock-in Amplifier
- PC and Software Package for Measurement and Data Analysis

B.2.3 Features for T-light: 1560 nm femtosecond fibre laser

- Flexible fibre coupled solution
- TPX polymer lenses
- High-power terahertz antennas
- Fast and slow scanning
- Transmission and reflection geometry
- Ultra-stable PM-fibre laser
- Fast and slow scanning
- Truly Turnkey Operation by Self Starting Mode-Locking Mechanism

B.2.4 Applications for T-light: 1560 nm femtosecond fibre laser

- Amplifier Seeding
- Time resolved and Ultrafast Spectroscopy
- Material Characterization
- Microfabrication
- Bioimaging
- Terahertz Physics
- Chemical Fingerprinting
- Material Characterisation

B.2.5 Specefications for T-light: 1560 nm femtosecond fibre laser

- Antenna Structure –TERA 15
- Spectral Range (min) – 0.1–2 THz
- Dynamic Range $>$ 50 dB (Typical 60 dB)

- Scan Range – 300 ps
- Laser Model – T-light
- Wavelength – 1560 $\pm$20 nm
- Average Output Power $>$ 150 mW
- Spectral Width $>$ 40 nm
- Repetition Rate 100 $\pm$1 MHz
- Repetition Rate Instability $<$ 1 ppm
- Output Port (Standard) – Free Space, Linearly Polarized
- Beam Height – 60 mm
- Output Port (Optional Configuration) – Two fibre-Coupled FC/APC, PM fibre. Power Ratio Between the Two Ports is Tunable.
- Pulse Duration (Width) $<$ 90 fs, After 1 m Patch Cord
- Total Average Output Power $>$ 100 mW

B.3 TERA15: Terahertz antennas for 1550 nm

The TERA15 terahertz-antennas allow for an all fibre-coupled terahertz system.

B.3.1 Features for TERA15: Terahertz antennas for 1550 nm

- Optimized for laser $\sim$ 1550 nm and pulse width $<$150 fs
- Patented LT InGaAs/In-AlAs on InP Multi Layer Structure
- Antenna Design Specified for Emitter/Receiver Applications

Specifications	**Emitter SL25**	**Detector DP25**
Photoconductive Material	LT InGaAs/InAlAs	LT InGaAs/InAlAs
Photosensitivity	up to 1.57 μm	up to 1.57 μm
Antenna Type	Strip Line 25 μm	Dipole 25 μm; gap 10 μm
Chip Size	4 mm$\times$4 mm, d = 0.35 mm°C	4 mm$\times$4 mm, d = 0.35 mm
Characteristics measured in fibre testbed		
Terahertz pulse Shape	Peak-to-Peak Time Difference $<$ 700 fs	
Maximum of Fourier Spectrum	$>$ 0.5 THz	
1/10 Bandwidth of Fourier Spectrum	$>$ 1.5 THz	
Noise Floor	$>$ 3 THz	
Recommended optical light sources		
Menlo Systems Femtosecond fibre Lasers	T-light, C-fibre HP	

Table B.2. Specifications for TERA15: Terahertz antennas and optical light source. The Table includes the specifications for terahertz antennas and optical source for 1550 nm.

Bibliography

ABBOTT-D., AND ZHANG-X.-C. (2007). Special issue on T-ray imaging, sensing, and retection, *Proceedings of the IEEE*, **95**(8), pp. 1509–1513.

ABRAHAM-E., YOUNUS-A., DELAGNES-J.-C., AND MOUNAIX-P. (2010). Non-invasive investigation of art paintings by terahertz imaging, *Applied Physics A*, **100**(3), pp. 585–590.

ADAMU-A. I., HABIB-M. S., SMITH-C. R., LOPEZ-J. E. A., JEPSEN-P. U., AMEZCUA-CORREA-R., BANG-O., AND MARKOS-C. (2020). Noise and spectral stability of deep-UV gas-filled fiber-based supercontinuum sources driven by ultrafast mid-IR pulses, *Scientific Reports,* **10**, Art. No. 4912.

ADEMGIL-H. (2014). Highly sensitive octagonal photonic crystal fiber based sensor, *Optik*, **125**(20), pp. 6274–6278.

AGRAWAL-G. P. (2012). *Fiber-optic Communication Systems*, Vol. 222, John Wiley and Sons.

ALLEN-L., AND EBERLY-J. H. (1987). *Optical Resonance and Two-level Atoms*, Vol. 28, Courier Corporation.

ANKAN-I. M., MOLLAH-M. A., SULTANA-J., AND ISLAM-M. S. (2020). Negative curvature hollow-core anti-resonant fiber for terahertz sensing, *Applied Optics*, **59**(28), pp. 8519–8525.

ANTHONY-J., LEONHARDT-R., AND ARGYROS-A. (2013). Hybrid hollow core fibers with embedded wires as THz waveguides, *Optics Express*, **21**(3), pp. 2903–2912.

ANTHONY-J., LEONHARDT-R., ARGYROS-A., AND LARGE-M. C. (2011a). Characterization of a microstructured Zeonex terahertz fiber, *JOSA B*, **28**(5), pp. 1013–1018.

ANTHONY-J., LEONHARDT-R., LEON-SAVAL, SERGIO-G., AND ARGYROS-A. (2011b). THz propagation in kagome hollow-core microstructured fibers, *Optics Express*, **19**(19), pp. 18470–18478.

ARGYROS-A. (2013). Microstructures in polymer fibres for optical fibres, THz waveguides, and fibre-based metamaterials, *International Scholarly Research Notices,* **2013**, Art. No. 785162.

ARGYROS-A., AND PLA-J. (2007). Hollow-core polymer fibres with a kagome lattice: Potential for transmission in the infrared, *Optics Express*, **15**(12), pp. 7713–7719.

ARROSPIDE-E., DURANA-G., AZKUNE-M., ALDABALDETREKU-G., BIKANDI-I., RUIZ-RUBIO-L., AND ZUBIA-J. (2018). Polymers beyond standard optical fibres–fabrication of microstructured polymer optical fibres, *Polymer International*, **67**(9), pp. 1155–1163.

ATAKARAMIANS-S., AFSHAR-S., EBENDORFF-HEIDEPRIEM-H., NAGEL-M., FISCHER-B. M., ABBOTT-D., AND MONRO-T. M. (2009a). THz porous fibers: Design, fabrication and experimental characterization, *Optics Express*, **17**(16), pp. 14053–14062.

ATAKARAMIANS-S., AFSHAR-S., FISCHER-B. M., ABBOTT-D., AND MONRO-T. M. (2008). Porous fibers: A novel approach to low loss THz waveguides, *Optics Express*, **16**(12), pp. 8845–8854.

ATAKARAMIANS-S., AFSHAR-S., FISCHER-B. M., ABBOTT-D., AND MONRO-T. M. (2009b). Low loss, low dispersion and highly birefringent terahertz porous fibers, *Optics Communications*, **282**(1), pp. 36–38.

ATAKARAMIANS-S., AFSHAR V-S., NAGEL-M., RASMUSSEN-H. K., BANG-O., MONRO-T. M., AND ABBOTT-D. (2011). Direct probing of evanescent field for characterization of porous terahertz fibers, *Applied Physics Letters*, **98**(12), Art. No. 121104.

BAI-J., GE-M., WANG-S., YANG-Y., LI-Y., AND CHANG-S. (2018). Characteristics of a liquid-crystal-filled composite lattice terahertz bandgap fiber, *Optics Communications*, **419**, pp. 8–12.

BAI-J., LI-J., ZHANG-H., FANG-H., AND CHANG-S. (2011). A porous terahertz fiber with randomly distributed air holes, *Applied Physics B*, **103**(2), pp. 381–386.

BALAKRISHNAN-J., FISCHER-B. M., AND ABBOTT-D. (2009). Sensing the hygroscopicity of polymer and copolymer materials using terahertz time-domain spectroscopy, *Applied Optics*, **48**(12), pp. 2262–2266.

BAO-H., NIELSEN-K., BANG-O., AND JEPSEN-P. U. (2015). Dielectric tube waveguides with absorptive cladding for broadband, low-dispersion and low loss THz guiding, *Scientific Reports*, **5**, Art. No. 7620.

BAO-H., NIELSEN-K., RASMUSSEN-H. K., JEPSEN-P. U., AND BANG-O. (2012). Fabrication and characterization of porous-core honeycomb bandgap THz fibers, *Optics Express*, **20**(28), pp. 29507–29517.

BARH-A., PAL-B. P., AGRAWAL-G. P., VARSHNEY-R. K., AND RAHMAN-B. A. (2015). Specialty fibers for terahertz generation and transmission: A review, *IEEE Journal of Selected Topics in Quantum Electronics*, **22**(2), pp. 365–379.

BARWICZ-T., AND HAUS-H. A. (2005). Three-dimensional analysis of scattering losses due to sidewall roughness in microphotonic waveguides, *Journal of Lightwave Technology*, **23**(9), Art. No. 2719.

BEARD-M. C., TURNER-G. M., AND SCHMUTTENMAER-C. A. (2001). Subpicosecond carrier dynamics in low-temperature grown gaas as measured by time-resolved terahertz spectroscopy, *Journal of Applied Physics*, **90**(12), pp. 5915–5923.

BEARD-M. C., TURNER-G. M., AND SCHMUTTENMAER-C. A. (2002). Measuring intramolecular charge transfer via coherent generation of THz radiation, *The Journal of Physical Chemistry A*, **106**(6), pp. 878–883.

BECKMAN-J., AND HARRIES-J. (1975). Submillimeter-wave atmospheric and astrophysical spectroscopy, *Applied Optics*, **14**(2), pp. 470–485.

BELARDI-W., AND KNIGHT-J. C. (2014). Hollow antiresonant fibers with reduced attenuation, *Optics Letters*, **39**(7), pp. 1853–1856.

BENABID-F., KNIGHT-J. C., ANTONOPOULOS-G., AND RUSSELL-P. S. J. (2002). Stimulated raman scattering in hydrogen-filled hollow-core photonic crystal fiber, *Science*, **298**(5592), pp. 399–402.

BERAVAT-R., WONG-G. K., FROSZ-M. H., XI-X. M., AND RUSSELL-P. S. J. (2016). Twist-induced guidance in coreless photonic crystal fiber: A helical channel for light, *Science Advances*, **2**(11), Art. No. e1601421.

BERRY-E., WALKER-G. C., FITZGERALD-A. J., ZINOV'EV-N., CHAMBERLAIN-M., SMYE-S. W., MILES-R. E., AND SMITH-M. A. (2003). Do in vivo terahertz imaging systems comply with safety guidelines?, *Journal of Laser Applications*, **15**(3), pp. 192–198.

BINGHAM-A. L., AND GRISCHKOWSKY-D. R. (2008). Terahertz 2D photonic crystal waveguides, *IEEE Microwave and Wireless Components Letters*, **18**(7), pp. 428–430.

BIRKS-T. A., KNIGHT-J. C., AND RUSSELL-P. S. J. (1997). Endlessly single-mode photonic crystal fiber, *Optics Letters*, **22**(13), pp. 961–963.

BOLIVAR-P. H., BRUCHERSEIFER-M., RIVAS-J. G., GONZALO-R., EDERRA-I., REYNOLDS-A. L., HOLKER-M., AND DE MAAGT-P. (2003). Measurement of the dielectric constant and loss tangent of high dielectric-constant materials at terahertz frequencies, *IEEE Transactions on Microwave Theory and Techniques*, **51**(4), pp. 1062–1066.

BOWDEN-B., HARRINGTON-J. A., AND MITROFANOV-O. (2007). Silver/polystyrene-coated hollow glass waveguides for the transmission of terahertz radiation, *Optics Letters*, **32**(20), pp. 2945–2947.

BOWDEN-B., HARRINGTON-J. A., AND MITROFANOV-O. (2008a). Fabrication of terahertz hollow-glass metallic waveguides with inner dielectric coatings, *Journal of Applied Physics*, **104**(9), Art. No. 093110.

BOWDEN-B., HARRINGTON-J. A., AND MITROFANOV-O. (2008b). Low-loss modes in hollow metallic terahertz waveguides with dielectric coatings, *Applied Physics Letters*, **93**(18), Art. No. 181104.

BROENG-J., BARKOU-S. E., BJARKLEV-A., KNIGHT-J. C., BIRKS-T. A., AND RUSSELL-P. S. J. (1998). Highly increased photonic band gaps in silica/air structures, *Optics Communications*, **156**(4-6), pp. 240–244.

CHANG-T., ZHANG-X., ZHANG-X., AND CUI-H.-L. (2017). Accurate determination of dielectric permittivity of polymers from 75 GHz to 1.6 THz using both S-parameters and transmission spectroscopy, *Applied Optics*, **56**(12), pp. 3287–3292.

CHEN-D., AND CHEN-H. (2010). A novel low-loss terahertz waveguide: Polymer tube, *Optics Express*, **18**(4), pp. 3762–3767.

CHEN-H., LEE-W.-J., HUANG-H.-Y., CHIU-C.-M., TSAI-Y.-F., TSENG-T.-F., LU-J.-T., LAI-W.-L., AND SUN-C.-K. (2011). Performance of THz fiber-scanning near-field microscopy to diagnose breast tumors, *Optics Express*, **19**(20), pp. 19523–19531.

CHEN-H.-T., KERSTING-R., AND CHO-G. C. (2003). Terahertz imaging with nanometer resolution, *Applied Physics Letters*, **83**(15), pp. 3009–3011.

CHEN-H.-W., CHIU-C.-M., LAI-C.-H., KUO-J.-L., CHIANG-P.-J., HWANG-Y.-J., CHANG-H.-C., AND SUN-C.-K. (2009). Subwavelength dielectric-fiber-based THz coupler, *Journal of Lightwave Technology*, **27**(11), pp. 1489–1495.

CHEN-J.-Y., KNAB-J., CERNE-J., AND MARKELZ-A. (2005). Large oxidation dependence observed in terahertz dielectric response for cytochrome c, *Physical Review E*, **72**(4), Art. No. 040901.

CHEN-L.-J., CHEN-H.-W., KAO-T.-F., LU-J.-Y., AND SUN-C.-K. (2006). Low-loss subwavelength plastic fiber for terahertz waveguiding, *Optics Letters*, **31**(3), pp. 308–310.

CHEN-N.-N., LIANG-J., AND REN-L.-Y. (2013). High-birefringence, low-loss porous fiber for single-mode terahertz-wave guidance, *Applied Optics*, **52**(21), pp. 5297–5302.

CHEN-T., HAN-Z., LIU-J., AND HONG-Z. (2014). Terahertz gas sensing based on a simple one-dimensional photonic crystal cavity with high-quality factors, *Applied Optics*, **53**(16), pp. 3454–3458.

CHIU-C.-M., CHEN-H.-W., HUANG-Y.-R., HWANG-Y.-J., LEE-W.-J., HUANG-H.-Y., AND SUN-C.-K. (2009). All-terahertz fiber-scanning near-field microscopy, *Optics Letters*, **34**(7), pp. 1084–1086.

CHO-M., KIM-J., PARK-H., HAN-Y., MOON-K., JUNG-E., AND HAN-H. (2008). Highly birefringent terahertz polarization maintaining plastic photonic crystal fibers, *Optics Express*, **16**(1), pp. 7–12.

CHO-Y., LEE-I., AND CHO-D.-W. (2005). Laser scanning path generation considering photopolymer solidification in micro-stereolithography, *Microsystem Technologies*, **11**(2-3), pp. 158–167.

CLOTHIER-R. H., AND BOURNE-N. (2003). Effects of THz exposure on human primary keratinocyte differentiation and viability, *Journal of Biological Physics*, **29**(2), pp. 179–185.

COLE-B., WILLIAMS-J., KING-B., SHERWIN-M., AND STANLEY-C. (2001). Coherent manipulation of semiconductor quantum bits with terahertz radiation, *Nature*, **410**(6824), pp. 60–63.

COOKE-D., MACDONALD-A., HRYCIW-A., WANG-J., LI-Q., MELDRUM-A., AND HEGMANN-F. (2006). Transient terahertz conductivity in photoexcited silicon nanocrystal films, *Physical Review B*, **73**(19), Art. No. 193311.

COOK-K., CANNING-J., LEON-SAVAL-S., REID-Z., HOSSAIN-M. A., COMATTI-J.-E., LUO-Y., AND PENG-G.-D. (2015). Air-structured optical fiber drawn from a 3D-printed preform, *Optics Letters*, **40**(17), pp. 3966–3969.

CORDEIRO-C. M., FRANCO-M. A., CHESINI-G., BARRETTO-E. C., LWIN-R., CRUZ-C. B., AND LARGE-M. C. (2006). Microstructured-core optical fibre for evanescent sensing applications, *Optics Express*, **14**(26), pp. 13056–13066.

CORKUM-P., ROLLAND-C., AND SRINIVASAN-RAO-T. (1986). Supercontinuum generation in gases, *Physical Review Letters*, **57**(18), Art. No. 2268.

COUNY-F., AND BENABID-F. (2006). Large-pitch kagome-structured hollow-core photonic crystal fiber, *Optics Letters*, **31**(24), pp. 3574–3576.

COUNY-F., BENABID-F., ROBERTS-P., LIGHT-P., AND RAYMER-M. (2007). Generation and photonic guidance of multi-octave optical-frequency combs, *Science*, **318**(5853), pp. 1118–1121.

CROWE-T. W., GLOBUS-T., WOOLARD-D. L., AND HESLER-J. L. (2004). Terahertz sources and detectors and their application to biological sensing, *Philosophical Transactions of the Royal Society of London. Series A: Mathematical, Physical and Engineering Sciences*, **362**(1815), pp. 365–377.

CRUZ-A. L., CORDEIRO-C., AND FRANCO-M. A. (2018). 3D printed hollow-core terahertz fibers, *Fibers*, **6**(3), Art. No. 43.

CRUZ-A. L., FRANCO-M. A., CORDEIRO-C. M., RODRIGUES-G. S., OSÓRIO-J. H., AND DA SILVA-L. E. (2017). Exploring THz hollow-core fiber designs manufactured by 3D printing, *2017 SBMO/IEEE MTT-S Intl. Microwave and Optoelectronics Conference (IMOC)*, IEEE. DOI: 10.1109/IMOC.2017.8121109.

CRUZ-A. L., MIGLIANO-A. C., AND FRANCO-M. A. (2013). Refractive index sensor based on terahertz multimode interference fiber device, *Proc. SPIE Fifth European Workshop on Optical Fibre sensors,* **8794**, Art. No. 87940L.

CRUZ-A. L., SERRÃO-V. A., BARBOSA-C. L., FRANCO-M. A., CORDEIRO-C. M., ARGYROS-A., AND TANG-X. (2015). 3D printed hollow core fiber with negative curvature for terahertz applications, *Journal of Micr. Opto. and Electro. Applications*, **14**, pp. 45–53.

CUI-W., SCHIFF-KEARN-A. W., ZHANG-E., COUTURE-N., TANI-F., NOVOA-D., RUSSELL-P. S. J., AND MÉNARD-J.-M. (2018). Broadband and tunable time-resolved THz system using argon-filled hollow-core photonic crystal fiber, *APL Photonics,* **3**(11), Art. No. 111301.

CUNNINGHAM-P. D., VALDES-N. N., VALLEJO-F. A., HAYDEN-L. M., POLISHAK-B., ZHOU-X.-H., LUO-J., JEN-A. K.-Y., WILLIAMS-J. C., AND TWIEG-R. J. (2011). Broadband terahertz characterization of the refractive index and absorption of some important polymeric and organic electro-optic materials, *Journal of Applied Physics,* **109**(4), Art. No. 043505.

DAVIDSON-D. B. (2010). Computational Electromagnetics for RF and Microwave Engineering, Cambridge University Press.

DAVIES-A. G., BURNETT-A. D., FAN-W., LINFIELD-E. H., AND CUNNINGHAM-J. E. (2008). Terahertz spectroscopy of explosives and drugs, *Materials Today*, **11**(3), pp. 18–26.

DEBORD-B., AMSANPALLY-A., CHAFER-M., BAZ-A., MAUREL-M., BLONDY-J.-M., HUGONNOT-E., SCOL-F., VINCETTI-L., AND GÉRÔME-F. (2017). Ultralow transmission loss in inhibited-coupling guiding hollow fibers, *Optica*, **4**(2), pp. 209–217.

DE MELO-A. A., DA SILVA-T. B., DA SILVA SANTIAGO-M. F., DA SILVA MOREIRA-C., AND SANTA CRUZ-R. M. (2018). Theoretical analysis of sensitivity enhancement by graphene usage in optical fiber surface plasmon resonance sensors, *IEEE Transactions on Instrumentation and Measurement*, **68**(5), pp. 1554–1560.

DEXHEIMER-S. L. (2017). Terahertz Spectroscopy: Principles and Applications, CRC press.

DICKINSON-E. J., EKSTRÖM-H., AND FONTES-E. (2014). COMSOL Multiphysics®: Finite element software for electrochemical analysis. a mini-review, *Electrochemistry communications*, **40**, pp. 71–74.

DOWNER-M. (2002). A new low for nonlinear optics, *Science*, **298**(5592), pp. 373–375.

DUGUAY-M., KOKUBUN-Y., KOCH-T. L., AND PFEIFFER-L. (1986). Antiresonant reflecting optical waveguides in SiO_2-Si multilayer structures, *Applied Physics Letters*, **49**(1), pp. 13–15.

DUPUIS-A. (2010). Dielectric THz Waveguides, PhD thesis, École Polytechnique de Montréal.

DUPUIS-A., ALLARD-J.-F., MORRIS-D., STOEFFLER-K., DUBOIS-C., AND SKOROBOGATIY-M. (2009). Fabrication and THz loss measurements of porous subwavelength fibers using a directional coupler method, *Optics Express*, **17**(10), pp. 8012–8028.

DUPUIS-A., MAZHOROVA-A., DÉSÉVÉDAVY-F., ROZÉ-M., AND SKOROBOGATIY-M. (2010). Spectral characterization of porous dielectric subwavelength THz fibers fabricated using a microstructured molding technique, *Optics Express*, **18**(13), pp. 13813–13828.

DUPUIS-A., STOEFFLER-K., UNG-B., DUBOIS-C., AND SKOROBOGATIY-M. (2011). Transmission measurements of hollow-core THz Bragg fibers, *JOSA B*, **28**(4), pp. 896–907.

EBENDORFF-HEIDEPRIEM-H., AND MONRO-T. M. (2007). Extrusion of complex preforms for microstructured optical fibers, *Optics Express*, **15**(23), pp. 15086–15092.

EGGLETON-B. J., KERBAGE-C., WESTBROOK-P., WINDELER-R. S., AND HALE-A. (2001). Microstructured optical fiber devices, *Optics Express*, **9**(13), pp. 698–713.

EISELE-H., AND HADDAD-G. I. (1998). Two-terminal millimeter-wave sources, *IEEE Transactions on Microwave Theory and Techniques*, **46**(6), pp. 739–746.

FAISAL-M., AND ISLAM-M. S. (2018). Extremely high birefringent terahertz fiber using a suspended elliptic core with slotted airholes, *Applied Optics*, **57**(13), pp. 3340–3347.

FAN-J., LI-Y., ZHANG-X., HU-M., CHAI-L., AND WANG-C. (2015). Predicting mode properties of porous-core honeycomb bandgap THz fibers by semi-analytical theory, *Journal of Lightwave Technology*, **33**(10), pp. 1931–1936.

FEDERICI-J. F., SCHULKIN-B., HUANG-F., GARY-D., BARAT-R., OLIVEIRA-F., AND ZIMDARS-D. (2005). THz imaging and sensing for security applications—explosives, weapons and drugs, *Semiconductor Science and Technology*, **20**(7), Art. No. S266.

FEDULOVA-E., NAZAROV-M. M., ANGELUTS-A., KITAI-M., SOKOLOV-V., AND SHKURINOV-A. (2012). Studying of dielectric properties of polymers in the terahertz frequency range, *Saratov Fall Meeting 2011: Optical Technol. in Biophy. and Medicine XIII*, **8337**, Art. No. 833701.

FERGUSON-B., AND ZHANG-X.-C. (2002). Materials for terahertz science and technology, *Nature Materials*, **1**, pp. 26–33.

FISCHER-B. M., HELM-H., AND JEPSEN-P. U. (2007). Chemical recognition with broadband THz spectroscopy, *Proceedings of the IEEE*, **95**(8), pp. 1592–1604.

FISCHER-B. M., HOFFMANN-M., HELM-H., WILK-R., RUTZ-F., KLEINE-OSTMANN-T., KOCH-M., AND JEPSEN-P. U. (2005). Terahertz time-domain spectroscopy and imaging of artificial RNA, *Optics Express*, **13**(14), pp. 5205–5215.

FITZGERALD-A., BERRY-E., MILES-R., ZINOVEV-N., SMITH-M., AND CHAMBERLAIN-J. (2002). Evaluation of image quality in terahertz pulsed imaging using test objects, *Physics in Medicine and Biology*, **47**(21), Art. No. 3865.

FRANKEL-M. Y., GUPTA-S., VALDMANIS-J. A., AND MOUROU-G. A. (1991). Terahertz attenuation and dispersion characteristics of coplanar transmission lines, *IEEE Transactions on Microwave Theory and Techniques*, **39**(6), pp. 910–916.

FUKUNAGA-K., OGAWA-Y., HAYASHI-S., AND HOSAKO-I. (2007). Terahertz spectroscopy for art conservation, *IEICE Electronics Express*, **4**(8), pp. 258–263.

GALLOT-G., JAMISON-S., MCGOWAN-R., AND GRISCHKOWSKY-D. (2000). Terahertz waveguides, *JOSA B*, **17**(5), pp. 851–863.

GAO-S.-F., WANG-Y.-Y., LIU-X.-L., DING-W., AND WANG-P. (2016). Bending loss characterization in nodeless hollow-core anti-resonant fiber, *Optics Express*, **24**(13), pp. 14801–14811.

GÉRÔME-F., JAMIER-R., AUGUSTE-J.-L., HUMBERT-G., AND BLONDY-J.-M. (2010). Simplified hollow-core photonic crystal fiber, *Optics Letters*, **35**(8), pp. 1157–1159.

GIOVANARDI-F., CUCINOTTA-A., ROZZI-A., CORRADINI-R., BENABID-F., ROSA-L., AND VINCETTI-L. (2019). Hollow core inhibited coupling fibers for biological optical sensing, *Journal of Lightwave Technology*, **37**(11), pp. 2598–2604.

GLOGE-D. (1971). Weakly guiding fibers, *Applied Optics*, **10**(10), pp. 2252–2258.

GOTO-M., QUEMA-A., TAKAHASHI-H., ONO-S., AND SARUKURA-N. (2004). Teflon photonic crystal fiber as terahertz waveguide, *Japanese Journal of Applied Physics*, **43**(2B), Art. No. L317.

GRISCHKOWSKY-D., KEIDING-S., VAN EXTER-M., AND FATTINGER-C. (1990). Far-infrared time-domain spectroscopy with terahertz beams of dielectrics and semiconductors, *JOSA B*, **7**(10), pp. 2006–2015.

GROVES-R., PRADARUTTI-B., KOULOUMPI-E., OSTEN-W., AND NOTNI-G. (2009). 2D and 3D non-destructive evaluation of a wooden panel painting using shearography and terahertz imaging, *NDT and E International*, **42**(6), pp. 543–549.

HABIB-M. S., ANTONIO-LOPEZ-J., MARKOS-C., SCHÜLZGEN-A., AND AMEZCUA-CORREA-R. (2019). Single-mode, low loss hollow-core anti-resonant fiber designs, *Optics Express*, **27**(4), pp. 3824–3836.

HABIB-M. S., BANG-O., AND BACHE-M. (2015). Low-loss hollow-core silica fibers with adjacent nested anti-resonant tubes, *Optics Express*, **23**(13), pp. 17394–17406.

HAN-H., PARK-H., CHO-M., AND KIM-J. (2002). Terahertz pulse propagation in a plastic photonic crystal fiber, *Applied Physics Letters*, **80**(15), pp. 2634–2636.

HAN-P., CHO-G., AND ZHANG-X.-C. (2000). Time-domain transillumination of biological tissues with terahertz pulses, *Optics Letters*, **25**(4), pp. 242–244.

HARRINGTON-J. A., GEORGE-R., PEDERSEN-P., AND MUELLER-E. (2004). Hollow polycarbonate waveguides with inner Cu coatings for delivery of terahertz radiation, *Optics Express*, **12**(21), pp. 5263–5268.

HASAN-M. I., AKHMEDIEV-N., AND CHANG-W. (2017). Positive and negative curvatures nested in an antiresonant hollow-core fiber, *Optics Letters*, **42**(4), pp. 703–706.

HASANUZZAMAN-G., IEZEKIEL-S., MARKOS-C., AND HABIB-M. S. (2018). Hollow-core fiber with nested anti-resonant tubes for low-loss THz guidance, *Optics Communications*, **426**, pp. 477–482.

HASNAIN-G., DIENES-A., AND WHINNERY-J. (1986). Dispersion of picosecond pulses in coplanar transmission lines, *IEEE Transactions on Microwave Theory and Techniques*, **34**(6), pp. 738–741.

HASSANI-A., DUPUIS-A., AND SKOROBOGATIY-M. (2008a). Low loss porous terahertz fibers containing multiple subwavelength holes, *Applied Physics Letters*, **92**(7), Art. No. 071101.

HASSANI-A., DUPUIS-A., AND SKOROBOGATIY-M. (2008b). Porous polymer fibers for low-loss terahertz guiding, *Optics Express*, **16**(9), pp. 6340–6351.

HAUS-H. (1984). *Waves and fields in optoelectronics.*, Prentice-hall, Inc., Englewood Cliffs, NJ 07632, USA, 402.

HIDAKA-T., MINAMIDE-H., ITO-H., NISHIZAWA-J.-I., TAMURA-K., AND ICHIKAWA-S. (2005). Ferroelectric PVDF cladding terahertz waveguide, *IEE Journal of Lightwave Technology*, **23**(8), pp. 2469–2473.

HIRATA-A., KOSUGI-T., TAKAHASHI-H., YAMAGUCHI-R., NAKAJIMA-F., FURUTA-T., ITO-H., SUGAHARA-H., SATO-Y., AND NAGATSUMA-T. (2006). 120-GHz-band millimeter-wave photonic wireless link for 10-Gbps data transmission, *IEEE Transactions on Microwave Theory and Techniques*, **54**(5), pp. 1937–1944.

HIRATA-A., YAMAGUCHI-R., KOSUGI-T., TAKAHASHI-H., MURATA-K., NAGATSUMA-T., KUKUTSU-N., KADO-Y., IAI-N., AND OKABE-S. (2009). 10-Gbps wireless link using InP HEMT MMICs for generating 120-GHz-band millimeter-wave signal, *IEEE Transactions on Microwave Theory and Techniques*, **57**(5), pp. 1102–1109.

HO-L., PEPPER-M., AND TADAY-P. (2008). Signatures and fingerprints, *Nature Photonics*, **2**(9), pp. 541–543.

HONG-B., SWITHENBANK-M., GREENALL-N., CLARKE-R. G., CHUDPOOTI-N., AKKARAEKTHALIN-P., SOMJIT-N., CUNNINGHAM-J. E., AND ROBERTSON-I. D. (2017). Low-loss asymptotically single-mode THz Bragg fiber fabricated by digital light processing rapid prototyping, *IEEE Transactions on Terahertz Science and Technology*, **8**(1), pp. 90–99.

HUANG-P.-P., HUANG-T.-W., WANG-H., LIN-E. W., SHU-Y., DOW-G. S., LAI-R., BIEDENBENDER-M., AND ELLIOTT-J. H. (1997). A 94-GHz 0.35-W power amplifier module, *IEEE Transactions on Microwave Theory and Techniques*, **45**(12), pp. 2418–2423.

HU-B. B., AND NUSS-M. C. (1995). Imaging with terahertz waves, *Optics Letters*, **20**(16), pp. 1716–1718.

HUBER-R., TAUSER-F., BRODSCHELM-A., BICHLER-M., ABSTREITER-G., AND LEITENSTORFER-A. (2001). How many-particle interactions develop after ultrafast excitation of an electron–hole plasma, *Nature*, **414**(6861), pp. 286–289.

HUMPHREYS-K., LOUGHRAN-J., GRADZIEL-M., LANIGAN-W., WARD-T., MURPHY-J. A., AND O'SULLIVAN-C. (2004). Medical applications of terahertz imaging: A review of current technology and potential applications in biomedical engineering, *The 26th Annual International Conference of the IEEE Engineering in Medicine and Biology Society*, IEEE. DOI: 10.1109/IEMBS.2004.1403410, pp. 1302–1305.

ISHIGAKI-K., SHIRAISHI-M., SUZUKI-S., ASADA-M., NISHIYAMA-N., AND ARAI-S. (2012). Direct intensity modulation and wireless data transmission characteristics of terahertz-oscillating resonant tunnelling diodes, *Electronics Letters*, **48**(10), pp. 582–583.

ISLAM-M. S., CORDEIRO-C. M., NINE-M. J., SULTANA-J., CRUZ-A. L., DINOVITSER-A., NG-B. W.-H., EBENDORFF-HEIDEPRIEM-H., LOSIC-D., AND ABBOTT-D. (2020). Experimental study on glass and polymers: Determining the optimal material for potential use in terahertz technology, *IEEE Access*, **8**, pp. 97204–97214.

ISLAM-M. S., FAISAL-M., AND RAZZAK-S. A. (2017a). Dispersion flattened porous-core honeycomb lattice terahertz fiber for ultra low loss transmission, *IEEE Journal of Quantum Electronics*, **53**(6), Art. No. 8500608.

ISLAM-M. S., RANA-S., ISLAM-M. R., FAISAL-M., RAHMAN-H., AND SULTANA-J. (2016). Porous core photonic crystal fibre for ultra-low material loss in THz regime, *IET Communications*, **10**(16), pp. 2179–2183.

ISLAM-M. S., SULTANA-J., ATAI-J., ISLAM-M. R., AND ABBOTT-D. (2017b). Design and characterization of a low-loss, dispersion-flattened photonic crystal fiber for terahertz wave propagation, *Optik*, **145**, pp. 398–406.

ISLAM-M. S., SULTANA-J., DORRAKI-M., ATAI-J., ISLAM-M. R., DINOVITSER-A., NG-B. W.-H., AND ABBOTT-D. (2018a). Low loss and low dispersion hybrid core photonic crystal fiber for terahertz propagation, *Photonic Network Communications*, **35**(3), pp. 364–373.

ISLAM-M. S., SULTANA-J., OSÓRIO-J. H., DINOVITSER-A., NG-B. W., BENABID-F., EBENDORFF-HEIDEPRIEM-H., ABBOTT-D., AND CORDEIRO-C. M. (2021). Single-step tabletop fabrication for low-attenuation terahertz special optical fibers, *Advanced Photonics Research*, **2**(12), Art. No. 2100165.

ISLAM-M. S., SULTANA-J., RANA-S., ISLAM-M. R., FAISAL-M., KAIJAGE-S. F., AND ABBOTT-D. (2017c). Extremely low material loss and dispersion flattened Topas based circular porous fiber for long distance terahertz wave transmission, *Optical Fiber Technology*, **34**, pp. 6–11.

ISLAM-M. S., SULTANA-J., RIFAT-A. A., AHMED-R., DINOVITSER-A., NG-B. W.-H., EBENDORFF-HEIDEPRIEM-H., AND ABBOTT-D. (2018b). Dual-polarized highly sensitive plasmonic sensor in the visible to near-IR spectrum, *Optics Express*, **26**(23), pp. 30347–30361.

ISLAM-M. S., SULTANA-J., RIFAT-A. A., DINOVITSER-A., NG-B. W.-H., AND ABBOTT-D. (2018c). Terahertz sensing in a hollow core photonic crystal fiber, *IEEE Sensors Journal*, **18**(10), pp. 4073–4080.

ISLAM-M., SULTANA-J., CORDEIRO-C. M., CRUZ-A. L., DINOVITSER-A., NG-B.-H., AND ABBOTT-D. (2019). Broadband characterization of glass and polymer materials using THz-TDS, *44th Intl. Conf. on Infra. Milli. and Tera. Waves (IRMMW-THz)*, IEEE. DOI: 10.1109/IRMMW-THz.2019.8874013.

ISLAM-R., HASANUZZAMAN-G., HABIB-M. S., RANA-S., AND KHAN-M. (2015). Low-loss rotated porous core hexagonal single-mode fiber in THz regime, *Optical Fiber Technology*, **24**, pp. 38–43.

ITO-T., MATSUURA-Y., MIYAGI-M., MINAMIDE-H., AND ITO-H. (2007). Flexible terahertz fiber optics with low bend-induced losses, *JOSA B*, **24**(5), pp. 1230–1235.

JACKSON-J. B., BOWEN-J., WALKER-G., LABAUNE-J., MOUROU-G., MENU-M., AND FUKUNAGA-K. (2011). A survey of terahertz applications in cultural heritage conservation science, *IEEE Transactions on Terahertz Science and Technology*, **1**(1), pp. 220–231.

JAMISON-S., MCGOWAN-R., AND GRISCHKOWSKY-D. (2000). Single-mode waveguide propagation and reshaping of sub-ps terahertz pulses in sapphire fibers, *Applied Physics Letters*, **76**(15), pp. 1987–1989.

JEON-T.-I., AND GRISCHKOWSKY-D. (2004). Direct optoelectronic generation and detection of sub-ps-electrical pulses on sub-mm-coaxial transmission lines, *Applied physics Letters*, **85**(25), pp. 6092–6094.

JEON-T.-I., AND GRISCHKOWSKY-D. (2006). THz Zenneck surface wave (THz surface plasmon) propagation on a metal sheet, *Applied Physics Letters,* **88**(6), Art. No. 061113.

JEON-T.-I., ZHANG-J., AND GRISCHKOWSKY-D. (2005). THz Sommerfeld wave propagation on a single metal wire, *Applied Physics Letters,* **86**(16), Art. No. 161904.

JIN-Y.-S., KIM-G.-J., AND JEON-S.-G. (2006). Terahertz dielectric properties of polymers, *Journal of the Korean Physical Society*, **49**(2), pp. 513–517.

KARPOWICZ-N., DAI-J., LU-X., CHEN-Y., YAMAGUCHI-M., ZHAO-H., ZHANG-X.-C., ZHANG-L., ZHANG-C., AND PRICE-GALLAGHER-M. (2008). Coherent heterodyne time-domain spectrometry covering the entire "terahertz gap", *Applied Physics Letters,* **92**(1), Art. No. 011131.

KARPOWICZ-N., ZHONG-H., ZHANG-C., LIN-K.-I., HWANG-J.-S., XU-J., AND ZHANG-X.-C. (2005). Compact continuous-wave subterahertz system for inspection applications, *Applied Physics Letters,* **86**(5), Art. No. 054105.

KAWANO-Y. (2013). Terahertz waves: A tool for condensed matter, the life sciences and astronomy, *Contemporary Physics*, **54**(3), pp. 143–165.

KAWASE-K., OGAWA-Y., WATANABE-Y., AND INOUE-H. (2003). Non-destructive terahertz imaging of illicit drugs using spectral fingerprints, *Optics Express*, **11**(20), pp. 2549–2554.

KEMP-M. C. (2011). Explosives detection by terahertz spectroscopy—a bridge too far?, *IEEE Transactions on Terahertz Science and Technology*, **1**(1), pp. 282–292.

KEMP-M. C., TADAY-P., COLE-B. E., CLUFF-J., FITZGERALD-A. J., AND TRIBE-W. R. (2003). Security applications of terahertz technology, *Terahertz for Military and Security Applications.* DOI: https://doi.org/10.1117/12.500491, Proc. SPIE 5070, pp. 44–52.

KITAGAWA-S., SUZUKI-S., AND ASADA-M. (2016). Wide frequency-tunable resonant tunnelling diode terahertz oscillators using varactor diodes, *Electronics Letters*, **52**(6), pp. 479–481.

KIWA-T., TONOUCHI-M., YAMASHITA-M., AND KAWASE-K. (2003). Laser terahertz-emission microscope for inspecting electrical faults in integrated circuits, *Optics Letters,* **28**(21), pp. 2058–2060.

KLEINE-OSTMANN-T., AND NAGATSUMA-T. (2011). A review on terahertz communications research, *Journal of Infrared, Millimeter, and Terahertz Waves*, **32**(2), pp. 143–171.

KNIGHT-J. C., BROENG-J., BIRKS-T. A., AND RUSSELL-P. S. J. (1998). Photonic band gap guidance in optical fibers, *Science*, **282**(5393), pp. 1476–1478.

KOENIG-S., LOPEZ-DIAZ-D., ANTES-J., BOES-F., HENNEBERGER-R., LEUTHER-A., TESSMANN-A., SCHMOGROW-R., HILLERKUSS-D., AND PALMER-R. (2013). Wireless sub-THz communication system with high data rate, *Nature Photonics*, **7**(12), pp. 977–981.

KÖHLER-E., RAHIMINEJAD-S., AND ENOKSSON-P. (2016). Evaluation of 3D printed materials used to print WR10 horn antennas, *Journal of Physics: Conference Series,* **757**(1), Art. No. 012026, IOP Publishing.

KOLYADIN-A. N., KOSOLAPOV-A. F., PRYAMIKOV-A. D., BIRIUKOV-A. S., PLOTNICHENKO-V. G., AND DIANOV-E. M. (2013). Light transmission in negative curvature hollow core fiber in extremely high material loss region, *Optics Express*, **21**(8), pp. 9514–9519.

KOOPMANS-R. (1999). Die swell or extrudate swell, *Polypropylene*, Springer, pp. 158–162.

KOWALSKI-M., KASTEK-M., PISZCZEK-M., ŻYCZKOWSKI-M., AND SZUSTAKOWSKI-M. (2015). Harmless screening of humans for the detection of concealed objects, *Safety and Security Engineering VI*, **151**, pp. 215–23.

KRUMBHOLZ-N., HOCHREIN-T., VIEWEG-N., HASEK-T., KRETSCHMER-K., BASTIAN-M., MIKULICS-M., AND KOCH-M. (2009). Monitoring polymeric compounding processes inline with THz time-domain spectroscopy, *Polymer Testing*, **28**(1), pp. 30–35.

KULESA-C. (2011). Terahertz spectroscopy for astronomy: From comets to cosmology, *IEEE Transactions on Terahertz Science and Technology*, **1**(1), pp. 232–240.

LAI-C.-H., CHANG-T., AND YEH-Y.-S. (2014). Characteristics of bent terahertz antiresonant reflecting pipe waveguides, *Optics Express*, **22**(7), pp. 8460–8472.

LAI-C.-H., HSUEH-Y.-C., CHEN-H.-W., HUANG-Y.-J., CHANG-H.-C., AND SUN-C.-K. (2009). Low-index terahertz pipe waveguides, *Optics Letters*, **34**(21), pp. 3457–3459.

LAI-C.-H., YOU-B., LU-J.-Y., LIU-T.-A., PENG-J.-L., SUN-C.-K., AND CHANG-H.-C. (2010). Modal characteristics of antiresonant reflecting pipe waveguides for terahertz waveguiding, *Optics Express*, **18**(1), pp. 309–322.

LAURIN-P., GIRARD-M., MARKOV-A., AND SKOROBOGATIY-M. (2014). Hollow core terahertz optical fibers with hyperuniform disordered dielectric reflectors, *39th Int. Conf. on Infra. Milli. and Tera. Waves (IRMMW-THz)*, IEEE. DOI: 10.1109/IRMMW-THz.2014.6956268.

LEAHY-HOPPA-M., FITCH-M., ZHENG-X., HAYDEN-L., AND OSIANDER-R. (2007). Wideband terahertz spectroscopy of explosives, *Chemical Physics Letters*, **434**(4), pp. 227–230.

LEE-H., SCHMIDT-M., TYAGI-H., SEMPERE-L. P., AND RUSSELL-P. S. J. (2008). Polarization-dependent coupling to plasmon modes on submicron gold wire in photonic crystal fiber, *Applied Physics Letters,* **93**(11), Art. No. 111102.

LEE-P., CASPERSON-D., SCHAPPERT-G., AND OLSON-G. L. (1990). X-ray generation from subpicosecond superintense laser- atom interaction, *JOSA B*, **7**(3), pp. 272–275.

LEVITSKAYA-T., AND STERNBERG-B. (2019). Parameters describing the material behavior in an electromagnetic field, *Electrical Spectroscopy of Earth Materials*, Elsevier, Chapter 2.

LEWIS-R. A. (2014). A review of terahertz sources, *Journal of Physics D: Applied Physics,* **47**(37), Art. No. 374001.

LIANG-J., REN-L., CHEN-N., AND ZHOU-C. (2013). Broadband, low-loss, dispersion flattened porous-core photonic bandgap fiber for terahertz (THz)-wave propagation, *Optics Communications*, **295**, pp. 257–261.

LI-H., ATAKARAMIANS-S., LWIN-R., TANG-X., YU-Z., ARGYROS-A., AND KUHLMEY-B. T. (2016a). Flexible single-mode hollow-core terahertz fiber with metamaterial cladding, *Optica*, **3**(9), pp. 941–947.

LI-H., REN-G., ATAKARAMIANS-S., KUHLMEY-B. T., AND JIAN-S. (2016b). Linearly polarized single tm mode terahertz waveguide, *Optics Letters*, **41**(17), pp. 4004–4007.

LI-H., REN-G., ZHU-B., GAO-Y., YIN-B., WANG-J., AND JIAN-S. (2017a). Guiding terahertz orbital angular momentum beams in multimode kagome hollow-core fibers, *Optics Letters*, **42**(2), pp. 179–182.

LI-J., NALLAPPAN-K., GUERBOUKHA-H., AND SKOROBOGATIY-M. (2017b). 3D printed hollow core terahertz Bragg waveguides with defect layers for surface sensing applications, *Optics Express*, **25**(4), pp. 4126–4144.

LI-S., DAI-Z., WANG-Z., QI-P., SU-Q., GAO-X., GONG-C., AND LIU-W. (2019). A 0.1 THz low-loss 3D printed hollow waveguide, *Optik*, **176**, pp. 611–616.

LITCHINITSER-N., ABEELUCK-A., HEADLEY-C., AND EGGLETON-B. (2002). Antiresonant reflecting photonic crystal optical waveguides, *Optics Letters*, **27**(18), pp. 1592–1594.

LIU-C., SU-W., LIU-Q., LU-X., WANG-F., SUN-T., AND CHU-P. K. (2018). Symmetrical dual D-shape photonic crystal fibers for surface plasmon resonance sensing, *Optics Express*, **26**(7), pp. 9039–9049.

LIU-J., LIANG-H., ZHANG-M., AND SU-H. (2015). Terahertz wave transmission within metal-clad antiresonant reflecting hollow waveguides, *Applied Optics*, **54**(14), pp. 4549–4555.

LI-X.-G., ZHANG-Y.-N., ZHOU-X., AND CAI-L. (2018). Simultaneous measurement of electric field and strain with a tandem-interferometric device, *IEEE Transactions on Instrumentation and Measurement*, **67**(4), pp. 965–970.

LÖFFLER-T., BAUER-T., SIEBERT-K., ROSKOS-H. G., FITZGERALD-A., AND CZASCH-S. (2001). Terahertz dark-field imaging of biomedical tissue, *Optics Express*, **9**(12), pp. 616–621.

LU-D., WAN-M., LI-Z., HUANG-S., ZHANG-W., LI-B., LU-X., LI-X., AND FANG-X. (2021). Photonic bandgap terahertz fibers based on honeycombed tubes, *Optics Express*, **29**(26), pp. 43516–43530.

LU-J.-T., HSUEH-Y.-C., HUANG-Y.-R., HWANG-Y.-J., AND SUN-C.-K. (2010). Bending loss of terahertz pipe waveguides, *Optics Express*, **18**(25), pp. 26332–26338.

LU-J.-Y., KUO-C.-C., CHIU-C.-M., CHEN-H.-W., HWANG-Y.-J., PAN-C.-L., AND SUN-C.-K. (2008a). THz interferometric imaging using subwavelength plastic fiber based THz endoscopes, *Optics Express*, **16**(4), pp. 2494–2501.

LU-J.-Y., YU-C.-P., CHANG-H.-C., CHEN-H.-W., LI-Y.-T., PAN-C.-L., AND SUN-C.-K. (2008b). Terahertz air-core microstructure fiber, *Applied Physics Letters*, **92**(6), Art. No. 064105.

LUUKANEN-A., APPLEBY-R., KEMP-M., AND SALMON-N. (2012). Millimeter-wave and terahertz imaging in security applications, *Terahertz Spectroscopy and Imaging*, **171**, Springer, pp. 491–520.

LU-W., AND ARGYROS-A. (2014). Terahertz spectroscopy and imaging with flexible tube-lattice fiber probe, *Journal of Lightwave Technology*, **32**(23), pp. 4621–4627.

LU-W., LOU-S., AND ARGYROS-A. (2015a). Investigation of flexible low-loss hollow-core fibres with tube-lattice cladding for terahertz radiation, *IEEE Journal of Selected Topics in Quantum Electronics*, **22**(2), pp. 214–220.

LU-W., LOU-S., WANG-X., SHEN-Y., AND SHENG-X. (2015b). Demonstration of low-loss flexible fiber with Zeonex tube-lattice cladding for terahertz transmission, *2015 Optical Fiber Communications Conference and Exhibition (OFC)*, https://doi.org/10.1364/OFC.2015.M3D.2.

MANTSCH-H. H., AND NAUMANN-D. (2010). Terahertz spectroscopy: The renaissance of far infrared spectroscopy, *Journal of Molecular Structure*, **964**(1), pp. 1–4.

MARCUSE-D. (1976). Curvature loss formula for optical fibers, *JOSA*, **66**(3), pp. 216–220.

MARKOV-A., GORGUTSA-S., QU-H., AND SKOROBOGATIY-M. (2012). Practical metal-wire THz waveguides, *arXiv preprint arXiv:1206.2984*.

MARQUES-T. H., LIMA-B. M., OSÓRIO-J. H., DA SILVA-L. E., AND CORDEIRO-C. M. (2017). 3D printed microstructured optical fibers, *2017 SBMO/IEEE MTT-S International Microwave and Optoelectronics Conference (Imoc)*, IEEE. DOI: 10.1109/IMOC.2017.8121093.

MA-T., GIRARD-M., SQUIRES-A., LEWIS-R., SJOERD-R., AND SKOROBOGATIY-M. (2017). Hollow-core terahertz optical waveguides with hyperuniform disordered reflectors, *arXiv preprint arXiv:1702.05521*.

MA-T., GUERBOUKHA-H., GIRARD-M., SQUIRES-A. D., LEWIS-R. A., AND SKOROBOGATIY-M. (2016). 3D printed hollow-core terahertz optical waveguides with hyperuniform disordered dielectric reflectors, *Advanced Optical Materials*, **4**(12), pp. 2085–2094.

MA-T., MARKOV-A., WANG-L., AND SKOROBOGATIY-M. (2015). Graded index porous optical fibers–dispersion management in terahertz range, *Optics Express*, **23**(6), pp. 7856–7869.

MATSUURA-Y., AND TAKEDA-E. (2008). Hollow optical fibers loaded with an inner dielectric film for terahertz broadband spectroscopy, *JOSA B*, **25**(12), pp. 1949–1954.

MA-Y., SYCH-Y., ONISHCHUKOV-G., RAMACHANDRAN-S., PESCHEL-U., SCHMAUSS-B., AND LEUCHS-G. (2009). Fiber-modes and fiber-anisotropy characterization using low-coherence interferometry, *Applied Physics B*, **96**(2), pp. 345–353.

MAZHOROVA-A., MARKOV-A., NG-A., CHINNAPPAN-R., SKOROBOGATA-O., ZOUROB-M., AND SKOROBOGATIY-M. (2012a). Label-free bacteria detection using evanescent mode of a suspended core terahertz fiber, *Optics Express*, **20**(5), pp. 5344–5355.

MAZHOROVA-A., MARKOV-A., UNG-B., ROZÉ-M., GORGUTSA-S., AND SKOROBOGATIY-M. (2011). Thin chalcogenide capillaries as efficient waveguides in the mid-IR-THz spectral range, *arXiv preprint arXiv:1112.5079*.

MAZHOROVA-A., MARKOV-A., UNG-B., ROZÉ-M., GORGUTSA-S., AND SKOROBOGATIY-M. (2012b). Thin chalcogenide capillaries as efficient waveguides from mid-infrared to terahertz, *JOSA B*, **29**(8), pp. 2116–2123.

MCCLATCHEY-R. A. (1972). *Optical Properties of the Atmosphere*, number 411, Air Force Cambridge Research Laboratories, Office of Aerospace Research.

MCGOWAN-R., GALLOT-G., AND GRISCHKOWSKY-D. (1999). Propagation of ultrawideband short pulses of terahertz radiation through submillimeter-diameter circular waveguides, *Optics Letters*, **24**(20), pp. 1431–1433.

MEI-S., KONG-D., WANG-L., MA-T., ZHU-Y., ZHANG-X., HE-Z., HUANG-X., AND ZHANG-Y. (2019). Suspended graded-index porous core POF for ultra-flat near-zero dispersion terahertz transmission, *Optical Fiber Technology,* **52**, Art. No. 101946.

MENDIS-R. (2006). Nature of subpicosecond terahertz pulse propagation in practical dielectric-filled parallel-plate waveguides, *Optics Letters*, **31**(17), pp. 2643–2645.

MENDIS-R., AND GRISCHKOWSKY-D. (2000). Plastic ribbon THz waveguides, *Journal of Applied Physics*, **88**(7), pp. 4449–4451.

MENDIS-R., AND GRISCHKOWSKY-D. (2001a). THz interconnect with low-loss and low-group velocity dispersion, *IEEE Microwave and Wireless Components Letters*, **11**(11), pp. 444–446.

MENDIS-R., AND GRISCHKOWSKY-D. (2001b). Undistorted guided-wave propagation of subpicosecond terahertz pulses, *Optics Letters*, **26**(11), pp. 846–848.

MICHIELETTO-M., LYNGSØ-J. K., JAKOBSEN-C., LÆGSGAARD-J., BANG-O., AND ALKESKJOLD-T. T. (2016). Hollow-core fibers for high power pulse delivery, *Optics Express*, **24**(7), pp. 7103–7119.

MITROFANOV-O., AND HARRINGTON-J. A. (2010). Dielectric-lined cylindrical metallic THz waveguides: Mode structure and dispersion, *Optics Express*, **18**(3), pp. 1898–1903.

MITTENDORFF-M., LI-S., AND MURPHY-T. E. (2017). Graphene-based waveguide-integrated terahertz modulator, *ACS Photonics*, **4**(2), pp. 316–321.

MITTLEMAN-D. (2013a). *Sensing with Terahertz Radiation*, Vol. 85, Springer.

MITTLEMAN-D. M. (2013b). Frontiers in terahertz sources and plasmonics, *Nature Photonics*, **7**(9), pp. 666–669.

MITTLEMAN-D. M., HUNSCHE-S., BOIVIN-L., AND NUSS-M. C. (1997). T-ray tomography, *Optics Letters*, **22**(12), pp. 904–906.

MITTLEMAN-D. M., JACOBSEN-R. H., AND NUSS-M. C. (1996). T-ray imaging, *IEEE Journal of Selected Topics in Quantum Electronics*, **2**(3), pp. 679–692.

MITTLEMAN-D. M., JACOBSEN-R. H., NEELAMANI-R., BARANIUK-R. G., AND NUSS-M. C. (1998). Gas sensing using terahertz time-domain spectroscopy, *Applied Physics B*, **67**(3), pp. 379–390.

MOHR-P. J., TAYLOR-B. N., AND NEWELL-D. B. (2008). Codata recommended values of the fundamental physical constants: 2006, *Journal of Physical and Chemical Reference Data*, **80**(3), pp. 633–1284.

MOLLAH-M. A., HABIB-M. S., AND HABIB-M. S. (2020a). Novel hollow-core asymmetric conjoined-tube anti-resonant fiber for low-loss THz wave guidance, *OSA Continuum*, **3**(5), pp. 1169–1176.

MOLLAH-M. A., RANA-S., AND SUBBARAMAN-H. (2020b). Polarization filter realization using low-loss hollow-core anti-resonant fiber in THz regime, *Results in Physics,* **17***,* Art. No. 103092.

MULLINS-J. (2002). Using unusable frequencies [solid-state terahertz laser], *IEEE Spectrum*, **39**(7), pp. 22–23.

NAFTALY-M., AND MILES-R. E. (2007). Terahertz time-domain spectroscopy for material characterization, *Proceedings of the IEEE*, **95**(8), pp. 1658–1665.

NAGATSUMA-T., DUCOURNAU-G., AND RENAUD-C. C. (2016). Advances in terahertz communications accelerated by photonics, *Nature Photonics*, **10**(6), pp. 371–379.

NAGATSUMA-T., SONG-H.-J., FUJIMOTO-Y., MIYAKE-K., HIRATA-A., AJITO-K., WAKATSUKI-A., FURUTA-T., KUKUTSU-N., AND KADO-Y. (2009). Giga-bit wireless link using 300–400 GHz bands, *2009 IEEE International Topical Meeting on Microwave Photonics*, pp. 1–4.

NAGEL-M., FÖRST-M., AND KURZ-H. (2006a). THz biosensing devices: Fundamentals and technology, *Journal of Physics: Condensed Matter,* **18**(18)*,* Art. No. S601.

NAGEL-M., HARING BOLIVAR-P., BRUCHERSEIFER-M., KURZ-H., BOSSERHOFF-A., AND BÜTTNER-R. (2002). Integrated THz technology for label-free genetic diagnostics, *Applied Physics Letters*, **80**(1), pp. 154–156.

NAGEL-M., MARCHEWKA-A., AND KURZ-H. (2006b). Low-index discontinuity terahertz waveguides, *Optics Express*, **14**(21), pp. 9944–9954.

NAVARRO-CÍA-M., VITIELLO-M. S., BLEDT-C. M., MELZER-J. E., HARRINGTON-J. A., AND MITROFANOV-O. (2013). Terahertz wave transmission in flexible polystyrene-lined hollow metallic waveguides for the 2.5–5 THz band, *Optics Express*, **21**(20), pp. 23748–23755.

NAZAROV-M. M., SHILOV-A. V., BZHEUMIKHOV-K. A., MARGUSHEV-Z. C., SOKOLOV-V. I., SOTSKY-A. B., AND SHKURINOV-A. P. (2018). Eight-capillary cladding THz waveguide with low propagation losses and dispersion, *IEEE Transactions on Terahertz Science and Technology*, **8**(2), pp. 183–191.

NGUEMA-E., FÉRACHOU-D., HUMBERT-G., AUGUSTE-J.-L., AND BLONDY-J.-M. (2011). Broadband terahertz transmission within the air channel of thin-wall pipe, *Optics Letters*, **36**(10), pp. 1782–1784.

NICHOLS-E., AND TEAR-J. (1925). Joining the infra-red and electric wave spectra, *The Astrophysical Journal*, **9**(6), pp. 211–214.

NIELSEN-K. (2011). *Polymer Fiber Waveguides for Terahertz Radiations*, DTU Fotonik.

NIELSEN-K., RASMUSSEN-H. K., ADAM-A. J., PLANKEN-P. C., BANG-O., AND JEPSEN-P. U. (2009). Bendable, low-loss Topas fibers for the terahertz frequency range, *Optics Express*, **17**(10), pp. 8592–8601.

NIELSEN-K., RASMUSSEN-H. K., JEPSEN-P. U., AND BANG-O. (2011). Porous-core honeycomb bandgap THz fiber, *Optics Letters*, **36**(5), pp. 666–668.

NIKODEM-M., GOMÓŁKA-G., KLIMCZAK-M., PYSZ-D., AND BUCZYŃSKI-R. (2019). Demonstration of mid-infrared gas sensing using an anti-resonant hollow core fiber and a quantum cascade laser, *Optics Express*, **27**(25), pp. 36350–36357.

NISSEN-M., DOHERTY-B., HAMPERL-J., KOBELKE-J., WEBER-K., HENKEL-T., AND SCHMIDT-M. A. (2018). UV absorption spectroscopy in water-filled antiresonant hollow core fibers for pharmaceutical detection, *Sensors,* **18**(2), Art. No. 478.

OGAWA-Y., HAYASHI-S., OIKAWA-M., OTANI-C., AND KAWASE-K. (2008). Interference terahertz label-free imaging for protein detection on a membrane, *Optics Express*, **16**(26), pp. 22083–22089.

O'HARA-J. F., EKIN-S., CHOI-W., AND SONG-I. (2019). A perspective on terahertz next-generation wireless communications, *Technologies,* **7**(2), Art. No. 43.

OLIVERO-M., VALLAN-A., ORTA-R., AND PERRONE-G. (2017). Single-mode–multimode–single-mode optical fiber sensing structure with quasi-two-mode fibers, *IEEE Transactions on Instrumentation and Measurement*, **67**(5), pp. 1223–1229.

OYAMA-Y., ZHEN-L., TANABE-T., AND KAGAYA-M. (2009). Sub-terahertz imaging of defects in building blocks, *NDT and E International*, **42**(1), pp. 28–33.

PEARCE-G., WIEDERHECKER-G., POULTON-C. G., BURGER-S., AND RUSSELL-P. S. J. (2007). Models for guidance in kagome-structured hollow-core photonic crystal fibres, *Optics Express*, **15**(20), pp. 12680–12685.

PENG-Y., HOU-J., ZHANG-Y., HUANG-Z., XIAO-R., AND LU-Q. (2013). Temperature sensing using the bandgap-like effect in a selectively liquid-filled photonic crystal fiber, *Optics Letters*, **38**(3), pp. 263–265.

PICKWELL-E., AND WALLACE-V. (2006). Biomedical applications of terahertz technology, *Journal of Physics D: Applied Physics,* **39**(17), Art. No. R301.

PIESIEWICZ-R., KLEINE-OSTMANN-T., KRUMBHOLZ-N., MITTLEMAN-D., KOCH-M., SCHOEBEL-J., AND KURNER-T. (2007). Short-range ultra-broadband terahertz communications: Concepts and perspectives, *IEEE Antennas and Propagation Magazine*, **49**(6), pp. 24–39.

POLETTI-F. (2014). Nested antiresonant nodeless hollow core fiber, *Optics Express*, **22**(20), pp. 23807–23828.

POLI-F., CUCINOTTA-A., AND SELLERI-S. (2007). *Photonic Crystal Fibers: Properties and Applications*, Vol. 102, Springer Science and Business Media.

POLI-F., CUCINOTTA-A., SELLERI-S., AND BOUK-A. (2004). Tailoring of flattened dispersion in highly nonlinear photonic crystal fibers, *IEEE Photonics Technology Letters*, **16**(4), pp. 1065–1067.

PONSECA JR-C. S., POBRE-R., ESTACIO-E., SARUKURA-N., ARGYROS-A., LARGE-M. C., AND VAN EIJKELENBORG-M. A. (2008). Transmission of terahertz radiation using a microstructured polymer optical fiber, *Optics Letters*, **33**(9), pp. 902–904.

POPMINTCHEV-T., CHEN-M.-C., ARPIN-P., MURNANE-M. M., AND KAPTEYN-H. C. (2010). The attosecond nonlinear optics of bright coherent x-ray generation, *Nature Photonics*, **4**(12), pp. 822–832.

PUC-U., ABINA-A., RUTAR-M., ZIDANŠEK-A., JEGLIČ-A., AND VALUŠIS-G. (2015). Terahertz spectroscopic identification of explosive and drug simulants concealed by various hiding techniques, *Applied Optics*, **54**(14), pp. 4495–4502.

REID-C. B., PICKWELL-MACPHERSON-E., LAUFER-J. G., GIBSON-A. P., HEBDEN-J. C., AND WALLACE-V. P. (2010). Accuracy and resolution of THz reflection spectroscopy for medical imaging, *Physics in Medicine and Biology,* **55**(16), Art. No. 4825.

REINTJES-J. F. (2012). *Nonlinear Optical Parametric Processes in Liquids and Gases*, Elsevier Academic Press.

REN-G., GONG-Y., SHUM-P., YU-X., AND HU-J. (2009). Polarization maintaining air-core bandgap fibers for terahertz wave guiding, *IEEE Journal of Quantum Electronics*, **45**(5), pp. 506–513.

RONNE-C., THRANE-L., ÅSTRAND-P.-O., WALLQVIST-A., MIKKELSEN-K. V., AND KEIDING-S. R. (1997). Investigation of the temperature dependence of dielectric relaxation in liquid water by THz reflection spectroscopy and molecular dynamics simulation, *The Journal of chemical physics*, **107**(14), pp. 5319–5331.

ROZE-M., UNG-B., MAZHOROVA-A., WALTHER-M., AND SKOROBOGATIY-M. (2011). Suspended core subwavelength fibers: Towards practical designs for low-loss terahertz guidance, *Optics Express*, **19**(10), pp. 9127–9138.

RUSSELL-P. (2003). Photonic crystal fibers, *Science*, **299**(5605), pp. 358–362.

RUSSELL-P. S. J., HÖLZER-P., CHANG-W., ABDOLVAND-A., AND TRAVERS-J. (2014). Hollow-core photonic crystal fibres for gas-based nonlinear optics, *Nature Photonics*, **8**(4), pp. 278–286.

SAKAI-K. (2005). *Terahertz Optoelectronics*, Vol. 6, Springer.

SCHALL-M., WALTHER-M., AND JEPSEN-P. U. (2001). Fundamental and second-order phonon processes in CdTe and ZnTe, *Physical Review B,* **64**(9), Art. No. 094301.

SCHERMER-R. T., AND COLE-J. H. (2007). Improved bend loss formula verified for optical fiber by simulation and experiment, *IEEE Journal of Quantum Electronics*, **43**(10), pp. 899–909.

SEBASTIAN-M., SILVA-M., SOMBRA-A., UBIC-R., AND JANTUNEN-H. (2017). Measurement of microwave dielectric properties and factors affecting them, *Microwave Materials and Applications, Chapter 1*, Wiley.

SEDRA-A., SMITH-K., CARUSONE-T. C., AND GAUDET-V. (2020). Microelectronic Circuits 8th edition, *Chapter 14*, pp. 1235–1236.

SENLIK-Ö., TANG-L., TOR-NGERN-P., AND YOSHIE-T. (2010). Optical microcavities clad by low-absorption electrode media, *IEEE Photonics Journal*, **2**(5), pp. 794–801.

SETTI-V., VINCETTI-L., AND ARGYROS-A. (2013). Flexible tube lattice fibers for terahertz applications, *Optics Express*, **21**(3), pp. 3388–3399.

SHEN-Y.-C. (2011). Terahertz pulsed spectroscopy and imaging for pharmaceutical applications: A review, *International Journal of Pharmaceutics*, **417**(1-2), pp. 48–60.

SHEN-Y., LO-A. T., TADAY-P., COLE-B., TRIBE-W., AND KEMP-M. (2005). Detection and identification of explosives using terahertz pulsed spectroscopic imaging, *Applied Physics Letters*, **86**(24), Art. No. 241116.

SHI-Z., SONG-L., AND ZHANG-T. (2019). Optical and electrical characterization of pure PMMA for terahertz wide-band metamaterial absorbers, *Journal of Infrared, Millimeter, and Terahertz Waves*, **40**(1), pp. 80–91.

SIEBERT-K. J., LÖFFLER-T., QUAST-H., THOMSON-M., BAUER-T., LEONHARDT-R., CZASCH-S., AND ROSKOS-H. G. (2002). All-optoelectronic continuous wave THz imaging for biomedical applications, *Physics in Medicine and Biology*, **47**(21), Art. No. 3743.

SIEGEL-P. (2010). THz for space: The golden age, *2010 IEEE MTT-S International Microwave Symposium*, pp. 816–819.

SIEGEL-P. H. (2002). Terahertz technology, *IEEE Transactions on Microwave Theory and Techniques*, **50**(3), pp. 910–928.

SIEGEL-P. H. (2003). THz technology: An overview, *Terahertz Sensing Technology: Volume 1: Electronic Devices and Advanced Systems Technology*, pp. 1–44.

SIEGEL-P. H. (2004). Terahertz technology in biology and medicine, *IEEE Transactions on Microwave Theory and Techniques*, **52**(10), pp. 2438–2447.

SIRTORI-C. (2002). Bridge for the terahertz gap, *Nature*, **417**(6885), pp. 132–133.

SKOROBOGATIY-M., AND DUPUIS-A. (2007). Ferroelectric all-polymer hollow Bragg fibers for terahertz guidance, *Applied Physics Letters*, **90**(11), Art. No. 113614.

SMYE-S., CHAMBERLAIN-J., FITZGERALD-A., AND BERRY-E. (2001). The interaction between terahertz radiation and biological tissue, *Physics in Medicine and Biology*, **46**(9), Art. No. R101.

SNYDER-A. W., AND LOVE-J. (2012). *Optical Waveguide Theory*, Springer Science and Business Media.

SOLLAPUR-R., KARTASHOV-D., ZÜRCH-M., HOFFMANN-A., GRIGOROVA-T., SAUER-G., HARTUNG-A., SCHWUCHOW-A., BIERLICH-J., KOBELKE-J., CHEMNITZ-M., SCHMIDT-M. A., AND SPIELMANN-C. (2017). Resonance-enhanced multi-octave supercontinuum generation in antiresonant hollow-core fibers, *Light: Science and Applications*, **6**(12), Art. No. e17124.

SONG-H.-J., AJITO-K., MURAMOTO-Y., WAKATSUKI-A., NAGATSUMA-T., AND KUKUTSU-N. (2012). 24 gbit/s data transmission in 300 GHz band for future terahertz communications, *Electronics Letters*, **48**(15), pp. 953–954.

SONG-H.-J., AND NAGATSUMA-T. (2011). Present and future of terahertz communications, *IEEE Transactions on Terahertz Science and Technology*, **1**(1), pp. 256–263.

SONG-H.-J., KIM-J.-Y., AJITO-K., KUKUTSU-N., AND YAITA-M. (2014). 50-Gb/s direct conversion qpsk modulator and demodulator mmics for terahertz communications at 300 GHz, *IEEE Transactions on Microwave Theory and Techniques*, **62**(3), pp. 600–609.

SRIVASTAVA-T., DAS-R., AND JHA-R. (2013). Highly sensitive plasmonic temperature sensor based on photonic crystal surface plasmon waveguide, *Plasmonics*, **8**(2), pp. 515–521.

STEFANI-A., FLEMING-S. C., AND KUHLMEY-B. T. (2018). Terahertz orbital angular momentum modes with flexible twisted hollow core antiresonant fiber, *APL Photonics,* **3**(5), Art. No. 051708.

STEFANI-A., LWIN-R., AND ARGYROS-A. (2009). Hybrid antiresonant metamaterial waveguides for THz and IR, *41st International Conference on Infrared, Millimeter, and Terahertz waves (IRMMW-THz)*, IEEE. DOI: 10.1109/IRMMW-THz.2016.7758901.

SULTANA-J., ISLAM-M., CORDEIRO-C., DINOVITSER-A., KAUSHIK-M., NG-B. W.-H., AND ABBOTT-D. (2020a). Terahertz hollow core antiresonant fiber with metamaterial cladding, *Fibers,* **8**(2), Art. No. 14.

SULTANA-J., ISLAM-M., HABIB-M., CORDEIRO-C. M., CORDEIRO-M., DINOVITSER-A., NG-B.-H., KOWSHIK-M., EBENDORFF-HEIDEPRIEM-H., AND ABBOTT-D. (2019a). Novel hollow core antiresonant terahertz fiber with metamaterial cladding, *44th Int. Conf. on Infra., Milli.,and Tera. Waves (IRMMW-THz)*, IEEE. DOI: 10.1109/IRMMW-THz.2019.8873836.

SULTANA-J., ISLAM-M. R., FAISAL-M., TALHA-K. M. A., AND ISLAM-M. S. (2019b). Design and analysis of a Zeonex based diamond-shaped core kagome lattice photonic crystal fiber for T-ray wave transmission, *Optical Fiber Technology*, **47**, pp. 55–60.

SULTANA-J., ISLAM-M. S., CORDEIRO-C. M., HABIB-M. S., DINOVITSER-A., KAUSHIK-M., NG-B. W.-H., EBENDORFF-HEIDEPRIEM-H., AND ABBOTT-D. (2022). 3D printed low loss antiresonant terahertz waveguide, *In progress*, Journal of Lightwave Technology.

SULTANA-J., ISLAM-M. S., CORDEIRO-C. M., HABIB-M. S., DINOVITSER-A., NG-B. W.-H., AND ABBOTT-D. (2020b). Exploring low loss and single mode in antiresonant tube lattice terahertz fibers, *IEEE Access*, **8**, pp. 113309–113317.

SULTANA-J., ISLAM-M. S., CORDEIRO-C. M., HABIB-M. S., KAUSHIK-M., DINOVITSER-A., NG-B. W.-H., EBENDORFF-HEIDEPRIEM-H., AND ABBOTT-D. (2020c). Hollow core inhibited coupled antiresonant terahertz fiber: A numerical and experimental study, *IEEE Transactions on Terahertz Science and Technology*, **11**(3), pp. 245–260.

SULTANA-J., ISLAM-M. S., HABIB-M. S., KAUSHIK-M., DINOVITSER-A., NG-B. W.-H., AND ABBOTT-D. (2021). Linearity and nonlinearity in hollow-core antiresonant fiber sensors in the terahertz regime, *IEEE Instrumentation and Measurement Magazine*, **24**(5), pp. 5–11.

SULTANA-J., SAIFUL-M., HABIB-M., CORDEIRO-C. M., DINOVITSER-A., NG-B. W.-H., KAUSHIK-M., EBENDORFF-HEIDEPRIEM-H., AND ABBOTT-D. (2019c). Five-capillary cladding terahertz fiber with low loss and single mode, *44th Int. Conf. on Infra. Milli. and Tera. Waves (IRMMW-THz)*, IEEE. DOI: 10.1109/IRMMW-THz.2019.8874476.

SYSTEM-M. (n.d.a). Discover the world of THz-menlo systems.

SYSTEM-M. (n.d.b). Menlo systems navigation, *https://hobbydocbox.com/Radio/101209369-Menlo-systems-navigation.html*.

TADAY-P. F., BRADLEY-I., ARNONE-D., AND PEPPER-M. (2003). Using terahertz pulse spectroscopy to study the crystalline structure of a drug: A case study of the polymorphs of ranitidine hydrochloride, *Journal of pharmaceutical sciences*, **92**(4), pp. 831–838.

TAHERKHANI-M., SADEGHZADEH-R., TAIBER-J., ORNIK-J., AND KOCH-M. (2019). The effect of humidity and temperature on dielectric fibre–bound THz transmission, *Journal of Infrared, Millimeter, and Terahertz Waves*, **40**(11), pp. 1092–1102.

TALATAISONG-W., GORECKI-J., ISMAEEL-R., BERESNA-M., SCHWENDEMANN-D., APOSTOLOPOULOS-V., AND BRAMBILLA-G. (2020). Singlemoded THz guidance in bendable TOPAS suspended-core fiber directly drawn from a 3D printer, *Scientific Reports,* **10**(1), Art. No. 11045.

TALATAISONG-W., GORECKI-J., VAN PUTTEN-L. D., ISMAEEL-R., WILLIAMSON-J., ADDINALL-K., SCHWENDEMANN-D., BERESNA-M., APOSTOLOPOULOS-V., AND BRAMBILLA-G. (2021). Hollow-core antiresonant terahertz fiber-based TOPAS extruded from a 3D printer using a metal 3D printed nozzle, *Photonics Research*, **9**(8), pp. 1513–1521.

TALATAISONG-W., ISMAEEL-R., BERESNA-M., AND BRAMBILLA-G. (2019). Suspended-core microstructured polymer optical fibers and potential applications in sensing, *Sensors,* **19**(16), Art. No. 3449.

TALATAISONG-W., ISMAEEL-R., MARQUES-T. H., MOUSAVI-S. A., BERESNA-M., GOUVEIA-M., SANDOGHCHI-S. R., LEE-T., CORDEIRO-C. M., AND BRAMBILLA-G. (2018). Mid-IR hollow-core microstructured fiber drawn from a 3D printed PETG preform, *Scientific Reports,* **8**, Art. No. 8113.

TANG-X.-L., SHI-Y.-W., MATSUURA-Y., IWAI-K., AND MIYAGI-M. (2009). Transmission characteristics of terahertz hollow fiber with an absorptive dielectric inner-coating film, *Optics Letters*, **34**(14), pp. 2231–2233.

TANG-X., YU-Z., TU-X., CHEN-J., ARGYROS-A., KUHLMEY-B. T., AND SHI-Y. (2015). Elliptical metallic hollow fiber inner-coated with non-uniform dielectric layer, *Optics Express*, **23**(17), pp. 22587–22601.

THEMISTOS-C., RAHMAN-B. A., RAJARAJAN-M., GRATTAN-K. T., BOWDEN-B., AND HARRINGTON-J. (2007). Characterization of silver/polystyrene (PS)-coated hollow glass waveguides at THz frequency, *Journal of Lightwave Technology*, **25**(9), pp. 2456–2462.

TIAN-D., ZHANG-H., WEN-Q., WANG-Z., LI-S., CHEN-Z., AND GUO-X. (2010). Dual cylindrical metallic grating-cladding polymer hollow waveguide for terahertz transmission with low loss, *Applied Physics Letters,* **97**(13), Art. No. 133502.

TONG-L., GATTASS-R. R., ASHCOM-J. B., HE-S., LOU-J., SHEN-M., MAXWELL-I., AND MAZUR-E. (2003). Subwavelength-diameter silica wires for low-loss optical wave guiding, *Nature*, **426**(6968), pp. 816–819.

TONOUCHI-M. (2007). Cutting-edge terahertz technology, *Nature Photonics*, **1**(2), pp. 97–105.

TRAVERS-J. C., CHANG-W., NOLD-J., JOLY-N. Y., AND RUSSELL-P. S. J. (2011). Ultrafast nonlinear optics in gas-filled hollow-core photonic crystal fibers, *JOSA B*, **28**(12), pp. A11–A26.

TRIBE-W. R., NEWNHAM-D. A., TADAY-P. F., AND KEMP-M. C. (2004). Hidden object detection: Security applications of terahertz technology, *Proc. Terahertz and Gigahertz Electronics and Photonics III,* **5354**,, pp. 168–176.

TUNIZ-A., LWIN-R., ARGYROS-A., FLEMING-S. C., AND KUHLMEY-B. T. (2012). Fabricating metamaterials using the fiber drawing method, *Journal of Visualized Experiments: JoVE,* (68), Art. No. 4299.

UEBEL-P., GÜNENDI-M. C., FROSZ-M. H., AHMED-G., EDAVALATH-N. N., MÉNARD-J.-M., AND RUSSELL-P. S. J. (2016). Broadband robustly single-mode hollow-core PCF by resonant filtering of higher-order modes, *Optics Letters*, **41**(9), pp. 1961–1964.

UNG-B., DUPUIS-A., STOEFFLER-K., DUBOIS-C., AND SKOROBOGATIY-M. (2011). High-refractive-index composite materials for terahertz waveguides: Trade-off between index contrast and absorption loss, *JOSA B*, **28**(4), pp. 917–921.

UTHMAN-M., RAHMAN-B., KEJALAKSHMY-N., AGRAWAL-A., AND GRATTAN-K. (2012). Design and characterization of low-loss porous-core photonic crystal fiber, *IEEE Photonics Journal*, **4**(6), pp. 2315–2325.

VAN EXTER-M., FATTINGER-C., AND GRISCHKOWSKY-D. (1989). Terahertz time-domain spectroscopy of water vapor, *Optics Letters*, **14**(20), pp. 1128–1130.

VAN PUTTEN-L. D. (2019). *Design and Fabrication of Novel Polymer Antiresonant Waveguides*, PhD thesis, University of Southampton.

VAN PUTTEN-L., GORECKI-J., FOKOUA-E. N., APOSTOLOPOULOS-V., AND POLETTI-F. (2018). 3D-printed polymer antiresonant waveguides for short-reach terahertz applications, *Applied Optics*, **57**(14), pp. 3953–3958.

VINCETTI-L. (2009a). Hollow core photonic band gap fiber for THz applications, *Microwave and Optical Technology Letters*, **51**(7), pp. 1711–1714.

VINCETTI-L. (2009b). Numerical analysis of plastic hollow core microstructured fiber for terahertz applications, *Optical Fiber Technology*, **15**(4), pp. 398–401.

VINCETTI-L. (2010). Single-mode propagation in triangular tube lattice hollow-core terahertz fibers, *Optics Communications*, **283**(6), pp. 979–984.

VINCETTI-L., AND SETTI-V. (2010). Waveguiding mechanism in tube lattice fibers, *Optics Express*, **18**(22), pp. 23133–23146.

VINCETTI-L., AND SETTI-V. (2011). Fano resonances in polygonal tube fibers, *Journal of Lightwave Technology*, **30**(1), pp. 31–37.

VINCETTI-L., AND SETTI-V. (2012a). Confinement loss in kagome and tube lattice fibers: Comparison and analysis, *Journal of Lightwave Technology*, **30**(10), pp. 1470–1474.

VINCETTI-L., AND SETTI-V. (2012b). Extra loss due to fano resonances in inhibited coupling fibers based on a lattice of tubes, *Optics Express*, **20**(13), pp. 14350–14361.

VINCETTI-L., AND SETTI-V. (2013). Elliptical hollow core tube lattice fibers for terahertz applications, *Optical Fiber Technology*, **19**(1), pp. 31–34.

VINCETTI-L., SETTI-V., AND ZOBOLI-M. (2010). Terahertz tube lattice fibers with octagonal symmetry, *IEEE Photonics Technology Letters*, **22**(13), pp. 972–974.

VITIELLO-M. S., XU-J.-H., KUMAR-M., BELTRAM-F., TREDICUCCI-A., MITROFANOV-O., BEERE-H. E., AND RITCHIE-D. A. (2011). High efficiency coupling of terahertz micro-ring quantum cascade lasers to the low-loss optical modes of hollow metallic waveguides, *Optics Express*, **19**(2), pp. 1122–1130.

WÅCHTER-M., NAGEL-M., AND KURZ-H. (2005). Frequency-dependent characterization of THz sommerfeld wave propagation on single-wires, *Optics Express*, **13**(26), pp. 10815–10822.

WÄCHTER-M., NAGEL-M., AND KURZ-H. (2007). Metallic slit waveguide for dispersion-free low-loss terahertz signal transmission, *Applied Physics Letters*, **90**(6), Art. No. 061111.

WALKER-G. C., BOWEN-J. W., MATTHEWS-W., ROYCHOWDHURY-S., LABAUNE-J., MOUROU-G., MENU-M., HODDER-I., AND JACKSON-J. B. (2013). Sub-surface terahertz imaging through uneven surfaces: Visualizing neolithic wall paintings in çatalhöyük, *Optics Express*, **21**(7), pp. 8126–8134.

WALLACE-V. P., TADAY-P. F., FITZGERALD-A. J., WOODWARD-R. M., CLUFF-J., PYE-R. J., AND ARNONE-D. D. (2004). Terahertz pulsed imaging and spectroscopy for biomedical and pharmaceutical applications, *Faraday Discussions*, **126**, pp. 255–263.

WALLIS-R., DEGL'INNOCENTI-R., JESSOP-D., REN-Y., KLIMONT-A., SHAH-Y., MITROFANOV-O., BLEDT-C., MELZER-J., HARRINGTON-J., BEERE-H., AND RITCHIE-D. (2015). Efficient coupling of double-metal terahertz quantum cascade lasers to flexible dielectric-lined hollow metallic waveguides, *Optics Express*, **23**(20), pp. 26276–26287.

WALLIS-R., INNOCENTI-R. D., JESSOP-D., MITROFANOV-O., BLEDT-C., MELZER-J., HARRINGTON-J., BEERE-H., AND RITCHIE-D. (2016). Investigation of hollow cylindrical metal terahertz waveguides suitable for cryogenic environments, *Optics Express*, **24**(26), pp. 30002–30014.

WALTHER-M., FISCHER-B. M., AND JEPSEN-P. U. (2003). Noncovalent intermolecular forces in polycrystalline and amorphous saccharides in the far infrared, *Chemical Physics*, **288**(3), pp. 261–268.

WALTHER-M., PLOCHOCKA-P., FISCHER-B., HELM-H., AND UHD JEPSEN-P. (2002). Collective vibrational modes in biological molecules investigated by terahertz time-domain spectroscopy, *Biopolymers: Original Research on Biomolecules*, **67**(4-5), pp. 310–313.

WANG-K., AND MITTLEMAN-D. M. (2004). Metal wires for terahertz wave guiding, *Nature*, **432**(7015), pp. 376–379.

WANG-Y., WHEELER-N. V., COUNY-F., ROBERTS-P., AND BENABID-F. (2011). Low loss broadband transmission in hypocycloid-core kagome hollow-core photonic crystal fiber, *Optics Letters*, **36**(5), pp. 669–671.

WEI-C., WEIBLEN-R. J., MENYUK-C. R., AND HU-J. (2017). Negative curvature fibers, *Advances in Optics and Photonics*, **9**(3), pp. 504–561.

WHITMIRE-S., WOLPERT-D., MARKELZ-A., HILLEBRECHT-J., GALAN-J., AND BIRGE-R. (2003). Protein flexibility and conformational state: A comparison of collective vibrational modes of wild-type and D96N bacteriorhodopsin, *Biophysical Journal*, **85**(2), pp. 1269–1277.

WICKRAMASINGHE-S., DO-T., AND TRAN-P. (2020). FDM-based 3D printing of polymer and associated composite: A review on mechanical properties, defects and treatments, *Polymers*, **12**(7), Art. No. 1529.

WILTSE-J. C. (1984). History of millimeter and submillimeter waves, *IEEE Transactions on Microwave Theory and Techniques*, **32**(9), pp. 1118–1127.

WITHAYACHUMNANKUL-W. (20o9). *Design and Fabrication of Novel Polymer Antiresonant Waveguides*, PhD thesis, The University of Adelaide.

WOODWARD-R., COLE-B., WALLACE-V., ARNONE-D. D., PYE-R., LINFIELD-E., PEPPER-M., AND DAVIES-A. (2001). Terahertz pulse imaging of in-vitro basal cell carcinoma samples, *Technical Digest. Summaries of papers presented at the Conference on Lasers and Electro-Optics. Postconference Technical Digest (IEEE Cat. No. 01CH37170)*, IEEE, pp. 329–330.

WOODWARD-R. M., WALLACE-V. P., COLE-B. E., PYE-R. J., ARNONE-D. D., LINFIELD-E. H., AND PEPPER-M. (2002). Terahertz pulse imaging in reflection geometry of skin tissue using time-domain analysis techniques, *Clinical Diagnostic Systems: Technologies and Instrumentation*, Vol. 4625, pp. 160–169.

WOOLARD-D. L., BROWN-R., PEPPER-M., AND KEMP-M. (2005). Terahertz frequency sensing and imaging: A time of reckoning future applications?, *Proceedings of the IEEE*, **93**(10), pp. 1722–1743.

WOYESSA-G. (2017). *Speciality and Microstructured Polymer Optical* FBG *Sensors*, PhD thesis, Technical University of Denmark.

WU-D. S., ARGYROS-A., AND LEON-SAVAL-S. G. (2011a). Reducing the size of hollow terahertz waveguides, *Journal of Lightwave Technology*, **29**(1), pp. 97–103.

WU-Z., NG-W.-R., GEHM-M., AND XIN-H. (2010). Hollow-core electromagnetic band gap (EBG) waveguide fabricated by rapid prototyping for low-loss terahertz guiding, *2010 IEEE MTT-S International Microwave Symposium*, IEEE, pp. 644–647.

WU-Z., NG-W.-R., GEHM-M. E., AND XIN-H. (2011b). Terahertz electromagnetic crystal waveguide fabricated by polymer jetting rapid prototyping, *Optics Express*, **19**(5), pp. 3962–3972.

XIAO-H., LI-H., WU-B., DONG-Y., XIAO-S., AND JIAN-S. (2019). Low-loss polarization-maintaining hollow-core anti-resonant terahertz fiber, *Journal of Optics*, **21**(8), Art. No. 085708.

XIAO-M., LIU-J., ZHANG-W., SHEN-J., AND HUANG-Y. (2013). THz wave transmission in thin-wall PMMA pipes fabricated by fiber drawing technique, *Optics Communications*, **298**, pp. 101–105.

XIAO-Y.-Y., AND LU-S.-F. (2017). Terahertz circular fiber polarizers using suspended-core spiral fibers, *Applied Optics*, **56**(3), pp. 558–562.

XU-G., NALLAPPAN-K., CAO-Y., AND SKOROBOGATIY-M. (2021). Continuous fabrication of microstructured fibers for THz communications using infinite 3D printing, *2021 IEEE Photonics Society Summer Topicals Meeting Series (SUM)*, 10.1109/SUM48717.2021.9505784.

YAMAMOTO-K., YAMAGUCHI-M., MIYAMARU-F., TANI-M., HANGYO-M., IKEDA-T., MATSUSHITA-A., KOIDE-K., TATSUNO-M., AND MINAMI-Y. (2004). Noninvasive inspection of C-4 explosive in mails by terahertz time-domain spectroscopy, *Japanese Journal of Applied Physics,* **43**(3B), Art. No. L414.

YAN-D., AND LI-J. (2019). Design and analysis of the influence of cladding tubes on novel THz waveguide, *Optik*, **180**, pp. 824–831.

YANG-J., ZHAO-J., GONG-C., TIAN-H., SUN-L., CHEN-P., LIN-L., AND LIU-W. (2016). 3D printed low-loss THz waveguide based on kagome photonic crystal structure, *Optics Express*, **24**(20), pp. 22454–22460.

YANG-S., SHENG-X., ZHAO-G., LOU-S., AND GUO-J. (2020). Anti-deformation low loss double pentagon nested terahertz hollow core fiber, *Optical Fiber Technology,* **56**, Art. No. 102199.

YANG-S., SHENG-X., ZHAO-G., LOU-S., AND GUO-J. (2021). 3D printed effective single-mode terahertz antiresonant hollow core fiber, *IEEE Access*, **9**, pp. 29599–29608.

YANG-S., SHENG-X., ZHAO-G., WANG-Y., AND YU-Y. (2019). Novel pentagram THz hollow core anti-resonant fiber using a 3D printer, *Journal of Infrared, Millimeter, and Terahertz Waves*, **40**(7), pp. 720–730.

YANG-Y., MANDEHGAR-M., AND GRISCHKOWSKY-D. R. (2012). Understanding THz pulse propagation in the atmosphere, *IEEE Transactions on Terahertz Science and Technology*, **2**(4), pp. 406–415.

YAN-S., LOU-S., WANG-X., ZHAO-T., AND ZHANG-W. (2018). High-birefringence hollow-core anti-resonant THz fiber, *Optical and Quantum Electronics,* **50**, Art. No. 162.

YEH-C., SHIMABUKURO-F., AND SIEGEL-P. H. (2005). Low-loss terahertz ribbon waveguides, *Applied optics*, **44**(28), pp. 5937–5946.

YOSHIE-T., TANG-L., AND SU-S.-Y. (2011). Optical microcavity: Sensing down to single molecules and atoms, *Sensors*, **11**(2), pp. 1972–1991.

YOU-B., AND LU-J.-Y. (2016). Remote and in situ sensing products in chemical reaction using a flexible terahertz pipe waveguide, *Optics Express*, **24**(16), pp. 18013–18023.

YOU-B., LIU-T.-A., PENG-J.-L., PAN-C.-L., AND LU-J.-Y. (2009). A terahertz plastic wire based evanescent field sensor for high sensitivity liquid detection, *Optics Express*, **17**(23), pp. 20675–20683.

YOU-B., LU-J.-Y., LIOU-J.-H., YU-C.-P., CHEN-H.-Z., LIU-T.-A., AND PENG-J.-L. (2010). Subwavelength film sensing based on terahertz anti-resonant reflecting hollow waveguides, *Optics Express*, **18**(18), pp. 19353–19360.

YOU-B., LU-J.-Y., YU-C.-P., LIU-T.-A., AND PENG-J.-L. (2012). Terahertz refractive index sensors using dielectric pipe waveguides, *Optics Express*, **20**(6), pp. 5858–5866.

YU-C., FAN-S., SUN-Y., AND PICKWELL-MACPHERSON-E. (2012). The potential of terahertz imaging for cancer diagnosis: A review of investigations to date, *Quantitative Imaging in Medicine and Surgery,* **2**(1), Art. No. 33.

YUDASARI-N., ANTHONY-J., AND LEONHARDT-R. (2014). Terahertz pulse propagation in 3D-printed waveguide with metal wires component, *Optics Express*, **22**(21), pp. 26042–26054.

YU-R.-J., ZHANG-B., ZHANG-Y.-Q., WU-C.-Q., TIAN-Z.-G., AND BAI-X.-Z. (2007a). Proposal for ultralow loss hollow-core plastic Bragg fiber with cobweb-structured cladding for terahertz waveguiding, *IEEE Photonics Technology Letters*, **19**(12), pp. 910–912.

YU-R.-J., ZHANG-Y.-Q., ZHANG-B., WANG-C.-R., AND WU-C.-Q. (2007b). New cobweb-structure hollow Bragg optical fibers, *Optoelectronics Letters*, **3**(1), pp. 10–13.

ZEITLER-J. A., TADAY-P. F., NEWNHAM-D. A., PEPPER-M., GORDON-K. C., AND RADES-T. (2007). Terahertz pulsed spectroscopy and imaging in the pharmaceutical setting-a review, *Journal of Pharmacy and Pharmacology*, **59**(2), pp. 209–223.

ZHANG-X. (2002). Terahertz wave imaging: Horizons and hurdles, *Physics in Medicine and Biology*, **47**(21), Art. No. 3667.

ZHAO-Y., LI-X.-G., CAI-L., AND ZHANG-Y.-N. (2016). Measurement of RI and temperature using composite interferometer with hollow-core fiber and photonic crystal fiber, *IEEE Transactions on Instrumentation and Measurement*, **65**(11), pp. 2631–2636.

ZHOU-X., LI-X., LI-S., AN-G.-W., AND CHENG-T. (2018). Magnetic field sensing based on SPR optical fiber sensor interacting with magnetic fluid, *IEEE Transactions on Instrumentation and Measurement*, **68**(1), pp. 234–239.

ZUBEL-M., FASANO-A., WOYESSA-G., SUGDEN-K., RASMUSSEN-H. K., AND BANG-O. (2016). 3D-*printed* PMMA *Preform for Hollow-core* POF *Drawing*, PhD thesis, Aston University.

Glossary

The physical constants used in this thesis for generating material properties are in accordance with the recommendation of the Committee on Data for Science and Technology (Mohr et al. 2008).

Name of the constants	Symbol	Value
Speed of light in vacuum	c, c_0	2.99792458×10^8 m/s
Vacuum permittivity	ϵ	$8.854187817 \times 10^{-12}$ F/m
Vacuum permeability (magnetic constant)	μ_0	$4\pi \times 10^{-12}$ F/m
Electron charge	e	1.6×10^{-19} C
Electron mass	m_e	$9.1093837015 \times 10^{-15}$ kg
Boltzmann's constant	k_B	1.38064×10^{-23} m^2kg $s^{-2}K^{-1}$
Reduced Planck's constant	$\hbar = \frac{h}{2\pi}$	1.055×10^{-34} Js
Zeonex permittivity	ϵ_z	2.3
Zeonex refractive index	η_{eff}	1.529
UV-resin refractive index	η_{eff}	1.69
Aluminium complex refractive index	$a - ib$	517.34 − i561.13 at 1 THz
Printed Zeonex effective material loss	α_{eff}	5 dB/mm

List of abbreviations

Al	aluminium
Au	gold
ABS	acrylonitrile butadiene styrene
ARC	Australian Research Council
CL	confinement loss
CNC	computer numerical controlled
COC	cyclic-olefin copolymer
COP	cyclo-olefin polymer
CVD	chemical vapor deposition
CW	continuous wave
dB	decibel
DNA	deoxyribonucleic acid
DTG	derivative thermogravimetric
EHF	extended high frequency
EML	effective material loss
EWFD	electromagnetic waves, frequency domain
FDM	fused deposition modelling
FEM	finite element method
FFT	fast Fourier transforms

FOM	figure of merit
F-P	Fabry-Pérot
FTS	fourier transform spectroscopy
FIR	far infrared
FWHM	full width at half maxima
GHz	gigahertz
GVD	group velocity dispersion
HC	hollow-core
HCF	hollow-core fibre
HC-ARPCF	hollow-core antiresonant fibre
HDPE	high-density polyethylene
HRS	high resistivity silicon
IC	inhibited coupling
ITO	indium tin oxide
IR	infrared
LOD	limit of detection
MOF	microstructured optical fibre
MMA	methyl methacrylate
mTIR	modified total internal reflection
NA	numerical aperture
NDT	non-destructive testing
OAM	orbital angular momentum
PBG	photonic bandgap
PC	porous core
PCF	photonic crystal fibre
PLA	polylactic acid

PMD	polarization mode dispersion
PML	perfectly matched layer
PMMA	poly(methyl methacrylate)
PP	polypropylenes
PPO	polypyrrole-polyethylene oxide
QDs	quantum dots
RNA	ribonucleic acid
RI	refractive index
RIU	refractive index unit
SEM	scanning electron microscope
SLA	stereolithography
Teflon	tetrafluoroethylene
TIR	total internal reflection
TPX	polymethylpentene
THz	terahertz
THz-TDS	terahertz time-domain spectroscopy
TM	transverse magnetic
THz	terahertz
UV	ultraviolet

Index

Biography

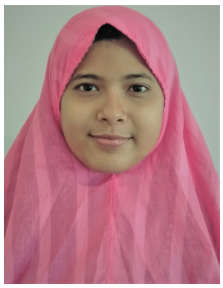

Jakeya Sultana received the B.Sc Engg. degree in Electronics & Telecommunication Engineering from Rajshahi University of Engineering & Technology. After her graduation at 2014 she started working as a Specialist at Robi Axiata Ltd, Bangladesh. Then she took up a post as a Lecturer at Bangladesh University in 2016. Whilst simultaneously teaching, she carried out her M.Sc. degree in Electrical and Electronic Engineering at Islamic University of Technology (IUT), Gazipur, Bangladesh and finished in 2018 securing the highest possible CGPA 4.00 out of 4.00 with a number of high quality publications.

In 2018 she joined the School of Electrical and Electronic Engineering of The University of Adelaide, Australia under a Adelaide Scholarship International (ASI) to study towards her PhD under the supervision of **Prof. Derek Abbott**, **A/Prof. Brian W.-H. Ng** and **Dr Mayank Kaushik**. Sultana was also awarded the Research Travel Scholarship in 2019 and Frank Perry Travelling Scholarship in 2020.

Sultana is a member of Institute for Photonics & Advanced Sensing (IPAS). Her research interests include optical fibre communication, terahertz waveguides, and terahertz sensors for developing advanced electromagnetic devices in the terahertz regime. Sultana has published 40 peer-reviewed articles and 11 conference papers. She actively reviews for *IEEE Access*, *Photonics Research*, *IEEE Journal of Lightwave Technology*, *IEEE Photonics Journal*, *IEEE Sensors Journal*, *IEEE Photonics Technology Letters*, *Optics Express*, *Optics Letters*, and *Applied Optics*, etc.

Jakeya Sultana
jakeya.sultana@adelaide.edu.au
Researcher Profile
Google Scholar
Researchgate
Publons

ORCiD

Linkedin

Scientific genealogy